Modeling of dual-fuel jet break-up, phase change, and mixing

Hesham Gaballa

université PARIS-SACLAY

Modeling of dual-fuel jet break-up, phase change, and mixing

Modélisation de la rupture, du changement de phase, et du mélange d'un jet de double carburant

Thèse de doctorat de l'université Paris-Saclay

École doctorale n°579 : Sciences mécaniques et énergétiques, matériaux et géosciences (SMEMAG)
Spécialité de doctorat: Mécanique des fluides
Graduate School : Sciences de l'ingénierie et des systèmes
Référent : CentraleSupélec

Thèse préparée dans la unité de recherche **IFP Energies Nouvelles**, sous la direction de **Chaouki HABCHI**, chercheur-HDR.

Thèse soutenue à Rueil-Malmaison, le 4 Mai 2023, par

Hesham GABALLA

Composition du jury

Luc VERVISCH Professeur, CORIA-CNRS, INSA Rouen Normandie (FR)	Président
Manolis GAVAISES Professeur, City University of London (UK)	Rapporteur & Examinateur
Michele BATTISTONI Professeur, University of Perugia (IT)	Rapporteur & Examinateur
Aymeric VIÉ Maître de conférences-HDR, EM2C-CNRS, CentraleSupélec, Université Paris-Saclay (FR)	Examinateur
Jean-Charles DE HEMPTINNE Docteur, HDR, IFPEN (FR)	Examinateur

THESE DE DOCTORAT
NNT : 2023UPAST063

université PARIS-SACLAY
ÉCOLE DOCTORALE
Sciences mécaniques et énergétiques, matériaux et géosciences (SMEMAG)
ifp Energies nouvelles

Abstract

The recent stringent emissions legislation poses new challenges to the continuous use of diesel-powered internal combustion engines due to their carbon dioxide emissions and urban pollution, which accelerate climate change and are linked to severe health problems, respectively. Dual-fuel internal combustion engines (DFICE) using alternative renewable fuels are among the promising concepts for reducing pollutant emissions in applications where electrification is not considered a feasible solution to the emissions problem, such as cargo ships and heavy-duty trucks. The effective design of the fuel injection equipment (FIE) is considered a key priority for the industrial development of the DFICEs. Thus, advanced design and simulation tools are required to achieve better designs of such dual-fuel systems. Accordingly, the main objective of the current thesis is to develop a predictive and efficient CFD model for multi-component two-phase flow simulations in the context of DFICE employing renewable fuels such as methanol or ammonia under different thermodynamic (sub- and super-critical) regimes, allowing an automatic/smooth transition between these regimes that can coexist during the fuel injection and mixing events. More specifically, the current work proposes a fully compressible multi-component two-phase real-fluid model (RFM) with a diffused interface and closed by a thermodynamic equilibrium tabulation method based on various real-fluid equations of state (EoSs). The proposed real-fluid thermodynamic tabulation approach can further handle ternary systems in addition to binary systems. The thermodynamic table is generated using the in-house Carnot thermodynamic library, which performs the vapor-liquid equilibrium (VLE) calculation using a robust isothermal–isobaric (TPn) flash coupled to various real-fluid EoSs. The proposed model is first applied to investigate the phase change and mixing processes of a single n-dodecane droplet in a bi-component environment composed of nitrogen and methanol at high pressure and temperature, mimicking a dual-fuel configuration using highly resolved simulations. Next, to address high-pressure fuel injection, a real-fluid atomization model is proposed, in which the RFM model is coupled to a subgrid-scale (SGS) model employing a surface density approach to model fuel atomization within the LES framework. The Engine Combustion Network (ECN) Spray A injector is used as a reference for the proposed model validation. The obtained numerical results have shown good agreement with the various ECN experimental data. Besides, a parametric variation of the ECN Spray A conditions has shown the capability of the RFM model to well predict the experimental variations of the spray characteristics. Following the model validation, the ECN Spray A baseline condition is investigated in a dual-fuel (DF) configuration using methanol as a primary fuel. Finally, the cavitation modeling using the RFM model is investigated in two different configurations, including a transparent injector using water and an industrial injector using ammonia. It has been demonstrated that the model is able to dynamically predict the phase transition process under different operating conditions.

Keywords: Dual-fuel, Real-fluid model, Two-phase flow, Thermodynamic tabulation, high-pressure fuel injection and atomization, Cavitation.

Résumé

Titre: Modélisation de la rupture, du changement de phase, et du mélange d'un jet bi-carburant.

La récente législation stricte sur les émissions pose de nouveaux défis à l'utilisation continue des moteurs à combustion interne en raison de leurs émissions de dioxyde de carbone et de la pollution urbaine, qui accélèrent le changement climatique et sont liées à de graves problèmes de santé, respectivement. Les moteurs à combustion interne à double carburant (DFICE) utilisant des carburants renouvelables alternatifs font partie des concepts prometteurs pour réduire les émissions de polluants dans les applications où l'électrification n'est pas considérée comme une solution réalisable au problème des émissions, comme les cargos et les camions lourds. La conception efficace des équipements d'injection de carburant est considérée comme une priorité essentielle pour le développement industriel des moteurs DFICE. Ainsi, des outils de simulations avancés sont nécessaires pour obtenir de meilleures conceptions de tels systèmes à double carburant. En conséquence, l'objectif principal de cette thèse est de développer un modèle CFD prédictif et efficace pour les simulations d'écoulements diphasiques multi-composants dans le contexte des moteurs DFICE utilisant des carburants renouvelables tels que le méthanol ou l'ammoniac sous différentes conditions thermodynamiques (sous- et super-critiques), permettant une transition automatique et en douceur entre ces régimes qui peuvent coexister pendant l'injection et la préparation du mélange. Plus précisément, cette thèse propose un modèle de fluide réel (RFM) diphasique multi-composants entièrement compressible utilisant l'approche interface diffuse, et fermé par une méthode de tabulation basée sur diverses équations d'état de fluide réel (EoS). L'approche de tabulation thermodynamique des fluides réels proposée peut en outre gérer les systèmes ternaires en plus des systèmes binaires. La table thermodynamique est générée à l'aide de la librairie thermodynamique IFPEN-Carnot, qui effectue le calcul de l'équilibre liquide-vapeur (VLE) à l'aide d'un flash robuste isotherme-isobare (TPn-flash) couplé à divers EoS de fluide réel. Le modèle proposé est d'abord appliqué pour étudier les processus de changement de phase et de mélange d'une seule gouttelette de n-dodécane dans un environnement bi-composant d'azote et de méthanol à hautes pression et temperature, imitant une configuration moteur DFICE à l'aide de simulations hautement résolues. Ensuite, pour traiter l'injection de carburant à haute pression, un modèle d'atomisation de fluide réel est proposé, dans lequel le modèle RFM est couplé à un modèle de sous-maille (SGS), utilisant une approche de densité de surface pour modéliser l'atomisation du carburant dans le cadre de simulations LES. L'injecteur Engine Combustion Network (ECN) Spray A est utilisé comme une référence pour la validation du modèle proposé. Les résultats numériques obtenus ont montré un bon accord avec les différentes données expérimentales ECN. En outre, une variation paramétrique des conditions ECN Spray A a montré la capacité du modèle RFM à bien prédire les variations expérimentales des caractéristiques de spray. Suite à la valida-

tion du modèle, la condition de référence ECN Spray A est étudiée dans une configuration bi-carburant utilisant du méthanol comme carburant principal. Enfin, la modélisation de la cavitation à l'aide du modèle RFM est étudiée dans deux configurations différentes, dont un injecteur transparent utilisant de l'eau et un injecteur industriel utilisant de l'ammoniac. Il a été démontré que le modèle est capable de prédire dynamiquement le processus de transition de phase dans différentes conditions de fonctionnement.

Mots clés: Bi-carburant, modèle à fluide réel, écoulement diphasique, tabulation thermodynamique, injection et atomisation de carburant à haute pression, cavitation.

Acknowledgment

At first, I would like to express my gratitude and thanks to my thesis director, Dr. Chaouki HABCHI for his valuable guidance and engagement along this PhD thesis. Thanks to his advice and remarks, I developed my skills either on the scientific or the personal side throughout the PhD period. I would like also to convey my thanks to my co-supervisor, Dr. Jean-Charles DE-HEMPTINNE for the fruitful discussions, continuous support, and valuable insights, especially for the thermodynamic parts of this work.

I would like also to thank Dr. Angela DI LELLA and Dr. Pascal MOUGIN for providing the Carnot thermodynamic library and the continuous support to resolve the encountered technical issues. I am also grateful to my colleague Sajad JAFARI for his help during my thesis. I would like to express my gratitude to Dr. Gilles BRUNEAUX for always supporting and encouraging me during the thesis. Special thanks go to all my colleagues at IFPEN for the nice moments we had together.

I would like to thank the coordination of the EDEM project, including Prof. Manolis GAVAISES, Dr. Carlos RODRIGUEZ, and Mrs. Amalia PETROVA for their effort to organize every EDEM progress meeting, as well as arranging several trainings and seminars, which have enriched my knowledge significantly. I would also like to thank the other 14 ESRs for sharing happy moments and interesting discussions even though we only met once in person, due to the Coronavirus pandemic.

Finally, I want to express my gratitude to my lovely parents and brother for providing me with unfailing support and continuous encouragement throughout my years of study and through my PhD thesis. This accomplishment would not have been possible without them. I would also like to thank my friends in Egypt and France, who have always been supporting me during the PhD period.

List of Publications

Journal articles

- H. Gaballa, C. Habchi, and J.-C. de Hemptinne. Modeling and LES of high-pressure liquid injection under evaporating and non-evaporating conditions by a real fluid model and surface density approach. *International Journal of Multiphase Flow*, 160: 104372, 2023.

- H. Gaballa, S. Jafari, C. Habchi, and J.-C. de Hemptinne. Numerical investigation of droplet evaporation in high-pressure dual-fuel conditions using a tabulated real-fluid model. *International Journal of Heat and Mass Transfer*, 189:122671, 2022.

- S. Jafari, H. Gaballa, C. Habchi, J.-C. de Hemptinne, and P. Mougin. Exploring the interaction between phase separation and turbulent fluid dynamics in multi-species supercritical jets using a tabulated real-fluid model. *The Journal of Supercritical Fluids*, page 105557, 2022.

- S. Jafari, H. Gaballa, C. Habchi, and J.-C. de Hemptinne. Towards Understanding the Structure of Subcritical and Transcritical Liquid-Gas Interfaces Using a Tabulated Real Fluid Modeling Approach. *Energies*, 14(18):5621, 2021.

Conference articles

- H. Gaballa, C. Habchi, J.-C. de Hemptinne. Real-fluid effects of primary methanol fuel on dual-fuel injection and mixing. *ILASS-Americas, 32nd Annual Conference on Liquid Atomization and Spray Systems*, May 2022, Madison, United States.

- H. Gaballa, C. Habchi, J.-C. de Hemptinne. A tabulated real-fluid model and surface density approach for LES of liquid jets primary atomization. *ILASS-Americas, 32nd Annual Conference on Liquid Atomization and Spray Systems*, May 2022, Madison, United States.

- H. Gaballa, S. Jafari, A. Di-Lella, C. Habchi, and J.-C. de Hemptinne. A tabulated real-fluid modeling approach applied to renewable dual-fuel evaporation and mixing. *International Conference on Liquid Atomization and Spray Systems (ICLASS)*, 1 (1), 2021.

- S. Jafari, H. Gaballa, A. Di-Lella, C. Habchi, and J.-C. de Hemptinne. A tabulated real-fluid modeling approach applied to cryogenic LN2-H2 jets evaporation and mixing at transcritical regime. *International Conference on Liquid Atomization and Spray Systems (ICLASS)*, 1(1), 2021.

Contents

List of Figures

List of Tables

Nomenclature

Latin Symbols

C_p	Heat capacity at constant pressure, $(J\,kg/K)$
C_s	Sound speed, (m/s)
C_v	Heat capacity at constant volume, $(J\,kg/K)$
$C_{s,mix,wood}$	Mixture sound speed using Wood formula, (m/s)
D_k	Diffusion coefficient of species k, (m^2/s)
e	Specific internal energy, (J/kg)
h_k	Specific enthalpy of species k, (J/kg)
$J_{k,i}$	Diffusion flux of species k in the direction i, $(kg/m^2\,s)$
k	Turbulent kinetic energy, (m^2/s^2)
k_{ij}	Binary interaction parameter
K_i	Equilibrium constant
L	Characteristic length, (m)
Oh	Ohnesorge number
P	Pressure, (Pa)
P_c	Critical pressure, (Pa)
Pr	Prandtl number
q_i	Heat flux in the direction i, $(J/s\,m^2)$
R	Specific gas constant, $(J/Kg\,K)$
Re	Reynolds number
S	Entropy, (J/K)
Sc	Schmidt number
T	Temperature, (K)
t	Time, (s)
T_c	Critical temperature, (K)
u_i	Velocity component in the direction i, (m/s)

v	Molar volume, (m^3/mol)
V_c	Computational cell volume, (m^3)
We	Weber number
x_i	Mole fraction of species i in the liquid-phase
y_i	Mole fraction of species i in the vapor-phase
Y_k	Mass fraction of species k in the overall mixture/feed
z_k	Mole fraction of species k in the overall mixture/feed

Greek Symbols

α_g	Gas volume fraction
β_T	Isothermal compressibility
Δ_x	Mesh size, (m)
δ_{ij}	Kronecker delta
Δ_{LES}	Filter size, (m)
ϵ	Turbulent dissipation rate, (m^2/s^3)
λ	Thermal conductivity, $(W/m\,K)$
μ	Dynamic viscosity, $(Pa\,s)$
μ_k	Chemical potential of component k, (J/mol)
ν	kinematic viscosity, (m^2/s)
ω	Acentric factor
ϕ	Pressure ratio
ψ_v	Vapor mole fraction
ρ	Density, (kg/m^3)
Σ	Interfacial surface area density, $(1/m)$
σ	Surface tension coefficient, (N/m)
τ	Viscous stress tensor, (N/m^2)
τ_t	Turbulent time scale, (s)

Abbreviations

2D	Two dimensional
3D	Three dimensional
4D	Four dimensional
ANN	Artificial neural network
CFD	Computational Fluid Dynamics

CFL	Courant-Friedrichs-Lewy
CPA	Cubic Plus Association
DBI	Diffused back illumination
DDM	Discrete Droplet Model
DF	Dual-fuel
DFICE	Dual-fuel internal combustion engine
DIM	Diffuse Interface Model
DNS	Direct Numerical Simulation
ECN	Engine Combustion Network
EE	Eulerian-Eulerian
EL	Eulerian-Lagrangian
ELSA	Eulerian-Lagrangian Spray Atomisation
EoS	Equation of state
FIE	Fuel injection equipment
HEM	Homogeneous Equilibrium Model
HPDI	High pressure direct injection
HRM	Homogeneous Relaxation Model
ICE	Internal combustion engine
IDW	Inverse distance weighting
ISAT	In situ adaptive tabulation
LDV	Laser Doppler Velocimetry
LES	Large Eddy Simulation
LSM	Level Set Method
NIST	National Institute of Standards and Technology
PC-SAFT	Perturbed Chain Statistical Association Fluid Theory
PFI	Port fuel injection
PHI	Phase indicator
PISO	Pressure Implicit with Splitting of Operator
PR	Peng Robinson
RFM	Real-fluid model
RNG $k-\epsilon$	Re-Normalisation Group $k-\epsilon$
SF	Single-fuel

SGS	Subgrid-scale
SIMPLE	Semi-Implicit Method for Pressure-Linked Equations
SMD	Sauter mean diameter
SRK	Soave-Redlich-Kwong
TPn flash	Isothermal-isobaric flash
URANS	Unsteady Reynolds Averaged Navier-Stokes
USAXS	Ultra small-angle X-ray scattering
UVn flash	Isoenergetic-isochoric flash
VLE	Vapor-liquid equilibrium
VOF	Volume of Fluid
VT	Volume translation

Chapter 1

Introduction

Contents

1.1 Background and Motivation

Economic, geopolitical and social trends are forcing the electrification of vehicles. However, the ever-increasing energy needs associated with world population growth and the growing transportation needs in developing economies will only be met by medium/large internal combustion engines (ICE), for which no electrification strategy can reasonably be implemented. In addition, the recent strict emissions legislation in Europe [109] or the US [85], respectively poses new challenges to the continuous use of diesel powered ICEs, owing to their carbon dioxide (CO_2) and soot emissions. These emissions are accelerating climate change as well as linked to severe health problems [211].

Dual-fuel internal combustion engines (DFICE) using alternative renewable fuels are among the promising solutions for reducing combustion emissions. Indeed, DFICEs can be used in applications, where electrification is not considered as a feasible solution to the emissions problem such as cargo ships, heavy duty trucks, and marine engines [126]. The idea of the DFICE is based on the partial substitution of the diesel fuel by high octane gaseous or liquid fuels such as natural gas, short-chained alcohols (methanol/ethanol), hydrogen, and ammonia, which are considered as cleaner fuels that reduce the harmful emissions and (CO_2) in particular.

The high octane gaseous/liquid fuel can be introduced into the cylinder in different manners. The first DFICE configuration, termed port fuel injection (PFI), is illustrated in Fig. 1.1a, where the primary high octane fuel is injected into the intake manifold to be mixed uniformly with air, then the air-primary fuel mixture is drawn into the cylinder during the intake stroke. Then, near the end of the compression stroke, a moderate amount of diesel fuel is directly injected into the cylinder as a pilot injection to ignite the mixture.

The second DFICE configuration, termed high pressure direct injection (HPDI), is depicted in Fig. 1.1b, where a small amount of pilot diesel fuel is firstly injected late in the compression stroke followed by direct injection of the primary fuel. At some instant in the time interval between the two injection events, the pilot diesel fuel auto-ignites and consequently initiates the combustion of the primary fuel. In this configuration, two separate injectors are employed for the injection of the primary fuel and the pilot diesel fuel. However, a single fuel injection equipment (FIE) can be designed to directly inject both fuels as done in the high-pressure dual-fuel (HPDF) injector [89] shown in Fig. 1.2.

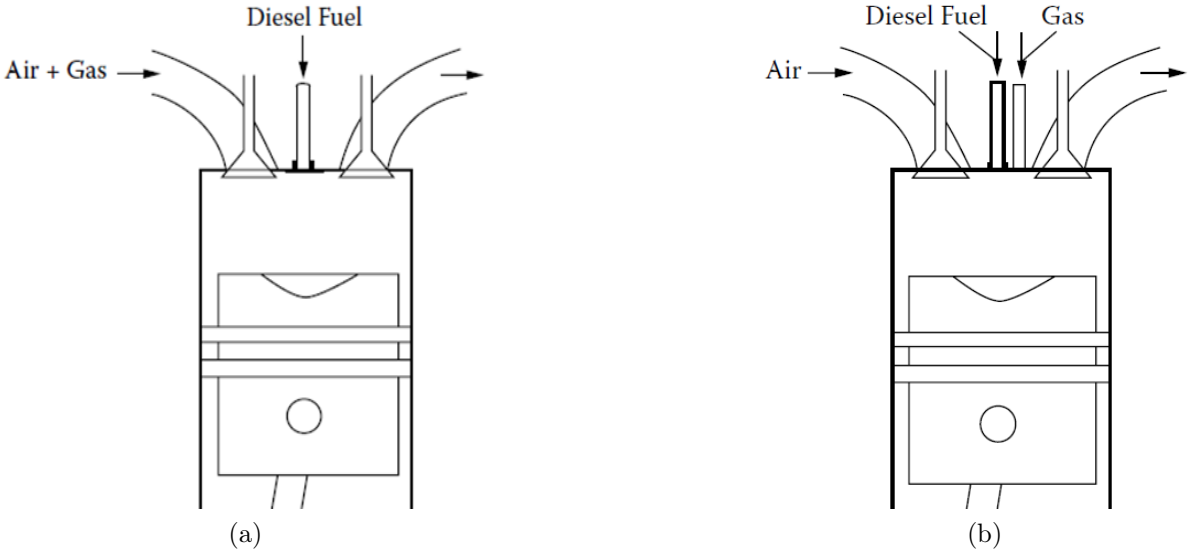

Figure 1.1: Schematics of (a) port fuel injection (PFI) and (b) high pressure direct injection (HPDI) dual-fuel engines [126]

Figure 1.2: High pressure dual-fuel (HPDF) injector [89]

The two main configurations of dual-fuel engines discussed above show the challenges in the employment of such engines. Indeed, the fact that two different fuels are injected in the dual fuel mode leads to more complexity concerning the design of the fuel injection equipment compared to conventional diesel engines. The fuel injectors design must enable short pilot injection duration under high pressure and handle efficiently the variety of fuel mixtures considered in the dual fuel engines. Accordingly, the effective design of the FIE is considered as a key priority for the industrial development of the DFICEs. Thus, advanced design and simulation tools are required by the fuel injectors manufacturers to achieve better design of such dual fuel systems. The current work aims to develop new state of the art Computaional Fluid Dynamics (CFD) models applicable to DFICEs in the framework of the European project entitled "Experimentally validated Direct Numerical Simulation (DNS) and Large Eddy Simulation (LES) approaches for fuel injection, mixing and combustion of dual-fuel engines" (EDEM) [10].

As previously mentioned, several fuels can be employed as primary fuels in the DFICE. For example, natural gas is a highly attractive fuel due to its low cost, widespread distribution and clean burning properties. Natural gas can significantly reduce the (NOx) emissions along with almost zero Particulate matter (PM) production [222]. It has been widely employed as a primary fuel in the DFICE for its economical and environmental benefits [245, 186, 221]. Moreover, short chain alcohols such as methanol and ethanol could also be employed as primary fuels in the dual fuel mode [138, 67, 41, 174]. Indeed, there are several advantages of these fuels, including being renewable, lower cost, and can be produced from biomass. In addition to the previous fuels, ammonia is one of the promising alternative fuels, due to its carbon-free structure, its storage and transportation safety, and reasonable production cost [66]. Recent research [94, 40, 50] is also carried out using hydrogen as a primary fuel, showing its potential for energy efficiency improvement and emissions reduction. However, the employment of the proposed primary fuels, is accompanied by the need of fuel injectors that are designed to function efficiently in the dual-fuel operation mode.

The CFD models have been long used for the design of efficient ICE. However, the existing models fail to predict the processes, where a variety of fuel mixtures are injected and combust simultaneously. Indeed, today's industry-related engine simulations are mostly based upon Reynolds Averaged Navier-Stokes (RANS) numerical approach, where fuel injection and turbulence/chemistry interactions, spray-dynamics phenomena such as droplets break up, turbulence dispersion, collision, evaporation, entrainment of the surrounding gas and eventual mixing with the oxidizer, are modeled. Several spray-breakup modeling approaches have been reported in the literature. However, these phenomenological models could require adjustment to simulate DFICE. Indeed, DFICE requires considering the interaction between the pilot spray and the premixed primary fuel-air charge, which would affect not only the breakup modes, but also the actual mixing between the pilot and the premixed primary fuel-air charge. Since the dynamics of initial spray formation near the nozzle orifices have significant effects on the kinetics of chemical reactions during combustion, highly resolved simulations are needed to accurately quantify the liquid jet fragmentation (i.e. atomization), mixing, and evaporation processes.

Therefore, to gain further insight into such two-phase flow, highly resolved numerical methods such as Direct Numerical Simulation (DNS) and Large-Eddy Simulation (LES) are required. However, DNS is associated with increased computational cost, as very fine grids must be employed with cell size smaller than the smallest characteristic size (few

micrometers for droplets and few nanometers for liquid-gas interface). Therefore, it becomes a necessity to adopt physical models and numerical techniques capable of reducing the computational cost. An improvement in terms of the computational cost could be to use LES in conjunction with the Diffuse Interface Model (DIM). Under subcritical conditions, this approach could be coupled to a subgrid-scale (SGS) model based on the surface density approach, as done in the Eulerian-Lagrangian Spray Atomisation (ELSA) model [239]. Indeed, the computational cost is less as DIM avoids interface reconstruction, such as in the Volume of Fluid (VOF) method [108].

In summary, a predictive and efficient CFD model for multi-component two-phase flow simulations in the context of diesel and dual-fuel engines under different thermodynamic regimes is indeed required for further development of these engines. Therefore, this thesis aims to develop and validate such a new model.

1.2 Fuel injection regimes and modeling approaches

Fuel injection is an essential step toward the combustion process in internal combustion engines. Indeed, the preparation of the fuel-ambient gases mixture significantly affects the combustion efficiency and emissions formation. Computational fluid dynamics (CFD) models capable of simulating fuel injection under various operating conditions are thus essential for the design and optimization of the fuel injection equipment (FIE).

For a single component system, the fuel injection regimes are illustrated in Fig. 1.3. Under a subcritical injection regime, the injected fuel undergoes classical evaporation from liquid state to gaseous state by crossing the saturation line.

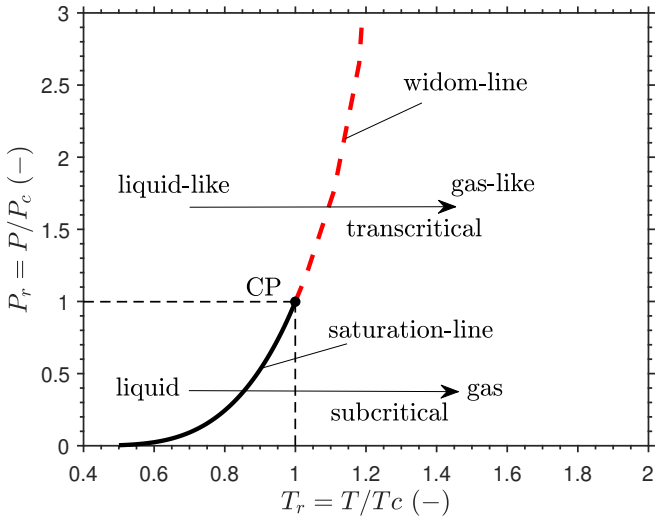

Figure 1.3: Reduced pressure (P_r)-reduced temperature (T_r) diagram of pure fluid demonstrating subcritical and transcritical injection regimes. (CP) denotes the critical point and (T_c, P_c) are the critical temperature and pressure.

Under a transcritical injection regime, the fuel at supercritical pressure but subcritical temperature is injected into an environment, where both pressure and temperature exceed the fuel critical conditions. In such case, the fuel at a liquid-like state is thus heated and crosses the widom-line [21], towards the gas-like region. The widom-line can be interpreted

as the extension of the saturation line in the supercritical region, where it separates liquid-like (high density) and gas-like (low density) regions. The widom line is usually identified based on the maximum of the specific heat under isobaric conditions [21]. Besides, a supercritical injection regime can be also defined when both the temperature and pressure of the injected fuel exceeds its critical point.

For a multi-component system, the definition of the fuel injection regimes is more complex compared to a single component system. This is attributed to the fact that the mixture critical point, which depends on the mixture composition should be considered instead of the pure components critical points, to separate the different thermodynamic regimes.

For instance, Fig. 1.4 shows the variation of the mixture critical point (C.P.m) and the phase boundary for a binary mixture of (n-dodecane/nitrogen) with different nitrogen concentrations. In such case, the involved binary mixture may exhibit different thermodynamic regimes based on the local pressure, temperature, and species composition. Accordingly, both subcritical and supercritical regimes may exist simultaneously [253, 113] in different locations of the chamber.

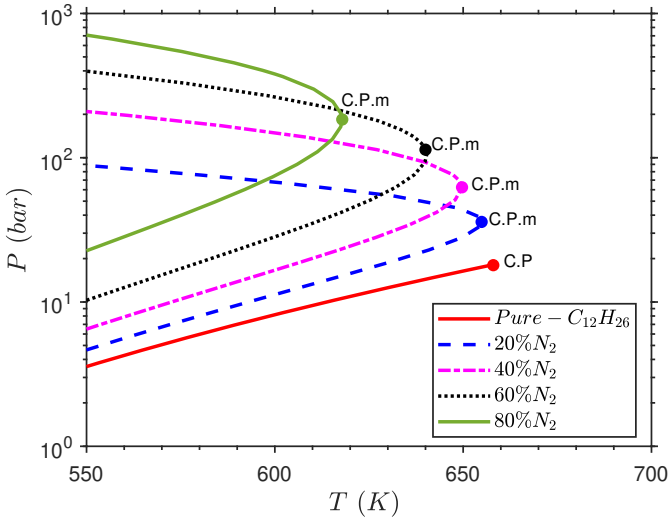

Figure 1.4: Pressure (P)-temperature (T) diagram of a binary mixture of n-dodecane ($C_{12}H_{26}$) and nitrogen (N_2) showing the variation of the mixture critical point (C.P.m) for different nitrogen concentrations in the mixture compared to the pure n-dodecane critical point (C.P). The results here are obtained using the PR-EoS and the nitrogen concentration is by mass fraction.

Modeling of fuel injection also remains a challenge as the scenario of the liquid jet breakup, phase change, and mixing varies significantly depending on whether the fuel is injected under subcritical, transcritial, or supercritical conditions. Accordingly, the physics of the fuel injection process and modeling approaches under the different thermodynamic regimes will be thoroughly discussed in the following subsections.

1.2.1 Subcritical injection

In this section, the physics of liquid jet breakup and atomization under subcritical conditions is first presented. Then, the numerical modeling approaches are thoroughly discussed.

1.2.1.1 Physics of atomization

The physics of liquid jet breakup and atomization under subcritical conditions has been widely investigated in the literature. The classical liquid jet atomization scenario under subcritical conditions is illustrated in Fig. 1.5. Typically, the fuel spray can be divided into two regions, dense spray in the near field and the dilute spray in the far-field. The dense spray region indicates the near nozzle region, where primary atomization initiates from the intact liquid core extending from the injector nozzle exit. In this region, a strong shear force acts on the liquid core surface that lead to the generation of ligaments and droplet, overcoming the stabilizing surface tension effect. This process is usually termed primary atomization. The further disintegration of these droplets/ligaments into smaller droplets is termed secondary atomization, and will continue in the dilute spray region. The fuel droplets are then evaporated, mixed with the ambient gas and subsequently the combustion process starts. The effect of possible cavitation development inside the injector nozzle on the atomization of the liquid jet is also depicted in Fig. 1.5. Indeed, the cavitation phenomenon may takes place inside the injector nozzle, due to an abrupt geometrical variation causing the local pressure to drop to or below the fuel saturation pressure, leading to the generation of gaseous bubbles, which usually starts at the sharp edges of the orifice inlet.

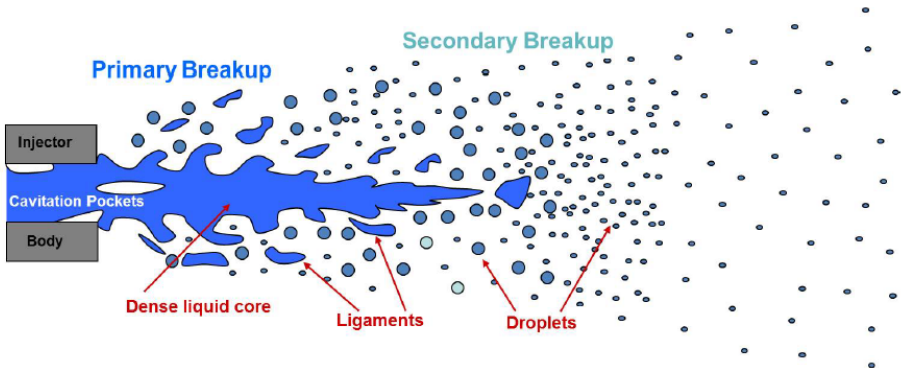

Figure 1.5: Schematic of classical liquid jet atomization under subcritical conditions [65].

The fuel jet breakup and atomization regimes are usually characterized in terms of dimensionless numbers such as the Reynolds number (Re), Weber number (We), and Ohnesorge number (Oh). The definition and physical meaning of each dimensionless number are listed in Table. 1.1.

The liquid jet breakup (primary atomization) regimes defined as function of the (We) and (Re) are depicted in Fig. 1.6, along with schematics of the jet behavior in each regime. At low Reynolds number, Rayleigh jet breakup takes place, due to the growth of axisymmetric oscillations on the jet surface induced by surface tension, where the formed droplets exceed the jet diameter. Further increasing the (Re), droplets are produced by surface waves on the jet surface caused by the relative motion of the jet and the ambient

gas, leading to wind induced breakup. At ultimate (Re) and (Oh), the jet breakup takes place shortly after the nozzle exit leading to a smaller liquid core length.

The secondary droplet breakup has also been classified into different modes as function of the (We) and (Oh) as proposed by Hsiang and Faeth [110] and shown in Fig. 1.7a. Besides, the variation of the droplet breakup modes and morphologies with the Weber number are schematically illustrated in Fig. 1.7b. Detailed description of each breakup mechanism can be found in [93, 181].

No.	Name	Definition	Physical meaning
R_e	Reynolds number	$\frac{\rho U D}{\mu}$	$\frac{Inertial\ force}{Viscous\ force}$
W_e	Weber number	$\frac{\rho U^2 D}{\sigma}$	$\frac{Inertial\ force}{surface\ tension\ force}$
Oh	Ohnesorge number	$\frac{\mu}{\sqrt{\rho \sigma D}}$	$\frac{Viscous\ force}{\sqrt{inetria * surface\ tension}}$

Table 1.1: Dimensionless numbers relevant for primary and secondary atomization. The dimensionless numbers can be defined for both a single droplet and liquid jet. For a single droplet, (ρ, μ) are the density and dynamic viscosity of the gas, (D) is the droplet diameter and (U) is the relative velocity between the droplet and the gas. For a liquid jet, (ρ, μ) are the density and dynamic viscosity of the liquid, (D) is the nozzle diameter and (U) is the injection velocity. (σ) is the surface tension coefficient.

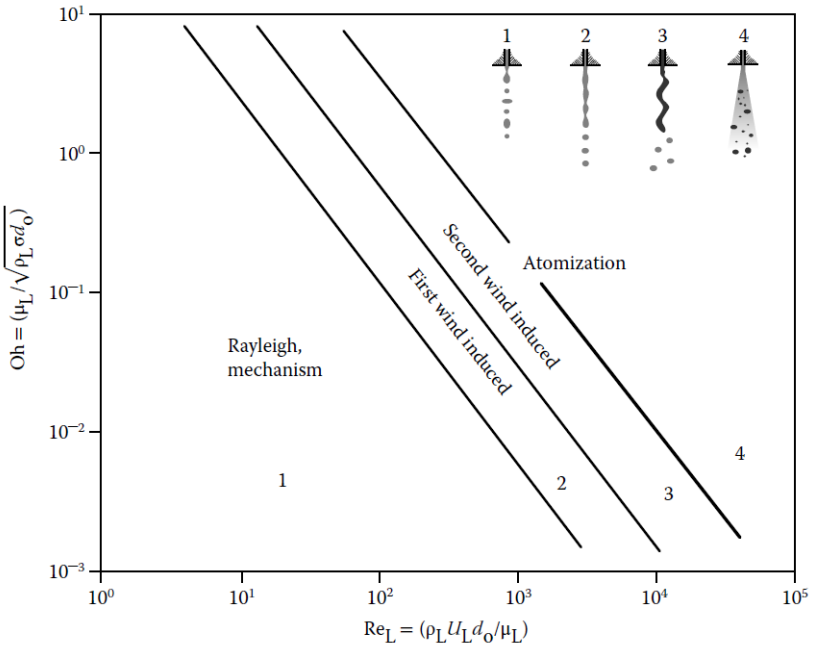

Figure 1.6: Liquid jet breakup regimes [141].

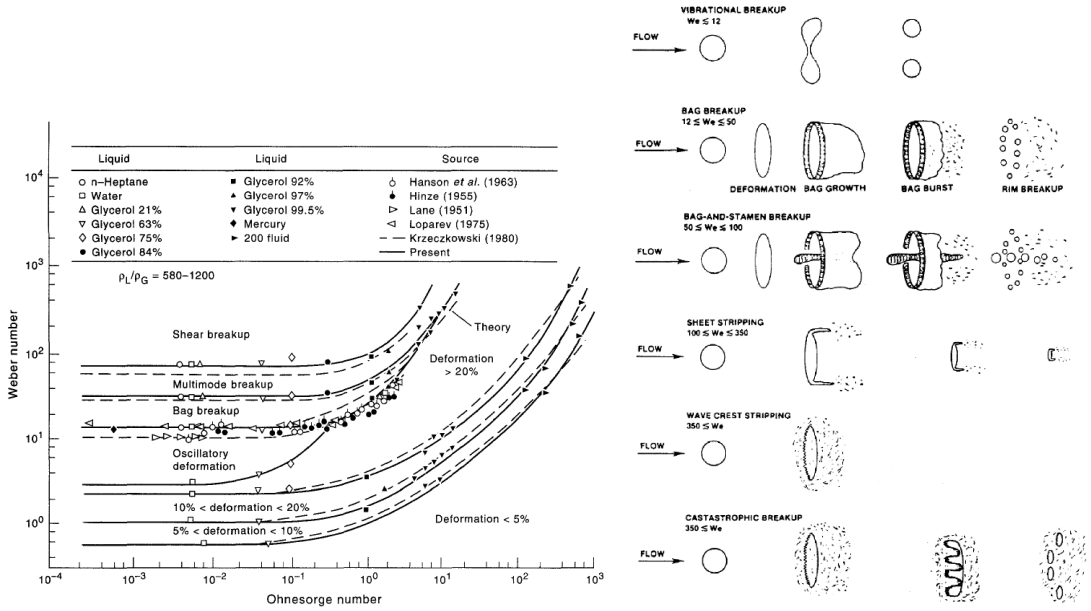

(a) (b)

Figure 1.7: (a) Secondary breakup regimes of single droplets as a function of Weber and Ohnesorge number [110] (b) Schematic of droplet break-up modes [181].

1.2.1.2 Numerical modeling approaches

On the numerical side, extensive work has been carried out in the literature to model the fuel injection and atomization. Indeed, spray simulation is considered one of the main challenges in the automotive design processes [215]. The complexity of spray injection and combustion is due to the variety of length, times scales, and physical processes that take place during the injection process. Indeed, the spatial scale ranges from O (1-10 μm) of individual droplets to O (0.1-1 m) of the entire spray, and the temporal scales vary accordingly. The physical processes include in-nozzle cavitation, liquid atomization, phase change, mixing, and chemical reactions, which all take place under turbulent conditions (see Fig. 1.5). The complexity is highly increased owing to the interaction with turbulence.

Generally, the spray modeling approaches can be divided into two main approaches: Eulerian-Lagrangian (EL) and Eulerian-Eulerian (EE) approaches. In the EL approach [100, 96, 99], the liquid phase is described by Lagrangian parcels (i.e. a group of droplets with identical properties, such as diameter and velocity), whereas the gas phase is considered as the continuous Eulerian carrier fluid. The different interactions (drag, heat and mass transfer,...,etc) between the parcels and the gas are modeled by a one-way or a two-way coupling numerical methods. This Lagrangian method is often referred to as the Discrete Droplet Model (DDM) [71].

Several studies [119, 225, 120, 194, 100, 192] have adapted the EL approach for spray simulation. These simulations have shown the effectiveness of this approach to describe the spray dynamics in the dilute spray region under turbulent conditions. However, an essential issue related to this approach is that it is pre-assumed that the droplet number, velocity, and size distribution are given/known, and the liquid core near the nozzle exit, as well as the in-nozzle effects on the spray formation, are not considered. Indeed, these simulations are performed by specifying the initial and boundary conditions

of the droplets without considering how these droplets are physically generated from the core of the liquid jet by the primary atomization process. Besides, this modeling approach requires various calibration coefficients, which are not universal. It is well known that the near-nozzle physical phenomena have significant impact on the development of the entire spray. Therefore, including the primary atomization region and the associated physics is essential for conducting full spray simulations.

Several models have been proposed to model the primary atomization in the EL framework. The basic idea of these models is to extend the physics of the secondary atomization models to be used in the primary atomization region. Indeed, hypothetical blobs with a characteristic size similar to the nozzle diameter are injected, to which primary atomization models are applied for the spray droplets formation. These blobs could be viewed as a rough representation of the realistic continuous liquid core from the nozzle exit. Examples of primary atomization models employed in such simulations are the WAVE model [192], Kelvin-Helmholtz Rayleigh-Taylor (KH-RT) hybrid model [193], and WAVE-FIPA hybrid model [100]. These models are relatively easy to implement, but an essential issue related to these models is determining the blobs breakup rate. In practice, the break-up rate of blobs is estimated based on experimental data so that the experimental characteristics such as the spray penetration and the droplet distribution are recovered. However, these models fail to predict by themselves the spray characteristics and the problem is further increased for the spray cases, where experimental data are not available.

Accordingly, a more suitable approach to model the dense near-nozzle region and the primary atomization including the in-nozzle flow effects is the Eulerian-Eulerian (EE) approach. In the EE approach, both the liquid and gas phases are treated in an Eulerian framework. Recent studies [27, 250, 102, 200] have demonstrated the superior performance of the Eulerian approach to simulate the dense near-nozzle region along with the in-nozzle flow, compared to the classical Lagrangian method.

Several atomization models have also been proposed within the Eulerian framework based on the surface density approach as initially introduced by (Vallet and Borghi [238], Vallet et al. [239]) in the so-called $(\Sigma - Y)$ model. This model has two main transport equations: the liquid mass fraction (Y) transport equation to track the liquid phase dispersion, and the interfacial surface area density (Σ) transport equation, which is introduced to model the unresolved liquid-gas interface. The (Σ) equation was postulated by analogy with the transport equation of the flame surface density [147]. The first motivation for the surface density equation was to avoid any assumptions concerning the liquid surface shape and allow for a more realistic description of the two-phase flow. The liquid mass fraction and surface density can be used to estimate an equivalent Sauter Mean Diameter (SMD) defined as, $(SMD = 6\alpha_l/\Sigma)$, where $(\alpha_l = \rho Y/\rho_l)$ is the liquid volume fraction.

The known spray SMD may then be used to initiate a Lagrangian description of the spray when it becomes sufficiently diluted, as proposed in the Eulerian-Lagrangian Spray Atomization (ELSA) model [34, 139, 140]. The Lagrangian description of the spray is indeed more appropriate for modeling the diluted spray region, allowing to track individual droplet's velocity, size, and temperature, in contrast to the Eulerian approach, which assumes a single temperature and velocity for both the droplets and the gas phase, and can't consider spray polydispersity, making it unsuitable to model such dispersed spray region. Similar to the ELSA approach, Devassy et al. [65] proposed an Eulerian-Eulerian atomization model using two surface density transport equations to separately model the liquid core atomization and droplet's secondary breakup. In addition, a Probability

Density Function (PDF) based formulation of the $(\Sigma - Y)$ or ELSA model has also been proposed in [12, 234], where a joint PDF of liquid volume fraction and surface density is used to consider the subgrid fluctuations of these two scalars.

Although the EE framework offers a better prediction of the near-nozzle dense spray, there is still some challenges related to this modeling approach. One problem is the large spatial gradient from the injector to the chamber, leading to the difficulty of the continuous modeling from the in-nozzle flow subjected to various phenomena such as cavitation to the external spray in the far-field of the nozzle. However, with the increase in computing power, EE simulations are becoming more efficient and commonplace [63, 27, 200].

Albeit the significant contribution provided by previous studies in the literature for fuel injection and atomization investigation under subcritical conditions, the physics of the liquid jet break-up and mixing change drastically as the ambient pressure and temperature increase towards transcritical or supercritical conditions. Indeed, under such conditions, the classical atomization scenario of the liquid jet depicted in Fig. 1.5 tends to be progressively replaced by a diffusive mixing-like phenomenon. Such conditions are relevant to modern diesel and dual fuel engines and thus has been the subject of investigation of several studies. A detailed review of transcritical and supercritical injection and modeling approaches will be presented in the following subsection.

1.2.2 Transcritical and supercritical injection

In this section, the experimental investigations of transcritical and supercritical jets are first presented. Subsequently, the numerical investigations and the employed models are discussed.

1.2.2.1 Experimental investigations

The physics of the fuel jet break-up and mixing may experience significant variations with increasing the ambient pressure and temperature conditions. Based on the operating conditions, the involved thermodynamic states can be divided into subcritical and supercritical. The liquid jet in the chamber under subcritical conditions is dominated by classical two-phase atomization and spray droplets evaporation with a well defined liquid-gas interface as discussed in the previous subsection. However, at high ambient pressures (typically supercritical relatively to the critical pressure of the injected fuel), the situation becomes significantly different, and a distinct gas-liquid interface may formally not exist, where a diffusion dominated mixing behavior replaces the classical two-phase atomization [113].

Initial experimental observations of transcritical and supercritical injection were in the field of liquid rocket engines (LRE), where typically the fuel and the oxidizer are injected into the combustion chamber at pressure and temperature far exceeding the injected pure species critical points. The experimental investigation by Chehroudi [45] of cryogenic nitrogen injection into gaseous nitrogen at different chamber pressures is illustrated in Fig. 1.8. The effect of increasing the chamber pressure from subcritical to supercritical pressures can be clearly observed.

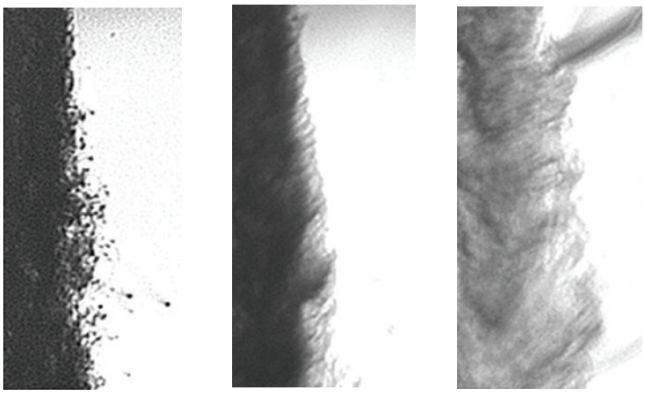

(a) (b) (c)

Figure 1.8: Software-magnified back-illuminated images of a liquid nitrogen jet injected into gaseous nitrogen at a fixed supercritical temperature of 300 K, but varying subcritical to supercritical pressures. (a) $P_{ch} = 3.13$MPa, $P_r = 0.92$, (b) $P_{ch} = 4.14$MPa, $P_r = 1.22$ and (c) $P_{ch} = 9.19$MPa, $P_r = 2.71$. (P_{ch}) denotes the chamber pressure and ($P_r = P_{ch}/P_c$) denotes the reduced pressure, where (P_c) is the critical pressure. For nitrogen, $P_c = 3.39$ MPa and $T_c = 126.2$ K. The images are taken from [45].

Under subcritical pressure, the formation of droplets and two-phase atomization is obvious. Further, increasing the pressure to supercritical pressure, the jet atomization is suppressed, where droplets and ligaments are no longer detected. However, finger-like structures can be observed and the interface tends to be dissolved into the surrounding environment. At the highest chamber pressure (Fig. 1.8c), turbulent mixing appears to be the dominant process.

Similar diffusion dominated mixing at high pressures was observed experimentally for multi-component mixtures. Indeed, the experimental images obtained by Mayer et al. [150], for nitrogen/helium injected in a coaxial injector are illustrated in Fig. 1.9. As the pressure increases from 1 MPa to 6 MPa, the jet morphology changes from subcritical breakup process with clear droplets and ligaments formation to a diffusive mixing process.

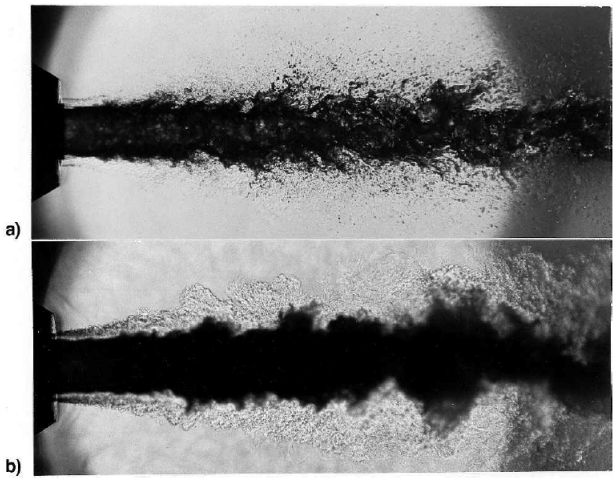

Figure 1.9: Injection of Liquid nitrogen (LN_2) at 97 K with coaxially flowing helium (He) at 280 K into gaseous helium (GHe) at 300 K at chamber pressures of (a) 1 MPa and (b) 6 MPa. The images are taken from [150].

For multi-component mixtures, the identification of the thermodynamic state (subcritical or supercritical) is not straight forward, as the mixture critical point, which depends on the mixture composition should be considered instead of the pure components critical points. Besides, the critical pressure of the mixture may significantly exceed the critical pressures of the pure components, and thus phase separation may take place even at very high pressures (under initially supercritical conditions with respect to the pure components critical points).

Under diesel operating conditions, several studies have also been performed to investigate the morphology of the liquid jet and the transition from classical two-phase atomization to single-phase diffusive mixing behavior. Manin et al. [146] investigated the atomization and mixing processes of n-dodecane fuel sprays injected into environments with progressively higher pressure and temperature, where high-speed imaging is performed using long-distance microscopy and diffused back-illumination techniques. Imaging of spray at the end of injection has showed droplet and ligament formation under low ambient pressure and temperature, but not at high pressure and temperature typical of engine operation, indicating diminished effects of surface tension. Besides, a transition line has been introduced on the $(P - T)$ diagram of pure n-dodecane to separate the classical subcritical evaporation and atomization region from the diffusive mixing region.

Crua et al. [53] performed a high-resolution microscopic visualization of hydrocarbon fuel droplets at the end of the fuel injection event under ambient temperatures and pressures higher than the critical point of the injected fuel. It has been observed that the fuel droplets undergo a gradual transition from subcritical evaporation to dense-fluid mixing, where the transition time depends on the pressure and temperature of the surrounding gas as well as the fuel properties. In addition, a transition criterion from classical evaporation to diffusive mixing has been proposed based on the value of $(T_r\sqrt{P_r})$, as depicted in Fig. 1.10 for n-dodecane droplets. It has also been demonstrated that two-phase classical evaporation is still a significant feature of the diesel spray even at ambient conditions initially above the pure fuel critical point.

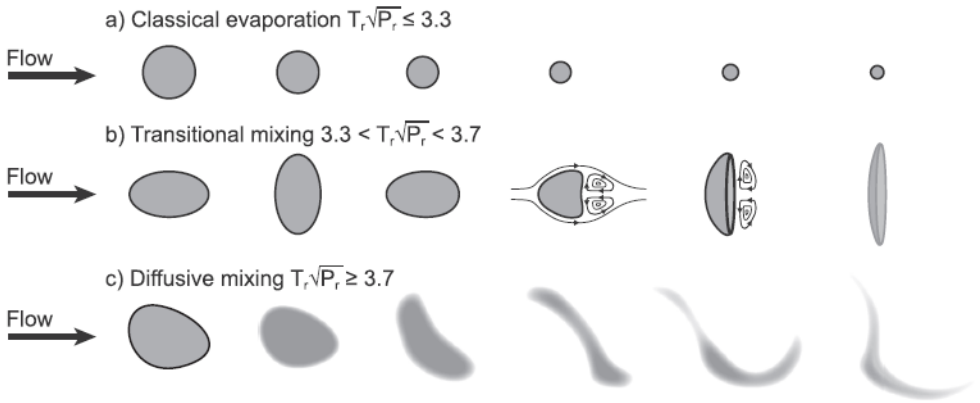

Figure 1.10: The time evolution of moving single n-dodecane droplet into gas at different ambient temperature and pressure, where $(T_r = T/T_c)$ is the reduced temperature and $(P_r = P/P_c)$ is the reduced pressure [53].

1.2.2.2 Numerical investigations

The previously discussed experimental investigations have lead to questions regarding the correct numerical modeling approach of high temperature and pressure diesel relevant conditions. Thereby, various theoretical and numerical investigations have been carried out to complement the experimental observations and provide a better understanding of the fuel injection and mixing process under trans/supercritical conditions.

For instance, Dahms et al. [54, 55] presented a theoretical analysis of the transition from classical two-phase spray atomization to single-phase diffusion dominated mixing for multi-component systems using a real-fluid model that combined a modified 32-term Benedict-Webb-Rubin (BWR) equation of state (EoS) and the linear gradient theory. The performed analysis revealed that the two-phase interface breaks down not necessarily due to vanishing surface tension forces, but also due to broadening the interface thickness (ℓ) coupled with an inherent reduction of the mean free molecular path (λ), which is accompanied by a reduction of the Knudsen number ($Kn = \lambda/\ell$) below a certain critical value.

The employed numerical models are commonly based on the Diffuse Interface Model (DIM) and using a real-fluid EoS to accurately model the fluid properties under transcritical and supercritical conditions. On the one hand, some numerical investigations [159, 137, 104] have relied on a single-phase dense-gas approach, where possible phase change is not considered. On the other hand, more recent studies [149, 254, 135, 78] have included the possible phase change, by solving additional vapor-liquid equilibrium calculations.

Müller et al. [159] performed Large Eddy Simulations (LES) of cryogenic nitrogen injection using the single-phase dense-gas approach and the Peng-Robinson (PR) [176] EoS. Among the results of these LES simulations, the volume translation of the PR-EoS was shown to provide better agreement with the experimental data, due to the improved accuracy of liquid density. Petit et al. [177] investigated the effects of different sub-grid scale turbulence models and EoSs on LES simulations of the cryogenic nitrogen injections.

Rodriguez et al. [198] proposed a model using the Perturbed Chain Statistical Association Fluid Theory (PC-SAFT) EoS, as a more accurate alternative to the cubic EoSs, such as the PR-EoS for trans/supercritical injection. The model was tested for cryogenic nitrogen and n-dodecane injection under supercritical conditions. Similarly, Ningegowda et al. [162] investigated cryogenic nitrogen and n-dodecane injection under supercritical conditions, however using the PR-EoS. The performed study has shown that the variation of the chamber pressure affects the supercritical mixing processes more significantly than the injection temperature.

Using a single-phase dense-gas approach without considering the possible phase change, Lacaze et al. [137] performed LES of the Engine Combustion Network (ECN) Spray A [9], where n-dodecane fuel at 363 K is injected into nitrogen ambient at 60 bar and 900 K. The obtained results have shown good agreement with the experimental data, although phase separation was neglected. It has also been demonstrated the importance of considering real-fluid effects, where the PR-EoS has been employed to capture the non-linearity of the fluid properties at high-pressure conditions.

One of the pioneering work to simulate fuel injection with phase separation was that by Qiu and Reitz [187]. Indeed, the PR-EoS was combined with vapor-liquid equilibrium (VLE) calculations and implemented in a CFD solver. This model has also been used to investigate fuel injection under high-pressure diesel relevant conditions [188]. It has been revealed that the predicted thermodynamic states without considering phase transition

can be very different from the corresponding correct thermodynamic states. Besides, the model predicted the existence of two-phases locally in the dense liquid jet under high temperature and pressure ambient conditions.

Matheis and Hickel [149] proposed a diffused interface two-phase flow model using a thermodynamic model based on the PR-EoS and VLE calculations to consider the phase separation. The model was applied to simulate the ECN Spray A, where the numerical results agreed well with the experimental data, and the occurrence of two-phase states under the high pressure and temperature conditions has been confirmed. They also highlighted some deviation from the experimental data due to the inherent error of the liquid density predicted by the PR-EoS.

Similarly, Yang et al. [254] proposed a multi-component two-phase flow model, where the flow solver is coupled to a VLE solver also based on the PR-EoS. The model have shown good results for the ECN spray A, including the in-nozzle flow. However, one of the encountered issues was the high computational cost of the direct evaluation of the VLE solver during the CFD simulation, especially, when using a non-linear real-fluid EoS.

Rodriguez et al. [199] combined the PC-SAFT EoS and VLE calculations to simulate fuel injection under high-pressure diesel relevant conditions. Besides, a method to model hydrocarbon mixtures as a single pseudo-component has been proposed based on the PC-SAFT EoS to be used in CFD simulations.

Traxinger et al. [231] investigated numerically and experimentally the mixing induced phase separation of n-hexane injected at supercritical temperatures into pure nitrogen. The numerical model included Vapor-liquid equilibrium (VLE) calculations along with the PR-EoS. Besides, simultaneous shadowgraphy and elastic light scattering (ELS) experiments were conducted to capture both the flow structure as well as the phase separation. The comparison between the simulation and the experiments showed good agreement. It was shown that as the initial fuel temperature decreases, classical two-phase atomization tends to take place, due to the mixing induced phase separation.

The direct evaluation of the VLE calculations during CFD simulations especially, when using a complex real-fluid EoS, could be computationally expensive [252, 254]. Accordingly, some recent studies have employed a tabulation approach, where the VLE calculation result and thermodynamics and transport properties are tabulated before the CFD simulation, and then interpolated during the simulation, which is more computationally efficient.

For instance, a tabulated thermodynamic approach based on the PC-SAFT EoS has been proposed by Koukouvinis et al. [135] and applied to the ECN Spray A injector simulation. Jafari et al. [114] used a tabulation approach to investigate the cryogenic injection of liquid nitrogen co-axially injected with hot hydrogen into supercritical nitrogen. The latter model is further used to explore the interaction between phase separation and turbulent fluid dynamics for n-hexane injection in supercritical nitrogen [114]. Fathi et al. [78] employed a rapid phase-equilibrium calculation method [77] that is formulated in a reduced space based on the molar specific volume function. The proposed model was used to simulate the transcritical inert and reacting ECN spray A. Besides, in the proposed model, the combustion source terms are evaluated using a finite-rate chemistry model including real-gas effects based on the fugacity of the species in the mixture.

Among also the challenges faced for the simulation of transcritical injection conditions, is the spurious pressure oscillations that are generated from the non-linearities of the real-fluid EoS. Indeed, it is well-known that such oscillations appear, when fully conservative (FC) two-phase models are combined with a real-fluid EoS [142, 149]. Several treatments

to overcome such spurious pressure oscillations issue have been proposed in the literature. For instance, Ma et al. [142] proposed a double flux model based on a stable entropy formulation to damp the pressure oscillations faced in the transcritical regime. Terashima and Koshi [229] developed a quasi-conservative (QC) scheme solving a pressure evolution equation instead of the energy conservation equation. In addition, some studies [198, 143] have compared between the fully conservative (FC) and quasi-conservative (QC) formulations for the simulation of transcritical conditions. The comparison of the FC and QC formulations under the ECN Spray A condition has shown that the large energy conservation error in QC schemes may produce a nonphysical quick heat-up of the jet [149].

In summary, the previous discussion demonstrated that the correct modeling of high pressure and temperature fuel injection requires certain prerequisites, namely real-fluid EoS, possible phase separation modeling, and proper numerical schemes to avoid spurious pressure oscillations. Besides, the situation tends to be more complex as the involved system is multi-species. It is can be also concluded that a CFD model capable of modeling the fuel injection under subcritical, transcritical, and supercritical regimes, allowing an automatic transition between the different regimes, remains a challenge addressed by the proposed model in the current work.

1.3 Two-phase flow modeling

In this section, the different families of two-phase flow models are first reviewed. Next, the diffuse-interface two-phase flow models are thoroughly discussed along with the different approaches to include the phase change.

1.3.1 Families of two-phase flow models

The flow encountered during the fuel injection process in internal combustion engines is a compressible multi-component two-phase flow undergoing phase change. Modeling and simulation of such two-phase flows is more challenging, when compared to single-phase flows. One of the major challenges is the modeling of the liquid-gas interface and the associated interfacial dynamics. The difficulty arises from the discontinuity of the material properties across the phase interface. Various types of numerical methods have been proposed in the literature to track the interface accurately and to capture its dynamics such as breakup and coalescence. Mainly, two types of methodologies have been adopted, interface tracking and interface capturing methods.

The interface tracking method involves tracking of the interface on the grid points such as front tracking method [121]. In the front tracking method, the interface is tracked by the motion of particles (markers) on the interface and is located explicitly with accurate calculation of the curvature. However, it requires special modeling for capturing the interfacial dynamics.

In the interface capturing methodology, the interface is captured implicitly on a fixed grid with an additional scalar. Three main methods have been proposed in this class, namely Volume of Fluid method (VOF), Level Set Method (LSM), and Diffuse Interface Method (DIM).

In the VOF method [108], a transport equation for the phase-volume fraction (α) is solved to determine the phase nature (pure liquid or pure gas or two-phase) in each computational cell. Cells with two-phases will have a volume fraction value between 0

and 1 and cells with pure single phase will have a value of zero (pure liquid phase) or unity (pure gas phase). One of the main advantages of the VOF method is that mass conservation is ensured, meanwhile owing to the discontinuity of the volume fraction at the interface, special geometric algorithms need to be employed to avoid numerical diffusion.

In the level set method [227], a scalar (ϕ) is defined and set to a constant value (ϕ_o) at the interface, and thus ($\phi > \phi_o$) represents fluid 1 and ($\phi < \phi_o$) represents fluid 2. The main drawback of the LSM is the mass conservation error, due to re-initialization required at every time step [214]. Thus, coupling VOF and LS methods (CLSVOF), can combine the benefits of the two methods and ensure mass conservation as carried out in [151]. Indeed, the comparison between different interface capturing methods performed in [35], has shown that the (CLSVOF) could be the most promising method for two-phase flow simulations due to its inherent conservation properties and topology accuracy.

The VOF and LSM are usually used to preserve a sharp interface between the liquid and gas phases. On the contrary, in the Diffuse Interface Method (DIM) [226, 13, 204], the interface has a finite width, where the liquid and gas phases are assumed to be homogeneously mixed in each computational cell and the discontinuity of the fluid properties as well as jump conditions are smoothed across the diffused interface. The main advantage of the DIM is that explicitly satisfying the interface conditions are not required, and the variation of the interface topology is automatically handled, which is computationally efficient. In addition, the DIM constitutes a consistent framework able to deal with real-fluid fully compressible multi-phase flows at subcritical and supercritical regimes using appropriate equations of state. However, the diffused interface has to be maintained relatively sharp in the subcritical state case. To this goal, high order numerical schemes [242] and interface sharpening techniques [49] could be employed.

1.3.2 Diffuse-interface two-phase flow models

In the DIM framework, several two-phase flow models have been proposed in the literature with number of transport equations ranging from four to seven based on the initial equilibrium assumptions. Baer and Nunziato [18] proposed a fully compressible non-equilibrium two-fluid seven-equation model, which is adopted for two-phase flows by Saurel and Abgrall [203]. The model consists of six equations obtained from conservation principles applied to each phase, completed by a seventh equation for the evolution of the volume fraction. The model takes into account the pressure and velocity non-equilibrium effects, where each phase owe its own pressure, velocity, and temperature. However, for many physical situations, it could be reasonable to simplify the model by introducing mechanical or thermal equilibrium assumptions between the two phases and reduced models can be derived from the seven-equation model.

Kapila et al. [123] derived two reduced models starting from the seven-equation model. The first reduced model is a six-equation model derived in the asymptotic limit of only stiff velocity relaxation (single velocity, but two pressures for the two-phases). The second model is further reduced to a five-equation model derived in the asymptotic limit of both stiff velocity and pressure relaxation (single velocity and single pressure for the two-phases). Each reduction is associated with a relaxation process, which eliminates a non-equilibrium degree of freedom.

Saurel et al. [205] also discussed a five-equation model with a single pressure and a single velocity, but two different temperatures and entropies similar to the work of Kapila et al. [123]. The model is composed of two mass balance equations, one mixture

momentum equation, one mixture energy equation, and a volume fraction equation. The system is closed by two equations of state (EoS), where each fluid possess its own EoS. Relaxation towards equilibrium is achieved using additional temperature and chemical potential relaxation, whose kinetics are considered fast at the evaporation fronts compared to the flow characteristic time.

The seven-equation model can be further reduced to a four-equation model by assuming that the flow system is subjected to both thermal and mechanical equilibrium. In such system, both existing phases owe the same velocity, pressure, and temperature. The four equation system includes the mass balance equations for distinct species in the mixture, one mixture momentum equation, and one mixture energy equation.

For modeling phase change, the four-equation model can be combined with either non-equilibrium or equilibrium phase change models. On the one hand, non-equilibrium phase change models such as the Homogeneous Relaxation Model (HRM) [33, 202], considers the non-equilibrium effects during the phase change process, by assuming a finite relaxation time of the vapor fraction towards its equilibrium value. On the other hand, equilibrium phase change models are based on the thermodynamic equilibrium assumption, where the equilibrium state is assumed to be reached instantaneously. This implies that the characteristic time of reaching equilibrium is much smaller than the other flow time scales [256, 149]. The combination of the thermodynamic equilibrium assumption with the four-equation model (one-fluid mixture model) is usually termed the Homogeneous Equilibrium Model (HEM).

The four-equation model has been widely employed for fuel injection and cavitation simulations [254, 149, 137, 101] owing to its high efficiency. However, the main challenge in such models is estimating the phase change source term for the classical subcritical phase change and the ability to transit to a supercritical single-phase mixing regime. Indeed, several researchers have coupled the four-equation model with a vapor-liquid equilibrium (VLE) solver to estimate the phase change source term.

Yang et al. [254] coupled the four-equation model with a real fluid multi-component phase equilibrium solver based on the PR-EoS. The model considers both the liquid and gas phases as multi-component. Thus, the effect of dissolved gas in the liquid phase can be considered, which has a significant effect on physical phenomena such as in-nozzle cavitation [253]. Similar approach has been also proposed by Matheis and Hickel [149], employing a fully conservative formulation using the total energy equation compared to the non-conservative internal energy equation employed in [254]. Chiapolino et al. [48] also coupled the four-equation model with a VLE model based on the stiffened gas (SG) EoS, assuming the liquid phase as single component. Thus, the dissolved gas in the liquid phase is not considered.

However, one of the issues that arises in the employment of the four-equation model along with VLE solver as reported in [253] is the high computational cost of the direct evaluation of the VLE solver, especially when using a non-linear real-fluid EoS. Accordingly, different solutions have been proposed in the literature within the DIM framework to overcome the costly VLE solver. The first approach [255, 135, 114] involves tabulating the VLE calculation before the CFD simulation, which has been shown to be efficient, allowing for a reduction of the computational cost. Other recent approaches, include in situ adaptive tabulation (ISAT) approach [259], where the table is constructed during the CFD simulation or using an artificial neural network (ANN) as a regression model for the thermodynamic properties [136]. However, these approaches are still under investigation and their efficiency for multi-component two-phase flow simulations is not yet evaluated.

1.4 Cavitation in fuel injectors

In this section, the numerical and experimental investigations of the cavitation phenomenon in fuel injectors are reviewed. First, the experimental investigations are discussed. Then, the numerical investigations and the employed modeling approaches are reviewed.

1.4.1 Experimental investigations

The internal flow development inside the fuel injector has a significant effect on the subsequent fuel jet break-up and mixing, affecting the combustion process and the resultant emissions. Accordingly, further understanding of the physical phenomena that take place inside the fuel injector is indeed essential to enhance the engine efficiency and minimize the pollutants formation.

To cope with the recent strict emission legislation, the trend is increasing diesel engine injection pressure up to even more than 3000 bars. However, such high-pressure levels lead to very high velocities within the fuel injector internal passages and strong accelerations in regions of sharp changes of direction (such as the injector orifice inlet corners), which causes the static pressure to drop locally to or below the fuel saturation pressure leading to bubbles and vapor cavities formation. This phenomenon is known as cavitation.

Cavitation has been the subject of various numerical and experimental studies in the literature, due to its significant effect on both the internal injector flow and the external fuel jet break-up and mixing. The cavitation development in the fuel injector could be beneficial, but also a drawback. On the one hand, some studies [172, 173] have shown that cavitation development could enhance the fuel atomization and spray cone angle. On the other hand, the collapse of the cavitation bubbles may cause damage and erosion [17, 260, 132] inside the injector, changing its nominal geometry and leading to performance issues or even injector failure [17]. Accordingly, further understanding of the cavitation phenomenon and associated physics is indeed necessary for further improvements and optimization of the fuel injector design.

On the experimental side, measurements of cavitation in real fuel injectors is a challenging task. Indeed, the fuel injector orifice has extremely small size with an average length of 1 mm for most of automotive diesel engines, where the fuel velocity reaches up to hundreds of meters per second, making the experimental visualizations and measurements extremely difficult. Accordingly, several researchers [44, 219, 84, 220, 158] have employed transparent injectors, which facilitate the use of optical diagnostics for cavitation investigations.

Chaves et al. [44] investigated the in-nozzle cavitation using transparent nozzles of the same size as in diesel injectors. It has been shown that the cavitation appears at the sharp inlet corner of the nozzle, as the injection pressure exceeds a certain threshold, which depends on the nozzle geometry. Besides, as the injection pressure further increases, the cavitation reaches the nozzle exit (super cavitation).

Arcoumanis et al. [16] visualized the cavitation characteristics in a real-size conical sac-type injector using fast and high resolution CCD camera. Based on the obtained images, both cavitation initiation at the top inlet corner of the nozzle as well as string cavitation formed inside the sac volume that enters the nozzle at the bottom corner were identified. In addition, the comparison of the cavitation images of the real-size nozzle with those of an enlarged transparent nozzle replica has shown that similar flow regimes may

form in both nozzles. Although, the similarity of the macroscopic cavitation structures, the transient development of the cavitation bubbles was found to be different in the two nozzles due to the different residence and life time of the moving bubbles.

E. Winklhofer et al. [73] carried out a detailed optical study of the flow and cavitation phenomena in a transparent quasi two-dimensional throttle using diesel fuel. It has been shown that the onset of cavitation at the entrance of the throttle hole first appears in the shear layer between the incoming fluid separating from the entrance corner and the recirculating fluid near the throttle wall.

Gavaises and Andriotis [83] investigated the cavitating flow characteristics inside multi-hole injectors for large diesel engines, where flow imaging has been obtained inside transparent nozzle replicas using simultaneously two high speed cameras and various illumination light sources. The obtained experimental images have shown that the cavitation is formed not only at the nozzle inlet due to the local pressure drop induced by nozzle inlet geometry, but additionally inside the volume below the needle and upstream of the nozzle.

Sou et al. [219] investigated the effects of cavitation on water liquid jet under various conditions using two-dimensional (2D) nozzles, where the cavitation and liquid jet were visualized using high-speed cameras. They classified the in-nozzle cavitation and liquid jets into different regimes by varying the Reynolds number (Re) and cavitation number (σ_{cav}), namely developing cavitation-wavy jet, super cavitation-spray, and hydraulic flip-flipping jet (see Fig. 1.11). The impact of the strong turbulence induced by the collapse of cavitation clouds near the nozzle exit was shown to play a significant role in the ligaments formation and the resulting spray cone angle.

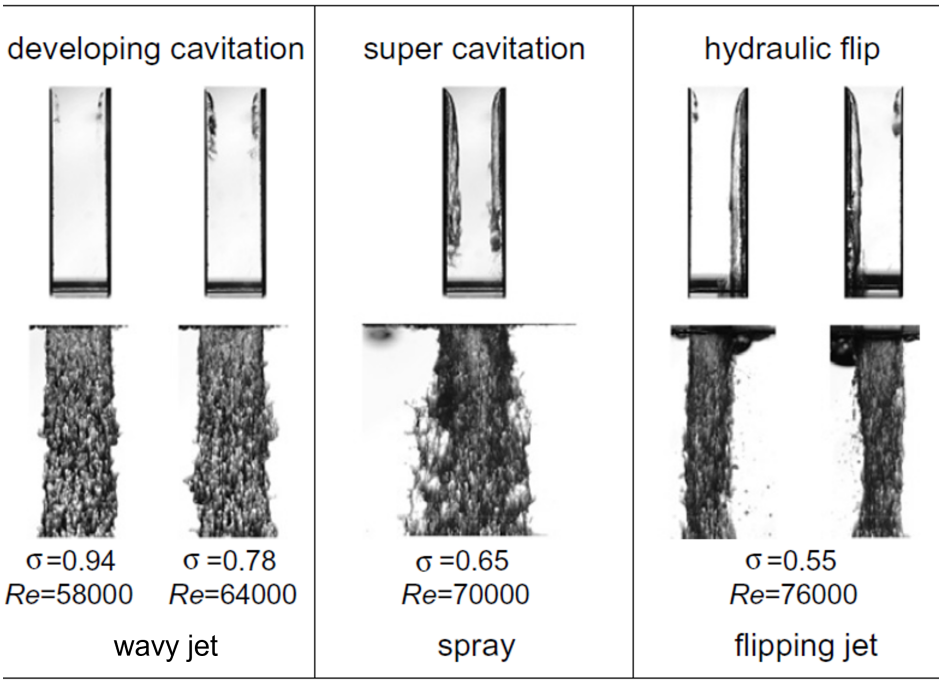

Figure 1.11: Images of cavitation in a 2D nozzle and water liquid jet for different cavitation (σ) and Reynolds (Re) numbers [219].

The aforementioned investigations have mainly relied on optical techniques. However, several cavitation investigations have also employed X-ray diagnostics [29, 157, 70, 68, 124, 213, 228, 125] to overcome some of the limitations of the optical techniques such as the substantial amount of scattering that occurs at the liquid-gas interface.

For instance, Bauer et al. [29] used X-ray computed tomography (CT) to measure the time-averaged void fraction distribution in a quasi-steady pipe flow. Mitroglou et al. [157] carried out quantitative measurements of the void fraction in a enlarged single orifice nozzle replica using X-ray micro-computed tomography technique. Duke et al. [70] also performed quantitative measurements of the line of sight projected void fraction in submerged cavitating nozzles by means of X-ray radiography. Karathanassis et al. [124] was first to investigate vortical cavitation using X-ray phase-contrast imaging (XPCI), showing the morphological fine features and dynamics of the vortical cavities and also providing estimations on the level of turbulence within the examined orifice. Tekawade et al. [228] carried out the first XPCI and tomographic reconstruction of the two-phase flow inside the ECN Spray C37 steel injector at engine-like operating conditions.

1.4.2 Numerical investigations

In addition to the experimental investigations, numerical models are also required to complement the experimental efforts for cavitation investigation and provide an alternative for the cases, where experimental measurements are not feasible.

Various cavitation models have been proposed in the literature and can be classified to different groups based on several aspects. On the one hand, in Eulerian-Lagrangian models [87, 88, 223], parcels of cavitation bubbles are tracked using Lagrangian formulation while the main liquid flow field is modeled in an Eulerian framework. On the other hand, the employed Eulerian-Eulerian two-phase flow models included the one-fluid [12, 253, 25] and two-fluid models [97, 24, 23].

As discussed above, in the one-fluid model, the two-phase mixture is modeled using one set of transport equations of the conservation laws, while in the two-fluid model, the transport equations are solved for each phase separately, along with an extra liquid fraction transport equation. Besides, the models can also be classified based on the treatment of the liquid-gas interface and modeling the mass transfer process (cavitation or condensation). The interface treatment includes sharp interface methods such as VOF or diffused interface treatment, where the liquid and gas are assumed to be homogeneously mixed in each computational cell.

Regarding the modeling of the phase change process, models include non-equilibrium mass transfer models and equilibrium mass transfer model assuming thermodynamic equilibrium. The non-equilibrium mass transfer models such as Schnerr and Sauer (SS) [210] and Zwart-Gerber-Belamri (ZGB) [261], assume the initial presence of gaseous bubbles (nucleation sites) in the liquid, that will grow as the pressure drops and rate of growth of these bubbles is modeled following a simplified Rayleigh-Plesset (RP) equation for bubble dynamics. Commonly, these models include several parameters that need to be tuned for the different conditions or configurations. Among the family of non-equilibrium phase change models, is the Homogeneous Relaxation Model (HRM) [33]. The HRM considers the non-equilibrium effects during the phase change process, by assuming a finite relaxation time of the vapor fraction towards its equilibrium value. The HRM model also include some constants that need to be fixed and tuned.

On the other hand, phase change models employing the thermodynamic equilibrium assumption have also been developed. The thermodynamic equilibrium assumption implies that the time scale of the phase change process is negligible compared to the other fluid time scales. Commonly, the thermodynamic equilibrium assumption has been employed with the one-fluid mixture model and thus termed as the Homogeneous Equilibrium Model (HEM) [209, 48, 253, 101]. In the HEM, an EoS is introduced to link the pressure and density, being the baratropic EoS widely used for cavitation simulations [165, 134, 235, 101], due to its simplicity leading to direct relation between the pressure and density. Recent studies [253, 241], have also employed the HEM based on real-fluid EoSs and vapor-liquid equilibrium calculations for cavitation simulations.

One crucial point regarding cavitation models, is that most of the models assume that liquid-phase is composed of single-species, neglecting the effect of dissolved non-condensable gas on the cavitation development. Generally, cavitation models considers the liquid, vapor, and ambient gas, excluding the dissolved gas in the liquid phase. However, recent studies [253, 25, 97] have highlighted the effect of dissolved non-condensable gas on the cavitation development. Indeed, two cavitation regimes have been identified, namely vaporous cavitation and gaseous cavitation. On the one hand, vaporous cavitation takes places, when the local pressure decreases to or below the liquid (including dissolved gas) saturation pressure. On the other hand, gaseous cavitation is formed, due to the expansion of non-condensable gas bubbles, as the pressure drops, but not necessarily below the liquid saturation pressure.

Different combinations of the previously mentioned two-phase flow and phase change models have been employed in the literature for cavitation investigations. Habchi [97] used a two-fluid diffused interface model for cavitation simulation in a single-hole transparent nozzle, where a Gibbs free energy relaxation model (GERM) has been proposed to compute the phase change at the liquid-gas interfaces.

Cristofaro et al. [52] investigated the cavitation induced erosion in diesel injector using a two-phase model that solves for two-momentum equations to consider the slip velocity between the liquid-vapor mixture and air, where the phase change was modeled by a non-equilibrium model based on a simplified RP equation.

Battistoni et al. [24] compared the single and two-fluid models for in-nozzle cavitation prediction. For the single fluid model, the HRM is used for phase change modeling, whereas for the two-fluid model, the phase change is modeled using a Rayleigh bubble-dynamics model. The two models have shown good predictive capabilities. However, the two-fluid model showed a better match with the total void fraction experimental data along the nozzle axis compared to the single-fluid model.

Mishra et al. [155] proposed a two-fluid model based on the VOF method, along with a modified Schnerr-Sauer model to capture the gaseous-cavitation. The model has shown good agreement with the experiments of [69]. However, the model has shown sensitivity to the cavitation model parameters, to better predict the void formation.

Guo et al. [95] studied the cavitation development of two different fuels (n-dodecane and iso-octane) in the ECN Spray C injector considering the full needle motion using a single-fluid model combined with the HRM. In the case of iso-octane, significant fuel vapor is generated due to the high saturation pressure compared to n-dodecane, for which the fuel vapor was almost absent, and the gaseous phase was mainly composed of non-condensable gas and ingested ambient gas.

The in-nozzle cavitation effects on liquid atomization has been studied by Mithun et al. [156] using a homogeneous equilibrium barotropic cavitation model with an implicit

sharp interface VOF method. The analysis of a water jet atomization into ambient air revealed that the developing cavitation is the most favorable for enhancing the primary atomization, in contrast to the hydraulic flip condition, where the atomization is drastically reduced.

Battistoni et al. [25] used the experiments of [69] to investigate the effect of dissolved non-condensable gas on the cavitation development and quantify the separate contributions of vaporous and gaseous cavitation to the total void fraction. Using a single fluid model and HRM for phase change modeling, it has been found that, when sufficient quantity of gas is dissolved in the fuel, a void is formed in the central region of the nozzle that can be attributed to local expansion of the dissolved non-condensable gas. Conversely, degassed fuel shows only intense cavitation at the nozzle wall, with very little contribution from the non-condensable gas. It should also be noted that the non-condensable gas was considered as free gas, that cannot be dissolved into the liquid and thus, not participating in the phase change process.

On the contrary, Yang and Habchi [253] proposed a fully compressible two-phase flow model, where both liquid and gas phases are considered multi-component and thus the dissolved non-condensable gas contributes to the phase change process. The flow solver was coupled to a thermodynamic solver based on the PR-EoS and VLE calculations. The model has been validated using the X-ray experiments of a cavitation nozzle [70], showing very promising results. It has been concluded that vaporous cavitation is the dominant phase transition process during the nucleation stage, especially for the degassed fuel. Then, gaseous cavitation becomes more significant during the growth of cavities. Besides, the carried out thermodynamic analysis has shown that as the initial concentration of nitrogen in the liquid phase increases, the mixture saturation pressure increase, which would facilitate the cavitation inception. However, one issue reported by the authors is the model computational efficiency, as thermodynamic solver calculations were computationally expensive.

Vidal et al. [241] employed a tabulated thermodynamic approach based on the PC-SAFT EoS and VLE calculations combined with a single fluid model to investigate the cavitation formation of a multi-component diesel fuel surrogate in a high-pressure fuel injector. Based on the composition of the fuel vapor, it has been found that the lighter components cavitate at a significantly greater amount than the heavy ones. One noting point about this study, is that the dissolved non-condensable gas was not taken into account.

Another important aspect for the simulation of the internal flow in fuel injectors is whether the transient needle motion is considered or not. Indeed, commonly the needle is assumed to be at a fixed lift position, to simplify the numerical setup. However, recent studies [131, 230, 26, 24, 28] have shown significant effects of the transient needle motion on the cavitation development within the fuel injector, emphasizing that including the needle motion effects would be essential for more realistic simulations of fuel injection.

The previous discussion has shown the essential role of cavitation in the fuel injection process. In addition, including the internal injector flow in spray simulations is required, to consider the effect of the in-nozzle cavitation on the subsequent fuel atomization and dispersion. However, such coupling of in-nozzle flow and external spray is indeed a challenging task, due to the various physics that need to be modeled from the internal flow development to the spray formation. Besides, the large spatial extent from the in-nozzle flow to the dilute spray formation could be computationally expensive.

1.5 Thesis Objectives and outline

The main objective of the current work is to develop a predictive and efficient CFD model for multi-component two-phase flow simulations in the context of diesel and dual-fuel engines under different thermodynamic (sub- and super-critical) regimes, allowing an automatic/smooth transition between these regimes that can coexist during the fuel injection and mixing events. This model is based on the Diffuse Interface Modeling (DIM) approach and closed by a thermodynamic equilibrium tabulation method based on various real-fluid equations of state (EoSs). The thermodynamic tabulation approach has been extended to handle ternary systems in addition to binary systems. Besides, the proposed model has been coupled to a subgrid-scale (SGS) model using a surface density approach for fuel atomization modeling. Finally, the cavitation modeling is investigated using the proposed model in different configurations.

The manuscript is structured as follows:

Chapter 2. describes the computational methodology, where the governing equations of the proposed RFM model are introduced along with the employed assumptions. The different turbulence modeling approaches are also discussed, followed by derivation of the filtered transport equations within the LES framework along with the employed subgrid-scale (SGS) models. The tabulated thermodynamic closure is subsequently discussed and the coupling of the flow solver with the thermodynamic table is detailed.

Chapter 3. starts with a fundamental introduction into real fluid thermodynamics and equation of states, followed by a discussion of the employed real-fluid equations of state, including PR and CPA EoSs. Next, the vapor-liquid equilibrium calculation based on the isothermal-isobaric (TPn) flash is discussed. Then, the methodology of the evaluation of the single and two-phase real-fluid thermodynamic and transport properties is detailed. An overview of the thermodynamic tabulation is subsequently discussed and the adopted tabulation approach for binary and ternary mixtures is presented. The tabulation procedure using the in-house Carnot thermodynamic library is then described. Finally, this chapter closes with the validation of the VLE solver based on the in-house Carnot library.

Chapter 4. presents an investigation of the phase change and mixing processes of a single n-dodecane droplet in a bi-component environment composed of nitrogen and methanol under different ambient conditions, mimicking a dual-fuel configuration using highly resolved simulations.

Chapter 5. starts with introducing the implemented sub-grid scale (SGS) model based on the surface density approach for fuel atomization modeling within the LES framework. The simulation of high-pressure fuel injection injection under diesel-like operating conditions (ECN Spray A non-evaporating and evaporating conditions) are then presented along with the model validation against the various experimental data. A parametric variation of the ECN Spray A conditions and validation against the experimental data is then presented. Finally, this chapter closes with an investigation of the evaporating ECN spray A under a dual-fuel configuration.

Chapter 6. is dedicated to cavitation simulation using the RFM model in different configuration, including a transparent injector using water and an industrial injector using ammonia.

Finally, the conclusions of the current work and future perspectives are discussed in **Chapter 7.**

Chapter 2

Computational methodology

Contents

In this chapter, the computational methodology of the current work is elaborated. First, the set of governing equations of the proposed two-phase multi-component real-fluid model (RFM) is introduced and the different turbulence modeling approaches are discussed. Subsequently, the filtered set of transport equations within the LES framework and the adopted subgrid-scale (SGS) models are presented. Finally, the tabulated thermodynamic closure of the flow solver is explained, along with the coupling of the thermodynamic table with the flow solver and the solution algorithm. The CONVERGE CFD solver [197] is used as a baseline for the development of the proposed model throughout the current work.

2.1 The Real-fluid model (RFM)

2.1.1 Governing equations

The diffused interface two-phase flow model adopted in the current work is a four equation model that is fully compressible and considers multi-component is both phases under the assumptions of thermal and mechanical equilibrium. In other words, the two-phases are assumed to have a single velocity, pressure, and temperature. The governing equations are presented through Eqs. (2.1−2.4), expressing the conservation of mixture mass, mixture momentum, mixture internal energy, and species mass fraction, respectively.

$$\frac{\partial \rho}{\partial t} + \frac{\partial \rho u_i}{\partial x_i} = 0 \tag{2.1}$$

$$\frac{\partial \rho u_i}{\partial t} + \frac{\partial \rho u_i u_j}{\partial x_j} = -\frac{\partial P}{\partial x_i} + \frac{\partial \tau_{ij}}{\partial x_j} \tag{2.2}$$

$$\frac{\partial \rho e}{\partial t} + \frac{\partial \rho e u_j}{\partial x_j} = -P\frac{\partial u_j}{\partial x_j} + \tau_{ij}\frac{\partial u_i}{\partial x_j} - \frac{\partial q_j}{\partial x_j} \tag{2.3}$$

$$\frac{\partial \rho Y_k}{\partial t} + \frac{\partial \rho u_j Y_k}{\partial x_j} = -\frac{\partial J_{k,j}}{\partial x_j} \tag{2.4}$$

where, (ρ) is the density, (u_i) is the velocity in the direction (x_i), (e) is the specific internal energy, (P) is the pressure, (t) is the time, and (Y_k) is the mass fraction of species k.

The viscous stress tensor (τ_{ij}) is given by:

$$\tau_{ij} = \mu\left(\frac{\partial u_i}{\partial x_j} + \frac{\partial u_j}{\partial x_i} - \frac{2}{3}\frac{\partial u_k}{\partial x_k}\delta_{ij}\right) \tag{2.5}$$

where (μ) is the dynamic viscosity and (δ_{ij}) is the Kronecker-Delta, which is one for $i = j$ and zero for $i \neq j$.

The heat flux (q_j) consists of heat conduction modeled based on Fourier's law plus the enthalpy flux by species diffusion as:

$$q_j = -\lambda\frac{\partial T}{\partial x_j} + \sum_k J_{k,j} h_k \tag{2.6}$$

where (λ) is the thermal conductivity, (T) is the temperature, and (h_k) is the specific enthalpy of species k.

The species diffusion flux $(J_{k,j})$ is modeled according to Fick's law:

$$J_{k,j} = -\rho D_k \frac{\partial Y_k}{\partial x_j} \tag{2.7}$$

where (D_k) is the mixture averaged diffusion coefficient of species k into the mixture.

It should be noted that the Soret and Dufour effects are neglected under the current modeling approach. The details of the evaluation of the thermodynamic and transport properties are gathered in Sec. 3.4. The thermodynamic closure of the two-phase flow system described above is achieved by a tabulated real-fluid EoS, adopting a local thermal equilibrium hypothesis. The tabulated thermodynamic closure is detailed in Sec. 2.1.4.

It is also worth noting that Eq. (2.3) can be employed based on a total energy formulation $(E = e + u_i^2/2)$ as:

$$\frac{\partial \rho E}{\partial t} + \frac{\partial \rho u_j E}{\partial x_j} = -\frac{\partial u_j P}{\partial x_j} + \frac{\partial u_i \tau_{ij}}{\partial x_j} - \frac{\partial q_j}{\partial x_j} \tag{2.8}$$

This total energy formulation is preferred especially for high-speed flows that include discontinuities such as shock waves.

Model assumptions

The assumptions of the current modeling approach for multi-component two-phase flow can be summarized in the following points:

- The two phases are in mechanical and thermal equilibrium.
- The fluid within a computational cell is in local thermodynamic equilibrium.
- Surface tension effects can be neglected.

The first assumption implies that the two-phases are assumed to have a single velocity, pressure, and temperature. Thus, the slip velocity between the two-phases is assumed to be not significant. Such assumption holds for dense two-phase flows, where the droplet sizes are small. However, in case of a diluted two-phase flow with large droplets and significant slip velocity between the dispersed liquid and the gas phase, the employed homogeneous mixture approach with a single velocity for both phases becomes inaccurate. This limitation could be overcome by adding a transition to the Lagrangain approach [34, 139] once the diluted regime is achieved or accounting for the liquid diffusion due to the slip velocity [169].

The second assumption implies that the characteristic to reach local thermodynamic equilibrium is much smaller than the other flow time scales. Accordingly, thermodynamic non-equilibrium effects are not considered.

The third assumption could be reasonable for high Weber number flows, which is typically the case for the main targeted application in the current work, namely high-pressure fuel injection.

2.1.2 Turbulence modeling

Under engines operating conditions, the involved flows are mainly turbulent. The transition between laminar and turbulent flow is characterized by the Reynolds number (Re), which expresses the ratio of the inertia forces to the viscous forces.

$$Re = \frac{uL}{\nu} \tag{2.9}$$

where (u) and (L) are the characteristic velocity and length scale of the flow and (ν) is the kinematic viscosity.

Fuel injection under diesel and dual-fuel relevant conditions takes place at high Reynolds number in the order of (10^5). Thus, the flow is highly turbulent and the inertia forces far exceeds the viscous forces. The turbulent flow is composed of a collection of three-dimensional eddies that interact together and cover a wide range of scales. The turbulence could be described by the turbulence energy spectrum (E) as function of the wave number ($k = 2\pi/l$), where (l) is the length scale of motion, as shown in Fig. 2.1. Such spectrum, usually termed as Kolmogorov spectrum, illustrates the transfer of energy from the large scales to the smaller scales. Three different regions can be identified on the energy cascade, namely the energy containing range, the inertial subrange, and the dissipation range. In the energy containing range (Largest scales associated with smallest wave numbers), the kinetic energy is extracted from the mean flow, where the large eddies exhibit the highest energy. The size of these largest eddies is determined by the dimensions of the considered system geometry. The inertial subrange is the wave number range, where the energy is

transferred from the larger scale eddies to the smaller eddies. Finally, the dissipation range is that of the largest wave numbers associated with the smallest eddies (smaller than Kolmogrov length scale), where the kinetic energy is dissipated by viscous friction.

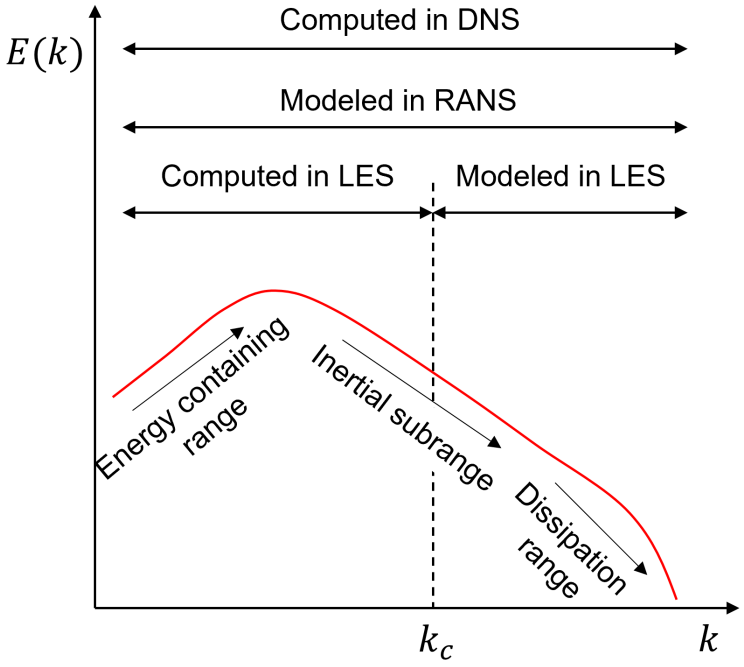

Figure 2.1: Turbulence energy spectrum as function of wave number (k). The computed and modeled wave number ranges in DNS, LES, and RANS are shown. (k_c) is the cut-off wave number used in LES.

The simulation of turbulent flows can be preformed using three main approaches as follows:

- Direct numerical simulation (DNS): It is the most general and accurate way, which directly solve the conversation equations (2.1-2.4) without any model and all turbulent scales are resolved (see Fig. 2.1). However, DNS is mainly limited to academic investigations, due to the associated high computational cost. This is attributed to that the required mesh size to resolve all the turbulent scales is proportional to $Re^{9/4}$. Besides, for a highly turbulent two-phase flow, the complexity increases, as the liquid-gas interface, which is a few nanometers in thickness, must be also resolved, which is usually unfeasible.

- Reynolds Averaged Navier-Stokes Simulation (RANS): In the RANS approach, only the mean flow field is solved by the corresponding time averaged Navier-Stokes equations, while all the turbulent scales are modeled (see Fig. 2.1). This approach has been widely applied due to its relatively low computational cost. However, it is also associated to extra modeling effort.

- Large Eddy Simulation (LES): In the LES approach, the Navier-Stokes equations are filtered, where only large-scale eddies containing most of the energy are resolved, and the small scales, which are supposed to be isotropic and universal are thus modeled. The modeling effort in LES is therefore less compared to RANS. The

filter size is usually chosen as the local grid size, where the scales smaller than the mesh size are modeled by suitable subgrid-scale (SGS) models. The computational cost of LES is also less than that of a DNS and still can provide high fidelity results of the highly turbulent flows.

In the current work, the LES approach was mainly adopted for the simulation of high-pressure fuel injection taking place under high Reynolds number, where a higher accuracy of two-phase turbulence modeling is required to accurately predict the fuel dispersion and atomization processes. The filtered governing equations within the LES framework and the adopted SGS models are detailed in the next subsection.

2.1.3 Large Eddy Simulation and filtered equations

The concept of Large-Eddy Simulation is based on the idea of scale separation using a specific cut-off length (see Fig. 2.1). The energy contained large scales are directly resolved by the computational grid, while the unresolved small scales are modeled. As defined above, the scale separation is achieved by applying a filtering operation, which decomposes a general quantity $\phi(x,t)$ into a resolved part $\bar{\phi}(x,t)$ and a subgrid part $\phi'(x,t)$, as follows:

$$\phi(x,t) = \bar{\phi}(x,t) + \phi'(x,t) \tag{2.10}$$

Here, no explicit filter is applied and the flow field is separated by the computational grid into resolved and SGS fields. In addition, for the considered variable-density flow, the Favre filtering is typically employed. Thus, a quantity $\phi(x,t)$ can be then decomposed as:

$$\phi(x,t) = \tilde{\phi}(x,t) + \phi''(x,t) \tag{2.11}$$

where, $(\tilde{\phi} = \overline{\rho\phi}/\bar{\rho})$ is the Favre-filtered quantity and (ϕ'') is the associated sub-grid scale contribution.

By applying the Favre filtering operations to the set of governing equations (2.1−2.4), the filtered equations for LES reads:

$$\frac{\partial \bar{\rho}}{\partial t} + \frac{\partial \bar{\rho}\tilde{u}_i}{\partial x_i} = 0 \tag{2.12}$$

$$\frac{\partial \bar{\rho}\tilde{u}_i}{\partial t} + \frac{\partial \bar{\rho}\tilde{u}_i\tilde{u}_j}{\partial x_j} = -\frac{\partial \bar{P}}{\partial x_i} + \frac{\partial}{\partial x_j}(\bar{\tau}_{ij} + \bar{\tau}_{ij}^{sgs}) \tag{2.13}$$

$$\frac{\partial \bar{\rho}\tilde{e}}{\partial t} + \frac{\partial \bar{\rho}\tilde{u}_j\tilde{e}}{\partial x_j} = -\bar{P}\frac{\partial \tilde{u}_j}{\partial x_j} + (\bar{\tau}_{ij} + \bar{\tau}_{ij}^{sgs})\frac{\partial \tilde{u}_i}{\partial x_j} - \frac{\partial}{\partial x_j}(\bar{q}_j + \bar{q}_j^{sgs}) \tag{2.14}$$

$$\frac{\partial \bar{\rho}\tilde{Y}_k}{\partial t} + \frac{\partial \bar{\rho}\tilde{u}_j\tilde{Y}_k}{\partial x_j} = -\frac{\partial}{\partial x_j}(\bar{J}_{k,j} + \bar{J}_{k,j}^{sgs}) \tag{2.15}$$

The overbar $(\overline{\odot})$ and tilde $(\widetilde{\odot})$ denote the Reynolds-filtered and Favre-filtered quantities, respectively. The subgrid-scale contributions in the governing equations are indicated by the superscript (sgs) and require additional modeling.

The subgrid stress tensor (τ_{ij}^{sgs}) is computed similarly to (τ_{ij}) with the eddy-viscosity assumption, replacing the molecular dynamic viscosity by the subgrid-scale dynamic viscosity (μ_{sgs}) as:

$$\tau_{ij}^{sgs} = \mu_{sgs}\left(\frac{\partial \tilde{u}_i}{\partial x_j} + \frac{\partial \tilde{u}_j}{\partial x_i} - \frac{2}{3}\frac{\partial \tilde{u}_k}{\partial x_k}\delta_{ij}\right) \tag{2.16}$$

The subgrid species ($J_{k,j}^{sgs}$) and heat (q_j^{sgs}) fluxes are modeled using the gradient assumption and treated by analogy to their laminar counterparts using turbulent transport coefficients as:

$$J_{k,j}^{sgs} = -\bar{\rho} D_t \frac{\partial \tilde{Y}_k}{\partial x_j} \tag{2.17}$$

$$q_j^{sgs} = -\lambda_t \frac{\partial \tilde{T}}{\partial x_j} + \sum_k J_{k,j}^{sgs} h_k \tag{2.18}$$

where, the turbulent diffusion coefficient (D_t) and the turbulent thermal conductivity (λ_t) are modeled by introducing a turbulent Prandtl ($Pr_t = 0.9$) and Schmidt ($Sc_t = 0.7$) numbers as:

$$D_t = \frac{\mu_{sgs}}{\rho Sc_t}, \lambda_t = \frac{C_p \mu_{sgs}}{Pr_t} \tag{2.19}$$

where (C_p) is the isobaric heat capacity.

Within the LES framework, the Sigma turbulence model [161] is used to compute the subgrid-scale dynamic viscosity (μ_{sgs}) as follows:

$$\mu_{sgs} = \bar{\rho}(C_m \Delta)^2 D_m \tag{2.20}$$

$$D_m = \frac{\sigma_3(\sigma_1 - \sigma_2)(\sigma_2 - \sigma_3)}{\sigma_1^2} \tag{2.21}$$

where ($C_m = 1.5$) is the model constant and ($\Delta = V_c^{-1/3}$) is the filter size estimated from the cell volume (V_c). The differential operator (D_m) is computed from the singular values (σ_i) of the resolved velocity gradient tensor with ($\sigma_1 \geqslant \sigma_2 \geqslant \sigma_3 \geqslant 0$) as detailed in [161].

It should be noted that additional SGS models could also be required for the equation of state (EoS) within the LES framework. In the current work, a non-linear real-fluid EoS is employed to account for the non-linear fluid behavior under high-pressure conditions. In such case, the filtered real-fluid EoS would introduce additional SGS effects that require additional modeling [237]. Such SGS effects have also been shown to be relevant for the filtered ideal-gas EoS under multi-species and reacting conditions [196]. Models for the SGS terms associated with the EoS have been proposed in different studies [212, 36, 195, 237]. However, the performance of such models is yet to be evaluated under practical applications. Besides, as reported in [90], detailed experimental or DNS data are required to validate such novel SGS models. Accordingly, in the current modeling approach, the additional SGS terms associated with the EoS are not yet considered, and thus quantification of the associated uncertainties should be the subject of future studies.

2.1.4 Tabulated thermodynamic closure

The fully compressible multi-component two-phase flow system described above is closed by a real-fluid equation of state (EoS) adopting a local thermodynamic equilibrium hypothesis, ensuring its mathematical hyperbolicity [256]. Two real-fluid EoSs have been

mainly employed in the current work, namely the Peng-Robinson (PR) and the Cubic Plus Association (CPA) EoSs. Such real-Fluid EoSs allow to well capture the single-phase fluid properties at high-pressure conditions far from the ideal-gas behavior. In addition, to consider the two-phase thermodynamic and transport properties as well as the phase change phenomenon, the EoS is not sufficient, and vapor-liquid equilibrium (VLE) calculations are also included in the current study.

The current work adapts a pre-tabulation approach, where the required thermodynamic and transport properties as well as the phase state and composition are tabulated before the CFD simulation. During the simulation, the various tabulated quantities are robustly interpolated over the entire range of the thermodynamic states using the inputs for the thermodynamic table, which are the temperature (T) , pressure (P), and species mass fraction ($Y_k, k = 1, N_s - 1$), where (N_s) is the total number of species.

The thermodynamic table is generated using the in-house Carnot thermodynamic library. The thermodynamic library performs the vapor-liquid equilibrium (VLE) calculation using a robust isothermal-isobaric (TPn) flash [152] coupled to various real-fluid EoSs. Using the Carnot thermodynamic library, it is possible to employ the appropriate EoS to calculate and tabulate all required properties for the specified ranges of temperature, pressure, and species mass fraction.

This tabulation approach offers the advantage of avoiding the direct evaluation of the non-linear real-fluid EoS along with the VLE calculation during the simulation, which has been shown to be computationally demanding [254, 256]. Moreover, the tabulation approach based on the Carnot thermodynamic library allows simulating different fuels/species using different EoSs without hard coding a (TPn) flash for each EoS of interest. Previous tabulation method was limited to binary systems [255, 114]. In this work, the tabulation method has been further extended to ternary (three-component) systems. The employed real-fluid EoS and the tabulation procedure along with the VLE calculation and its validation are detailed in Chapter 3.

2.1.5 Coupling of the flow solver with the thermodynamic table

The coupling between the flow solver and the phase-equilibrium solver is one of the critical elements in the proposed RFM model. Previous studies [47, 243, 200] in the literature have mainly carried out such coupling using a two-step approach. Using such approach, within a time step, the flow is solved without considering the possible phase change, as a first step. Then, the final equilibrium pressure, temperature, and phase composition in each cell are locally computed using a phase-equilibrium solver assuming an isolated system, where the flow is frozen and only phase change is considered. The phase equilibrium solver is commonly based on an isochoric-isoenergetic (UVn) flash [254, 256].

In the current work, a single-step method is employed, in which the thermodynamic table is directly used within the flow solver algorithm in contrast to the previous studies, as will be further discussed. The flow solver in CONVERGE [197] offers pressure-velocity coupling using a modified Pressure Implicit with Splitting of Operator (PISO) [111] or modified Semi-Implicit Method for Pressure-Linked Equations (SIMPLE) [171] algorithms, which are appropriate for compressible flows. The SIMPLE algorithm differs from the PISO algorithm in that the momentum equation is solved within the iterative algorithm, rather than as a predictor step.

The thermodynamic table is used during the simulation for the two following main tasks:

- *Table look-up*: compute the thermodynamic and transport properties, phase state, and composition from $(T, P, Y_k, k = 1, N_s - 1)$ obtained by the flow solver.
- *Temperature reverse look-up*: compute the temperature from the $(e, P, Y_k, k = 1, N_s - 1)$ provided by the flow solver.

The coupling of the thermodynamic table with the flow solver using the PISO algorithm can be explained through the flowchart in Fig. 2.2 and summarized as follows:

- Solve the momentum predictor followed by the first corrector step, which includes solving the derived pressure equation then updating the velocity.
- Solve the transport equations in the order shown in the PISO loop in the flow chart.
- After PISO convergence, the passive equations such as the surface density equation are solved, followed by evaluating the turbulence quantities.

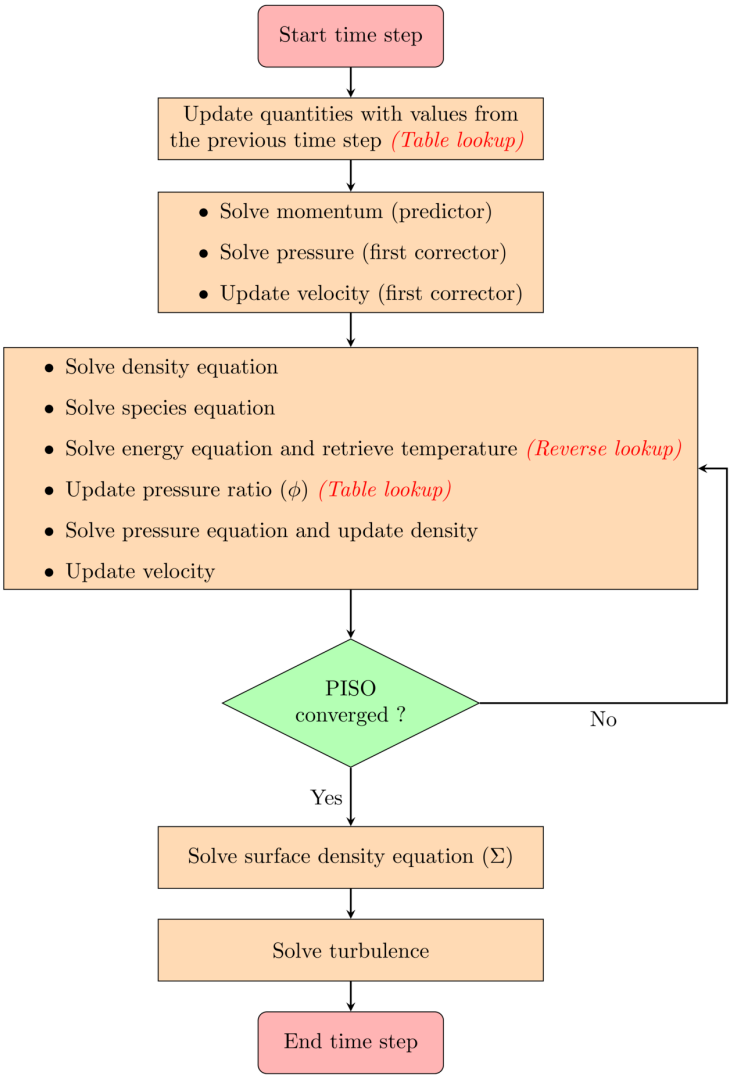

Figure 2.2: Flow chart of the coupling of the flow solver and the thermodynamic table using the PISO algorithm.

The above described coupling shows that the thermodynamic table is directly employed within the flow solver, unlike previous coupling method [256], where the thermodynamic solver is only evaluated after the flow solver is computed. It is also worth noting that the coupling of the thermodynamic table with the SIMPLE algorithm is similar to that of the PISO algorithm detailed above.

As described above, the solver here is pressure-based, where a pressure-Possion equation is derived from the momentum and continuity equation to obtain the pressure field. The derivation of the pressure equation is detailed in the following section.

2.1.5.1 Derivation of the pressure equation

An essential point of the solution procedure using the PISO or SIMPLE algorithms is the derivation of the pressure-Poisson equation, which is used to obtain the pressure field. The original implementation of the pressure equation in the CONVERGE solver, was mainly derived by assuming an ideal gas EoS to relate the pressure and the density in the pressure equation. Accordingly, further modification of the pressure equation was required to be compatible with the employed real-fluid EoS within the framework of the proposed RFM model. In the following paragraphs, both the original and the new pressure equation will be discussed.

First, by manipulating the semi-discretized forms of the momentum and the mass conservation equations, the pressure equation at the second correcter step reads (see the details in [2]):

$$\frac{\partial^2 \left(P^{**} - P^{*}\right)}{\partial x_i \partial x_i} = \frac{\left(\rho^{**} - \rho^{n}\right)}{dt^2} + \frac{1}{dt}\left(\frac{\partial \rho^{*} u_i^{**}}{\partial x_i} - S\right) \tag{2.22}$$

where, S is the source terms and the superscripts (n,*,**) denote the values at the previous time step, previous PISO level, and current PISO level, respectively. To be able to solve Eq. (2.22), the unknown density ρ^{**} (in the first term of the RHS), needs to be modeled using the EoS, which provide a relation between (ρ) and (P).

Original pressure equation

The original pressure equation was mainly relying on the ideal-gas EoS to relate the pressure and density in Eq. (2.22). Generally, the density is a function of the temperature, pressure, and species mass fraction as:

$$\rho = f(T, P, Y_k) \tag{2.23}$$

By neglecting the density variation with the mass fraction and temperature, the density change can be expressed as:

$$\frac{\partial \rho}{\partial t} = \left(\frac{\partial \rho}{\partial P}\right)_{T,Y_k} \frac{\partial P}{\partial t} \tag{2.24}$$

Using the ideal-gas EoS ($p = \rho RT$), then the pressure ratio (ϕ) can be defined as:

$$\phi = \left(\frac{\partial \rho}{\partial P}\right)_{T,Y_k} = 1/RT = \rho/P \tag{2.25}$$

The term $(\rho^{**} - \rho^{n})$ in Eq. (2.22) can then be expressed as:

$$\rho^{**} - \rho^{n} = \rho^{**} - \rho^{*} + \rho^{*} - \rho^{n} \tag{2.26}$$

and knowing that $(\phi^{*} = \rho^{*}/P^{*})$ and further assuming that (ϕ) is constant in the next PISO level, then $(\phi^{*} = \rho^{**}/P^{**})$. By substituting in Eq. (2.26), we get:

$$\rho^{**} - \rho^{n} = \phi^{*}(P^{**} - P^{*}) + \rho^{*} - \rho^{n} \tag{2.27}$$

Finally, Eq. (2.22) can be rearranged as:

$$\frac{\partial^{2}\left(P^{**} - P^{*}\right)}{\partial x_{i}\partial x_{i}} - \frac{\phi^{*}(P^{**} - P^{*})}{dt^{2}} = \frac{(\rho^{*} - \rho^{n})}{dt^{2}} + \frac{1}{dt}\left(\frac{\partial \rho^{*} u_{i}^{**}}{\partial x_{i}} - S\right) \tag{2.28}$$

The main assumption here $\left[(\frac{\partial \rho}{\partial P})^{**} = \phi^{*} = \frac{\rho^{*}}{P*}\right]$, is mainly compatible with the ideal-gas EoS. Thus, for a real-fluid, where generally $((\frac{\partial \rho}{\partial P})^{**} \neq \frac{\rho*}{P*})$, such assumption can lead to pressure fluctuations and consequently non-negligible density fluctuations, leading to difficulty in the PISO convergence. The original pressure equation, was mainly used in CONVEGRE V3.0 version, which has been used throughout the current work. However, under some conditions, a difficultly in the PISO convergence and excessive oscillations were encountered. Therefore, a new pressure equation compatible with the real-fluid was indeed necessary to improve the original one and efforts were made in collaboration of the Convergent Science, Inc. (CSI, the company owner of the software CONVERGE), to develop the new pressure equation in CONVERGE V3.1 release.

Real-fluid pressure equation

Within the real-fluid framework, due to the non-linearity of the EoS, it becomes necessary to modify the standard formulation of the pressure equation as reported in previous studies [115, 103, 159, 162, 232, 113]. A main required modification for using a real-fluid EoS is for the pressure ratio (ϕ) definition as follows:

$$\left(\frac{\partial \rho}{\partial P}\right)_{T,Y_{k}} = \begin{cases} \rho/P & Ideal - gas\ EoS \\ \rho\beta_{T} & Real - fluid\ EoS \end{cases} \tag{2.29}$$

where (β_{T}) is the isothermal compressibility.

Here, the derived new pressure equation for real-fluid starts from a general expansion of the density change, where $(\rho = f(T, P, Y_{k}))$ as:

$$\begin{aligned} \frac{\partial \rho}{\partial t} &= \left(\frac{\partial \rho}{\partial P}\right)_{T,Y_{k}} \frac{\partial P}{\partial t} + \left(\frac{\partial \rho}{\partial T}\right)_{P,Y_{k}} \frac{\partial T}{\partial t} + \sum_{k} \left(\frac{\partial \rho}{\partial Y_{k}}\right)_{T,P,Y_{j\neq Y_{k}}} \frac{\partial Y_{k}}{\partial t} \\ &= \phi \frac{\partial P}{\partial t} + \alpha \frac{\partial T}{\partial t} + \sum_{k} \gamma_{k} \frac{\partial Y_{k}}{\partial t} \end{aligned} \tag{2.30}$$

The term $(\rho^{**} - \rho^{n})$ in Eq. (2.22) can formulated using Eq. (2.30) as:

$$\begin{aligned} \rho^{**} - \rho^{n} &= (\rho^{**} - \rho^{eos*}) + (\rho^{eos*} - \rho^{n}) \\ &= \phi^{*}(P^{**} - P^{*}) + \alpha^{*}(T^{**} - T^{*}) + \sum_{k} \gamma_{k}^{*}(Y_{k}^{**} - Y_{k}^{*}) + (\rho^{eos*} - \rho^{n}) \end{aligned} \tag{2.31}$$

where $(\rho^{eos*} = f(T^*, P^*, Y_k^*))$ is the density from the EoS (i.e. from the thermodynamic table) at the previous PISO level. It is used instead of (ρ^*) to force the density to respect the EoS at PISO convergence.

By substituting Eq. (2.31) into Eq. (2.22), we get:

$$\frac{\partial^2 (P^{**} - P^*)}{\partial x_i \partial x_i} - \frac{\phi^*(P^{**} - P^*)}{dt^2} = \frac{\alpha^* \delta T^{**}}{dt^2} + \frac{\sum_k \gamma_k^* \delta Y_k^{**}}{dt^2} + \frac{(\rho^{eos*} - \rho^n)}{dt^2} + \frac{1}{dt}\left(\frac{\partial \rho^* u_i^{**}}{\partial x_i} - S\right) \tag{2.32}$$

with $(\delta T^{**} = T^{**} - T^*)$ and $(\delta Y_k^{**} = Y_k^{**} - Y_k^*)$. Equation (2.32) is the pressure equation that includes the effects of temperature, pressure, and species mass fraction on the density variation. However, the two terms (δT^{**}) and (δY_k^{**}) are unknown, as (T^{**}) and (Y_k^{**}) are unknown at the current PISO level. Accordingly, it is assumed that $(\delta T^{**} = \delta T^*)$ and $(\delta Y_k^{**} = \delta Y_k^*)$, and for consistency the intermediate density (ρ^{eos*}) is computed as $(\rho^{eos*m1} = f(T^{*m1}, P^*, Y_k^{*m1}))$, where the superscript $(*m1)$ denotes the value from the previous PISO iteration.

Thus, Eq. (2.32), reads:

$$\frac{\partial^2 (P^{**} - P^*)}{\partial x_i \partial x_i} - \frac{\phi^*(P^{**} - P^*)}{dt^2} = \frac{\alpha^* \delta T^*}{dt^2} + \frac{\sum_k \gamma_k^* \delta Y_k^*}{dt^2} + \frac{(\rho^{eos*m1} - \rho^n)}{dt^2} + \frac{1}{dt}\left(\frac{\partial \rho^* u_i^{**}}{\partial x_i} - S\right) \tag{2.33}$$

By further comparing (ρ^{eos}) and (ρ^{eos*m1}), we get:

$$\rho^{eos*} - \rho^{eos*m1} = f(T^*, P^*, Y_k^*) - f(T^{*m1}, P^*, Y_k^{*m1}) = \alpha^* \delta T^* + \sum_k \gamma_k^* \delta Y_k^* \tag{2.34}$$

Thus, by using Eq. (2.34) into Eq. (2.33), the final pressure equation reads:

$$\frac{\partial^2 (P^{**} - P^*)}{\partial x_i \partial x_i} - \frac{\phi^*(P^{**} - P^*)}{dt^2} = \frac{(\rho^{eos*} - \rho^n)}{dt^2} + \frac{1}{dt}\left(\frac{\partial \rho^* u_i^{**}}{\partial x_i} - S\right) \tag{2.35}$$

After the pressure equation is solved, the PISO density is updated at each PISO level from Eq. (2.31) as:

$$\rho^{**} = \phi^*(P^{**} - P^*) + \alpha^* \delta T^* + \sum_k \gamma_k^* \delta Y_k^* + \rho^{eos*m1} \tag{2.36}$$

Then further using Eq. (2.34), the final equation for the density update reads:

$$\rho^{**} = \rho^{eos*} + \phi^*(P^{**} - P^*) \tag{2.37}$$

Here, the density update can be regarded as a correction of the EoS density based on the correction error from the previous PISO error, so that when PISO converges, the final density should be close to that of the EoS. The (ρ^{eos*}) is used instead of (ρ^*), as (ρ^*) could deviate from the EoS. The main assumption employed here is $(\rho^{**} - \rho^{eos*}) = \phi^*(P^{**} - P^*)$, where (ϕ^*) should be well estimated to ensure convergence.

The partial derivative $(\phi = \frac{\partial \rho}{\partial P})$ is estimated numerically from the thermodynamic table using a perturbation method as:

$$\phi = \left(\frac{\partial \rho}{\partial P}\right)_{T,Y_k} = \frac{\rho(T, P + 0.5dP, Y_k) - \rho(T, P - 0.5dP, Y_k)}{dP} \tag{2.38}$$

where (dP) is typically smaller than the pressure step size in the thermodynamic table, and its default value is 1e-04 Pa. This new pressure equation is implemented by CSI in the CONVERGE V3.1.

Summary

The main differences between the previously discussed two pressure equations are summarized in Table. 2.1. In the current work, the original pressure equation was mainly employed in most of the performed simulations, as the new pressure equation was developed close to the end of the current thesis. In the results chapters, the employed CONVERGE version and pressure equation will be mentioned for clarity. For the high pressure fuel injection simulation presented in Chapter 5, some cases are re-simulated with the new pressure equation to quantify the accuracy and robustness of the new formulation compared to its original counterpart (see Appendix. A).

	New pressure equation for real-fluid	Original pressure equation
Formula	$\frac{\partial^2(P^{**}-P^*)}{\partial x_i \partial x_i} - \frac{\phi^*(P^{**}-P^*)}{dt^2} = \frac{(\rho^{eos*}-\rho^n)}{dt^2} + \frac{1}{dt}\left(\frac{\partial \rho^* u_i^{**}}{\partial x_i} - S\right)$	$\frac{\partial^2(P^{**}-P^*)}{\partial x_i \partial x_i} - \frac{\phi^*(P^{**}-P^*)}{dt^2} = \frac{(\rho^*-\rho^n)}{dt^2} + \frac{1}{dt}\left(\frac{\partial \rho^* u_i^{**}}{\partial x_i} - S\right)$
ϕ^* definition	$\phi^* = \left(\frac{\partial \rho}{\partial P}\right)_{T^*, Y_k^*}$	$\phi^* = \rho^*/P^*$
Density update	$\rho^{**} = \rho^{eos*} + \phi^*(P^{**} - P^*)$	$\rho^{**} = \phi^* P^{**}$
CONVERGE Version	V3.1	V3.0

Table 2.1: Comparison of the main differences of the original pressure equation and the new pressure equation for real-fluid.

2.2 Conclusion

In this chapter, the governing equations of the proposed RFM model are introduced along with the employed assumptions. The different turbulence modeling approaches were also discussed, followed by derivation of the filtered transport equations within the LES framework along with the employed subgrid-scale (SGS) models. Then, the tabulated thermodynamic closure is discussed and the coupling between the flow solver the thermodynamic table has been detailed. Finally, the pressure-Poisson equation is derived using the ideal-gas assumption, followed by the derivation of the updated pressure equation for the real-fluid framework.

Chapter 3

Real-fluid thermodynamics and tabulation approach

Contents

3.1 Introduction

It is well known that an equation of state (EoS) is required to close the compressible Navier-Stokes equation system presented in the previous chapter and to calculate the fluid thermodynamic properties. Indeed, an EoS is required to couple the density, pressure, and temperature. A wide range of EoSs are proposed in the literature, ranging from the simple ideal gas law over cubic equations up to multi-parameter EoSs. Each EoS has its

own pros and cons and the selection of the EoS is done based on the chemical system under consideration.

For instance, the simplest ideal gas law is limited to relatively low pressures and high temperatures. However, at high pressure conditions that are typically encountered during the fuel injection event, the fluid shows a significant deviation from the ideal-gas behavior and the physical properties exhibit different non-linearities, especially under trans/supercritical conditions [113, 114, 200, 149].

Thus, it is desirable to have an EoS that can accurately represent the $(P - v - T)$ behavior over a wide range of temperature and pressure conditions. Indeed, several real-fluid EoSs have been developed for the purpose of taking into account the fluid non-ideality. The very first attempt to improve the ideal-gas EoS was done by van der Waals [240], who included two of the effects that are not considered in the ideal-gas model as in Eq. (3.1). Theses two effects are, namely the inter-molecular attraction forces and the volume occupied by the molecules themselves represented by the terms (a/v^2) and $(v-b)$ in Eq. (3.1), respectively. The accuracy of the van der Waals EoS is often limited to a certain range, but it can be further enhanced by using values for a and b that are based on the real behavior of the fluid as will be demonstrated in the next section.

$$\left(P + \tfrac{a}{v^2}\right)(v - b) = RT \tag{3.1}$$

Over the years, a widely used family of EoSs inspired by van der Waals and termed the cubic EoSs has been proposed such as the Redlich-Kwong (RK) [191], Soave-Redlich-Kwong (SRK) [218], and Peng-Robinson (PR) [176]. The cubic EoSs have been widely used for their relative simplicity and the development of several ways to tune their parameters for specific applications. However, they also have some drawbacks, such as the poor prediction of the liquid molar volume (i.e. the liquid density). However, a volume translation method [175] can be adopted to improve such a drawback.

Another family of EoS that is becoming increasingly popular in engineering applications is the Statistical Association Fluid Theory (SAFT) EoS. The first version of the SAFT-EoS was proposed by Chapman et al. [42] based on the thermodynamic perturbation theory introduced by Wertheim [246]. The SAFT-EoS has two major contributions, namely introducing the association term and the chain term. They provided an analytical expression to consider the association of hydrogen bonding for polar compounds such as methanol and water. Whereas, for the chain term, they proposed to consider a chain molecule as a mixture of segments with infinite association strength.

In various engineering applications, the so-called hybrid EoSs have also been proposed. These equations combine different energy interaction terms that originate from different theories. For instance, Kontogeorgis et al. [133] proposed to use the SAFT association term as an additional term to the cubic equation of state. Based on the latter suggestion, they introduced the Cubic Plus Association (CPA) EoS, which combines the SRK cubic EoS along with the association term as formulated in [153]. The interesting fact about the CPA-EoS is that in the absence of associating compounds, the cubic equation is recovered and the existing cubic EoS correlations can be used.

The efficiency and accuracy of the CPA-EoS in the prediction of the phase equilibria for several hydrocarbons-methanol binary mixtures have been examined in [57]. They demonstrated that for hydrocarbons-methanol binaries, the additional association term in the CPA-EoS have a significant improvement on the phase equilibria prediction, since it explicitly considers the non-ideal behavior due to the formation of hydrogen bonding. They concluded that the CPA-EoS can be used efficiently for the phase equilbria of

complex systems composed of small association components such as methanol and water. Despite the power of the CPA-EoS, a difficulty arises to determine the pure component parameters for the different associating components, where five pure component parameters are needed as will be explained later in details.

Based on the previous discussion, the PR and the CPA EoSs are mainly employed in the current work. The PR-EoS is used to close the compressible set of governing equations, when the involved species do not include any associating compounds such as a binary system of n-dodecane and nitrogen. The PR-EoS has shown remarkable performance for modeling fuel injection under high-temperature/pressure conditions as demonstrated in [253, 149].

For mixtures involving short-chain alcohols, such as methanol along with hydrocarbons, the CPA-EoS is employed for the thermodynamic closure. Compared to the PR-EoS, the CPA EoS with its additional association term can be efficiently used to model mixtures including hydrocarbons and polar compounds (such as methanol) [57].

3.2 Real-fluid equations of state

The theoretical formulas of the Cubic Plus Association (CPA) and Peng-Robinson (PR) equations of state are detailed in the current section to highlight the differences between these two EoSs. Compared to the PR-EoS, the CPA-EoS combines the cubic Soave-Redlich-Kwong (SRK) EoS and an association term for modeling of associating compounds. Thus, in the absence of associating compounds, the SRK cubic equation is recovered, and the existing cubic EoS correlations can be used.

Generally, the pressure-explicit formulation of the EoS (Eq. (3.2)) includes repulsive contribution, attraction contributions, and it may include additional contributions such as the association contribution used in the CPA EoS. The different contributions are introduced in Table (3.1) for the two EoSs.

$$P = repulsive\,contribution + attractive\,contribution + association\,contribution \quad (3.2)$$

EoS	repulsive contribution	attractive contribution	association contribution
PR	$\frac{RT}{v-b}$	$-\frac{a(T)}{v\,(v+b)+b\,(v-b)}$	–
CPA	$\frac{RT}{v-b}$	$-\frac{a(T)}{v\,(v+b)}$	$-\frac{1}{2}\frac{RT}{v}\left(1+\rho\frac{\partial \ln g}{\partial \rho}\right)\sum_i x_i \sum_{A_i}\left(1-X_{A_i}\right)$

Table 3.1: Expressions for the different contributions in the EoS

where R is the ideal gas constant, T is the temperature, v is the molar volume, $a(T)$ is the energy parameter, b is the co-volume parameter, ρ is the inverse of the molar volume, g is the radial distribution function, X_{A_i} is the mole fraction of molecule i not bonded at site A and x_i is the mole fraction of the component i. The key element of the association term is X_{A_i} which is related to the association strength $\Delta^{A_iB_j}$ between 2 sites belonging to two different molecules (e.g. site A on molecule i and site B on molecule j) is expressed as:

$$X_{A_i} = \frac{1}{1+\rho\sum_i x_j \sum_{B_j} X_{B_j}\Delta^{A_iB_j}} \quad (3.3)$$

where the association strength term in the CPA EoS is formulated as:

$$\Delta^{A_iB_j} = g(\rho)\left[\exp\left(\frac{\varepsilon^{A_iB_j}}{RT}\right) - 1\right] b_{ij}\beta^{A_iB_j} \tag{3.4}$$

with the radial distribution function ($g(\rho)$) and b_{ij} given by:

$$g(\rho) = \frac{1}{1 - 1.9\eta},\ \eta = \frac{1}{4}b\rho,\ b_{ij} = \frac{b_i + b_j}{2} \tag{3.5}$$

The energy parameter $a_i(T)$ of the EoS for a pure component (i) is formulated as:

$$a_i(T) = (a_0)_i\left[1 + (c_1)_i\left(1 - \sqrt{\frac{T}{T_{c_i}}}\right)\right]^2 \tag{3.6}$$

where T_{c_i} is the critical temperature of pure component i.

The parameters $\varepsilon^{A_iB_j}$ and $\beta^{A_iB_j}$ are called the association energy and the association volume, respectively. These two parameters are only used for associating components such as alcohols and together with the three parameters of the SRK term (a_o, b, c_1), represent the five pure compound parameters of the CPA model. They are usually obtained by fitting vapor pressure and liquid density data. However, for inert components such as hydrocarbons, only the three parameters (a_o, b, c_1) of the SRK term are required, which can be obtained either from vapor pressures and liquid densities or calculated based on the critical point (T_c, P_c) and the acentric factor (ω) similar to the PR EoS as presented in Table. (3.2).

EoS	$(a_o)_i$	b_i	$(c_1)_i$
PR	$0.45724\frac{R^2T_c^2}{P_c}$	$0.07780\frac{RT_c}{P_c}$	$0.37464 + 1.5422\omega - 0.26992\omega^2$
CPA	$0.42747\frac{R^2T_c^2}{P_c}$	$0.08664\frac{RT_c}{P_c}$	$0.48508 + 1.55171\omega - 0.15613\omega^2$

Table 3.2: Pure component parameters used in the CPA (for non-associating compounds) and PR EoSs

when the CPA EoS or the PR EoS are used for mixtures, van der Waals mixing rules are applied for the energy and co-volume parameters $(a(T), b)$ as:

$$\begin{aligned} a(T) &= \textstyle\sum_i \sum_j x_i\, x_j \sqrt{a_i(T) a_j(T)}\,(1 - k_{ij}) \\ b &= \textstyle\sum_i x_i\, b_i \end{aligned} \tag{3.7}$$

where (k_{ij}) is the binary interaction parameter (BIP) that can be fitted to experimental data to well represent the phase diagram of a binary system.

Volume translation of cubic EoS

One of the drawbacks of the cubic EoS such as the PR is the inaccurate liquid density predictions. Thus, the volume translation [58] of the EoS can be employed to improve the liquid density predictions. The basic idea of the volume translation method is to correct the equation of state volume by translating it with a fixed value:

$$v^{VTEoS} = v^{EoS} + c \tag{3.8}$$

where (v^{VTEoS}) is the translated volume, (v^{EoS}) is the volume resulting from the EoS calculation, and (c) is the volume translation term. The parameter (c) can be temperature dependent and can be either directly fitted on experimental liquid volumes or calculated using another model. Further details on the volume translation method can be found in [20, 58]. It is also worth noting that volume translation does not influence the predicted phase equilibrium conditions.

3.3 Vapor-liquid equilibrium

To consider the two-phase properties as well as the phase change phenomenon, the EoS is not solely sufficient, but vapor-liquid equilibrium calculations are also required. According to the second law of thermodynamic, an isolated system at a fixed internal energy and volume, reaches its equilibrium state by a spontaneous process which maximizes its entropy. Thus, the equilibrium state corresponds to the stationary point of the entropy function:

$$dS = 0 \tag{3.9}$$

Using the internal energy equation (3.10), the entropy change can be formulated as in Eq. (3.11):

$$de = TdS - Pdv + \sum_k \mu_k dn_k \tag{3.10}$$

$$dS = \frac{de}{T} + \frac{P}{T}dv - \sum_k \frac{\mu_k}{T} dn_k \tag{3.11}$$

The total entropy change of a system composed of phase (I) and phase (II) can then be expressed as:

$$dS = dS^I + dS^{II} = \frac{de^I}{T^I} + \frac{P^I}{T^I}dv^I - \sum_k \frac{\mu_k^I}{T^I} dn_k^I + \frac{de^{II}}{T^{II}} + \frac{P^{II}}{T^{II}}dv^{II} - \sum_k \frac{\mu_k^{II}}{T^{II}} dn_k^{II} = 0 \tag{3.12}$$

Using the conservation principles lead to the following relations:

$$de^I + de^{II} = 0, \quad dv^I + dv^{II} = 0, \quad dn_k^I + dn_k^{II} = 0 \tag{3.13}$$

Thus, Eq. (3.12) can be reformulated as:

$$dS = \left(\frac{1}{T^I} - \frac{1}{T^{II}}\right) de^I + \left(\frac{P^I}{T^I} - \frac{P^{II}}{T^{II}}\right) dv^I - \sum_k \left(\frac{\mu_k^I}{T^I} - \frac{\mu_k^{II}}{T^{II}}\right) dn_k^I = 0 \tag{3.14}$$

As e^I, v^I, and n_k^I are independent variables, the three coefficients in the brackets must be zero to satisfy the condition ($dS = 0$). Accordingly, the thermodynamic equilibrium condition of the system is defined at equal temperature, pressure, and chemical potentials of the different components in each phase:

$$\begin{cases} T^I = T^{II} \\ P^I = P^{II} \\ \mu_k^I = \mu_k^{II} \end{cases} \tag{3.15}$$

Generally, a full vapor liquid equilibrium calculation starts with a stability test [200] to examine the stability of the system. If the stability test indicates that the system is unstable, it implies that an extra phase can be added or subtracted to stabilize the system. In such case, a phase equilibrium computation (usually called flash) has to be performed to obtain the final composition of each phase. In the current work, the phase equilibrium computation is based on the isothermal-isobaric (TPn) flash, which will be further discussed below.

3.3.1 Isothermal-isobaric flash

For a system at a fixed temperature and pressure, the equilibrium state is reached by a spontaneous process which minimizes its Gibbs energy. Thus, in this case, the equilibrium state corresponds to the global minimum of the Gibbs energy. For a given temperature, pressure, and feed composition (z_i), the objective of the isothermal-isobaric (TPn) flash calculation is to provide three unknowns, namely the vapor molar fraction (ψ_v) and the species molar composition in the liquid phase (x_i) and in the vapor phase (y_i).

The phase equilibrium condition is expressed by the equality of the chemical potential (μ_i) or fugacity (f_i) of each species (i) in the liquid (L) and vapor (V) phases as:

$$\begin{aligned} \mu_i^L &= \mu_i^V \\ f_i^L &= f_i^V \end{aligned} \tag{3.16}$$

In order to solve for the three unknowns (ψ_v, x_i, y_i), the iso-fugacity condition of Eq. (3.16) can be reformulated in terms of the fugacity coefficients (ϕ_i) as in Eq. (3.17) and accordingly the equilibrium constant (K_i) is defined, to which an additional constraint is added, as in Eq. (3.19). The equilibrium constant (K_i) provides a set of N_s equations and can be calculated from the selected thermodynamic model (EoS).

$$x_i\, \phi_i^L\, P = y_i\, \phi_i^V\, P \tag{3.17}$$

$$K_i = \frac{y_i}{x_i} = \frac{\phi_i^L}{\phi_i^V}, i = 1, N_s \tag{3.18}$$

$$\sum_i^{N_s} x_i - \sum_i^{N_s} y_i = 0 \tag{3.19}$$

By the use of the mass balance equation ($z_i = \psi_v\, y_i + (1 - \psi_v)\, x_i$) and substituting for ($y_i = K_i\, x_i$), one can obtain:

$$\begin{aligned} x_i &= \frac{z_i}{1 + \psi_v(K_i - 1)} \\ y_i &= \frac{z_i\, K_i}{1 + \psi_v(K_i - 1)} \end{aligned} \tag{3.20}$$

Further substitution of of Eq. (3.20) into Eq. (3.19) provides the well known Rachford-Rice equation [190]:

$$\sum_{i}^{N_s} \frac{z_i \left(K_i - 1\right)}{1 + \psi_v (K_i - 1)} = 0 \tag{3.21}$$

Finally, a system of $(N_s + 1)$ equations (3.18, 3.21) are solved iteratively to obtain the unknowns (K_i, ψ_v) for a given (T, P, z_i) using a (TPn) flash algorithm [152]. The phase composition (x_i, y_i) can be then obtained using Eq. (3.20).

3.4 Thermodynamic and transport properties

3.4.1 Single-phase properties

The evaluation of the single-phase real-fluid thermodynamic and transport properties is described in the current section. The calculation of the thermodynamic properties is performed based on the residual approach [58]. In this approach, any thermodynamic function (X) is computed as the sum of an ideal-gas part (X^o) and a residual part (X^{res}):

$$X = X^o + X^{res} \tag{3.22}$$

The ideal-gas part is determined from a specific polynomial equation [170]. While the residual part, which represents the deviation from the ideal-gas behavior can be expressed as:

$$X^{res} = \int_o^P \left(\left.\frac{\partial X}{\partial P}\right|_T - \left.\frac{\partial X^o}{\partial P}\right|_T \right) dP \tag{3.23}$$

As an example, the residual part of the molar internal energy (e^{res}) can be expressed as [58]:

$$e^{res}(T, P) = \int_\infty^v \left(T \left.\frac{\partial P}{\partial T}\right|_v - P \right) dv \tag{3.24}$$

Other energy properties can be found in [58]. An EoS which gives the relation between the pressure, volume, and temperature is then employed to evaluate the residual quantities. This implies that the choice of the thermodynamic model (EoS) has to be carefully done as it has an important role in the evaluation of the real-fluid thermodynamic properties.

In addition, some necessary thermodynamic derivatives such as the isobaric heat capacity (C_p), isochoric heat capacity (C_v), and sound speed (C_s) are required and defined as:

$$C_v = \left(\left.\frac{\partial e}{\partial T}\right|_v \right) \tag{3.25}$$

$$C_p = C_v - T \left(\left.\frac{\partial P}{\partial T}\right|_v \right)^2 \left(\left.\frac{\partial v}{\partial P}\right|_T \right) \tag{3.26}$$

$$C_s = \sqrt{\left.\frac{\partial P}{\partial \rho}\right|_s} \tag{3.27}$$

Regarding the evaluation of the transport properties, the thermal conductivity (λ) and dynamic viscosity (μ) are computed by the Chung et al. [51] correlations.

The species diffusion coefficient (D_k) is computed using two approaches in the current work. In the first approach, (D_k) is assumed species independent and deduced from a given molecular Schmidt number (Sc) as ($D = \mu/\rho Sc$). This approach is mainly employed for the simulation of high-pressure fuel injection cases with highly turbulent flow, presented in Chapters 5 and 6.

In the second approach, the mixture averaged diffusion coefficient (D_k) is computed as [130]:

$$\frac{1}{D_k} = \sum_{j \neq k}^{K} \frac{X_j}{D_{kj}} + \frac{X_k}{1 - Y_k} \sum_{j \neq k}^{K} \frac{Y_j}{D_{kj}} \tag{3.28}$$

where (X) and (Y) are the mole fraction and mass fraction of the species, respectively.

The binary diffusion coefficient (D_{kj}) is evaluated based on the Chapman-Enskog theory [130]:

$$D_{kj} = \frac{3}{16} \frac{\sqrt{2\pi k_B^3 T^3 / m_{kj}}}{P \pi \sigma_{kj}^2 \Omega_D} \tag{3.29}$$

where k_B is the Boltzmann's constant. The reduced molecular mass (m_{kj}), reduced collision diameter (σ_{kj}), and reduced collision integral (Ω_D) are calculated following the method of Hirschfelder et al. [107]. It is worth to note that (D_k) is obtained at pressures other than 1 atm by dividing the calculated diffusion coefficient by the actual pressure [130]. The second more detailed approach is mainly employed for simulations under laminar conditions. This approach is employed for the simulations carried out in Chapter 4.

3.4.2 Two-phase properties

The calculation of the two-phase properties is presented in the current section. After solving the TPn-flash, the composition of the phases is known, and thus the properties of each phase can be computed. Then, the two-phase mixture properties are calculated from the liquid and gas phase properties as described in Eqs. (3.30-3.36).

$$\rho = \sum_p \alpha_p \rho_p \tag{3.30}$$

$$e = \frac{1}{\rho} \sum_p \alpha_p \rho_p e_p \tag{3.31}$$

$$\lambda = \frac{1}{\rho} \sum_p \alpha_p \rho_p \lambda_p \tag{3.32}$$

$$\mu = \sum_p \alpha_p \mu_p \tag{3.33}$$

$$C_p = \frac{1}{\rho} \sum_p \alpha_p \rho_p C_{p_p} \tag{3.34}$$

$$C_v = \frac{1}{\rho} \sum_p \alpha_p \rho_p C_{v_p} \tag{3.35}$$

$$\frac{1}{\rho C^2_{s,mix,Wood}} = \sum_p \frac{\alpha_p}{\rho_p C^2_{s,p}} \tag{3.36}$$

where, (α_p) is the phase volume fraction and ($p = l, v$) stands for liquid and vapor phases, respectively. The vapor volume fraction (α_v) is computed from the vapor mole fraction (ψ_v) as ($\alpha_v = \frac{\psi_v v_v}{\psi_v v_v + (1-\psi_v) v_l}$). The symbols ($\rho$, e, $C_{s,mix,Wood}$) are the mixture density, specific internal energy, and Wood speed of sound [11], respectively. In addition, (λ, μ) are the mixture laminar thermal conductivity and dynamic viscosity, respectively. Finally, (C_p, C_v) are the mixture specific heats at constant pressure and volume, respectively.

It is worth noting that the calculation of the mixture's specific heats (C_p and C_v) in the VLE region is done by linearly blending the liquid and vapor phases specific heats as in Eqs. (3.34, 3.35). However, recently Tudisco and Menon [236] demonstrated that this simple blending approach could lead to significant departures from the actual definition of the specific heats. In addition, they demonstrated that the assumptions employed in the derivation of the Wood sound speed could lead to poor accuracy. Thus, further improvement of the calculation of the mixture specific heats and sound speed in the VLE region should be carried out in the future work.

3.5 Tabulation approach

3.5.1 Overview of the thermodynamic tabulation

The employment of a real-fluid EoS in CFD simulations can be computationally expensive especially for two-phase flow simulations, where vapor-liquid equilibrium (VLE) calculations are also required to consider the phase change.

Indeed, recent studies [254, 253, 200] have shown that the direct evaluation of VLE solver using a non-linear real-fluid EoS for the entire computational cells during each time step is computationally demanding. Thereby, a more robust approach is needed to overcome such cumbersome and costly VLE solver.

One of the proposed solutions in the literature [255, 135, 113, 59, 79, 37, 185] was to evaluate the required properties before the simulation and store them in a table. Thus, during the simulation, the stored quantities can be robustly interpolated, replacing the direct evaluation of the EoS along with the VLE calculations. Such tabulation approach could reduce significantly the computational effort. However, the storage memory requirements of the tables may be come an issue as the table dimensions are extended for multi-species systems. Therefore, the table look-up procedure has to be computationally efficient and the tabulation should have low-storage requirements.

The tabulation of the EoS has been employed in various studies. For instance, De Lorenzo et al. [59] proposed a table lookup method with bi-cubic interpolation based on the IAPWS-IF97 EoS to evaluate the water properties. This tabulation approach was coupled with the Homogeneous equilibrium model (HEM) and the Homogeneous relaxation model (HRM) to to simulate fast depressurization, water hammer, and steam explosion problems. Hempert et al. [105] investigated real gas effects of high-pressure supersonic methane jets using a tabulated EoS for methane. Fang et al. [76] adopted a tabulated EoS in the density-internal energy space for computing carbon dioxide properties. The tabulated EoS coupled to the HEM has been applied to simulate different configurations, including shock tube, tube depressurization, and converging-diverging nozzle, showing high

accuracy and efficiency. Föll et al. [79] proposed a tabulation method based on piece-wise polynomials and allows for adaptive refinement in state space. The proposed tabulation approach coupled with the HEM was applied to simulate the injection of transcritical nitrogen jets. Praneeth and Hickey [185] proposed a systematic error quantification and computational cost estimate of different EoS tabulation approaches for single species.

The previously-mentioned studies have mainly focused on single-species tabulation. However, other studies were also carried out for multi-species tabulation. For instance, Yi et al. [255] investigated n-dodecane droplets evaporation under transcritical conditions using a three-dimensional uniform tabulation approach based on the VLE solver developed in [254]. Jafari et al. [113] used a tabulation approach to investigate the cryogenic injection of liquid nitrogen co-axially injected with hot hydrogen into supercritical nitrogen. The latter model is further used to explore the interaction between phase separation and turbulent fluid dynamics for n-hexane injection into supercritical nitrogen [114]. Koukouvinis et al. [135] proposed uniform tabulation approach based on $(log_{10}P - T)$ tables using the PC-SAFT EoS to investigate the high pressure/temperature fuel injection under various ECN Spray A operating conditions. Vidal et al. [241] employed a tabulated thermodynamic approach based on the PC-SAFT EoS and VLE calculations to investigate the cavitation formation of a multi-component diesel fuel surrogate in a high-pressure fuel injector. Justino Vaz et al. [122] compared the behavior of multi-component diesel fuel surrogates injection using a tabulated thermodynamic approach based on the PC-SAFT EoS.

As previously mentioned, the storage memory requirements for the tables may become an issue as the table dimensions are extended for multi-species systems. Accordingly, other alternatives to the pre-tabulation approach have also been recently proposed. Zhang and Yang [259] employed an in situ adaptive tabulation (ISAT) approach, where the table is constructed during the CFD simulation. Besides, Koukouvinis et al. [136] employed an artificial neural network (ANN) as a regression model for the thermodynamic properties. Yue et al. [258] also proposed a method based on ANN as a potential alternative to the conventional algorithm applied in the engine spray models to achieve fast and robust phase equilibrium calculations. However, these approaches are still under investigation and their efficiency for multi-component problems is not yet evaluated.

Based on the above discussion, the current work employs a pre-tabulation approach that is applicable for multi-component mixtures, up to ternary mixtures, as will be detailed in the next sections.

3.5.2 Tabulation approach for binary & ternary mixtures

In the current work, a uniform pre-tabulation approach is proposed. Compared to previous research limited to binary mixtures tabulation [217, 114, 255], the proposed tabulation approach can further handle ternary (three-species) mixtures. The motivation of proposing a tabulation approach for ternary systems arises from the objective of the current work to investigate dual-fuel configurations, where a minimum of three species is required to mimic two different fuels and nitrogen as an air surrogate, for instance.

The thermodynamic table is generated for binary or ternary systems using the in-house Carnot thermodynamic library which uses a robust TPn-flash algorithm [152] coupled to various real-fluid EoSs, to tabulate all required properties for the specified ranges of temperature, pressure, and feed of the species.

Based on the Gibbs phase rule, Eq. (3.37), the number of independent variables (IV)

needed to fix a thermodynamic state can be determined as:

$$IV = C - PH + 2 \tag{3.37}$$

where (C) is the number of components/species in the mixture, (PH) is the number of phases present.

Therefore, for a binary mixture $(C = 2)$ in a single phase state $(PH = 1)$, the number of independent variables is $(IV = 3)$ and accordingly the thermodynamic table must be three dimensional (3D). Similarly for a ternary mixture $(C = 3)$ in a single phase state, the number of independent variables needed is $(IV = 4)$ and accordingly the thermodynamic table must be four dimensional $(4D)$.

Generally, the thermodynamic table axes are the temperature (T), pressure (P), and species mass fraction $(Y_k, k = 1, N_s - 1$,where N_s is the total number of species) as depicted in the schematic shown in Fig. 3.1. In addition, the pressure (P) axis could also be replaced by a decimal logarithm of pressure $(log_{10}P)$, as will be further discussed (see section. 3.5.3).

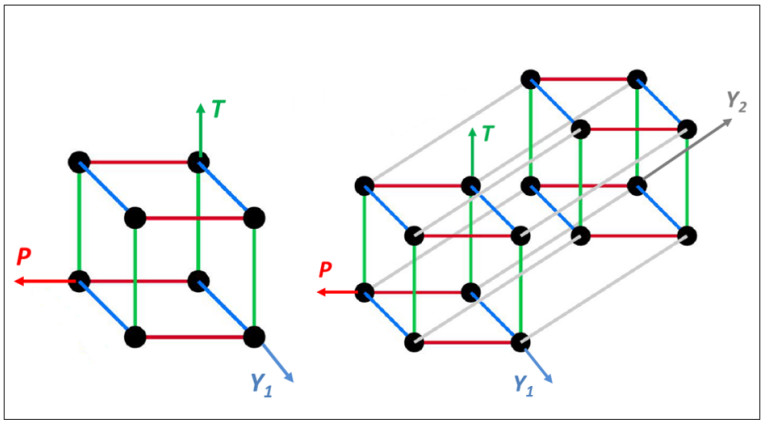

Figure 3.1: Table element structure for binary mixtures (3D) (left) and ternary mixture (4D) (right). T: Temperature , P: Pressure, Y_1 : mass fraction of first species , Y_2: mass fraction of the second species.

3.5.3 Thermodynamic table discretization approach

The discretization approach of the thermodynamic table axes is one of the critical elements of the thermodynamic table generation. Indeed, nonlinear and steep gradients for different properties exist mainly near the phase and phase-like boundaries (i.e. saturation and Widom lines). It is thus required to specify a proper table discretization in these regions. A detailed discussion of the thermodynamic table discretization approaches and the associated challenges can be found in [217].

Generally, the thermodynamic table axes can be discretized with uniform spacing or non-uniform spacing. On the one hand, in the uniform spacing approach, the searching task in the table could be very efficient. However, an issue with this approach is that for some physical phenomena such as cavitation in high injection pressure injectors, the pressure range for generating the table is often very large, and require high resolution to capture the phase change process, taking place at very low pressures. In such case, the size of the table could be cumbersome.

On the other hand, non-uniform spacing approach would allow for local refinement of the thermodynamic table near the critical regions (phase and phase-like boundaries), thus

decreasing the table size. However, the searching and interpolation in such case is more complex compared to the uniform approach and requires robust searching algorithms [217] to achieve the desired efficiency.

Accordingly, in the current work, a uniform discretization approach is mainly adopted for the table axes, that are structured in two different forms as:

1. $(T, P, Y_k, k = 1, N_s - 1)$
2. $(T, log_{10}P, Y_k, k = 1, N_s - 1)$

The main idea of the second form is to replace the linear pressure (P) with the decimal logarithm of pressure $(log_{10}P)$ as proposed in [135], also employing a uniform spacing.

To illustrate the advantage of using the decimal logarithm of pressure $(log_{10}P)$, Fig. 3.2 shows a comparison of the n-dodecane density variation with pressure at a constant temperature of 363 K for both the linear and logarithmic uniform tabulation approaches. The NIST data is also added as a reference. In both cases, 51 points have been used along a pressure range of 100 Pa to 1000 bar using the volume translated Peng-Robinson (VTPR) EoS. It can be seen the that $(log_{10}P)$ provides superior reconstruction of the density at both very low and high pressures, showing good agreement with the NIST reference data. On the other hand, the linear pressure, shows large errors compared to the NIST reference data, especially at low pressures and cannot capture correctly the density variation at the saturation pressure with the used number of points.

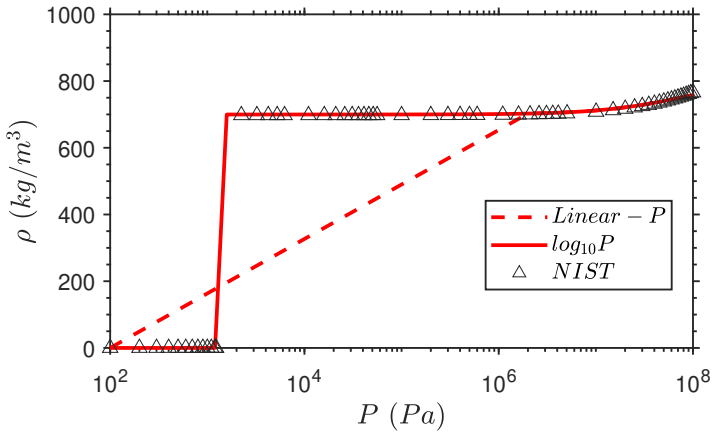

Figure 3.2: Comparison between the linear and log_{10} pressure axis discretization of pure n-dodecane density againest NIST reference data at T = 363 K. In both cases, 51 points have been used along a pressure range of 100 Pa to 1000 bar using the VTPR EoS.

Accordingly, the uniform tabulation based on the $(log_{10}P)$ is superior for cases such as fuel cavitation, as it can accurately capture the fuel saturation pressure (see Fig. 3.2) with an adequate number of points. This can be attributed to the non-linear distribution of sampling points, refined towards low pressures, where phase change takes place.

Whereas, the uniform tabulation based on linear (P) would require a huge number of points, to capture the fuel's saturation pressure, leading to a huge table size, and probably storage memory issues. In practice, the linear (P) approach can still be employed for cases with relatively small pressure variations, where a very high resolution of the pressure axis would not be required. In the current work, both the linear (P) and $(log_{10}P)$ approaches have been employed, as will be shown in the following Chapters.

3.5.4 Tabulation procedure

The thermodynamic table generation procedure based on the Carnot thermodynamic library is described in this section. The tabulation approach is similar for both binary and ternary systems. The tabulated properties include the thermodynamic equilibrium density, internal energy, fluid-phase state and composition, and necessary thermodynamic derivatives as heat capacity, sound speed, and transport properties. Noteworthy, it is possible to tabulate additional variables (such as the gas volume fraction or the phase composition) when required by the model or the analysis/post-processing of the numerical results.

The tabulation procedure is depicted in Fig. 3.3 and can be summarized in the following steps:

1. Specify the range of inputs: T , P , Y_k , where Y_k is the initial (feed) mass fraction of species k.
2. Solve VLE problem: $(\psi_v, x_k, y_k) = VLE\,(T, P, z_k)$ using the TPn flash (see Sec. 3.3.1), where z_k is mole fraction of species k calculated based on the input mass faction Y_k. (The conversion from the input Y_k to z_k is performed, since the VLE solver requires the species input to be the molar fraction).
3. If the mixture is in single liquid phase ($\psi_v = 0$) or single vapor phase ($\psi_v = 1$), then the single phase properties are directly computed (see Sec. 3.4.1).
4. If the mixture is in a two-phase state ($0 < \psi_v < 1$), both the liquid and gas phase properties are computed, then the two-phase mixture properties are evaluated (see Sec. 3.4.2).
5. Repeat steps (2 and 3) or (2 and 4), until the specified input's range of (T, P, Y_k) is completed.

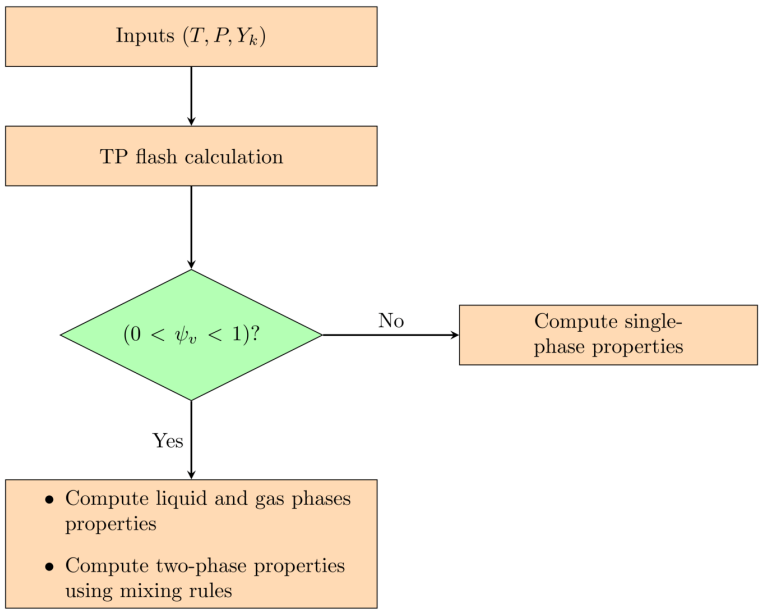

Figure 3.3: Flowchart of the thermodynamic library for generating the thermodynamic table.

3.5.5 Thermodynamic table interpolation

The interpolation of the thermodynamic table is carried out using the inverse distance weighting (IDW) method [244]. This method is based on the assumption that the value of the unsampled point is the average weight of the known values in the neighborhood, and the weight is inversely proportional to the distance between the prediction location and the sampled location. A general form of finding an interpolated value (p) at a given point (x) based on samples $p_i = p(x_i)$ for $i = 1, 2, ..., N$ using IDW can be expressed as follows,

$$p(x) = \begin{cases} \frac{\sum_i^N w_i(x) p_i}{\sum_i^N w_i(x)}, & if\ d(x, x_i) \neq 0\ for\ all\ i \\ p_i, & if\ d(x, x_i) = 0\ for\ some\ i \end{cases} \tag{3.38}$$

where, $w_i(x) = \frac{1}{d(x,x_i)}$, x denotes an interpolated (arbitrary) point, x_i is an interpolating (known) point, d is the given distance from the known point x_i to the unknown point x, N is the total number of known points used in interpolation.

3.6 Validation of the thermodynamic solver

The current section presents the validation of the thermodynamic solver based on the in-house Carnot thermodynamic library. Firstly, the VLE calculations for different binary mixtures of the species involved in the current work are computed and compared with available experimental data. Then, the computed properties for some species of interest in this thesis are validated against the NIST reference data [75]. Finally, the variation of the properties of binary and ternary mixtures is also illustrated and discussed.

3.6.1 Validation of vapor-liquid equilibrium

The VLE of a binary mixture of (n-dodecane/nitrogen) is computed using the PR-EoS with a binary interaction parameter ($k_{ij} = 0.19$) and compared with the experimental data [81]. The critical parameters for each pure compound are summarized in Table. 3.3. The comparison of the calculation results with the experimental data for the different iso-therms depicted in Fig. 3.4a, shows a satisfactory agreement between the calculations and the experiments for the majority of the considered pressures. Note also that the range of pressures where VLE exists is much larger than the critical pressures of the pure species individually. This confirms the fact that the single-phase assumption may fail when dealing with mixtures as the non-linear behavior due to the multi-component mixing can generate two-phases, even at supercritical pressure with respect to the pure species critical pressures.

Besides, the VLE of a binary mixture of (methanol/nitrogen) has been computed using the CPA-EoS and compared against the experimental data [38]. The CPA-EoS parameters for methanol are listed in Table. 3.4. Figure 3.4b presents the comparison of the calculation results with the experimental data. It shows that the VLE calculation agrees well with the experimental data for the different iso-therms, which demonstrates the reliability of the CPA-EoS with its additional association term to model mixtures including polar compounds (methanol).

Finally, the VLE of a binary mixture of (ammonia/nitrogen) is computed using the PR-EoS with ($k_{ij} = 0.24$) and compared with the experimental data [148] as depicted in

Fig. 3.4c, showing a fairly good agreement for the different iso-therms. The performed VLE calculations demonstrate the reliability of the Carnot thermodynamic library along with the different real-fluid EoSs to accurately model the considered mixtures.

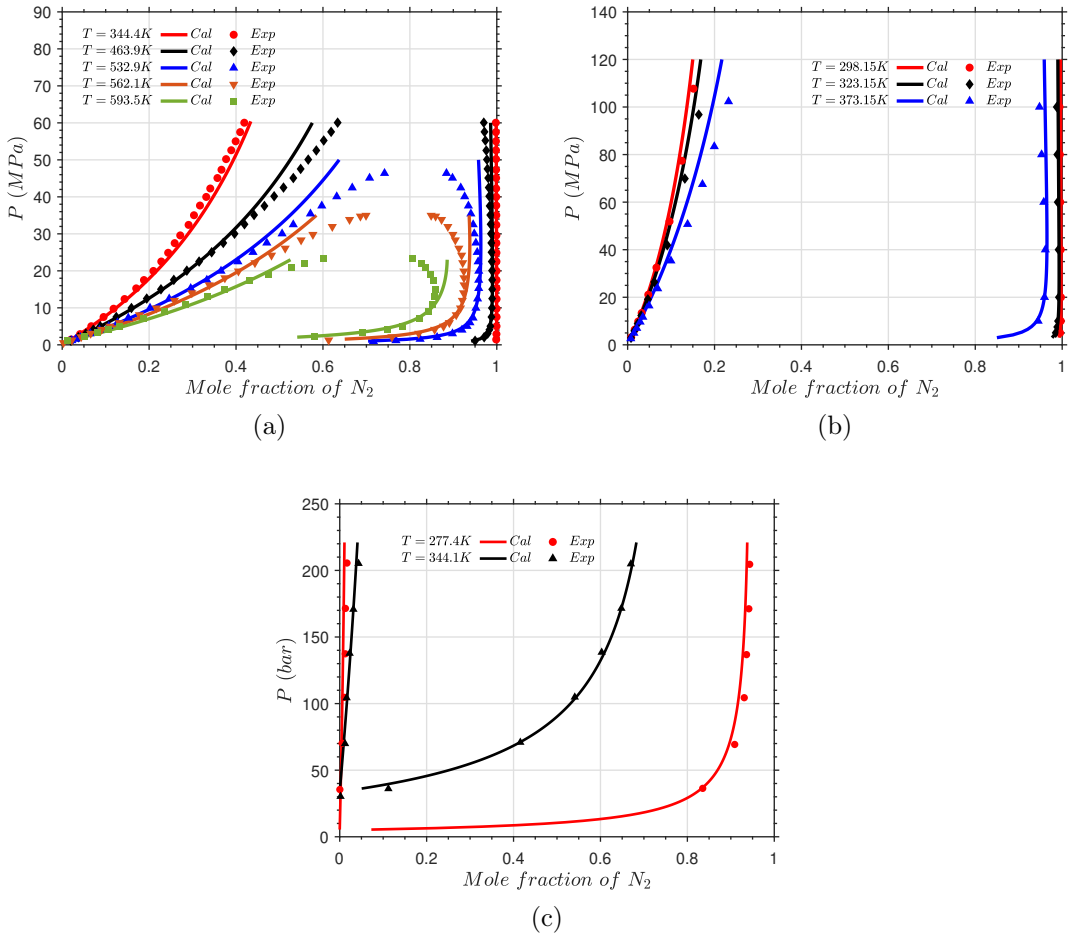

Figure 3.4: Phase diagram of binary mixtures (a) n-dodecane ($C_{12}H_{26}$) and nitrogen (N_2) using PR EoS, (b) methanol (CH_3OH) and nitrogen (N_2) using CPA EoS, and (c) ammonia (NH_3) and nitrogen (N_2) using PR EoS .

Species	T_c (K)	P_c (bar)	ω
n-dodecane	658.1	18.2	0.57344
Nitrogen	126.2	33.9	0.0403
Ammonia	405.6	113	0.25

Table 3.3: Critical parameters of n-dodecane, nitrogen, and ammonia including, the critical temperature (T_c), critical pressure (P_c), and the acentric factor (ω).

a_o (Pa.m^3/mol)	c_1	b (m^3/mol)	ϵ^{OH}/R (Pa.m^3/mol)	β^{OH}
0.40531	0.431	3.1e-05	2957.604	0.0161

Table 3.4: CPA EoS parameters for the polar compound (methanol).

3.6.2 Validation of pure component properties

For further validation of the thermodynamic library, the calculated properties of pure components (n-dodecane and nitrogen) using the PR and VTPR-EoS are compared with the NIST database [75], as depicted in Figs. (3.5, 3.6).

For the n-dodecane properties, the predicted density by the VTPR-EoS favorably agrees with the NIST reference data, especially for the low-temperature range, where the original (untranslated) PR-EoS underestimates the density. Besides, the predicted isobaric heat capacity by the VTPR and PR-EoSs show good agreement with the reference data, especially to reproduce the non-linear behavior of the heat capacity. At the considered pressure (2 MPa), higher than the n-dodecane critical pressure (1.8 MPa), the peak of the heat capacity that takes place around the pseudo-boiling or widom-line [21] is well captured by the EoS. The sound speed also shows good agreement with the reference data. Besides, the prediction of the transport properties (μ, λ) using the VTPR EoS, shows better agreement with the NIST data. This due to the fact that the density is an input parameter for the Chung model [51] used to compute the transport properties. Hence, the error in (μ, λ) decreases with more accurate density prediction.

For the nitrogen properties, Fig. 3.6 shows that the VTPR-EoS results match with great accuracy the NIST reference data. It is worth noting that for nitrogen properties, both the VTPR and PR EoSs provide the same results.

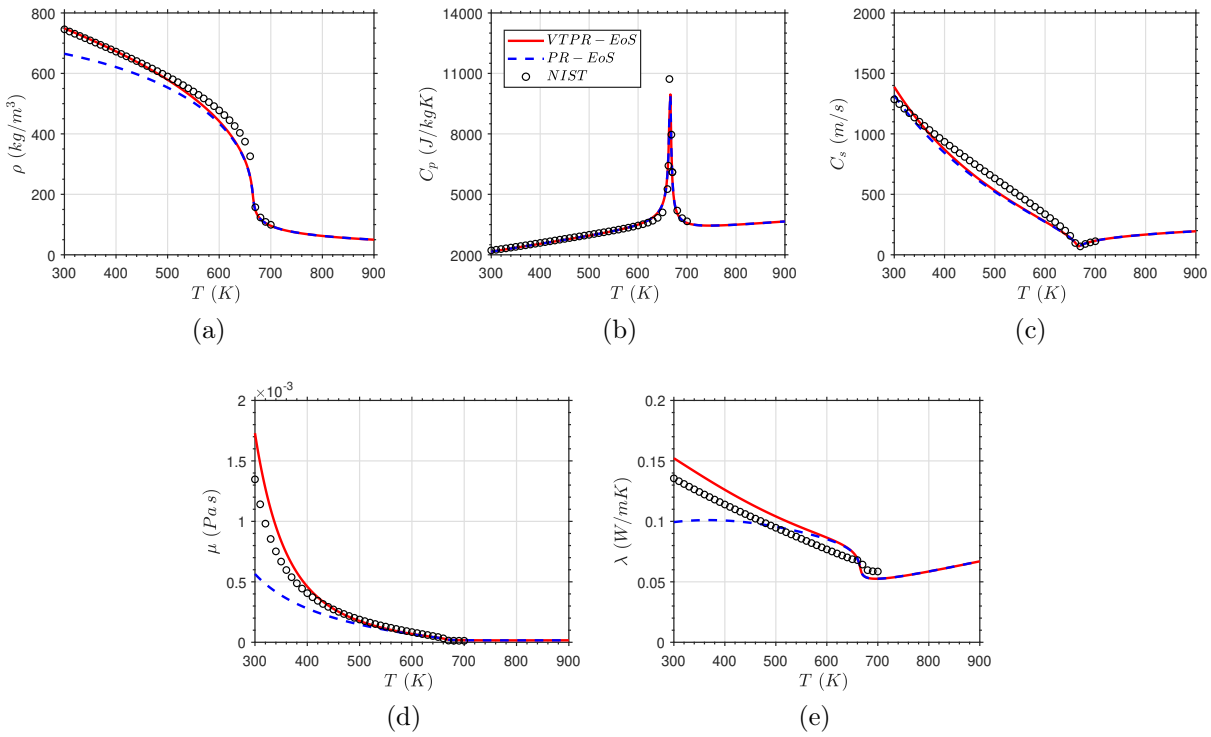

Figure 3.5: Pure n-dodecane: Comparison of the PR and VTPR EoSs prediction for the (a) density, (b) isobaric heat capacity, (c) sound speed, (d) dynamic viscosity, and (e) thermal conductivity against NIST reference data [75] at $P = 2$ MPa.

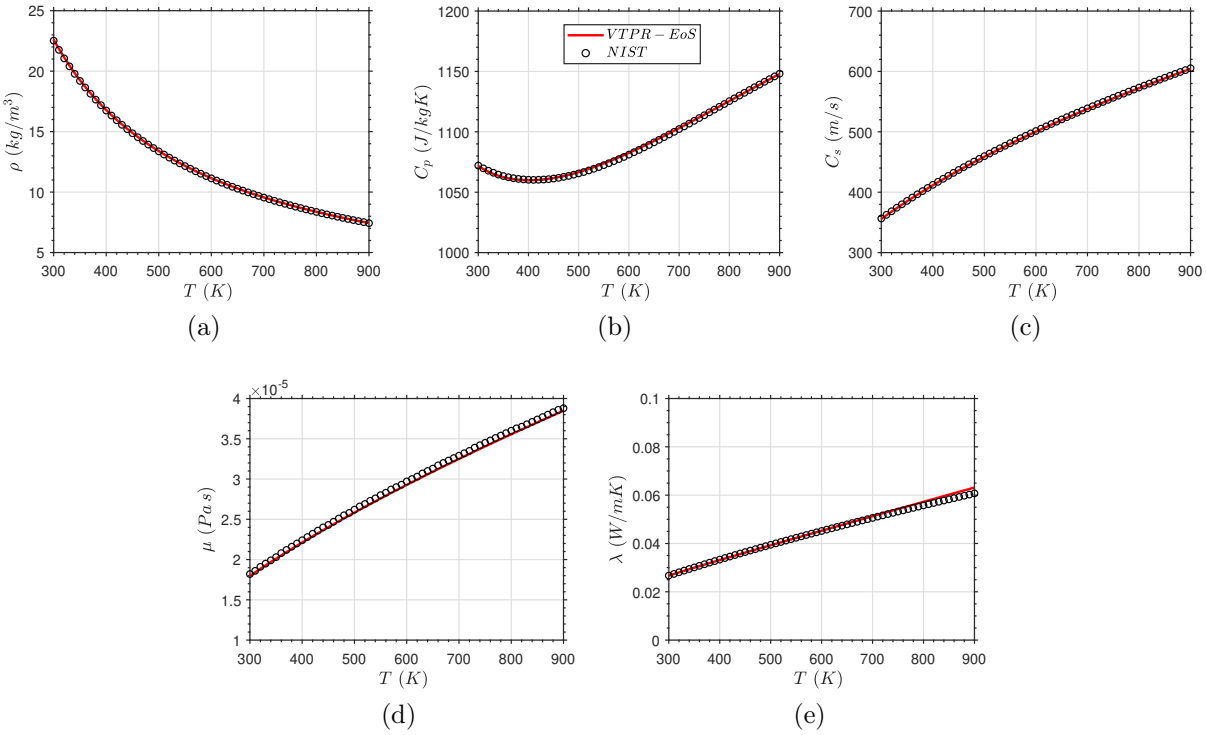

Figure 3.6: Pure nitrogen: Comparison of the VTPR-EoS prediction for the (a) density, (b) isobaric heat capacity, (c) sound speed, (d) dynamic viscosity, and (e) thermal conductivity against NIST reference data [75] at $P = 2\,\mathrm{MPa}$.

3.6.3 Properties of binary and ternary mixtures

After the validation of the single-species properties, the variation of the mixture properties is also visualized. Figure 3.7 shows the variation of the mixture properties for a binary mixture of (n-dodecane/nitrogen) at $P = 2\,\mathrm{MPa}$. These results show the variation of the different properties as a function of the temperature and nitrogen mass fraction. Besides, it can be seen the non-linear behavior of the properties which is captured by the employed real-fluid EoS.

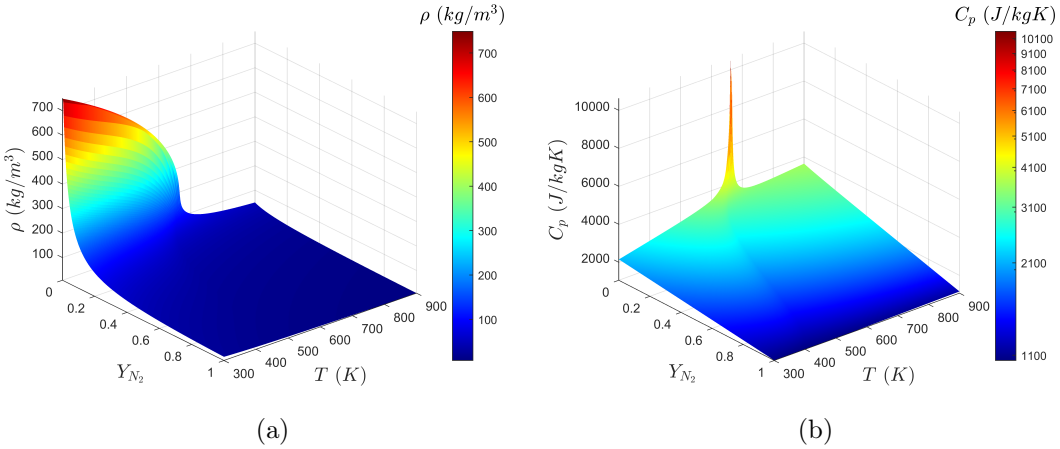

Figure 3.7: Contour plots of the binary (n-dodecane/nitrogen) mixture properties at $P = 2\,\mathrm{MPa}$ using the VTPR EoS. (a) density and (b) isobaric heat capacity.

In addition to binary mixtures, ternary mixtures are also investigated in the current work. One of the systems of interest is a ternary mixture of (n-dodecane/nitrogen/methanol), which is relevant to DFICE configuration. Figure 3.8 shows the variation of the mixture properties for the ternary mixture at $P = 106\,\text{bar}$ and $T = 500\,\text{K}$. These results show the variation of the properties as a function of the species composition. Under the considered high-pressure, the non-linear behavior of the properties can be observed. Indeed, Fig. 3.8b shows a peak of the isobaric heat capacity in the region, where the methanol mole fraction is approaching unity. Such behavior indicates that the considered pressure and temperature are in the vicinity of the widom-line for pure methanol, where the isobaric heat capacity exhibits a peak value.

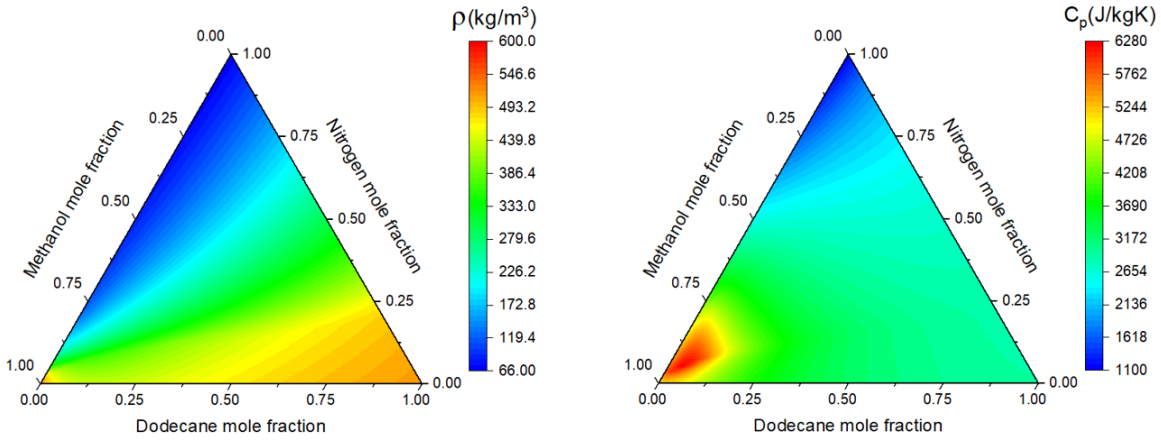

(a) (b)

Figure 3.8: Contour plots of the ternary (n-dodecane/nitrogen/methanol) mixture properties at ($P = 106\,\text{bar}$, $T = 500\,\text{K}$) using the CPA EoS. (a) density and (b) isobaric heat capacity.

3.7 Conclusions

This chapter started with a discussion of the different types of equation of states (EoSs) from the simple ideal-gas law to more complex real-fluid EoSs. The theoretical formulations of the PR and CPA EoS employed in the current work are then described. Next, the vapor-liquid equilibrium calculation based on the isothermal-isobaric (TPn) flash is discussed. Then, the methodology of the evaluation of the single and two-phase real-fluid thermodynamic and transport properties is detailed. An overview of the thermodynamic tabulation is subsequently discussed and the adopted tabulation approach for binary and ternary mixtures is detailed. The tabulation procedure using the in-house Carnot thermodynamic library is then described. Finally, this chapter closes with an evaluation of the VLE solver based on the in-house Carnot library. The thermodynamic library assessment is carried out by validating the VLE computations with available experimental data for different binary mixtures. In addition, the properties computation for some species of interest in this manuscript are validated against the NIST database. Finally, the variation of the properties of binary and ternary mixtures is illustrated and discussed.

Chapter 4

Droplet evaporation in dual-fuel conditions

Contents

This chapter is dedicated to the first objective of the current work, which is to investigate fuel droplet evaporation in a dual-fuel configuration using highly resolved simulations. Indeed, the goal here is to better understand the phase change and mixing of a single *n*-dodecane droplet in a bi-component environment composed of nitrogen and methanol at high pressure, mimicking a DFICE configuration. The study here is also the first application of the real-fluid model closed with the 4D-tabulation approach to investigate the mixing of a ternary system, including hydrocarbon (*n*-dodecane), short-chained alcohol (Methanol), and nitrogen. Due to the absence of experimental data for validation of this dual-fuel configuration, the current study first starts with the model validation against the experimental data of Crua et al. [53] for *n*-dodecane droplet evaporation in pure nitrogen. Then, the model is applied to the dual-fuel configuration to investigate the effect of the presence of methanol in the ambient on the phase change and mixing processes.

4.1 Introduction

Various experimental studies [138, 67, 174] have demonstrated the potential of employing primary fuels such as methanol or ethanol in DFICE to reduce the soot and nitrogen oxides (NOx) emissions. These fuels offer several advantages, including being renewable, lower cost, and can be produced from biomass. Despite the aforementioned advantages, the effective design of the fuel injection equipment (FIE) for DFICE is a challenging task and a key priority for the further development of these engines. To this goal, fuel injection and mixing need to be further understood. In this work, the evaporation and mixing of spray fuel droplets relevant to the dual-fuel configuration are investigated due to their direct impact on the combustion process and resulting emissions.
Extensive numerical and experimental investigations can be found in the literature regarding single or multi-component droplet evaporation of particular interest to those at high ambient pressures more relevant to realistic operating conditions. The droplet support method is one of the experimental techniques that has been widely used to study isolated droplet evaporation [163, 86]. However, a well-known problem of the support fiber method is the increase of the droplet evaporation rate due to the heat conduction through the support fiber when employing large fiber diameters [39, 43, 74]. Besides, the suspended droplet technique cannot be employed for supercritical fluid states, as the approach requires surface tension to attach the droplet onto the fiber. To circumvent these issues, Crua et al. [53] employed a fuel injector to generate droplets of normal alkanes (n-heptane, n-dodecane, n-hexadecane) under transcritical conditions, where the ambient temperature and pressure are higher than the critical point of the injected fuel. They performed a high-resolution microscopic visualization of individual droplets tracked at the end of the fuel injection event until they were completely vaporized. In addition, they proposed a transition criterion from the classical subcritical phase change to diffusive mixing regime.

On the numerical side, various investigations of droplet evaporation can be found in the literature. These investigations include detailed numerical models solving the Navier-Stokes (NS) equations to simpler models employing correlations to predict the heat and mass transfer processes. Schlottke et al. [208] studied the evaporation of deformed droplets based on the Volume of Fluid (VOF) method along with solving the incompressible NS equations, and the evaporation rate was computed based on the mass fraction gradient at the interface [207]. Strotos et al. [224] presented a model that solves the NS equations, energy conservation and species transport equations, and the VOF methodology to capture the liquid-gas interface. The simulated ambient temperatures range from 0.56 to 1.2 fuel's critical temperature under atmospheric pressure conditions. A local evaporation rate model was used based on the local vapor concentration gradient at the liquid-gas interface and assuming local thermodynamic equilibrium. Sacomano Filho et al. [201] proposed an evaporation model for multi-component droplets, which is derived from general energy and species transport equations, including differential diffusion effects. The proposed model was shown to be efficient for different binary liquid mixtures including polar and non-polar compounds under various atmosphere compositions and states. Extensive reviews of single or multi-component droplet evaporation models can be found in [206, 31, 154].

Regarding the evaporation modeling under elevated ambient pressures, many effects that are assumed negligible at low or moderate ambient pressures become important such as the solubility of the ambient gas in the liquid phase, non-ideal transport and thermo-

dynamic properties, the transient character of both the liquid and gas phases, and the real gas effect on the vapor-liquid equilibrium (VLE) condition at the droplet interface [116, 118]. Jia and Gogos [117] investigated the effect of the solubility of the ambient gas on the evaporation of n-hexane droplets. It was found that at ambient pressures lower than the fuel critical point, the droplet lifetime predicted with or without the ambient gas solubility agrees. However, as the ambient pressure exceeds the fuel critical point, neglecting the ambient gas solubility leads to underestimating the droplet lifetime. Ebrahimian and Habchi [74] proposed an evaporation model for multi-component hydrocarbon droplets, where they demonstrated that at high ambient pressures, the mixture non-ideality becomes significant, and the employment of real-gas equation of state (EoS) is needed. Accordingly, a real-fluid EoS is essential for accurate modeling of the fluid properties at such conditions.

The application of droplet evaporation models from the literature at high-pressure conditions in dual-fuel configurations could be questioned. Indeed, the evaporation models predict the heat and mass transfer processes using correlations, which may require further adjustments to consider the interaction and mixing between the pilot and primary fuels in dual-fuel engines, which subsequently affects the heat transfer and vaporization rates. Therefore, it is highly desirable to have computational fluid dynamics (CFD) software capable of performing highly resolved numerical simulations for dual-fuel conditions, considering the real-fluid thermodynamics, for further understanding of the interaction between the different fuels involved. The current work aims at providing such simulation tool, which after validation, could also offer an alternative for the cases that experimental techniques are not available.

In addition, the multi-component two-phase flow involved in such DFICE may exhibit different thermodynamic regimes based on the local pressure, temperature, and species composition compared to the mixture critical point. Indeed, it cannot be determined from an *a priori* analysis whether the Spatio-temporal variation of the involved thermodynamic states are subcritical or supercritical during the entire fuel injection event. As a matter of fact, both subcritical and supercritical regimes may exist simultaneously, as discussed in [253, 149, 112]. Thereby, two-phase flow models that can handle such multi-component mixtures accurately and robustly are required for the further development of DFICE.

Accordingly, in the current study, the RFM model is applied to investigate the evaporation of an n-dodecane droplet in a (methanol and nitrogen) bi-component ambient relevant to dual-fuel configuration compared to pure nitrogen ambient. The main aim is to investigate the impact of the primary fuel (methanol) ambient concentration on the n-dodecane droplet evaporation characteristics under the transcritical ambient conditions of Crua et al. [53] experimental work. Moreover, to analyze the effect of the different solubilities of methanol and nitrogen on the droplet evaporation at the high ambient pressures considered. Besides, whether the evaporation and mixing processes take place at a subcritical or supercritical thermodynamic regime will also be investigated.

4.2 Description of the simulated test cases

The simulated test cases represent the evaporation of an isolated stationary n-dodecane droplet in quiescent pure nitrogen or mixed (methanol and nitrogen) ambient, where the considered ambient temperatures and pressures are selected to match the typical transcritical conditions that can be found in modern diesel engines and were taken from the experimental work of [53]. The initial conditions of the simulated test cases are summarized in Table 4.1.

The performed simulations are carried out in two steps. In the first step, the temporal evolution of the n-dodecane droplet evaporation in a pure nitrogen ambient at the reference condition (case 1 in Table 4.1) is qualitatively compared with the experimental images of [53]. A qualitative comparison is only made since the initial temperature and diameter of the droplet are not known from the experiments. Thereby, the comparison is for the droplet behavior during its lifetime under the same ambient conditions.

In the second step, the n-dodecane droplet evaporation in a mixed (methanol and nitrogen) ambient relevant to the dual-fuel configuration will be investigated at the reference case condition (case 1 in Table 4.1) by adding methanol in the ambient gas with various initial concentrations. Besides, the ambient temperature and pressure are varied to investigate the effect of the methanol ambient concentration on the droplet evaporation at a relatively higher temperature and pressure (case 2 in Table 4.1).

Case	T_{amb} (K)	P_{amb} (bar)	d_o (µm)	$U_{d,o}$ (m/s)	$T_{d,o}$ (K)
1 (Reference case)	700	62	60	0	363
2	1200	106	60	0	363

Table 4.1: Operating conditions of the simulated test cases including the ambient temperature (T_{amb}), ambient pressure (P_{amb}), initial droplet diameter (d_o), initial droplet velocity ($U_{d,o}$), and initial droplet temperature ($T_{d,o}$).

4.2.1 Computational set-up and numerical methods

Computational set-up

The computational domain comprises a cube of edge length ($10\,d_o$) as depicted in Fig. 4.1a, where the droplet is placed at the domain center and accounts for less than 1% of the domain volume so that the changes in the ambient conditions due to the ongoing evaporation are negligible. The base grid size is set to (16 µm) at the droplet's far-field along with different embedding levels to achieve a mesh resolution at the droplet interior and interface of (2 µm) corresponding to 30 cells/diameter (see Fig. 4.1b). The total cell count is approximately 0.55 million cells. The employed grid size is chosen based on a grid sensitivity study using different levels of grid refinement, as will be demonstrated in the next section. Regarding the boundary conditions, the computational domain boundaries (Fig. 4.1a) are assumed as adiabatic walls with zero gradients for pressure and species mass fraction. The initial conditions are summarized in Table. 4.1. Finally, it should be noted that no turbulence model is used in these highly resolved two-phase simulations.

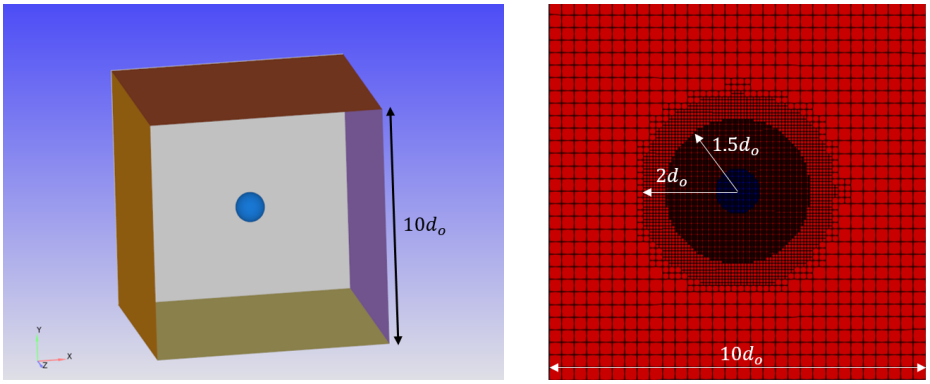

(a) (b)

Figure 4.1: (a) Computational domain size in terms of the initial droplet diameter (d_o), (b) Grid topology with different levels of grid refinement in the central section of the computational domain. The minimum cell size (2 µm) is located at the refinement region with a radius of (1.5 d_o).

Numerical methods

The current simulations are carried out using CONVERGE V3.0.15 employing the PISO algorithm (see Sec. 2.1.5.1). A second-order central difference scheme is used for the spatial discretization of each equation. The time discretization is achieved by the second-order Crank-Nicolson scheme for the momentum equation and the first-order Euler scheme for the rest of the equations. The time step is automatically controlled by a maximum Courant-Friedrichs-Lewy (CFL) number of 0.9, reaching a value in the range (1 ns−4 ns). The computational cost of the simulation using the newly developed tabulation approach is 48 h of wall clock time for a simulation time of 4 ms using 108 cores of the latest generation Intel Skylake G-6140 processors running at 2.3 GHz (ENER440 IFPEN Supercomputer).

The RFM model thermodynamic closure for the (n-dodecane/ nitrogen) binary mixture is based on the PR-EoS, with a uniform thermodynamic table resolution in (P, T, $Y_{C_{12}H_{26}}$) axes of (21×201×101) points covering ranges of (40-110 bar, 300-1300 K, 0-1).

However, for the droplet evaporation in a mixed ambient, the thermodynamic closure for the (n-dodecane/ nitrogen/ methanol) ternary mixture is based on the CPA-EoS, with a uniform thermodynamic table resolution in (P, T, $Y_{C_{12}H_{26}}$, Y_{N_2}) axes of (21×201×101×101) points covering same range of the binary case. Compared to the PR-EoS, the CPA EoS with its additional association term can be efficiently used to model mixtures including hydrocarbons and polar compounds (methanol) [58].

It should be noted that the surface tension effect was not considered in the current simulations and assumed to be negligible at the considered high ambient temperatures and pressures. However, this assumption should be further investigated in future work. Indeed, the main objective of this work is to study the effect of the presence of methanol in the ambient medium relevant to the dual-fuel configuration on the evaporation characteristics of an n-dodecane droplet under transcritical conditions.

4.2.2 Dodecane droplet evaporation in pure nitrogen ambient

A grid sensitivity study is performed at the reference case condition (Table 4.1) using different grid refinement levels to achieve a minimum cell size of (4, 2, 1 µm) corresponding to (15, 30, 60 cells/diameter) at the droplet interior and interface. Figure 4.2 shows that grid convergence is fairly achieved for the dimensionless droplet volume (V/V_o) temporal evolution with the minimum cell size of (30 cells/diameter). Accordingly, it has been employed for further calculations as a compromise between accuracy and computational cost.

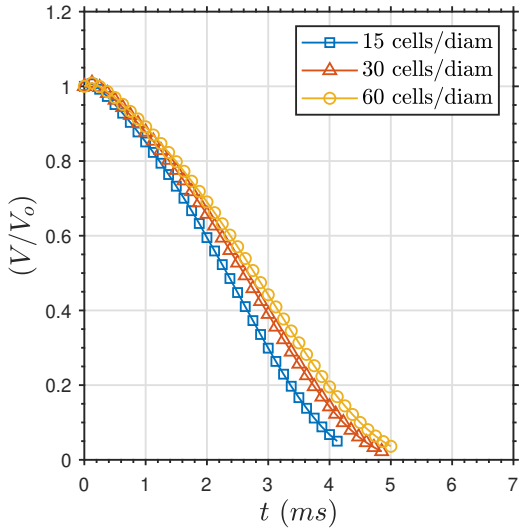

Figure 4.2: Temporal evolution of the dimensionless droplet volume (V/V_o) for case 1 (P_{amb} = 62 bar, T_{amb} = 700 K) using different levels of grid refinement. The droplet volume (V) is computed from the simulations as [$V = \sum_{cells} \alpha_L V_{cell}$].

The temporal evolution of the n-dodecane droplet evaporation under the reference condition (Table 4.1) is qualitatively compared with the experimental images [53] under the same ambient conditions. Figure 4.3 shows the temporal variation of the liquid volume fraction (α_L) obtained from the simulation at the central cut-section of the droplet compared with the experimental images. The initial time of the comparison is similar to that of the published experimental video sequence (t ≈ 0.03 ms). Overall a good qualitative agreement can be observed. Indeed, the droplet size is decreasing due to the ongoing evaporation, as illustrated by the blue isoline of (α_L = 0.5) depicted on the simulation images. This comparison shows that the RFM model proposed in this work is capable of providing the characteristics of droplet evaporation under such transcritical conditions and can therefore be applied with sufficient confidence to the study of ternary mixtures that are more representative of the dual-fuel configuration.

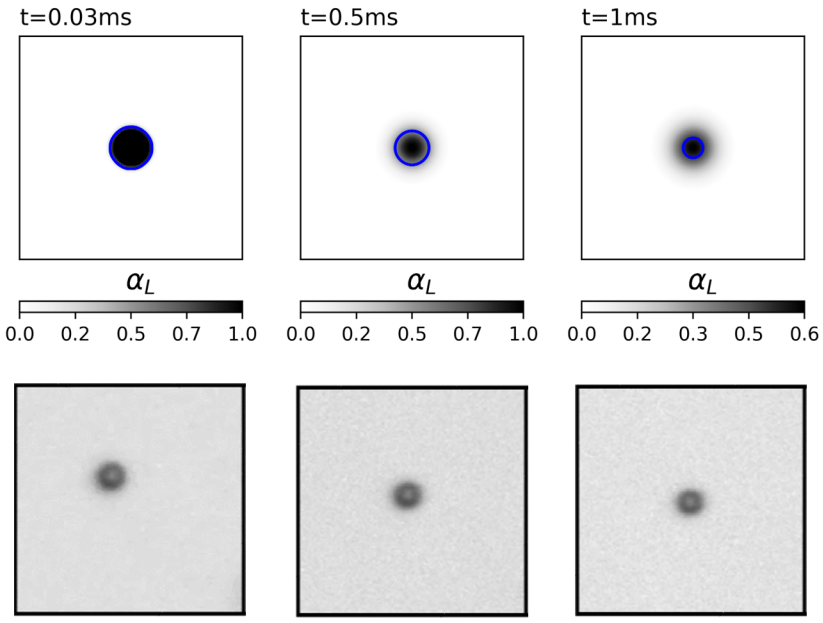

Figure 4.3: Qualitative comparison of the temporal evolution of the liquid volume fraction (α_L) obtained from the simulation in the central cut-section of the evaporating n-dodecane droplet (first row) with the experimental images [53] (second row) under the same ambient conditions ($P_{amb} = 62\,\text{bar}$, $T_{amb} = 700\,\text{K}$). The blue line depicted on the simulation images represents an isoline of ($\alpha_L = 0.5$). The size of the numerical images is ($300\,\mu\text{m} \times 300\,\mu\text{m}$) similar to the experimental ones. The initial time of the comparison is similar to that of the published experimental video sequence ($\text{t} \approx 0.03\,\text{ms}$).

4.3 Dodecane droplet evaporation in dual-fuel configuration

4.3.1 Effect of the methanol ambient concentration

In this section, the n-dodecane droplet is evaporating in a homogeneously mixed ambient of Nitrogen (N_2) and methanol (CH_3OH) at the same ambient pressure and temperature as the reference case (case 1 in Table 4.1). However, the initial methanol mass fraction (Y_{CH_3OH}) in the ambient mixture is varied from 0.2 to 0.6, and accordingly, the initial mass fraction of nitrogen in the ambient is ($Y_{N_2} = 1 - Y_{CH_3OH}$). It is worth noting that the employed methanol mass fractions could be relatively higher than that found in practice for dual-fuel engines. However, the goal here is to investigate if significant effects on the evaporation and mixing could take place as the methanol exhibits such relatively high concentrations.

The effect of the methanol ambient concentration on the temporal variation of the dimensionless squared droplet diameter $(d/d_o)^2$ is depicted in Fig. 4.4a. In this figure, the droplet diameter is computed from the simulations based on the liquid volume (V_L) as $[d = (6/\pi \sum_{cells} \alpha_L V_{cell})^{1/3}]$. Two main observations can be drawn from this figure. On the one hand, a higher methanol ambient concentration causes a greater rise in the droplet size during the early evaporation phase. On the other hand, a reduction in droplet lifetime can be observed with increasing methanol ambient concentration compared to the reference case ($Y_{CH_3OH} = 0$).

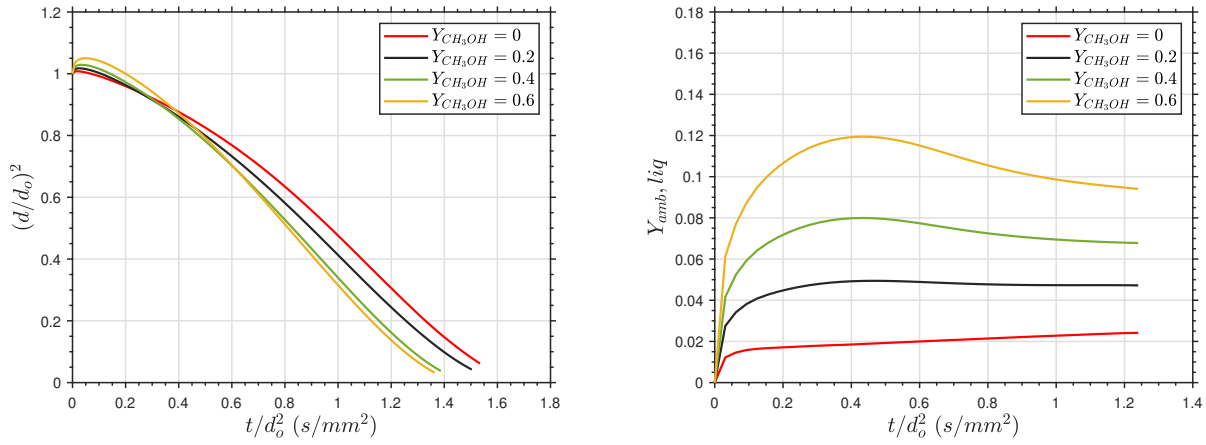

(a) (b)

Figure 4.4: (a) Temporal evolution of the dimensionless squared droplet diameter $(d/d_o)^2$, and (b) mean mass fraction of dissolved ambient gases (methanol + nitrogen) in the liquid phase ($Y_{amb,liq}$) at ($P_{amb} = 62\,\text{bar}$, $T_{amb} = 700\,\text{K}$) for different methanol ambient concentrations (Y_{CH_3OH}).

Regarding the initial droplet size increase, this phenomenon has been classically attributed to the liquid thermal expansion at the beginning of the evaporation [86]. However, in the current study, a larger droplet size increase at the beginning of the evaporation is found by increasing the methanol ambient concentration. This behavior can be explained through Fig. 4.4b, which shows the temporal evolution of the mean mass fraction of dissolved ambient gases (methanol + nitrogen) in the liquid phase ($Y_{amb,liq}$), computed as $\left[Y_{amb,liq} = \frac{\sum_{cells}(Y_{CH_3OH,liq}+Y_{N_2,liq})\alpha_l V_{cell}}{\sum_{cells}\alpha_l V_{cell}}\right]$, where ($Y_{CH_3OH,liq}$) and ($Y_{N_2,liq}$) are the mass fraction of methanol and nitrogen dissolved in the liquid phase, respectively. An increase of the mean mass fraction of dissolved ambient gases can be observed throughout the droplet lifetime with increasing the methanol ambient concentration, which would explain the initial droplet size increase behavior (Fig. 4.4a). Besides, this behavior demonstrates that methanol exhibits a relatively higher solubility in the liquid phase compared to nitrogen. Figure 4.4b also shows a non-trivial amount of dissolved gases, which emphasizes that considering the solubility of the ambient gases in the liquid phase at such high-pressure conditions is essential and cannot be neglected, for instance, in Lagrangian droplets evaporation models.

Figure 4.5a presents the temporal variation of the mean droplet temperature (T_d) computed from the simulations as $\left[T_d = \frac{\sum_{cells} T_{cell}\alpha_l V_{cell}}{\sum_{cells}\alpha_l V_{cell}}\right]$, where ($T_{cell}$) is the cell temperature. It can be seen that the mean droplet temperature is relatively higher throughout the droplet lifetime for higher methanol ambient concentrations. This temperature trend suggests that the droplet follows a different thermodynamic path based on the methanol ambient concentration.

For further understanding of the mean droplet temperature behavior, Fig. 4.5b shows the adiabatic mixing temperature (T_{AM}) variation with the fuel (n-dodecane) mole fraction. In this figure, the blue segment represents the two-phase region along the adiabatic mixing temperature lines for the different methanol ambient concentrations. The adiabatic mixing temperature is calculated using the following expression for the mixture enthalpy,

$$h_{mix}(T_{AM}, P_{amb}, Y_{C_{12}H_{26}}) = Y_{C_{12}H_{26}}\, h_{C_{12}H_{26}}(T_{C_{12}H_{26}}, P_{amb}) + Y_{amb}\, h_{amb}(T_{amb}, P_{amb}) \quad (4.1)$$

where h, $Y_{C_{12}H_{26}}$, Y_{amb} are the specific enthalpy, mass fraction of the n-dodecane, and the ambient gases, respectively. Besides, $T_{C_{12}H_{26}}$, T_{amb}, P_{amb} denote the initial temperature of the fuel (n-dodecane), the initial temperature of the ambient, and the ambient pressure, respectively. The ambient mass fraction is formulated as ($Y_{amb} = Y_{CH_3OH} + Y_{N_2}$), where $Y_{CH_3OH} = C\ Y_{amb}$, $Y_{N_2} = (1 - C)\ Y_{amb}$, and $C = \{0, 0.2, 0.4, 0.6\}$. The adiabatic mixing temperature is computed taking into account the phase change based on the VLE solver. Figure 4.5b shows the variation of the adiabatic mixing temperature as a function of the fuel (n-dodecane) mole fraction. The (T_{AM}) starts at the initial droplet temperature (363 K) on the figure right side and increases to the ambient temperature (700 K) on the left side. It can be seen that the adiabatic mixing temperature is relatively higher with increasing the methanol ambient concentration, which would explain the mean droplet temperature trend obtained from the simulations (see Fig. 4.5a). Besides, Fig. 4.5b shows that the two-phase region (in blue) along the adiabatic mixing temperature lines shrinks noticeably as methanol ambient concentration increases, which would contribute to the reduction of the droplet lifetime observed in Fig. 4.4a.

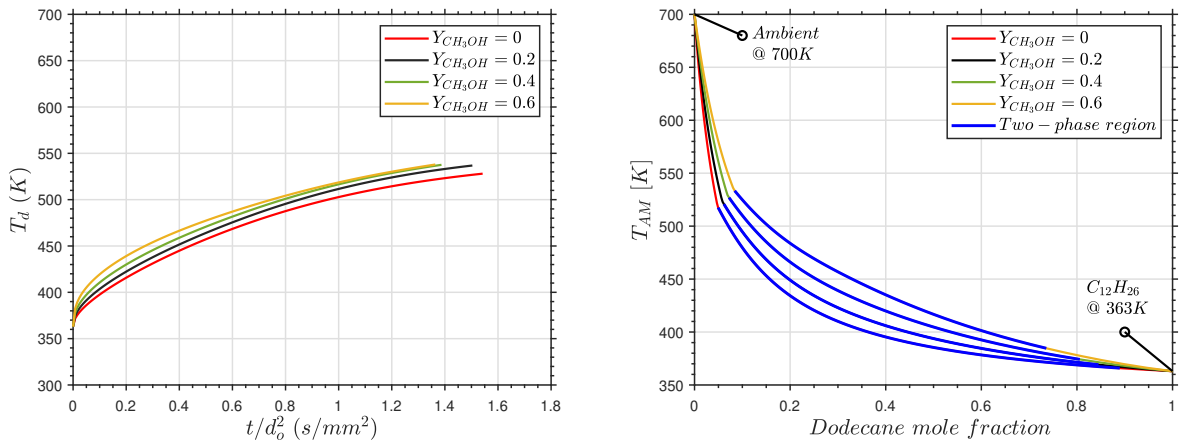

(a) (b)

Figure 4.5: (a) Temporal evolution of the mean droplet temperature (T_d) and (b) adiabatic mixing temperature (T_{AM}) along with the two-phase region represented by the blue lines at ($P_{amb} = 62$ bar, $T_{amb} = 700$ K) for different methanol ambient concentrations (Y_{CH_3OH}). The blue lines in (b) show how the two-phase region shrinks as the methanol increases in the ambient gas. The right side of (b) shows a smaller dodecane mole fraction at the start of the two-phase region (ie. higher mole fraction of dissolved gases in the liquid phase) as the methanol ambient concentration increases.

4.3.2 Effect of the ambient temperature and pressure

The effect of the variation of the ambient temperature and pressure on single or multi-component droplet evaporation has been extensively investigated in the literature [92, 74, 19, 116], whereas, in the current study, the main focus is to monitor the methanol ambient concentration effect on the droplet evaporation characteristics at various ambient temperatures and pressures. Accordingly, the impact of the methanol ambient concentration is investigated at a higher ambient temperature and pressure (case 2 in Table 4.1) compared to the reference case condition (case 1 in Table 4.1).

Figure 4.6a shows the temporal variation of the dimensionless squared droplet diameter for the second ambient condition. It can be seen that the droplet exhibits a relatively higher evaporation rate and shorter lifetime as the methanol ambient concentration increases. Besides, Fig. 4.6b shows a higher total amount of dissolved ambient gases than the reference case (Fig. 4.4b) as the ambient pressure and temperature increase.

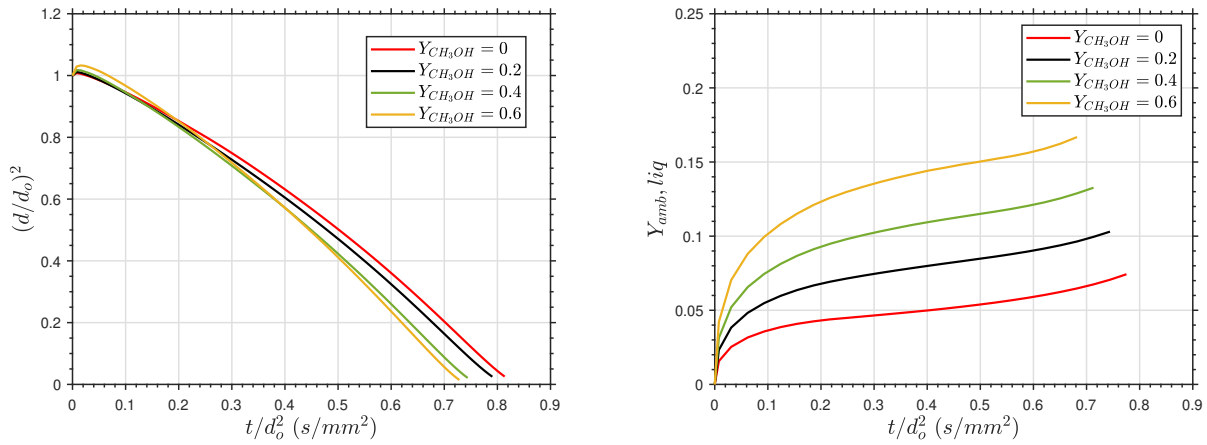

(a) (b)

Figure 4.6: (a) Temporal evolution of the dimensionless squared droplet diameter $(d/d_o)^2$ and (b) mean mass fraction of dissolved ambient gases (methanol + nitrogen) in the liquid phase ($Y_{amb,liq}$) at ($P_{amb} = 106\,\text{bar}$, $T_{amb} = 1200\,\text{K}$) for different methanol ambient concentrations (Y_{CH_3OH}).

The temporal variation of the mean droplet temperature (Fig. 4.7a) for the different methanol ambient concentrations tends to follow the adiabatic mixing temperature variation depicted in Fig. 4.7b. In addition, the relative reduction of the two-phase region along the adiabatic mixing temperature curves (Fig. 4.7b) with increasing the methanol ambient concentration is more significant than the reference case (Fig. 4.5b) at lower ambient pressure and temperature.

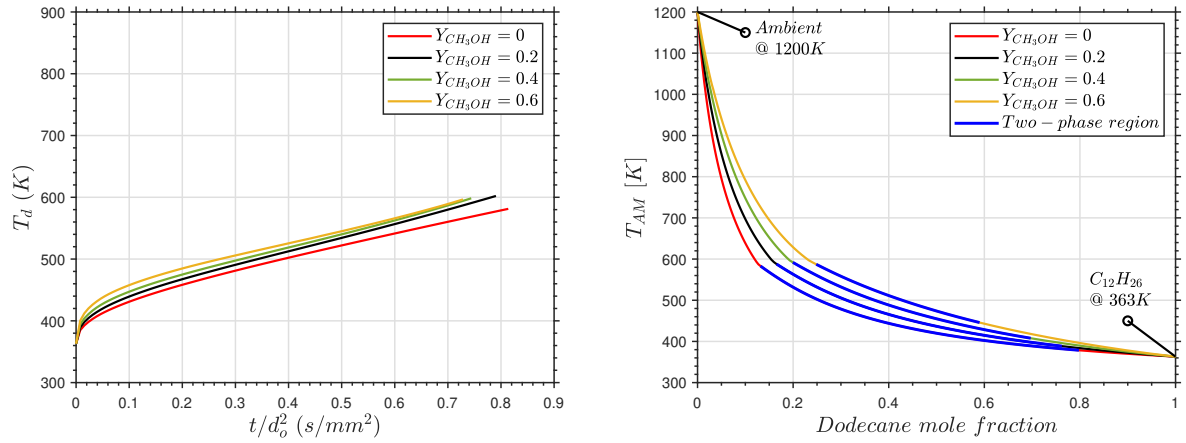

(a) (b)

Figure 4.7: (a) Temporal evolution of the mean droplet temperature (T_d) and (b) adiabatic mixing temperature (T_{AM}) along with the two-phase region represented by the blue lines at ($P_{amb} = 106$ bar, $T_{amb} = 1200$ K) for different methanol ambient concentrations (Y_{CH_3OH}).

Figure 4.7a also shows that the mean droplet temperature keeps increasing during the entire droplet lifetime without reaching a steady temperature, the so-called wet-bulb temperature for the different methanol ambient concentrations. This behavior has also been observed in the literature [116, 118] when the ambient pressure is higher than the fuel critical pressure. It can be attributed to the simultaneous occurrence of the droplet vaporization and heating-up processes, due to the relatively low latent heat of vaporization, in contrast to the low or moderate pressure conditions, where the droplet heating process takes place almost separately from the vaporization process. The behavior of not reaching a steady temperature can also be seen through Fig. 4.5a at the reference case condition, but it is more pronounced at the ambient conditions of case 2 (Fig. 4.7a).

To summarize the results of the considered ambient conditions, the droplet evaporation characteristics are evaluated in terms of evaporation rate constant (k), initial heat-up time (t_H), and droplet lifetime (t_L). The definitions of ($k, t_H/d_o^2, t_L/d_o^2$) are similar to previous experimental [86, 163] and numerical [92, 247] studies as illustrated in Fig. 4.8. The evaporation rate constant is defined as the slope of the best-fit straight line obtained by the least-squares linear fitting method in the range of $(d/d_o^2) = (0.1 - 0.8)$, after the initial heat-up period. The time at the intersection point of the fitting line and the straight line $(d/d_o^2 = 1)$ is regarded as the initial heat-up time, whereas the time at the intersection point of the fitting line and the straight line $(d/d_o^2 = 0)$ is regarded as the droplet lifetime. The previous definition of (k) is adopted (instead of mass evaporation rate ($\dot{m}$)) in the current analysis, as it can be directly determined from the droplet diameter temporal evolution obtained from the simulation (see Fig. 4.8). In addition, a mass evaporation rate can be deduced from (k) using ($\dot{m} = -\rho_m \frac{\pi}{4} kD$) as demonstrated in [91], where (ρ_m) is assumed to be a constant mean density of the liquid droplet. Thus, to avoid such assumption, only (k) was considered for the analysis of the current results.

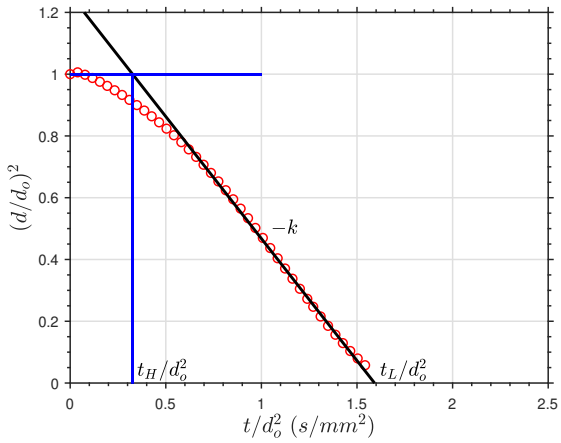

Figure 4.8: Definition of the droplet evaporation rate (k), initial heat-up time (t_H) and lifetime (t_L) at ($P_{amb} = 62\,\text{bar}$, $T_{amb} = 700\,\text{K}$, $Y_{CH_3OH} = 0$).

Figure 4.9 shows the variation of $(k, t_H/d_o^2, t_L/d_o^2)$ as a function of the initial methanol ambient concentration (Y_{CH_3OH}) for the considered ambient conditions. Figure 4.9c shows that the droplet lifetime decreases monotonically with increasing methanol ambient concentration. The droplet evaporation rate and heat-up time variation with the methanol ambient concentration are investigated to further understand the droplet lifetime behavior. The contribution of the evaporation rate and initial heat-up time to the droplet lifetime can be understood through Eq. (4.2), where the droplet lifetime is written as the sum of the heat-up time and the inverse of the evaporation rate constant.

$$t_L/d_o^2 = t_H/d_o^2 + 1/k \tag{4.2}$$

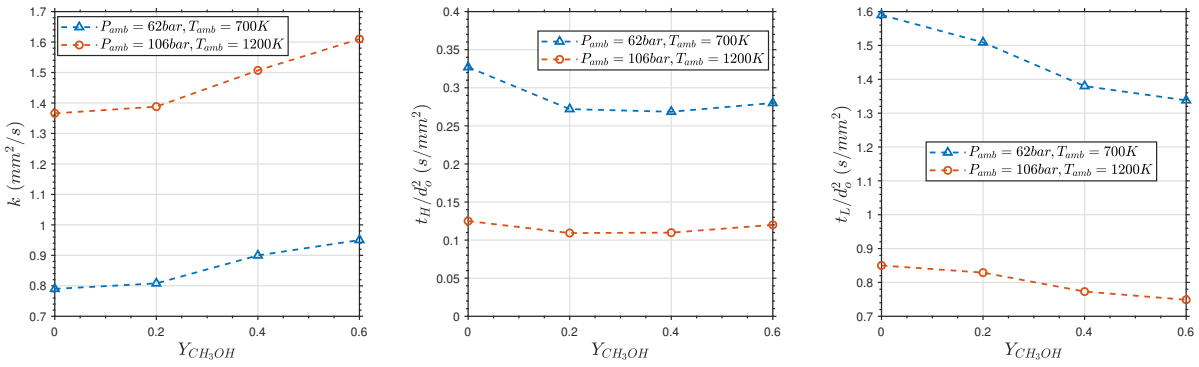

(a) (b) (c)

Figure 4.9: Variation of the (a) evaporation rate constant, (b) initial heat-up time, and (c) evaporation lifetime with the initial methanol ambient concentration (Y_{CH_3OH}) at different ambient temperatures (T_{amb}) and pressures (P_{amb}). The droplet evaporation lifetime and the initial heat-up time are divided by the squared initial droplet diameter d_o^2.

Figure 4.9a shows a monotonic increase of the evaporation rate with increasing the methanol ambient concentration. This behavior can be explained through Fig. 4.10, which shows the equilibrium mole fraction of vaporous n-dodecane (fuel) at the two-phase states along the adiabatic mixing temperature curves (bold blue lines of Figs. (4.5b, 4.7b)).

A relative increase in mole fraction of vaporous n-dodecane can be observed as the methanol ambient concentration increases, which would be accompanied by a higher spatial gradient of the vaporous n-dodecane outside the droplet, enhancing the mass transport away from the droplet. Besides, the increase of the ambient mixture thermal conductivity (Fig. 4.11a) as the methanol ambient concentration increases, would contribute to the increase of the evaporation rate (Fig. 4.9a).

Regarding the initial heat-up time depicted in Fig. 4.9b, it shows an initial decrease with increasing the methanol ambient concentration, then it tends to be less sensitive to the variation of the methanol ambient concentration and eventually tends to slightly increase at ($Y_{CH_3OH} = 0.6$). The increase of the ambient mixture thermal conductivity with the methanol ambient concentration would contribute to the reduction of the heat-up time. Meanwhile, Figs. (4.5b, 4.7b) shows that, as the methanol ambient concentration increases, the droplet will be heated to a higher temperature before entering the two-phase region, which would contribute to a longer heat-up time. Accordingly, the above competing mechanisms would determine the heat-up time. Thus, for the considered transcritical conditions, the contribution of the evaporation rate and the heat-up time leads to a monotonic reduction of the droplet lifetime with increasing the methanol ambient concentration.

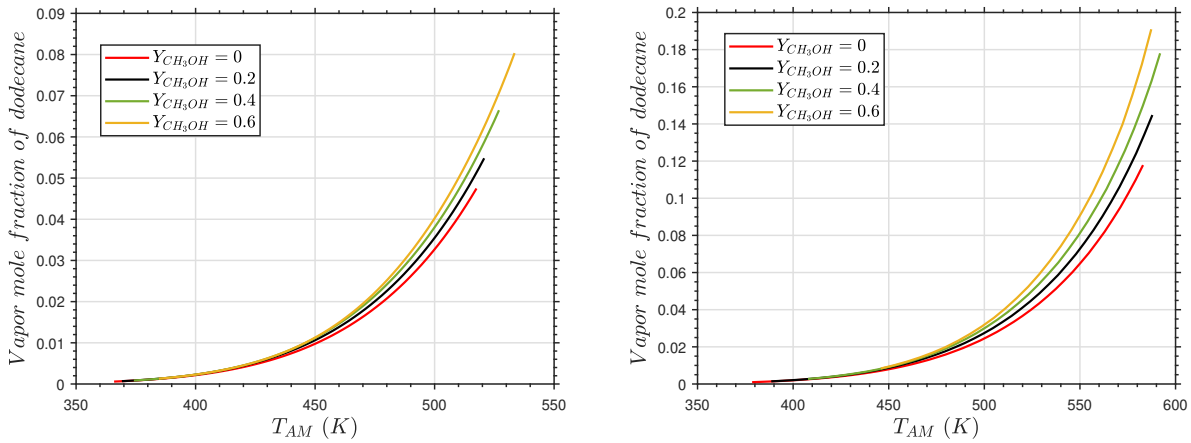

Figure 4.10: Variation of the equilibrium mole fraction of vaporous n-dodecane in the two-phase region along the adiabatic mixing temperature lines for the various methanol ambient concentrations (Y_{CH_3OH}) at (a) ($P_{amb} = 62\,\text{bar}$, $T_{amb} = 700\,\text{K}$), (b) ($P_{amb} = 106\,\text{bar}$, $T_{amb} = 1200\,\text{K}$).

For a given methanol ambient concentration, the droplet lifetime decreases, with increasing the (P_{amb}, T_{amb}) as shown in Fig. 4.9c. This reduction in the droplet lifetime is consistent with the increase in the evaporation rate (Fig. 4.9a) and the reduction of the heat-up time (Fig. 4.9b) as the ambient pressure and temperature increase compared to the reference case condition ($P_{amb} = 62\,\text{bar}$, $T_{amb} = 700\,\text{K}$).

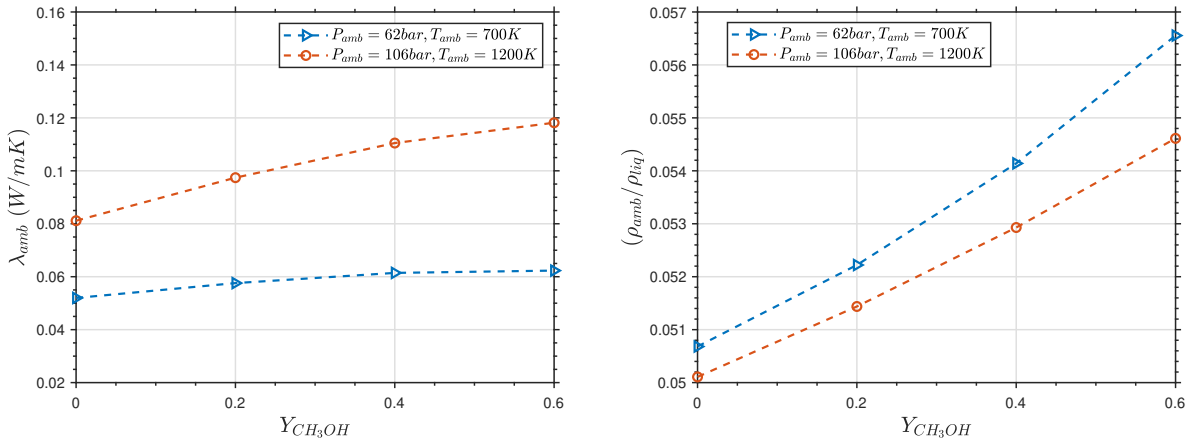

(a) (b)

Figure 4.11: Variation of (a) the ambient mixture thermal conductivity (λ_{amb}) and (b) the ambient gas to liquid phase density ratio (ρ_{amb}/ρ_{liq}) as a function of the methanol ambient concentration (Y_{CH_3OH}) at the ambient temperatures (T_{amb}) and pressures (P_{amb}) considered and the initial droplet temperature (363 K).

It is worth mentioning that the increase of the methanol ambient concentration is accompanied by a relative increase in the gas-phase density for a given ambient temperature and pressure. Thus, the gas to liquid phase density ratio tends to slightly increase as the methanol ambient concentration increases, as shown in Fig. 4.11b. The densities of the gas and liquid phases are computed for a given ambient pressure and initial temperature of the ambient gas and liquid droplet, respectively. This relative increase of the gas to liquid phase density ratio implies that the widely used gas-phase quasi-steady assumption in classical droplet evaporation models could be revised in such transcritical conditions as the density ratio increases towards unity [116].

In addition, the thermodynamic analysis has shown that droplet exhibits two-phase states during its lifetime (see Figs. (4.5b, 4.7b)), and the evaporation does not take place entirely in a supercritical regime, although the considered ambient temperatures and pressures are higher than the critical point of pure n-dodecane ($T_c = 658.1$ K, $P_c = 18.2$ bar). This behavior is due to the multi-component mixture critical point variation compared to that of the pure component. For instance, Yi et al. [256] have demonstrated that the transition from subcritical evaporation to diffusive mixing regime, is based on the mixture critical point for multi-species problem, not the pure-fuel critical point. It also implies that considering the vapor-liquid equilibrium theory is essential for the correctness of the modeling as subcritical and supercritical states may exist simultaneously in different regions of the simulated configuration, based on the local temperature, pressure, and species composition [112, 253, 149].

4.4 Conclusions

In this chapter, the proposed model in the current work is applied to investigate ternary mixtures relevant to the dual-fuel internal combustion engine configuration. The main goal is to investigate the evaporation characteristics of a single n-dodecane droplet in a bi-component ambient (methanol + nitrogen) through highly resolved simulations considering the real-fluid thermodynamics. The RFM model closed by a tabulated CPA EoS has been employed to investigate the effect of the methanol ambient concentration on the droplet evaporation under various ambient conditions.

The main conclusions obtained in this study include:

- A qualitative comparison of the numerical results with the experiments [53] has shown that the RFM model can capture well the evolution of the n-dodecane droplet evaporation throughout its lifetime under the considered transcritical conditions.

- For the considered ambient temperatures and pressures, the n-dodecane droplet lifetime decreases monotonically with increasing the methanol ambient concentration. However, such decrease in the droplet lifetime is relatively low with methanol ambient mass fraction less than 0.2. The thermodynamic analysis shows that the droplet follows a different thermodynamic path based on the methanol ambient concentration. The different mechanisms contributing to the droplet lifetime behavior have been thoroughly discussed.

- A higher droplet size increase at the initial stage of the evaporation process has been found with increasing the methanol concentration for a given ambient temperature and pressure, which can be attributed to a relatively higher solubility of methanol in the liquid phase compared to that of nitrogen.

- Increasing the ambient temperature and pressure is accompanied by a more significant reduction of the two-phase region along the adiabatic mixing temperature lines and an increase of the dissolved ambient gases.

- The methanol and nitrogen exhibit different behavior in terms of solubility in the liquid phase, which demonstrates that these two compounds should not be lumped in a single surrogate.

- The droplet exhibited two-phase states during its lifetime even if the considered ambient temperatures and pressures are higher than the n-dodecane critical point, which implies that considering the vapor-liquid equilibrium theory is indeed required for the correct modeling of such transcritical conditions.

- The RFM model closed by a tabulated EoS shows great potential for the computation of two-phase binary and ternary mixtures problems, avoiding the direct evaluation of costly phase equilibrium solver during the simulation run-time [254, 253].

Chapter 5

Fuel injection and atomization modeling

Contents

This chapter is dedicated to the second objective of the current work, which is related to high-pressure fuel injection and atomization modeling. To this goal, a real-fluid atomization model is proposed, in which the RFM model is coupled with a subgrid-scale (SGS) model using a surface density approach to deal with the atomization phenomenon under sub/transcritical operating conditions. More specific, the RFM model is complemented with a surface density equation for fuel atomization modeling within the LES framework. The Engine Combustion Network (ECN) Spray A injector non-evaporating and nominal evaporating conditions are used as a reference for the proposed model validation. In addition, a parametric variation of the ECN Spray A is carried out for further assessment and validation of the proposed model under various operating conditions. Finally, this chapter closes with an investigation of the ECN Spray A evaporating baseline condition in a dual-fuel configuration.

5.1 Introduction

Fuel injection is an essential step toward the combustion process in internal combustion engines. Indeed, the preparation of the fuel-ambient gases mixture significantly affects the combustion efficiency and emissions formation. Computational fluid dynamics (CFD) models capable of simulating fuel injection under various operating conditions are thus essential for the design and optimization of fuel injection equipment (FIE). However, modeling of fuel injection and combustion remains a challenge due to the variety of length and time scales and the involved physical processes during the injection process [215, 15, 64, 135, 182]. The physical processes include in-nozzle cavitation, liquid atomization, phase-change, mixing, and chemical reactions. The complexity is further increased owing to the interaction with turbulence.

Besides, the injected liquid jet undergoes a continuous change of state from classical two-phase atomization, droplet formation, and evaporation to a dense-fluid mixing phenomenon depending on the ambient pressure and temperature and the physical properties of the injected fuel. Indeed, experimental observations [146] of n-dodecane sprays after the end of injection have shown a dense-fluid mixing with vanishing surface tension as the ambient temperature and pressure exceed a certain limit. Besides, Crua et al. [53] observed that fuel droplets undergo a gradual transition from subcritical evaporation to dense-fluid mixing at pressures and temperatures higher than the pure fuel critical point, where the transition time depends on the pressure and temperature of the surrounding gas as well as the fuel properties. Accordingly, a CFD model capable of modeling the fuel injection under subcritical, transcritical, and supercritical regimes, allowing an automatic transition between the different regimes, remains a challenge addressed by the proposed model in the current work.

Several spray modeling approaches can be found in the literature, with varying complexity of describing the involved physical processes. The widely used spray model for engineering calculations is based on the Discrete Droplet Model (DDM) approach [71], where the liquid phase is described by Lagrangian parcels (i.e. a group of droplets with identical properties, such as diameter and velocity), whereas the gas-phase is modeled in an Eulerian framework. Several researchers (see [192, 96, 249, 144, 119], to cite a few) have adopted the DDM approach for spray simulations. These simulations have shown the effectiveness of the EL framework to describe the spray dynamics under turbulent conditions. However, as reported in [250, 27, 98], this approach also presents various shortcomings, especially to model the dense near-nozzle region, where parcels/blobs are injected to represent the intact liquid core. In addition, this modeling approach requires various calibration coefficients of sub-models, which are not universal. Recent developments [166, 167] have been also carried out in the literature for using the DDM approach within the dense regimes.

However, Eulerian modeling of fuel injection and atomization, where both the liquid and gas phases are treated in an Eulerian framework is more suited to model the dense near-nozzle region. For instance, Interface Capturing Methods (ICM) such as the Volume of Fluid (VOF) [108] and Level-Set (LS) [227] methods have been applied to simulate the fuel injection and atomization [151, 216, 106]. However, due to the high computational cost of these methods, their application to industrial cases is still limited. Accordingly, another alternative is the Eulerian Diffuse Interface Model (DIM), where the unresolved interface features are modeled using a surface density approach instead of being tracked.

Several atomization models have been proposed within the Eulerian framework based on the surface density approach as initially introduced by (Vallet and Borghi [238], Vallet et al. [239]) in the so-called $(\Sigma - Y)$ model. This model has two main transport equations: the liquid mass fraction (Y) transport equation to track the liquid-phase dispersion and the interfacial surface area density (Σ) transport equation to model the unresolved liquid-gas interface, where the surface area density provides a general description of the atomized liquid structures such as droplets or ligaments. The liquid mass fraction and surface density can be used to estimate an equivalent Sauter Mean Diameter (SMD) defined as, $(SMD = 6\alpha_l/\Sigma)$, where $(\alpha_l = \rho Y/\rho_l)$ is the liquid volume fraction.

The known spray SMD may then be used to initiate a Lagrangian description of the spray when it becomes sufficiently diluted, as proposed in the Eulerian-Lagrangian Spray Atomization (ELSA) model [34, 139]. The Lagrangian description of the spray is indeed more appropriate for modeling the diluted spray region, allowing to track individual droplet's velocity, size, and temperature, in contrast to the Eulerian approach, which assumes a single temperature and velocity for both the droplets and the gas phase, and can't consider spray polydispersity, making it unsuitable to model such dispersed spray region. Similar to the ELSA approach, Devassy et al. [65] proposed an Eulerian-Eulerian atomization model using two surface density transport equations to separately model the liquid core atomization and droplet's secondary breakup. A Probability Density Function (PDF) based formulation of the $\Sigma - Y$ or ELSA model has also been proposed in [233, 12, 160], where a joint PDF of liquid volume fraction and surface density is used to consider the subgrid fluctuations of these two scalars.

In addition, Chesnel et al. [46] formulated the $\Sigma - Y$ model within LES framework, where the surface density equation has been postulated to describe the subgrid spray characteristics. An atomization model which couples the ICM-DNS (resolved interface) and the ELSA (unresolved interface) approaches has been proposed by Anez et al. [15]. In this model, switching between the ICM and the ELSA approaches is implemented based on interface resolution criteria to determine whether or not the interface is well captured. Nykteri et al. [164] proposed a compressible Σ-Y two-fluid model which also combined a dynamic switching between the sharp and the diffuse interface approaches. The dynamic switching is carried out with an advanced flow topology detection algorithm. More recently, Pandal et al. [169] proposed a new formulation of the $\Sigma - Y$ model that accounts for liquid diffusion due to drift-flux velocities and allows coupling between liquid dispersion and spray atomization, as (Σ) actively affects the transport of the liquid mass fraction.

The potential of the $\Sigma - Y$ model to capture the fuel dispersion and atomization under diesel-like operating conditions, namely the ECN Spray A non-evaporating condition [5], has been shown in recent studies within the RANS [63, 168] and LES [64, 15] frameworks. Besides, the LES-based formulations of the $\Sigma - Y$ model have demonstrated superior performance to their RANS counterpart in capturing the fuel dispersion in the near-nozzle field [64, 15].

However, such above models (see [15] for instance) commonly assume constant fluid properties or rely on simple equations of state to model the liquid and gas phases. Besides, the phase change is usually neglected or considered using simple evaporation models that don't incorporate the essential real-fluid effects relevant to high temperature and pressure injection. Under these conditions, the fuel properties show significant deviation from the ideal-gas behavior, where a real-fluid EoS is needed to capture the non-linear behavior of the fluid properties, especially under transcritical conditions [114, 113]. Lacaze et al.

[137] also demonstrated the importance of real-gas effects in the simulation of the ECN Spray A evaporating condition [9] (high temperature and pressure condition) using the Peng-Robinson (PR) EoS.

Accordingly, in the current chapter, the real fluid model (RFM) is adopted as a fully compressible two-phase flow framework, which is supplemented with a surface density transport equation formulated within the LES framework to model the fuel jet atomization. The proposed model is first assessed using the non-evaporating and nominal (evaporating) baseline conditions of the ECN Spray A injector [9]. Under the non-evaporating condition, the ECN experimental database includes near-nozzle fuel dispersion and interfacial surface area measurements by means of X-ray radiography [129] and ultra small-angle X-ray scattering (USAXS) technique [127], respectively. Besides, the SMD experimental data [127] are also used for model validation. Then, under the nominal evaporating Spray A condition, model validation is carried out against experimental measurements of liquid and vapor penetrations [22] and fuel mixture fraction distribution [178]. In addition, a parametric variation of the ECN Spray A is carried out for further assessment and validation of the proposed model under various operating condition, where the model results are validated against spray liquid penetration measurements obtained by diffused back illumination (DBI) technique [145]. Finally, this chapter closes with an investigation of the evaporation and mixing of the ECN Spray A baseline condition in a dual-fuel configuration.

5.2 Interfacial surface area density modeling

The liquid jet atomization is modeled by introducing a transport equation for the evolution of the interfacial surface area density (Σ), which is defined as the liquid-gas interfacial area per unit volume, as initially proposed by Vallet and Borghi [238]. The surface area density allows for a more general description of the atomized liquid structures that can have more complex shapes compared to spherical droplets.

Following a phenomenological approach [239, 140, 46], the surface density equation can be written as:

$$\frac{\partial \Sigma}{\partial t} + \frac{\partial \tilde{u}_i \Sigma}{\partial x_i} = \frac{\partial}{\partial x_j}\left(D_\Sigma \frac{\partial \Sigma}{\partial x_j}\right) + S_\Sigma \tag{5.1}$$

where (D_Σ) is the diffusion coefficient computed as ($D_\Sigma = \mu_{sgs}/\rho Sc_t$). The first term on the RHS of Eq. (5.1) represents the turbulent flux of the surface density, modeled here using a gradient law closure [140, 239]. It is should be noted that such gradient closure is mainly valid in case of negligible slip velocity between the liquid and gas phases [14]. Otherwise, this approach should be improved as reported in [14, 30, 169].

The second term on the RHS of Eq. (5.1) is a source term to model the physical phenomena that contributes to the production or the destruction of the surface density and can be generally decomposed as [46]:

$$S_\Sigma = S_{\Sigma_{mix}} + S_{\Sigma_{int}} + S_{\Sigma_{vap}} \tag{5.2}$$

where ($S_{\Sigma_{mix}}$) represents the production of surface density due to liquid/gas mixing, ($S_{\Sigma_{int}}$) represents the surface production/destruction, due to turbulent flow stretching, mean shear, and collision and coalescence effects, and ($S_{\Sigma_{vap}}$) represents the vaporization effects on the surface density. The term ($S_{\Sigma_{mix}}$) ensures the presence of an interface due to

the coexistence of liquid and gas phases. To model this term, Vallet et al. [239] proposed a formulation based on the inverse of the size of the control volume near the injector tip assuming a flat interface at the boundary. Lebas et al. [140] assumed that the first liquid structure characteristic scales are related to the turbulent integral scale. In both cases, it is an initialization term to produce a minimum surface density after injection and should not have a strong impact on the whole simulation.

In the current work, the proposal by Chesnel et al. [46] within the LES framework has been adopted, where the total interfacial surface area is decomposed as:

$$\Sigma = \Sigma_{min} + \Sigma^{'} \tag{5.3}$$

where the (Σ_{min}) represents the minimum surface density that can be found for a given value of the resolved liquid volume fraction, whereas $(\Sigma^{'})$ stands for the subgrid level surface density.

The (Σ_{min}) is computed using the relation proposed in [46] based on DNS studies as:

$$\Sigma_{min} = \frac{2.4}{\Delta_{LES}}\sqrt{\bar{\alpha}_l(1-\bar{\alpha}_l)} \tag{5.4}$$

where (Δ_{LES}) is the filter length scale, which is estimated from the cell volume (V_c) as $(\Delta_{LES} = V_c^{-1/3})$ and $(\bar{\alpha}_l)$ is the resolved liquid volume fraction.

To close Eq. (5.3), the subgrid surface density $(\Sigma^{'})$ is thus transported as follows:

$$\frac{\partial \Sigma^{'}}{\partial t} + \frac{\partial \tilde{u}_i \Sigma^{'}}{\partial x_i} = \frac{\partial}{\partial x_j}\left(D_\Sigma \frac{\partial \Sigma^{'}}{\partial x_j}\right) + S_{\Sigma_{int}} \tag{5.5}$$

The source term $(S_{\Sigma_{int}})$ is modeled in a restoration to equilibrium form [239, 140], where (Σ_{eq}) is an equilibrium surface area density that should be reached within a characteristic time scale (τ_Σ) as:

$$S_{\Sigma_{int}} = \frac{\Sigma}{\tau_\Sigma}\left(1 - \frac{\Sigma}{\Sigma_{eq}}\right) \tag{5.6}$$

The subgrid surface density $(\Sigma^{'})$ equation thus reads:

$$\frac{\partial \Sigma^{'}}{\partial t} + \frac{\partial \tilde{u}_i \Sigma^{'}}{\partial x_i} = \frac{\partial}{\partial x_j}\left(D_\Sigma \frac{\partial \Sigma^{'}}{\partial x_j}\right) + \frac{\Sigma}{\tau_\Sigma}\left(1 - \frac{\Sigma}{\Sigma_{eq}}\right) \tag{5.7}$$

The time scale (τ_Σ) is related to the turbulent time scale (τ_t) by the coefficient (C_Σ) as:

$$\frac{1}{\tau_\Sigma} = \frac{C_\Sigma}{\tau_t} \tag{5.8}$$

The (Σ_{eq}) is again evaluated as $(\Sigma_{eq} = \Sigma_{min} + \Sigma^{'}_{eq})$, where $(\Sigma^{'}_{eq})$ is computed as function of a critical Weber number (We_c) [72] as:

$$\Sigma^{'}_{eq} = 4\frac{0.5(\rho_l + \rho_g)\bar{\alpha}_l(1-\bar{\alpha}_l)k_{sgs}}{\sigma We_c} \tag{5.9}$$

where (k_{sgs}) is the subgrid scale turbulent kinetic energy, (σ) is the surface tension coefficient computed by the Macleod-Sugden correlation [183], and (ρ_l, ρ_g) are the densities of the liquid and gas phases, respectively. In the validation section below, the two model constants (C_Σ, We_c) are set by comparison with the USAXS experimental measurements of the projected interfacial surface area.

It should be noted that within the LES formulation described above, the initialization source term ($S_{\Sigma_{mix}}$) is not required due to the presence of (Σ_{min}). Besides, the evaporation source term ($S_{\Sigma_{vap}}$) is not explicitly included in Eq. (5.7). However, the evaporation effects is implicitly considered through the terms (Σ_{min}) and (Σ_{eq}), which are dependent on (α_l) and the other the properties ($\rho_l, \rho_g, \sigma, ..., etc$) that vary locally as function of (T, P, Y_k).

Finally, a length scale (l_{32}) can then be defined for the liquid structures from (Σ) and (α_l) following [15] as:

$$l_{32} = \frac{6\alpha_l(1-\alpha_l)}{\Sigma} \tag{5.10}$$

This length scale definition considers on the one hand, the case of monodispersed spray of spherical droplets ($SMD = 6\alpha_l/\Sigma$) and on the other hand, the case tending to a bubbly flow ($SMD = 6(1-\alpha_l)/\Sigma$).

Another essential point regarding the function of the surface density (Σ) in the current model is that (Σ) here is a passive scalar, which is mainly used to compute the droplet's SMD distributions during the simulation. Thus, the surface density (Σ) is not fed back into Eqs. (2.12-2.15), as the liquid dispersion is assumed to be mainly governed by turbulent diffusion of the injected fuel (i.e., the n-dodecane species) through Eq. (2.15) and independent of the atomization dynamics under the considered diesel-relevant conditions (high ambient density and injection pressure). However, the accuracy of such passive (Σ) formulation is diminished under conditions of lower ambient density and injection pressure, where the slip velocity between the droplets and the gas phase becomes more significant [82, 169]. An enhanced formulation has been recently proposed by Pandal et al. [169] to overcome this limitation. The proposed model considered the diffusion due to the slip velocity between phases, allowing coupling between liquid dispersion and spray atomization, as (Σ) actively affects the transport of the liquid fraction. The enhanced model showed improved predictions under conditions of low ambient density and injection pressure. However, the improvements were less significant under high ambient density and injection pressure conditions.

Novelty of the real-fluid atomization model

The proposed RFM model coupled with the surface density equation differs from previous ($\Sigma - Y$) or ELSA models in several key points that can be summarized as follows:

- In the current model, the overall liquid volume/mass fraction is not directly transported as in previous ($\Sigma - Y$) or ELSA models, but the liquid volume fraction (α_l) is one of the VLE calculation results and obtained from the stored thermodynamic table as a function of (T, P, Y_k).

- The phase change effect on the surface density is implicitly considered through the terms (Σ_{min}) and (Σ_{eq}), which are dependent on (α_l). Besides, the variation of the properties ($\rho_l, \rho_g, \sigma, ..., etc$) involved in the ($\Sigma$) equation depends on the local conditions of (T, P, Y_k) as provided by the thermodynamic table.

Model assumptions

The assumptions of the proposed model within the context of high-pressure fuel injection and atomization simulation can be summarized in the following points:

- The fuel injection operates at high Reynolds and Weber numbers.

- The two phases are in mechanical and thermal equilibrium.
- The fluid within a computational cell is in local thermodynamic equilibrium.

The first assumption allows to assume that large scale flow features such as mass transport are separated from the atomization process occurring at smaller scales. Accordingly, Eqs. (2.1-2.4) describe the large-scale motion of the flow and the atomization occurring at smaller scales is modeled by the surface density equation. In addition, the high Weber number implies that surface tension has negligible effect on large scales, however its effect on the atomization is considered through the surface density equation.

The second assumption implies that the two-phases are assumed to have a single velocity, pressure and temperature. Thus, the slip velocity between the two-phases is assumed to be not significant. Such assumption loses its validity under lower injection pressure and ambient gas to liquid density ratio, where the slip velocity becomes more significant [82]. This limitation could be overcome by adding a transition to the Lagrangian approach once the spray is diluted [34, 139] or accounting for the liquid diffusion due to the slip velocity [169].

The third assumption implies that the characteristic time to reach local thermodynamic equilibrium is much smaller than the other flow time scales. Accordingly, thermodynamic non-equilibrium effects are not considered. However, the validity of the thermodynamic equilibrium assumption for high injection pressure diesel sprays has been demonstrated in previous studies [257, 149, 253] and will be further verified in the current study.

5.3 Application to diesel-like injection

5.3.1 Description of the simulated test cases

The current study is based on the ECN Spray A configuration [9], where a single-hole diesel injector is operated with pure n-dodecane ($C_{12}H_{26}$) injected into gaseous nitrogen (N_2) at the conditions listed in Table 5.1, including non-evaporating and evaporating conditions. The test case setup is described in the next section, followed by the comparison of the RFM-LES results against the ECN experimental data. The ECN experimental database of the non-evaporating condition will be used to validate the model results for the near-nozzle field, while the evaporating conditions experimental data will be used to validate the far-field spray.

Fuel	n-dodecane
Injection pressure (MPa)	150
Injection temperature (K)	$343^a/363^b$
Ambient temperature (K)	$303^a/900^b$
Ambient pressure (MPa)	$2^a/6^b$
Ambient density (kg/m^3)	22.8
Ambient composition	Pure N_2

Table 5.1: Injection and ambient conditions of ECN Spray A experiments under ^{a} Non-evaporating and ^{b} evaporating conditions.

5.3.2 Computational set-up and numerical methods

Computational set-up

A three dimensional (3D) rectangular computational domain is used in the current study, which is 20 mm in the stream-wise direction and 10 mm in the lateral directions. The nozzle outlet diameter is 0.0894 mm corresponding to Spray A injector serial #210675 [8]. The grid structure at the domain center-plan is depicted in Fig. 5.1, where the base grid size is 400 μm located at the outer edge of the domain, while various mesh refinement levels have been employed to achieve a minimum cell size of 6.25 μm. Thus, the nozzle outlet diameter is discretized with about 15 cells.

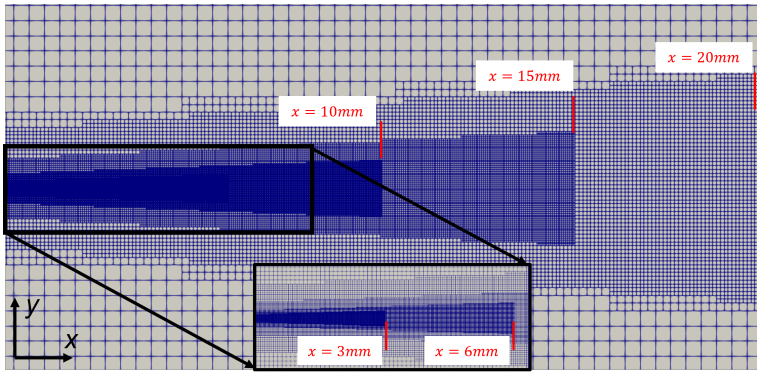

Figure 5.1: Computational domain with the grid structure at the domain central cut section, along with the length of the various embedding zones. The insert shows a zoom of the refined mesh in the near-nozzle exit region.

Grid convergence study has been performed, where three different grids have been tested. The minimum grid size for the three tested grids is fixed to 6.25 μm, located in the near nozzle region ($x < 3\,mm$). Then, the other embedding zones (see Fig. 5.1) are further refined from the coarsest grid to the most refined one, resulting in three grids with a total mesh count of 3 M (grid 1), 16 M (grid 2), and 21 M (grid 3) cells, respectively.

The injection conditions are applied at the domain inlet (the nozzle orifice exit) by an inlet boundary condition (BC). Thus, the injector in-nozzle flow is not simulated. The inlet BC is prescribed as a top-hat (TH) profile of axial velocity calculated from the time-dependent mass flow rate profile obtained from CMT virtual injection rate generator [1], which allows to partially reproduce the in-nozzle flow and the needle motion effects [62].

Under both evaporating and non-evaporating conditions, simulations are first carried out without imposing any synthetic turbulence fluctuations at the domain inlet. However, under the non-evaporating condition, the obtained initial results have shown an overestimation of the jet penetration and less fuel dispersion compared to the experimental data. Thus, a synthetic turbulence generator has been used to superimpose turbulent fluctuations over the inflow velocity profile following the method of [56]. A turbulent intensity of 3% has been employed following the recent work of [64] and the minimum length-scale of the imposed fluctuations was taken as twice the minimum cell size.

Under the evaporating condition, preliminary simulation results have shown that the injected liquid jet penetration and dispersion behaves correctly without adding such synthetic turbulent fluctuations. Fairly accurate predictions of the evaporating Spray A without imposing any artificial turbulence at the inflow patch have also been shown in [149]. It seems that the interaction between the counter flows of gas entrainment and

evaporation at the interface will trigger the jet instability, as suggested in [254]. Accordingly, future work should include the in-nozzle flow in the spray simulation to avoid such uncertainties on the inflow boundary conditions. A no-slip boundary condition is applied at the wall around the nozzle outlet (on left side of the chamber). All the rest of the domain boundaries are outlets with a pressure boundary condition equal to the ambient pressure.

Numerical methods

LES simulations are carried out using CONVERGE V3.0.15 employing the PISO algorithm (see Sec. 2.1.5.1). The LES Sigma model [161] is used for the turbulence modeling. The spatial discretization is second-order accurate using a central difference scheme. The time integration is achieved by a second-order Crank-Nicolson scheme for the momentum equation and a first-order implicit Euler scheme for the rest of the equations. The time step is around 2-3 ns and adjusted automatically based on a maximum Courant-Friedrichs-Lewy (CFL) number of 0.5. As an example of the computational cost of the performed LES simulations, it required about 9 days to simulate 1 ms under the evaporating condition with grid 2 (16 M cells), using 1024 cores of AMD EPYC Milan 7763 processors running at 2.45 GHz (Topaze CCRT supercomputer).

It is also worth noting that the computational cost of the same simulation is reduced to 7.5 days using CONVERGE V3.1.6 with the updated real-fluid PISO algorithm (see Sec. 2.1.5.1). Further details on the results obtained from the two versions and the computational cost can be found in Appendix A.

The RFM model thermodynamic closure for the (n-dodecane/nitrogen) binary mixture is based on the VTPR-EoS with a uniform thermodynamic table resolution in $(T, P, Y_{C_{12}H_{26}})$ axes of $(501 \times 61 \times 101)$ points covering ranges of (300-1300 K, 1-121 bar, 0-1). The employed thermodynamic table resolution is based on previous studies [114, 80, 113], and will be shown to provide sufficiently accurate results in the following sections.

5.3.3 Non-evaporating ECN Spray A

5.3.3.1 Spray dispersion

The RFM model predictions of the spray dispersion is validated using the ECN experimental data [5], which include the projected mass density (PMD) [129], transverse integrated mass (TIM) [128], and liquid volume fraction (α_l) [179]. The LES results are time-averaged between 0.4 and 1 ms after the start of injection (during the quasi-steady period) to be compared with the experiments. A first validation is performed using the PMD, which represents a path length-integrated measure of the fuel density along the X-ray beam path through the spray depth as shown in Fig. 5.2 and defined by Eq. (5.11).

$$PMD(x, r) = \int \rho_l(x, r, z) dz \tag{5.11}$$

Line of sight integration of the simulation results of the fuel density is carried out and compared with the experimental data as shown in Fig. 5.3. The comparison shows that the simulation capture well the fuel distribution in the near-nozzle region (first 6 mm), where a qualitatively good agreement is achieved between the computed and measured PMD.

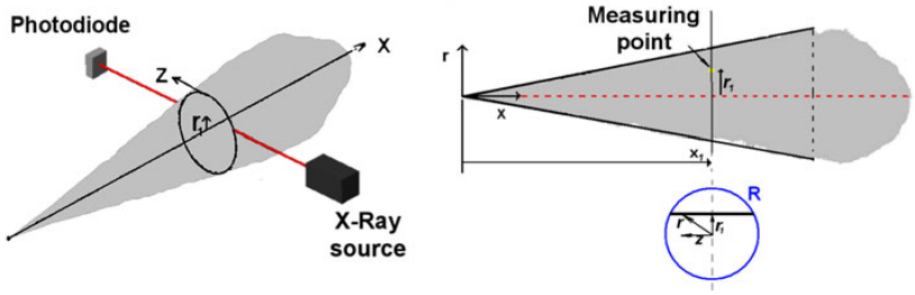

Figure 5.2: Schematic of the X-ray measurement technique and illustration of the integration for calculating the projected mass density (PMD). Image taken from [61].

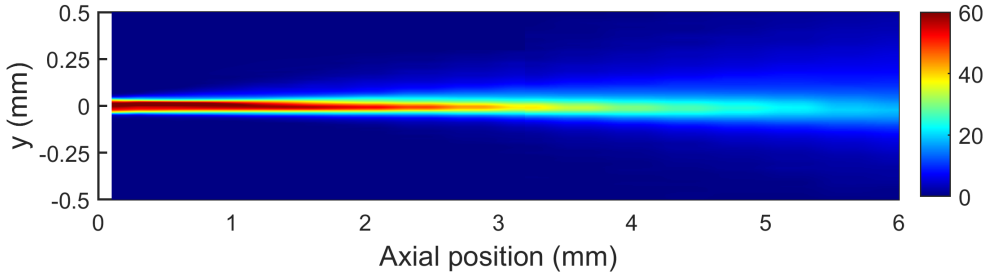

(a) ECN X-ray

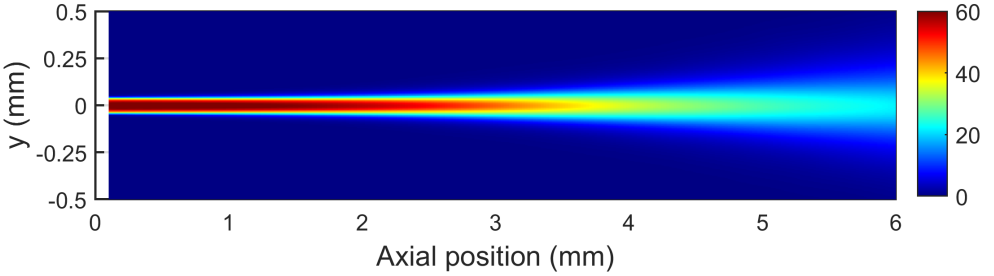

(b) LES-Grid 2

Figure 5.3: Non-evaporating Spray A condition: experimental (top) and numerical (bottom) projected mass density (µg/mm^2) distributions.

In addition, for more quantitative validation, the projected mass density radial profiles are compared at three different axial positions ($x = 0.1, 2, 6$ mm) from the nozzle outlet as depicted in Fig. 5.4. Overall, the model results are in good agreement with the experimental data in terms of the spray centerline peak-value and radial dispersion, especially when the grid 2 and 3 are employed.

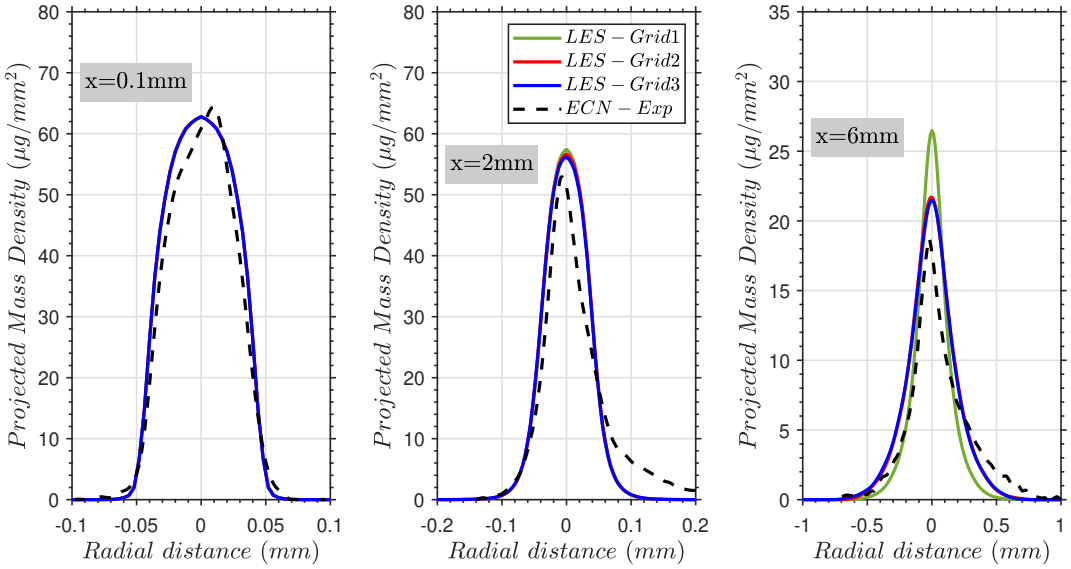

Figure 5.4: Non-evaporating Spray A condition: Numerical and experimental projected mass density (PMD) radial profiles at axial distances of 0.1 mm, 2 mm, 6 mm from the nozzle exit. The grid convergence study is also demonstrated.

Indeed, it can be seen the grid impact on the obtained results, especially at ($x = 6$ mm), where the predicted PMD profile matches better the experimental one as the mesh is further refined (less overestimation of the peak value). Besides, a minimal variation of the obtained results can be observed as the grid is further refined from grid 2 (16 M cells) to grid 3 (21 M cells), showing that grid convergence is fairly achieved. Thus, the intermediate grid resolution (grid 2- 16 M cells) has been used for further calculations, and the associated results are only shown in the following discussion.

In addition to the presented grid convergence study, the quality of the performed LES using (grid 2) is assessed based on the criterion proposed by Pope [184]. This criterion is satisfied when the ratio (M) of the subgrid-scale kinetic energy (k_{sgs}) to the sum of the modeled and resolved turbulent kinetic energy ($k_{sgs} + k_{res}$) is less than 20%, such that ($M = k_{sgs}/(k_{sgs} + k_{res}) < 0.2$). The time averaged ratio (M) at the center-plane of (grid 2) is depicted in Fig. 5.5, showing that ($M < 0.2$) is fairly accomplished within the spray limits (region of interest), identified by a time averaged liquid volume fraction iso-line of 0.15%. The carried out assessment shows that the employed grid resolution is sufficient to provide reliable results within the LES framework.

Another quantity used for validation is the TIM, obtained from the integral of the projected mass density across the radial direction at a particular axial location. Thus, a higher TIM value indicates a greater amount of liquid fuel along the radial direction. A comparison between the numerical and experimental TIM distributions is depicted in Fig. 5.6. The simulation result agrees reasonably with the experimental data in the first 5 mm. Then, the simulation overestimates the TIM as the axial distance increases, indicating that the PMD radial distribution is not accurately predicted at such axial positions (see PMD radial distribution at $x = 6$ mm in Fig. 5.4).

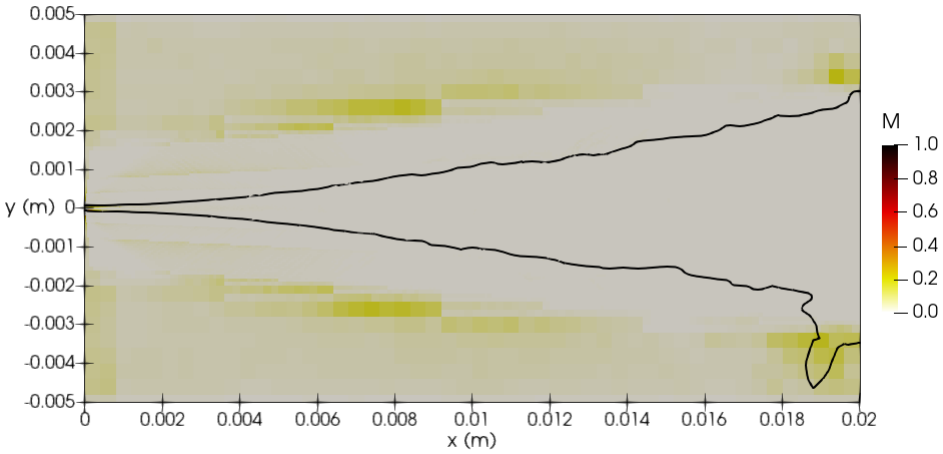

Figure 5.5: Non-evaporating Spray A condition: LES quality analysis based on the Pope criterion [184] : $(M = k_{sgs}/(k_{sgs} + k_{res}) < 0.2)$ for grid 2. The black iso-line of time averaged liquid volume fraction ($\alpha_l = 0.15\%$) shows the spray limits.

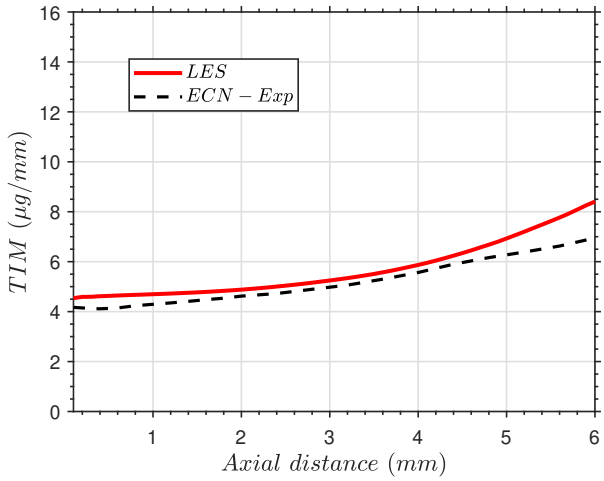

Figure 5.6: Non-evaporating Spray A condition: Numerical and experimental transverse integrated mass (TIM) along the spray axis.

In addition to the PMD and the TIM, the liquid volume fraction (α_l) distribution is also used for validation. The experimental data of liquid volume fraction is obtained by a tomographic reconstruction [179] of the X-ray radiography data. A comparison between the predicted and reconstructed liquid volume fraction distribution along the spray axis is shown in Fig. 5.7. It is worth noting that the experimental profile is only available in the first 12 mm. The comparison shows that the simulation result match with great accuracy the experimental profile, reproducing the intact liquid core ($\alpha_l > 0.9$) and the liquid volume fraction decay along the spray axis. It also shows that the model can capture well the fuel dispersion from the dense near-nozzle region to more diluted zones of the spray.

For a more detailed comparison, the numerical and reconstructed liquid volume fraction radial profiles are compared at three different axial locations similar to the PMD, as depicted in Fig. 5.8. The simulation results are in good agreement with the experimental profiles. The peak value at the spray center line is well captured by the model at

($x = 0.1, 6\,\text{mm}$), while overestimated at ($x = 2\,\text{mm}$), which is consistent with the liquid volume fraction distribution along the spray axis (see Fig. 5.7).

In summary, the performed assessment based on the projected mass density (PMD), transverse integrated mass (TIM), and liquid volume fraction experimental data shows that the RFM model can capture well the fuel dispersion with sufficient accuracy under the considered conditions.

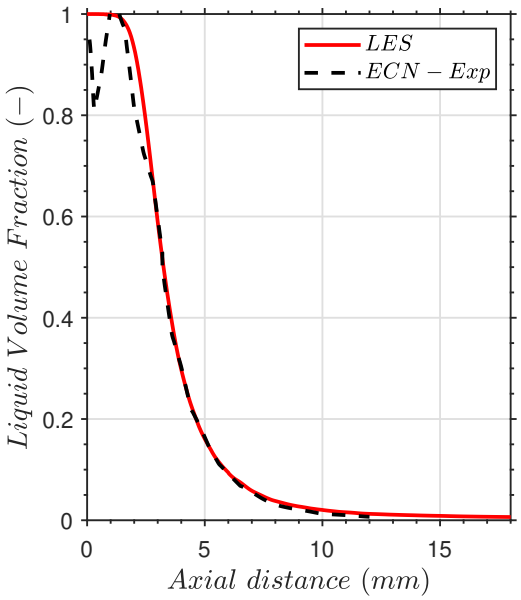

Figure 5.7: Non-evaporating Spray A condition: Numerical and experimental liquid volume fraction along the spray axis.

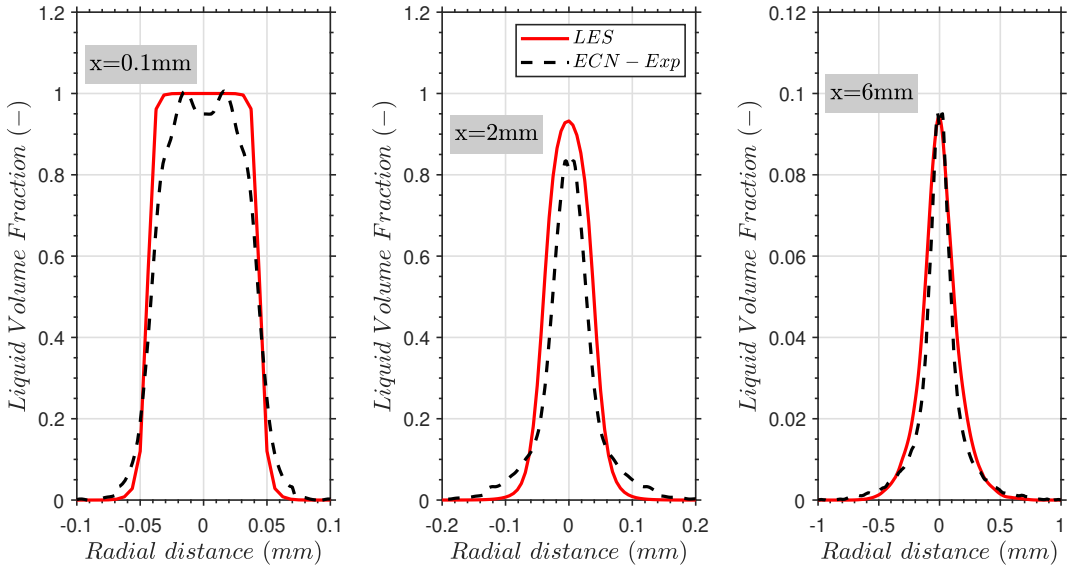

Figure 5.8: Non-evaporating Spray A condition: Numerical and reconstructed liquid volume fraction radial profiles at axial distances of 0.1 mm, 2 mm, 6 mm from the nozzle exit.

5.3.3.2 Spray atomization

The assessment of the proposed atomization model described above is carried out in the current section using the USAXS measurements of the projected interfacial surface area density [127, 168] and SMD experimental data [127]. It is worth recalling the surface density equation includes two modeling constants (C_Σ, We_c) that need to be calibrated against DNS or experimental data. The USAXS experimental data are used in the current work to fix the two model constants. The constant (C_Σ) is set by default to 1, as it has been shown in previous studies [64, 168], that a value in the vicinity of one is sufficient to match the experimental data. Regrading, the critical Weber number (We_c), two values $(1.5, 6)$ were assessed against the USAXS experimental data. The $(We_c = 1.5)$ is the value proposed in [60] based on two-phase DNS studies, while $(We_c = 6)$ is the result of a parametric variation carried out recently in [64]. The projected surface area density provided by the USAXS measurements represents the line-of-sight integrated interfacial area per X-ray beam area along the spray centerline. Thus, the time-averaged numerical surface area density is integrated along the spray depth to be compared with the experiments. The comparison of the numerical and experimental projected surface area density along the spray axis is shown in Fig. 5.9 for the different values of (We_c).

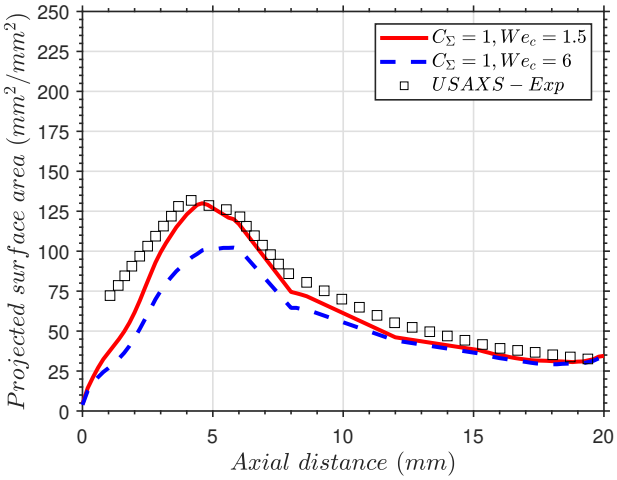

Figure 5.9: Non-evaporating Spray A condition: Numerical and experimental projected surface area along the spray axis.

Overall, the experimental surface area density is well reproduced by the model with $(We_c = 1.5)$, whereas more deviation from the experimental data is found for $(We_c = 6)$. Although some mismatches can still be observed with $(We_c = 1.5)$, the model fairly recovers the experimental projected surface area peak value and decay along the spray centerline. The obtained results also highlight that some parameters tuning is still necessary in the current model for the surface density equation constants (C_Σ, We_c) to well reproduce the experimental surface area density. Thus, the model is still not completely free from parameter tuning, but indeed it is less number of parameters compared to classical Lagrangian spray modeling approaches.

Simulation results with $(C_\Sigma = 1, We_c = 1.5)$ are also compared with available SMD measurements that are obtained by combining the X-ray radiography and the USAXS measurements [127]. A quantitative comparison of the SMD radial profiles between the simulation and the experimental data at different axial positions is depicted in Fig. 5.10.

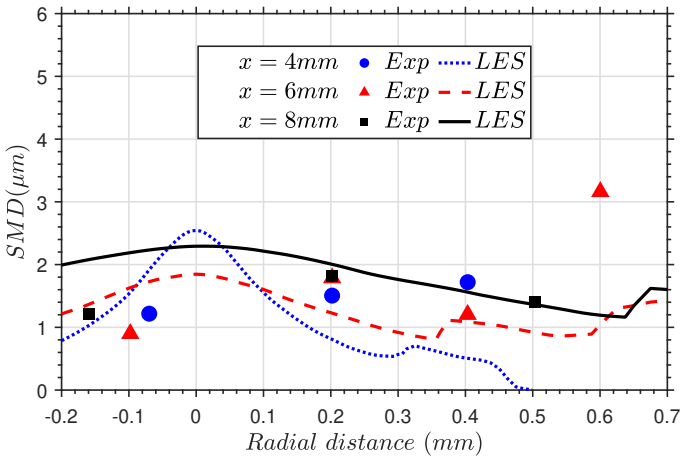

Figure 5.10: Non-evaporating Spray A condition: Numerical and experimental SMD radial profiles at axial distances of 4 mm, 6 mm, and 8 mm from the nozzle exit.

It can be observed that the drop sizes from the simulation fall into the same range as the experimental data. Besides, the simulation results tend to match better the experimental data at longer axial distances from the nozzle exit, where the intact liquid core vanishes and the spray is more diluted, for instance at ($x = 8$ mm).

In Figure 5.11, the time averaged projected surface area radial profiles are shown at axial positions of 2 and 6 mm from the nozzle exit. It can be seen that at ($x = 2$ mm), the projected surface area profile exhibits two peaks at the jet periphery, with a minimum at the spray centerline. This minimum can be attributed to the presence of an intact liquid core at this axial position (see Fig. 5.7). Whereas at further downstream locations ($x = 6$ mm), the double-peak profile disappears, and a transition to a bell-shaped profile with a peak value at the spray centerline takes over, indicating the absence of an intact liquid core. This transition in the projected surface area profiles is similar to that reported by the USAXS experimental measurements for the ECN Spray D [27].

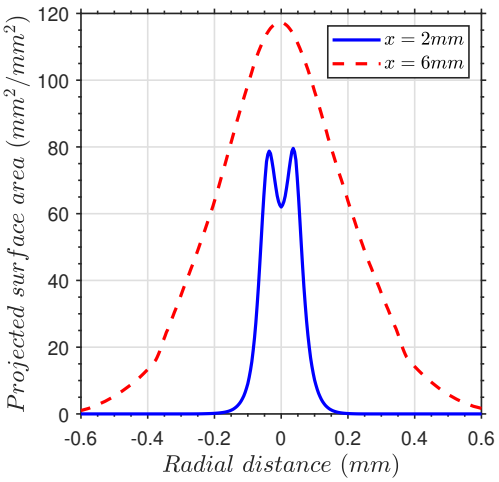

Figure 5.11: Non-evaporating Spray A condition: Numerical projected surface area profiles at axial distances of 2 mm and 6 mm from the nozzle exit.

Finally, the predictive capability of the surface density model using the constants ($C_\Sigma = 1, We_c = 1.5$) is assessed under a different operating condition with a reduced injection pressure ($P_{inj} = 50\,\text{MPa}$) compared to the baseline case ($P_{inj} = 150\,\text{MPa}$). Figure 5.12 shows the comparison of both the numerical and experimental projected surface area density for the two injection pressures. It can be seen that the lower injection pressure ($P_{inj} = 50\,\text{MPa}$) is accompanied by reduced surface area density. Besides, the model can fairly reproduce the experimental profile at ($P_{inj} = 50\,\text{MPa}$) using the same modeling constants, expect for the peak value, which is over-predicted. These results also show that the injection pressure effect on the surface density is fairly well predicted by the model.

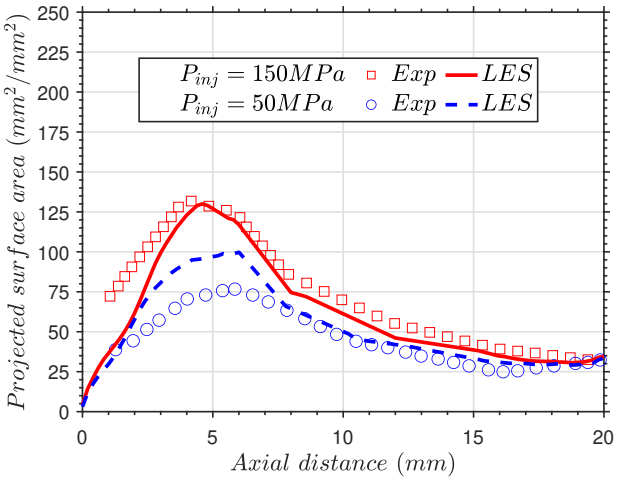

Figure 5.12: Numerical and experimental projected surface area along the spray axis at two different injection pressures (P_{inj}) with the constants ($C_\Sigma = 1, We_c = 1.5$).

5.3.4 Evaporating ECN Spray A

5.3.4.1 Comparison with experimental data

In the current section, the RFM model is further assessed under the nominal evaporating condition of the ECN Spray A (see Table. 5.1). Firstly, the temporal sequence of the n-dodecane injection in terms of mixture fraction at the grid center-plane is qualitatively compared against the experimental images obtained by diffused back illumination (DBI) technique [145, 3], as depicted in Fig. 5.13. The blue isoline superimposed on the n-dodecane mixture fraction field demonstrates the liquid penetration with a liquid volume fraction ($\alpha_l = 0.15\%$).

It can be observed the destabilization of the jet and the development of the instabilities at the shear layer, where liquid structures are detached from the liquid jet and further mix with the ambient gas. Overall, the simulation results show a good agreement with the experimental images with similar penetrations for both liquid and vapor at the various time instants.

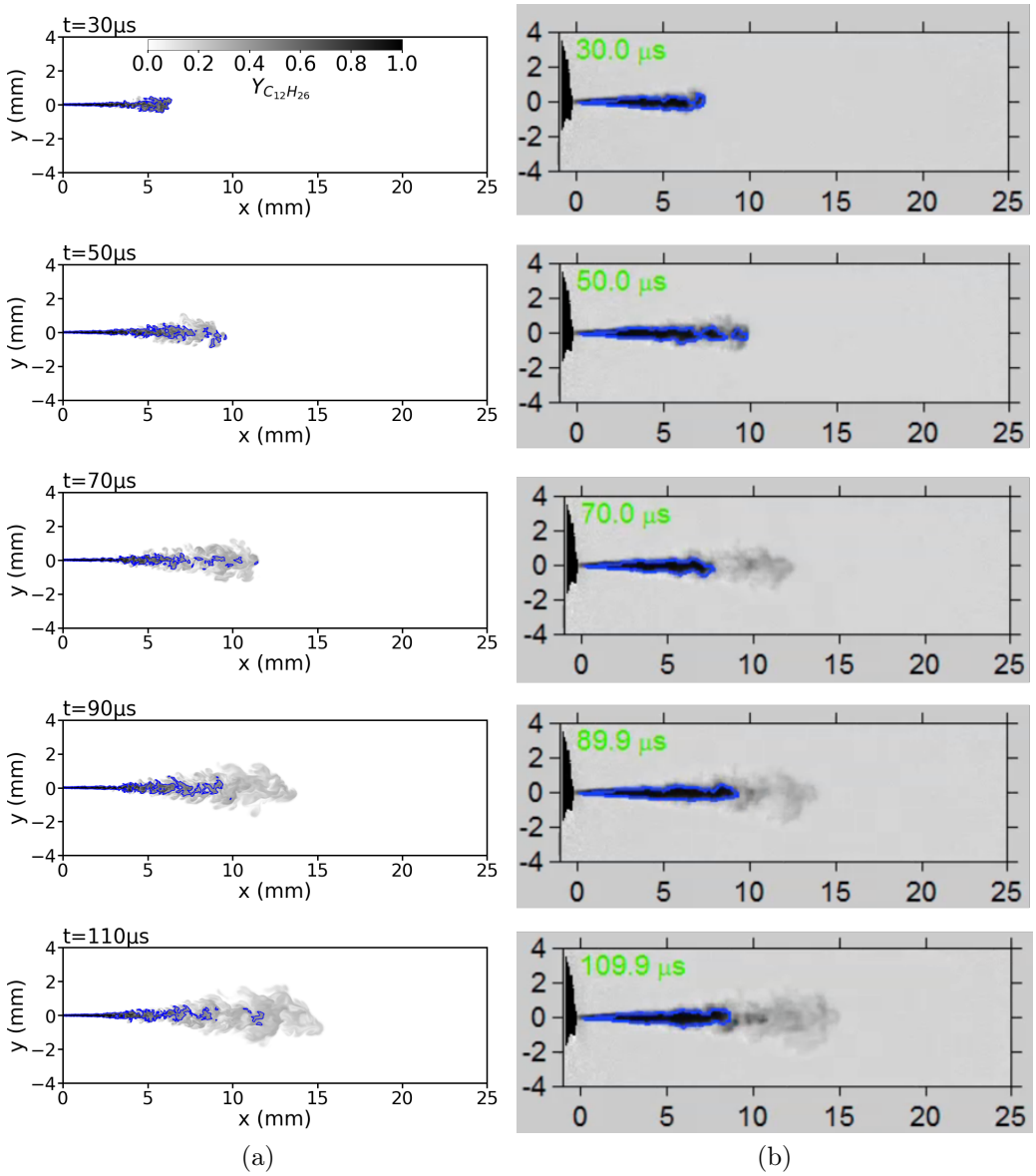

Figure 5.13: Evaporating Spray A condition: Temporal sequence of the n-dodecane injection. (a) LES results, (b) experimental data [145, 3]. Instantaneous n-dodecane mass fraction distribution at the grid center-plane is presented for the LES results. The blue line superimposed on the LES results represents a liquid volume fraction (α_l) iso-line of 0.15%, which illustrates the liquid penetration length.

A quantitative comparison of the spray penetrations between the LES results and the experimental data is shown in Fig. 5.14. The experimental data corresponds to liquid penetration obtained from diffused back illumination (DBI) [145] and Mie-Scattering [22, 6] techniques and vapor penetration obtained from Schlieren imaging [22, 6]. In the LES, the liquid penetration length is defined as $\max(x(\alpha_l = 0.15\%))$, where (x) is the axial distance from the nozzle exit. The criterion to evaluate the liquid penetration length is based on the Mie-scattering theory analysis [180], where the (α_l) threshold value representing the liquid length was found to be $(\alpha_l < 0.15\%)$ at Spray A condition. The vapor penetration length is defined as $\max(x(Y_{C_{12}H_{26}} = 0.1\%))$ as recommended by the ECN [7], where $(Y_{C_{12}H_{26}})$ is the n-dodecane mass fraction. It can be seen that the predicted

liquid penetration matches well the experimental measurements, lying between the DBI and Mie scattering data. Besides, the predicted vapor penetration also fairly agrees with the experimental data.

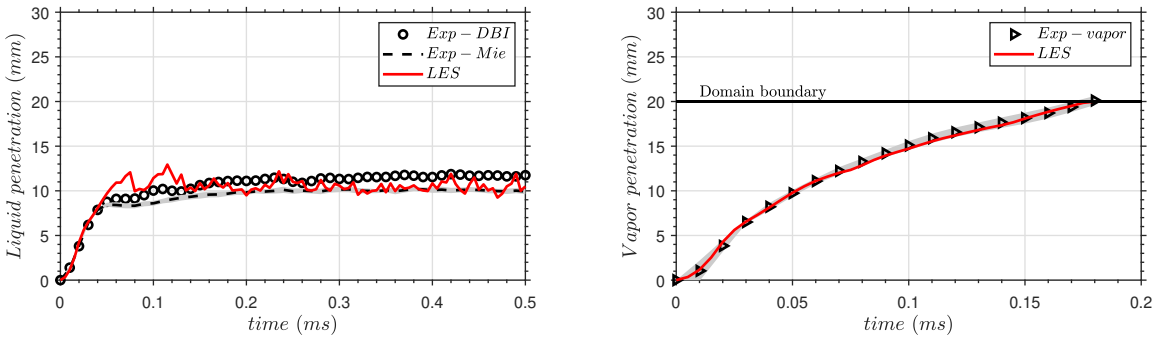

Figure 5.14: Evaporating Spray A condition: Comparison of LES and experimental data for (a) liquid and (b) vapor penetration lengths. The experimental data corresponds to liquid penetration obtained from diffused back illumination (DBI) [145, 3] and Mie-Scattering [22, 6] techniques and vapor penetration obtained from Schlieren imaging [22, 6]. The shaded grey area represents the uncertainty in the experimental measurements.

In addition, the radial distribution of n-dodecane mass fraction is compared between the simulation and the experimental data obtained by Rayleigh scattering technique [178, 4] as depicted in Fig. 5.15. The presented numerical result is obtained by time-averaging the LES results in the time interval between 0.4 and 1 ms after the start of injection (during the quasi-steady period). The shaded grey area in Fig. 5.15 represents 95% confidence interval in the experimental measurements. The simulation result agrees reasonably well with the experimental data within its confidence level. The predicted peak value on the jet axis tends to be slightly underestimated. However, the predicted mass fraction decay along the radial direction is well captured compared to the experimental profile.

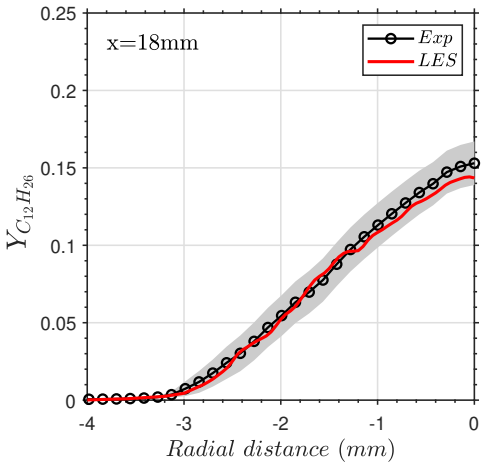

Figure 5.15: Evaporating Spray A condition: Numerical and experimental [178, 4] n-dodecane mass fraction radial distribution at an axial distance of 18 mm from the nozzle exit. The shaded grey area represents 95% confidence interval in the experimental measurements.

5.3.4.2 Thermodynamic analysis and VLE model results

To further analyze the phase change and mixing processes, the temperature-composition phase diagram for the (n-dodecane-nitrogen) mixture at ($P = 6\,\mathrm{MPa}$) along with the adiabatic mixing temperature (T_{AM}) are shown in Fig. 5.16. The (T_{AM}) is computed from,

$$h_{mix}(T_{AM}, P_{amb}, Y_{C_{12}H_{26}}) = Y_{C_{12}H_{26}}\, h_{C_{12}H_{26}}(T_{C_{12}H_{26}}, P_{amb}) + Y_{N_2}\, h_{N_2}(T_{N_2}, P_{amb}) \quad (5.12)$$

where ($h, Y_{C_{12}H_{26}}, Y_{N_2}$) are the specific enthalpy, the n-dodecane, and the nitrogen mass fractions, respectively. Besides, ($T_{C_{12}H_{26}}, T_{N_2}, P_{amb}$) denote the initial temperature of the fuel (n-dodecane), the initial temperature of the ambient N_2, and the ambient pressure, respectively. The adiabatic mixing temperature (T_{AM}) is computed considering the phase change based on the VLE solver. This is achieved by an offline iterative searching for the temperature (T_{AM}), such that the RHS of Equation 5.12 equals to the LHS, which represents the mixture's enthalpy evaluated from the VLE solver. The scattered data in Fig. 5.16 represents the thermodynamic states obtained from the LES simulation at $t = 110\mu s$.

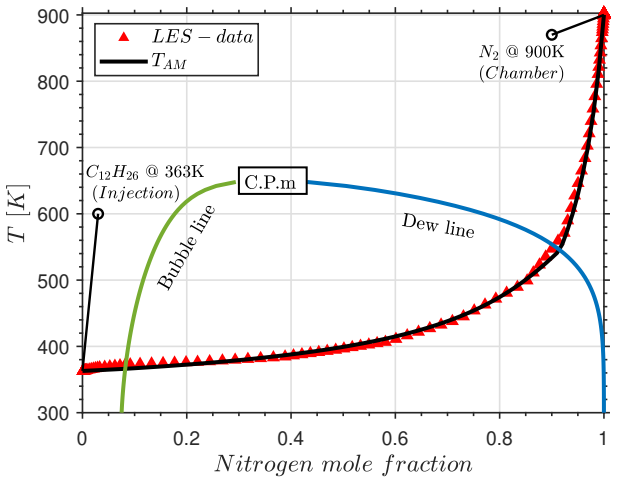

Figure 5.16: Evaporating Spray A condition: Temperature-composition diagram of ($C_{12}H_{26} - N_2$) binary mixture at pressure of 6 MPa along with the adiabatic mixing temperature (T_{AM}) obtained offline from the VLE solver. The scattered data (△) represents the thermodynamic states from the LES simulation at $t = 110\mu s$. The two-phase region is bounded by the bubble line and the dew line, which intersect at the critical point of the mixture denoted by C.P.m.

The mixture temperature distribution from the LES is observed to follow well the adiabatic mixing temperature as a function of the N_2 concentration. In addition, the temperature distribution has crossed the two-phase region bounded by the bubble and dew lines. This confirms that subcritical phase transition occurs for the ($C_{12}H_{26} - N_2$) binary mixture even at a pressure of 6 MPa, higher than the pure n-dodecane critical pressure ($P_{cr} = 1.8\,\mathrm{MPa}$), as also demonstrated in previous studies [149, 254]. Indeed, the involved binary mixture may exhibit different thermodynamic regimes based on the local pressure, temperature, and species composition. Accordingly, it cannot be determined from an *a priori* analysis whether the Spatio-temporal variation of the involved thermodynamic states are subcritical or supercritical during the entire fuel injection event. As a matter of

fact, both subcritical and supercritical regimes may exist simultaneously [254, 113, 114] in different locations of the chamber.

In addition to the previously discussed results, the employed VLE based model can provide valuable information regarding the phase change process and the composition of each species in each phase. The temporal evolution of the mass fractions of vaporous *n*-dodecane ($Y_{C_{12}H_{26},vap}$) and dissolved nitrogen in the liquid phase ($Y_{N_2,liq}$) are illustrated in Figs. (5.17a, 5.17b). The blue isoline of ($\alpha_l = 0.15\%$) demonstrates the liquid penetration length.

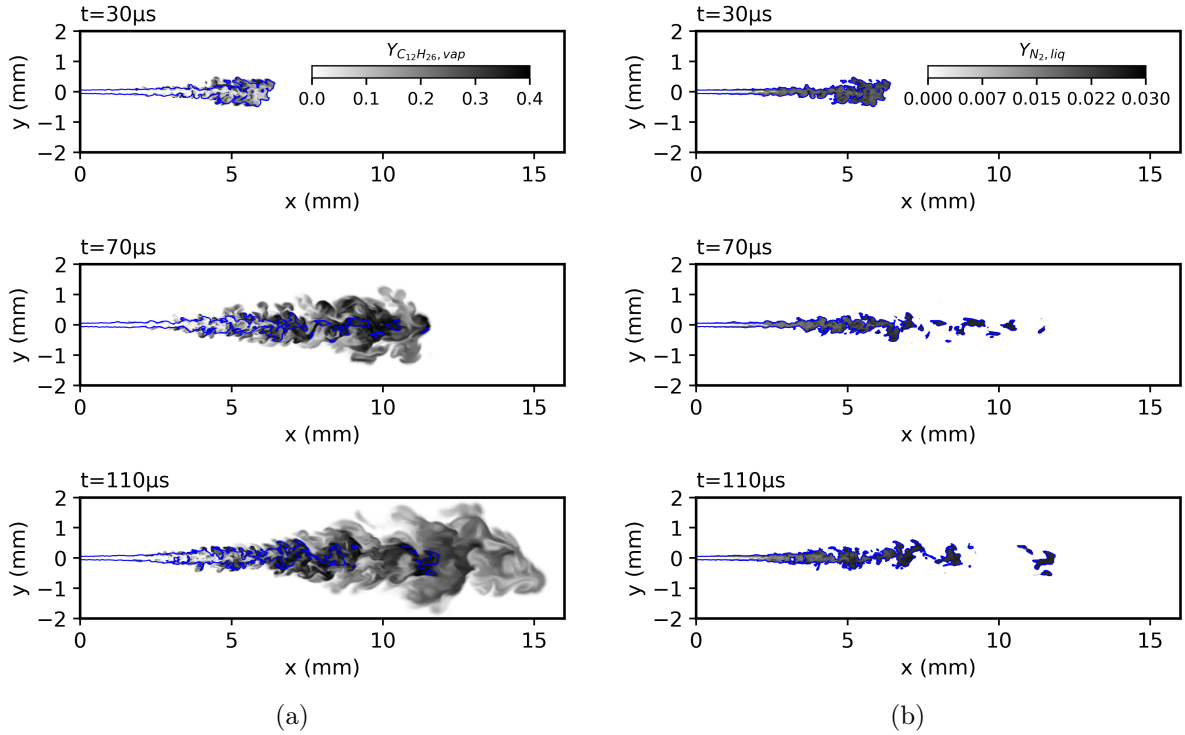

(a) (b)

Figure 5.17: Evaporating Spray A condition: Temporal evolution of the (a) mass fraction of vaporous *n*-dodecane ($Y_{C_{12}H_{26},vap}$) and (b) mass fraction of dissolved nitrogen in the liquid phase ($Y_{N_2,liq}$). The blue isoline illustrates the liquid penetration length based on the criterion ($\alpha_l = 0.15\%$).

It can be seen that the vaporous *n*-dodecane ($Y_{C_{12}H_{26},vap}$) is initially generated at the jet periphery with a significant accumulation at the jet tip, reaching a maximum of around 40%. Besides, a non-trivial amount of nitrogen is dissolved in the liquid jet, as shown in Fig. 5.17b, due to the enhanced solubility of the ambient gas in the liquid phase under the chamber high-pressure condition. One may also observe that the dissolved nitrogen in the liquid phase ($Y_{N_2,liq}$) increases sharply in the leading part of the liquid core and the atomized blobs, reaching a maximum of around 3%. This also demonstrates the role of the dissolution of non-condensable gases in the liquid phase as part of the phase change phenomenon.

Furthermore, the phase indicator (PHI) is depicted in Fig. 5.18, where ($PHI = 0, 1, 2$) denotes single liquid phase, single gas phase, and two-phase states, respectively. It can be seen that the jet exits the orifice with a single liquid phase state ($PHI = 0$) forming an intact liquid core, then as the jet travels in the chamber, it undergoes a transition to two-phase states ($PHI = 2$), due to the ongoing evaporation and mixing

with the hot ambient gas. In addition, regions of single gas phase states ($PHI = 1$), where the vaporous n-dodecane exhibits a peak value can be observed (see Fig. 5.17a), indicating that the liquid n-dodecane is fully vaporized.

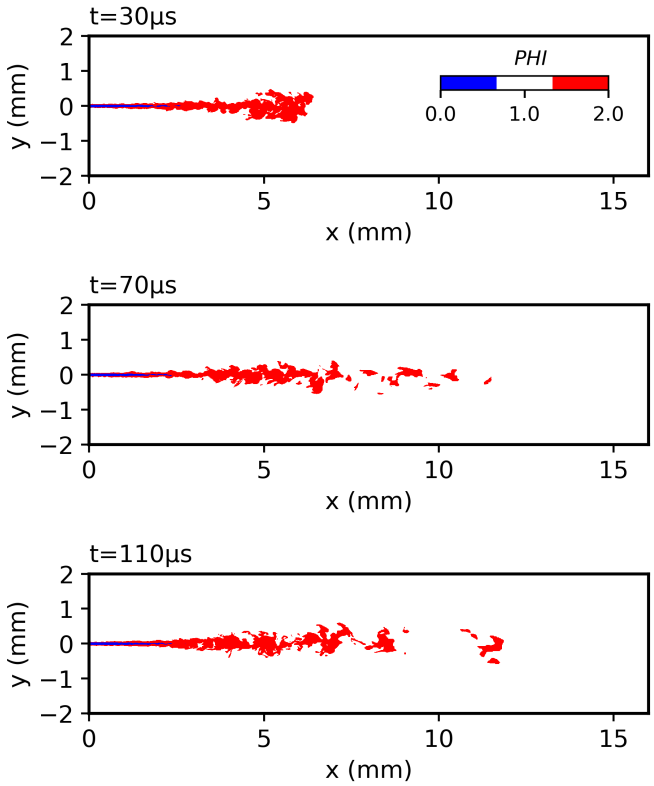

Figure 5.18: Evaporating Spray A condition: Temporal evolution of the phase indicator (PHI), where ($PHI = 0, 1, 2$) denotes single liquid phase, single gas phase, and two-phase states, respectively.

Further analysis is also carried out as an attempt to identify the distribution of the subcritical and supercritical states during the fuel injection event. For a multi-component mixture, the identification of the thermodynamic state (subcritical or supercritical) is not straightforward, as the mixture critical point, which depends on the mixture composition should be considered instead of the pure components critical points. Here, a simplified criterion to identify subcritical and supercritical states for the considered binary mixture is used. Assuming that the mixing process takes place at a constant pressure equal to the chamber pressure (6 MPa), then the mixture critical temperature ($T_{cr,mix}$) can be identified from the temperature-composition diagram in Fig. 5.16. Accordingly, if the temperature exceeds the mixture critical temperature, then the state is regarded as a supercritical state. Otherwise, the state is subcritical.

In Fig. 5.19, the temporal evolution of the reduced temperature ($T_r = T/T_{cr,mix}$) and gas volume fraction (α_g) distributions is shown. The vaporous n-dodecane mass fraction ($Y_{C_{12}H_{26},vap}$) distribution at the same time instants is also illustrated in Fig. 5.20. Only computational cells including mixture with nitrogen mole fraction (z_{N_2}) in the range of ($1e-03 < z_{N_2} < 0.999$) are illustrated. This is performed so that the pure or almost pure components regions are omitted. The black isoline of ($T_r = 1$) is also superimposed on the (α_g) and ($Y_{C_{12}H_{26},vap}$) contours.

At the early jet development ($t = 30\mu s$), the jet mainly exhibits a reduced temperature

less than one. The vaporous n-dodecane mass fraction contours (see Fig. 5.20) also show that the formed fuel vapor is located inside the isoline of $(T_r = 1)$, indicating that subcritical evaporation is taking place. As the jet further travels through the chamber and mixes with the hot ambient gas, more regions of $(T_r > 1)$ can be observed (see $t = 70, 110\mu s$). These regions correspond to locations composed of single gaseous-phase states (see α_g contours in Fig. 5.19) that have been heated to a temperature that exceeds the critical temperature of the mixture, reaching a supercritical state. At $(t = 70, 110\mu s)$, it can be also seen that the maximum mass fraction of the fuel vapor is located inside the $(T_r = 1)$ isoline, indicating that subcritical evaporation is the dominant phase-change process. This is consistent with the mixing path shown in Fig. 5.16, where the mixture has been through a large two-phase zone compared to much smaller single-phase zones.

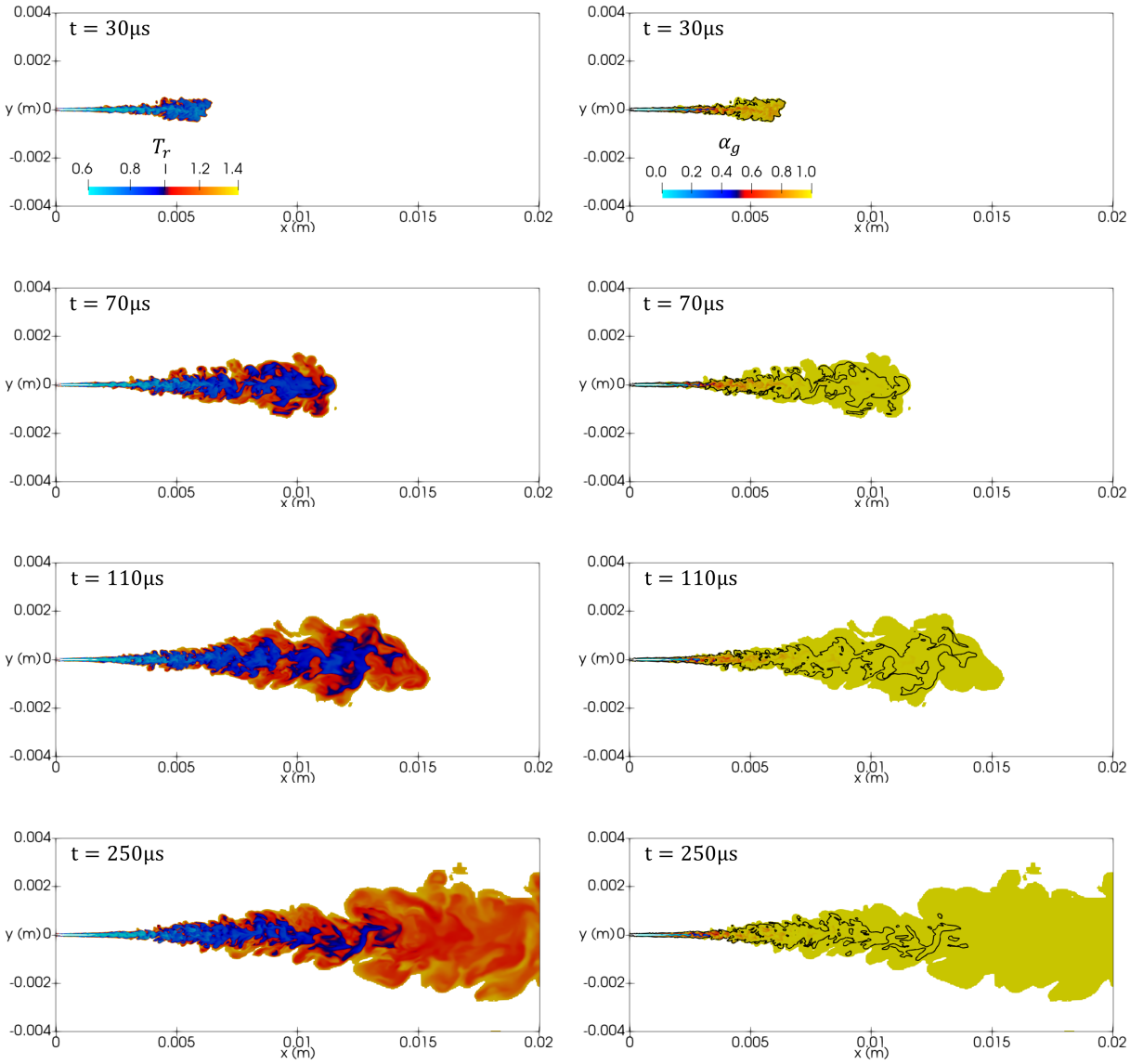

Figure 5.19: Evaporating Spray A condition: Temporal evolution of the reduced temperature $(T_r = T/T_{cr,mix})$ (left) and gas volume fraction (α_g) (right). Only cells with $(1e-03 < z_{N_2} < 0.999)$ are shown. The black isoline on the (α_g) contours represents $(T_r = 1)$ to illustrate the subcritical and supercritical regions.

Further, at ($t = 250\mu s$), during the quasi-steady state injection period, it can be observed that the supercritical regions with ($T_r > 1$) are more concentrated in the diluted spray locations. The contours of the reduced temperature again confirm that both subcritical and supercritical states may exist simultaneously during the fuel injection event under the considered conditions, and the transition from subcritical evaporation to single-phase diffusive mixing can be handled by the proposed model. It should also be noted that the presented analysis is an approximation as the pressure is generally not constant in the computational domain during the entire fuel injection event, but it fluctuates, especially during the early injection phase. Thus, the critical condition is not constant, as adopted here in the current simplified analysis.

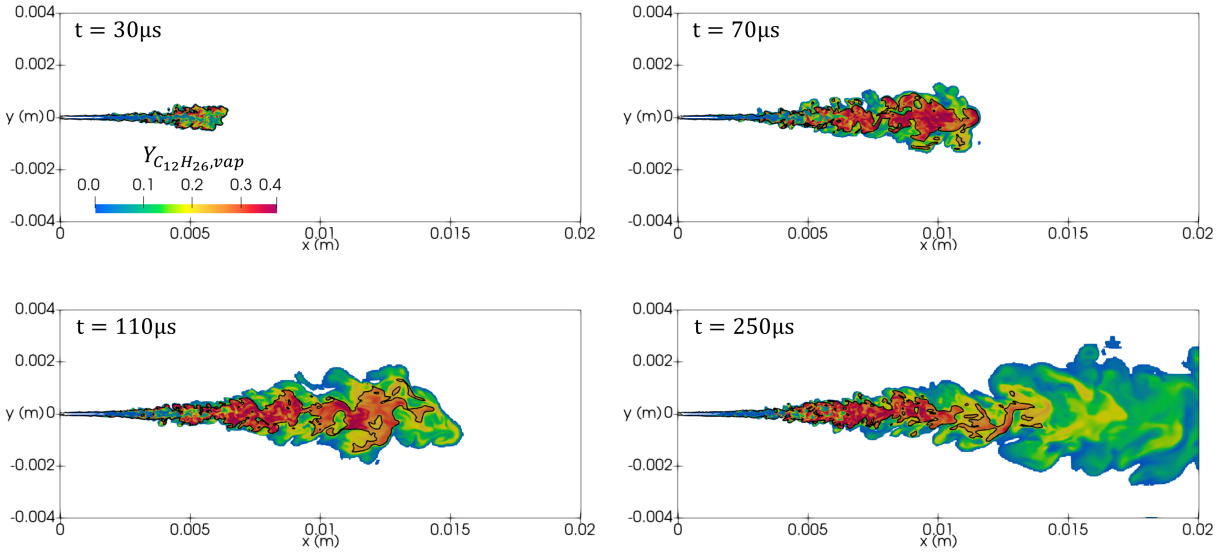

Figure 5.20: Evaporating Spray A condition: Temporal evolution of the vaporous n-dodecane mass fraction ($Y_{C_{12}H_{26},vap}$). Only cells with ($1e-03 < z_{N_2} < 0.999$) are shown. The black isoline represents reduced temperature ($T_r = 1$) to illustrate the subcritical and supercritical regions.

5.3.4.3 Effect of vaporization on the surface density

In the current section, the effect of the vaporization on the surface area density and the SMD is investigated. The results are obtained under the evaporating condition with the same modeling constants ($C_\Sigma = 1, We_c = 1.5$) for the Σ equation used under the non-evaporating condition. The vaporization effect is analyzed in both the dense and diluted spray regions. The time averaged surface area density radial distribution at two axial positions in the dense ($x = 2\,\text{mm}$) and diluted ($x = 8\,\text{mm}$) spray regions under both the evaporating and non-evaporating conditions are depicted in Fig. 5.21. The time averaged results are indicated by the operator $\langle . \rangle$.

In the dense spray region ($x = 2\,\text{mm}$), it seems that the vaporization tends to enhance the surface generation, with relatively higher surface area density at the jet periphery than the non-evaporating case. The jet atomization can be mainly attributed to the growth of instabilities on the jet surface due to the turbulent interaction with the gas phase. However, under the evaporating condition, it is also affected by the ongoing evaporation,

which tends to trigger and enhance the liquid jet instability. Indeed, the interaction between the counter flows of gas entrainment and evaporation at the interface could enhance its instability, as suggested in [254]. Besides, the variation of the properties would significantly affect the surface density variation. For instance, the surface tension is reduced as the ambient pressure and temperature increase. Thus, higher surface generation could be expected under the evaporating condition compared to the non-evaporating condition.

On the other hand, at a relatively diluted spray region ($x = 8\,\text{mm}$), a reduction of the surface area density can be observed under the evaporating condition compared to the non-evaporating case. Meanwhile, as the liquid volume fraction decreases due to the ongoing evaporation, a relatively smaller mean SMD is obtained under the evaporating condition as shown in Fig. 5.22 at the same axial position ($x = 8\,\text{mm}$).

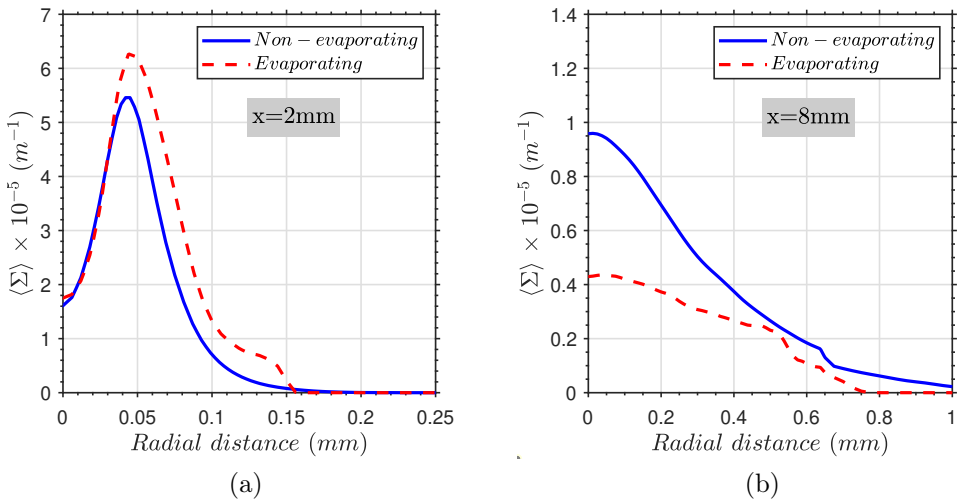

Figure 5.21: Time averaged surface area density radial distribution under non-evaporating and evaporating conditions at axial distances of (a) 2 mm and (b) 8 mm from the nozzle exit.

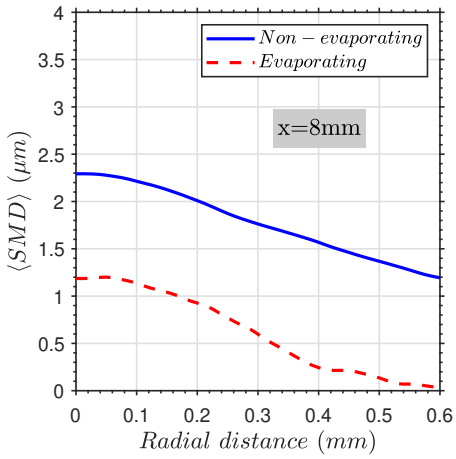

Figure 5.22: Time averaged SMD radial distribution under non-evaporating and evaporating conditions at axial distance of 8 mm from the nozzle exit.

These results confirm the sensitivity of the surface density model to the phase change. Indeed, in the current work, the phase change is implicitly considered through the terms (Σ_{min}) and (Σ_{eq}), which are dependent on (α_l) provided by the thermodynamic table. Besides, the variation of the properties ($\rho_l, \rho_g, \sigma, ..., etc$) involved in the ($\Sigma$) equation with the temperature, pressure, and species mass fraction is considered by the thermodynamic table, which would also impact the predicted surface area density. Overall, the current model allows considering the phase change effect in both the dense and dilute zones of the spray without employing evaporation models assuming a spray of droplets as previously proposed in [140], for instance.

5.3.5 Parametric variation of the ECN Spray A conditions

In addition to the baseline case of Spray A, the RFM model is further assessed for three additional operating conditions, which are listed in Table. 5.2. Cases 1 and 3 have the same ambient density as the baseline spray A condition ($T_{amb} = 900\,\mathrm{K}$, $P_{amb} = 6\,\mathrm{MPa}$), but varies in the ambient pressure and temperature. Thus, the effect of the ambient conditions variation can be analyzed based on these two cases. For case 4, the ambient density ($\rho_{amb} = 7.6\,\mathrm{kg/m^3}$) is much lower than the baseline case, but with similar ambient temperature. Thus, the effect of the ambient density variation can be analyzed based on case 4.

For the different operating conditions, the same computational setup and grid 2 (16M cells) are used similar to the baseline Spray A case. Besides, the mass flow rate profile is taken from the CMT injection rate generator for each operating condition and used for the inflow boundary condition. The LES results are validated using the available DBI measurements [145, 3] of the liquid penetration length under the different operating conditions (Table. 5.2).

Case no.	T_{amb}(K)	P_{amb}(MPa)	ρ_{amb}(kg/m^3)
1	1200	8	$22.8^a/22.04^b$
2 (Baseline)	900	6	$22.8^a/22.06^b$
3	700	4.6	$22.8^a/21.8^b$
4	900	2.04	$7.6^a/7.59^b$

Table 5.2: Operating conditions of ECN spray A parametric study. ^{a} ECN experimental operating conditions [3]. ^{b} calculated using the VTPR-EoS.

Firstly, the instantaneous n-dodecane mass fraction field from the LES is qualitatively compared against the DBI images as illustrated in Fig. 5.23 for the different operating conditions. The liquid penetration length is represented by the blue isoline of ($\alpha_l = 0.15\%$). Overall a good agreement with the experimental images can be observed for both liquid and vapor penetrations under the various operating conditions.

In Fig. 5.24, a quantitative comparison of the predicated liquid penetration and the available DBI measurements is presented for the different operating conditions (see Table. 5.2). Figures (5.24a-5.24c) show the effect of decreasing the ambient temperature at a constant ambient density. It can be observed the increase of the liquid penetration length, due to the reduction of the evaporation rate, as the ambient temperature is further reduced. Besides, the predicted liquid penetration agrees well with the experimental data, where both the initial transient phase and the steady state liquid length are fairly captured by the RFM model.

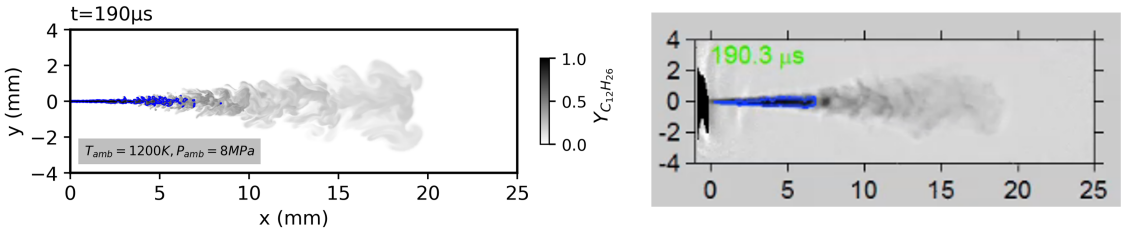

(a) Case 1

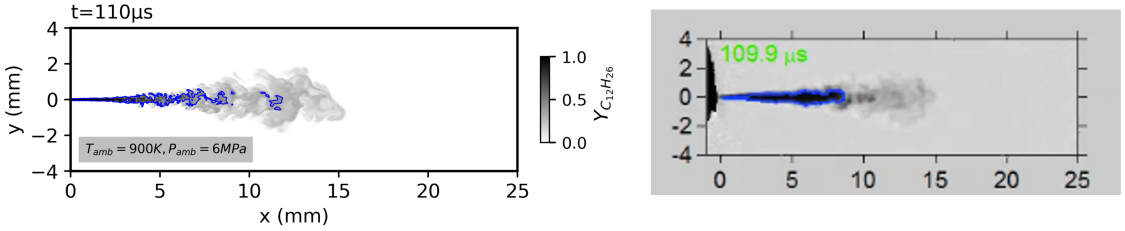

(b) Case 2 (Baseline)

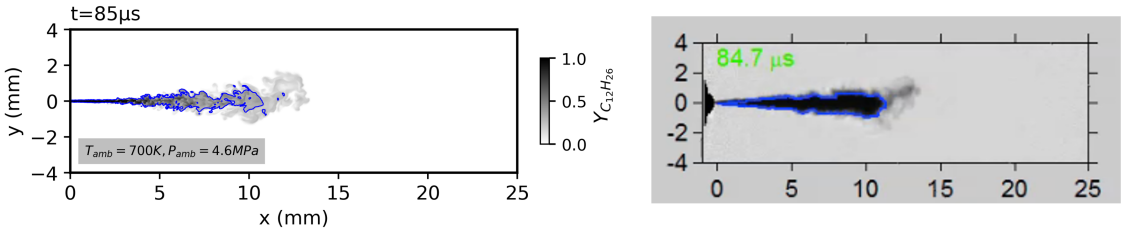

(c) Case 3

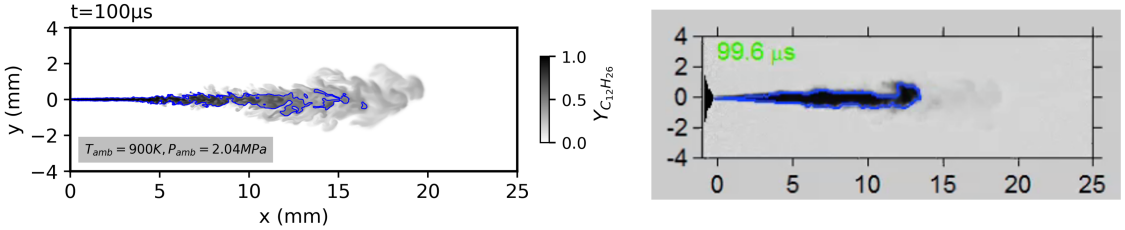

(d) Case 4

Figure 5.23: Instantaneous n-dodecane mass fraction distribution from LES (left) compared with the diffused back-illumination (DBI) images [145, 3] for the parametric study cases. The liquid penetration is represented by the blue isoline of ($\alpha_l = 1.5\%$) superimposed on the LES results. The ambient temperature (T_{amb}) and pressure (P_{amb}) of each case are depicted on the corresponding sub-figure .

The effect of decreasing the ambient density can be seen through Fig. 5.24d, where an increased liquid penetration length can be observed compared to the baseline case (Fig. 5.24b). Indeed, the reduction of the ambient density is accompanied by lower rate of gas entrainement, and thus high penetration length. Besides, Fig. 5.24d shows that the initial transient liquid penetration is well captured by the model, then some deviation from the experimental data can be observed near the end of the computational domain ($x = 20\,\text{mm}$).

In summary, these results show the capability of the RFM model to well predict the variation of the spray characteristics under the considered operating conditions, demonstrating a high predictive performance of the model without the need of any parameter tuning as commonly performed in classical Lagrangian spray models.

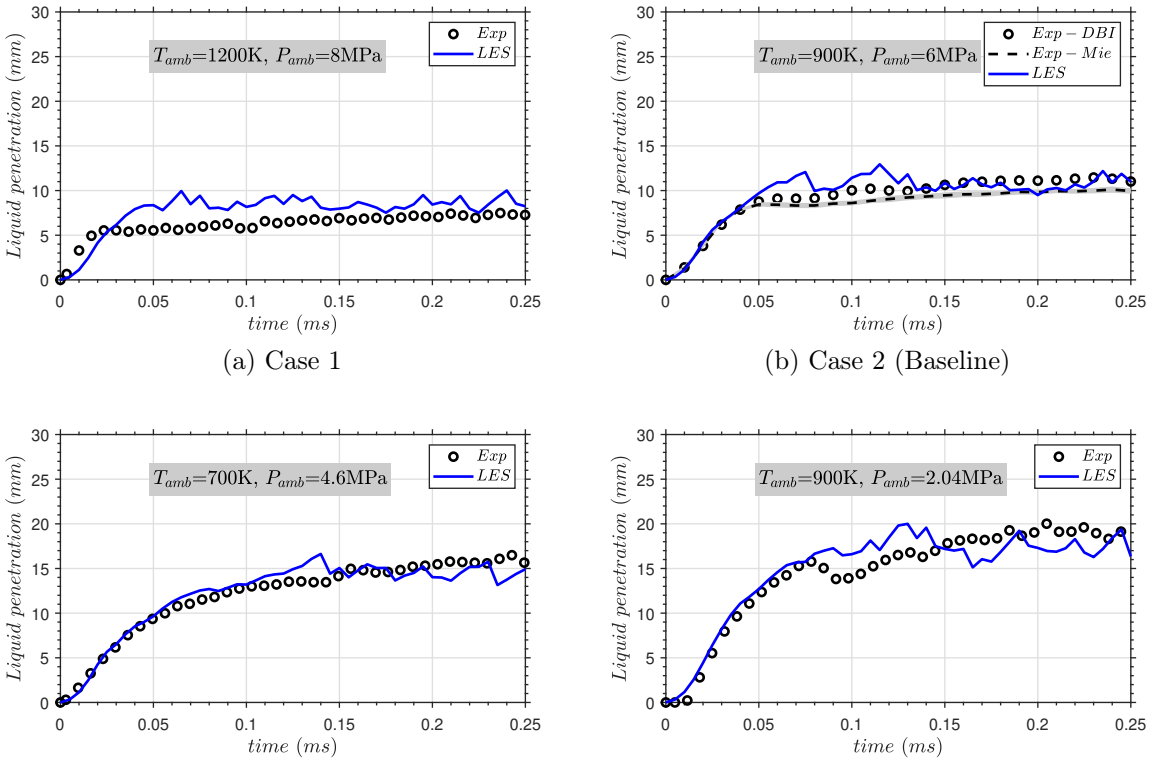

(a) Case 1

(b) Case 2 (Baseline)

(c) Case 3

(d) Case 4

Figure 5.24: Numerical and experimental liquid penetration for the ECN spray A under various operating conditions. Experimental data correspond to liquid penetration obtained from diffused back-illumination (DBI) technique [145, 3]. In sub-figure (b), the Mie-scattering data is also shown for the baseline spray A case. The ambient temperature (T_{amb}) and pressure (P_{amb}) of each case are depicted on the corresponding sub-figure

5.4 Application to dual-fuel configuration

In the current section, the evaporating ECN Spray A baseline condition is investigated under a dual-fuel configuration. Methanol is employed as a primary fuel in the current study. A schematic of the employed dual-fuel configuration of the ECN spray A compared to the single fuel configuration is illustrated in Fig. 5.25. The dual-fuel configuration was based on the ECN spray A condition, due to the lack of experimental data for dual-fuel configurations.

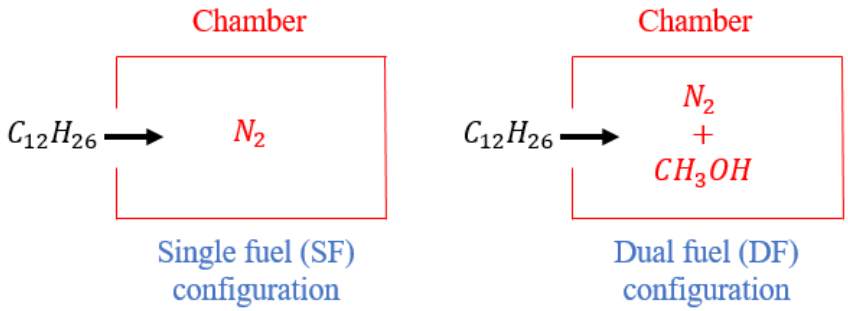

Figure 5.25: Schematic of fuel injection for single-fuel (left) and dual-fuel (right) configurations. For dual-fuel configuration, the ambient includes a premixed charge of primary fuel (methanol) and nitrogen.

In the previous sections, the RFM model has been validated for the single-fuel configuration under various operating conditions using the ECN experimental database. Thus, it can be further applied with sufficient confidence to investigate the spray evaporation and mixing in the dual-fuel configuration.

The main objectives of this investigation are:

- To further assess the proposed RFM model for multi-species simulations, where in the DF configuration, a ternary mixture of (n-dodecane/methanol/nitrogen) is studied.
- To answer to the question "What is the effect of the ambient methanol used as a primary fuel in the dual-fuel configuration on the evaporation and mixing processes?".

5.4.1 Test case setup

The employed numerical setup and computational grid are similar to that employed in the previous section of the single fuel (SF) ECN Spray A simulation (see Sec. 5.3.2). The injection and operating conditions of the SF and DF configurations are listed in Table. 5.3.

For the dual-fuel case the chamber is initialized with a mixed ambient of methanol (CH_3OH) and nitrogen (N_2) with mass fractions of 0.2 and 0.8, respectively. The employed initial mass fraction of methanol ($Y_{CH_3OH} = 0.2$) could be relatively higher than that found in dual-fuel engines powered with methanol. However, the goal here is to investigate if significant effects on the evaporation and mixing could take place even with such initial methanol ambient concentration.

Configuration	Single fuel (SF)	Dual-fuel (DF)
Injection pressure (MPa)	150	150
Injection temperature (K)	363	363
Ambient temperature (K)	900	900
Ambient pressure (MPa)	6	6
Ambient density (kg/m^3)	22.06	22.6
Ambient composition	$Y_{N_2} = 1, Y_{CH_3OH} = 0$	$Y_{N_2} = 0.8, Y_{CH_3OH} = 0.2$

Table 5.3: Injection and ambient conditions of ECN spray A under single and dual-fuel configurations. (Y) denotes the mass fraction of nitrogen (N_2) and methanol (CH_3OH)

The thermodynamic closure is achieved using two different EoSs for the DF and SF cases. Indeed, the tabulated thermodynamic closure is achieved using the volume-translated Peng-Robinson (VTPR) EoS for the (n-dodecane /nitrogen) binary system in the single-fuel Spray A simulation. However, for the dual-fuel simulation, a volume translated Cubic Plus Association (VTCPA) EoS is employed for the (n-dodecane/nitrogen/methanol) ternary system.

5.4.2 Results and discussion

Figure 5.26a shows a comparison of the spray liquid and vapor penetrations between the single-fuel (SF) and dual-fuel (DF) cases. Both the single and dual-fuel exhibit very similar liquid penetration length. Besides, in terms of vapor penetration, only a slightly higher vapor penetration can be observed in the time interval of 0.12 to 0.18 ms. Overall, the initial presence of methanol in the ambient gas tends to have small effect on the spray liquid and vapor penetrations. In addition, the time-averaged n-dodecane mass fraction radial distribution is compared between the SF and DF cases as depicted in Fig. 5.26b. The SF and DF cases show a highly similar radial fuel distribution with a slightly narrower profile at the jet periphery for the DF case.

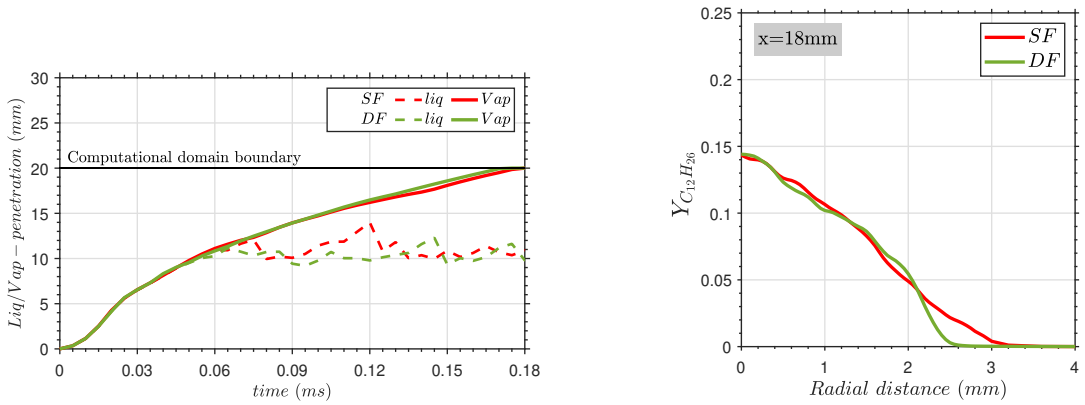

(a) (b)

Figure 5.26: (a) Comparison of jet liquid and vapor penetrations between Spray A single-fuel (SF) and dual-fuel (DF) cases. (b) Comparison of the time averaged n-dodecane mass fraction radial distribution between the (SF) and (DF) cases at an axial distance of 18 mm from the nozzle exit. The ambient of the DF case is composed of 20% methanol and 80% nitrogen by mass fraction.

To further understand the fundamental origin of such behavior of the DF case compared to the SF reference case, Fig. 5.27 shows the adiabatic mixing temperature variation with the n-dodecane mole fraction for the SF and DF cases. The two-phase states along the adiabatic mixing temperature line are superimposed with blue lines.

It can be observed that the adiabatic mixing temperature is relatively higher for the DF case than the SF case. Besides, the two-phase region shrinks slightly for the DF case compared to the SF case, as demonstrated by the insert on Fig. 5.27. This slight variation of the two-phase region between the SF and DF cases explains the differences observed mainly for the liquid penetration and fuel radial distribution. Moreover, the insert on Fig. 5.27 shows a smaller n-dodecane mole fraction at the start of the two-phase region for the DF case compared to the SF case. This implies that a higher amount of ambient gases are dissolved in the liquid phase for the DF case relatively to the SF case.

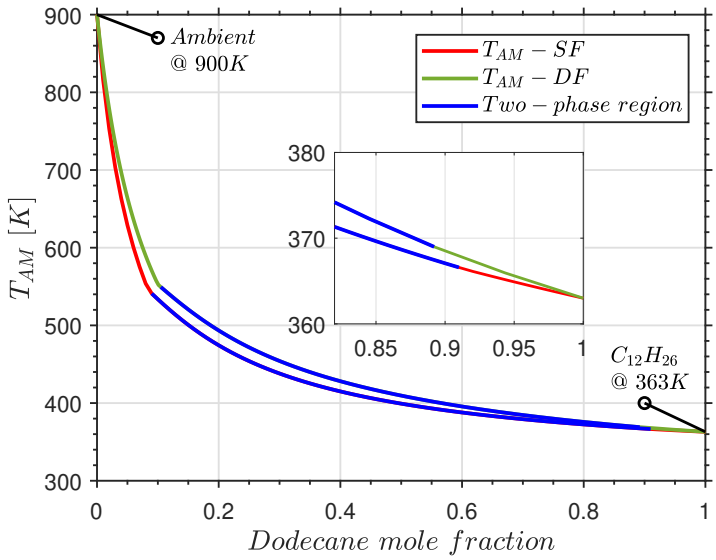

Figure 5.27: Adiabatic mixing temperature (T_{AM}) along with the two-phase region represented by the blue lines for the SF and DF cases at pressure of 6 MPa. The ambient of the DF case is composed of 20% methanol and 80% nitrogen by mass fraction.

Figure 5.28 shows the mass fraction of the dissolved ambient gases ($Y_{amb,liq}$) in the liquid phase at different time instants. For the single-fuel case, the dissolved gas includes only nitrogen, whereas, for the dual-fuel case, the dissolved gas is the sum of dissolved methanol and nitrogen in the liquid phase.

It can be observed that the dissolved gas for the DF case is relatively higher than that of the SF case. These results are consistent with the two-phase region shrink in the insert on Fig. 5.27, which shows a smaller mole fraction of n-dodecane at the start of the two-phase region for the DF case (i.e. a higher amount of dissolved gas in the liquid phase as illustrated in Fig. 5.28).

In addition, the methanol introduced in the chamber also impacts the ambient density. Indeed, the ambient gas density exhibits a relative increase as methanol is added to nitrogen in the chamber, since methanol is a heavier compound than nitrogen. The ambient gas density (ρ_{amb}) as computed by the CPA-EoS increases from ($22\,\mathrm{kg/m^3}$) for the SF case to ($22.6\,\mathrm{kg/m^3}$) for the DF case with methanol mass fraction of 0.2. This slight increase in the ambient density did not significantly affect the jet behavior.

Finally, although under the considered dual-fuel configuration, it has been found that the ambient methanol effects on the overall spray evaporation and mixing processes are insignificant (only a small variation of the spray penetrations and n-dodecane mass fraction distribution). However, a remarkable impact on on the flame lift-off length, ignition delay time, and pollutant emissions is to be expected. For instance, a lower NO_x formation rate in the dual-fuel configuration with methanol as primary fuel has been reported in [248].

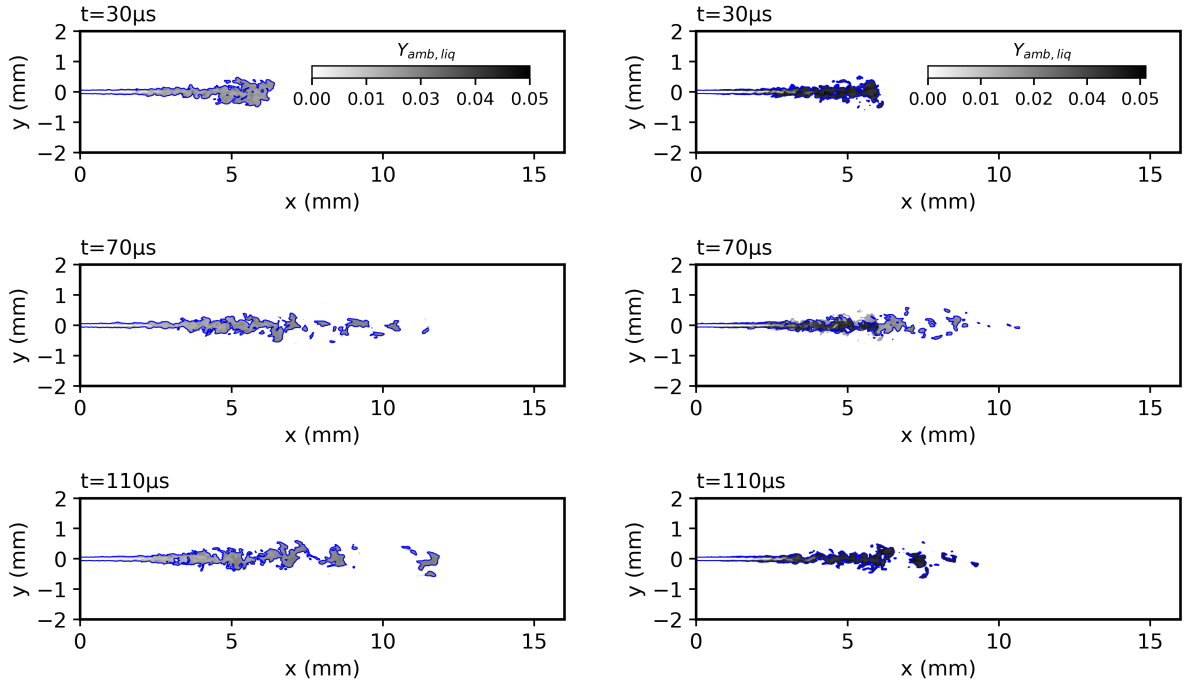

Figure 5.28: Instantaneous mass fraction of dissolved ambient gases in the liquid phase ($Y_{amb,liq}$) for (a) single fuel (SF) case and (b) dual-fuel (DF) case at different time instants. For dual-fuel case, the dissolved gas is the sum of dissolved methanol and nitrogen. The blue isoline illustrates the liquid penetration length based on the criterion ($\alpha_l = 0.15\%$).

5.5 Conclusions

This chapter has been focused on the modeling of high-pressure fuel injection and atomization. To this goal, the RFM model is complemented with a surface density transport equation for fuel atomization modeling within the LES framework. The Engine Combustion Network (ECN) Spray A injector non-evaporating and nominal evaporating conditions are used as a reference for the proposed model validation. In addition, a parametric variation of the ECN Spray A is carried out for further assessment and validation of the proposed model under various operating conditions. Finally, this chapter closes with an investigation of the ECN Spray A evaporating baseline condition in a dual-fuel configuration using methanol as a primary fuel. The main conclusions obtained can be summarized as follows:

- Under the non-evaporating ECN Spray A condition, the comparison of the LES-RFM results with the different experimental data in the near-nozzle field, including

projected mass density, transverse integrated mass, and liquid volume fraction, has shown a good agreement, which indicates that the RFM model can accurately capture the fuel dispersion under the considered conditions.

- Under the non-evaporating ECN Spray A condition, the assessment of the proposed (RFM-Σ) model is carried out by comparing the model results against the experimental projected surface area density along the spray centerline and the SMD radial profiles. The obtained results show that the RFM model coupled with the surface density equation can reproduce well the experimental projected surface density along the spray axis. Besides, further comparison with the SMD measurements has demonstrated that the model prediction for the SMD falls within the experimental data range. Overall, it can be concluded that the proposed RFM-Σ model can accurately predict the fuel dispersion and primary atomization under the considered conditions.

- Under the evaporating ECN Spray A condition, global spray metrics such as spray liquid and vapor penetrations are well captured by the RFM model compared to the experimental data. Moreover, local analysis shows that the mixture fraction radial distribution favorably agrees with the experimental data within its confidence level.

- The analysis of the of the surface density and SMD results under both the evaporating and non-evaporating conditions has demonstrated the sensitivity of the surface area density model to the vaporization effects. In the dense region of the spray, vaporization tends to enhance the surface area density production, whereas vaporization decreases the surface area density in the dilute spray region. Besides, the mean SMD relatively decreases in the dilute region under the evaporating condition

- The parametric variation of the ECN Spray A has shown the capability of the RFM model to well predict the variation of the spray penetration compared to the experimental data under various operating conditions, demonstrating a high predictive performance of the model.

- An investigation of the ECN Spray A baseline condition in a dual-fuel (DF) configuration using methanol as a primary fuel has been carried out. Under the considered dual-fuel configuration, the ambient methanol effects on the overall spray evaporation and mixing processes were found to be insignificant (only a small variation of the spray penetrations and n-dodecane mass fraction distribution). However, a remarkable impact on the flame lift-off length, ignition delay time, and pollutant emissions is to be expected. For instance, a lower NOx formation rate in the dual-fuel configuration with methanol as primary fuel has been reported in [248].

Chapter 6

Cavitation modeling

Contents

In this chapter, the proposed RFM model is employed to investigate the cavitation phenomenon under different configurations. The goal here is to assess and validate the RFM model for cavitation simulation. Firstly, the cavitation phenomenon is simulated in a transparent injector configuration using water, where the model results are compared against the available experimental data of Sou et al. [220]. Then, the model is further applied to investigate the cavitation formation in a heavy-duty injector using ammonia as a promising renewable fuel in the transport sector.

6.1 Transparent injector with rectangular nozzle

6.1.1 Case description

The investigated test case is based on the experimental work of Sou et al. [220], where tap water is injected into ambient air in a transparent injector, with a rectangular nozzle as illustrated in Fig. 6.1. The cavitation inside the nozzle has been recorded using a high-speed camera and quantitative measurements of the flow velocity and turbulent fluctuations are carried out using Laser Doppler Velocimetry (LDV). The operating conditions of the simulated test case are summarized in Table. 6.1. The cavitation number (σ_{cav}) and Reynolds number (Re) are defined as:

$$\sigma_{cav} = \frac{P_a - P_v}{0.5\rho_l V_n^2} \tag{6.1}$$

$$Re = \frac{V_n W_n}{\nu_l} \tag{6.2}$$

where (P_a) is the atmospheric pressure, (P_v) is the saturation pressure, and (V_n) is the mean liquid velocity in the nozzle, respectively. The (W_n) is the nozzle width and (ν_l, ρ_l) are the liquid kinematic viscosity and density, respectively.

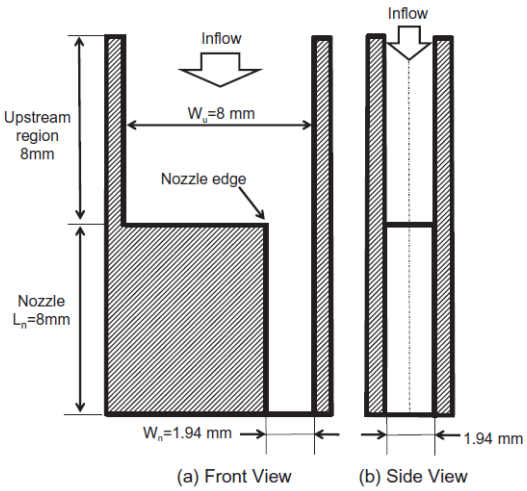

Figure 6.1: Transparent injector [220] cross-sectional view and dimensions.

Injection pressure (MPa)	V_n(m/s)	R_e	σ_{cav}	Cavitation regime
0.22	12.8	27,700	1.19	developing cavitation

Table 6.1: Operating conditions of the simulated test case [220].

6.1.2 Computational set-up and numerical methods

Computational set-up

A two-dimensional (2D) computational domain is employed as shown in Fig. 6.2. The external domain for the jet was not considered, as the focus here was mainly to perform a preliminary assessment for the model to capture in the in-nozzle cavitation. The base mesh size is set to 100 μm, while fixed mesh embedding has been employed to achieve minimum cell size of 6.25μm near the wall and 12.5μm at the nozzle center. A total pressure boundary condition of 2.38 bar is imposed at the inlet patch, which is taken from previous studies [134, 235] of the same test case. The upstream region of the nozzle have been slightly elongated to 12 mm to minimize the effect of the imposed total pressure boundary condition and allow for appropriate flow development. A pressure outlet boundary condition is set at the nozzle exit, which is relaxed from 2.38 bar to 1 bar in a time interval of 1 ms to facilitate the simulation start-up. The rest of domain boundaries are set to no-slip walls. The computational domain is initialized with pressure of 2.38 bar and temperature of 300 K. The initial phase state is single liquid phase ($\alpha_l = 1$), with mass fractions of ($Y_{N_2} = 1e-05, Y_{H_2O} = 1 - Y_{N_2}$). The initial mass fraction of dissolved nitrogen in the feed is chosen to be smaller than the saturation value ($Y_{N_2} \approx 1.74e-05$) estimated from the VLE solver at the inlet pressure and temperature, following previous cavitation studies [25, 253].

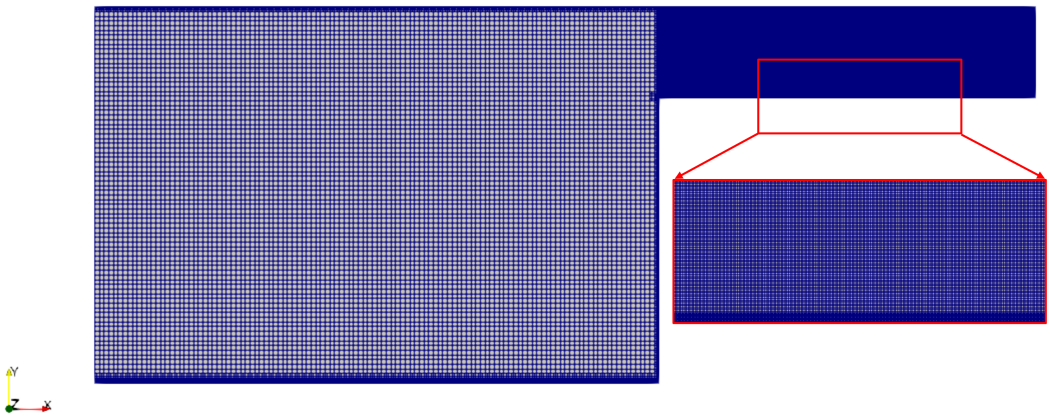

Figure 6.2: Computational domain with the grid structure. The insert shows the refined mesh in the nozzle region.

Numerical methods

URANS simulations are carried out using the RNG $k-\epsilon$ turbulence model [251], which has also been employed in previous cavitation simulations [32]. This turbulence model is employed here with its default constants. Simulations are carried out using CONVERGE V3.1.6 employing the updated real-fluid PISO algorithm (see Sec. 2.1.5.1). The spatial discretization is second-order accurate using a central difference scheme. The time integration is achieved by a second-order Crank-Nicolson scheme for the momentum equation and a first-order implicit Euler scheme for the rest of the equations. The time step is around (1e-08-1e-09)s and adjusted automatically based on a maximum CFL number of 0.7. The RFM model thermodynamic closure for the (water/nitrogen) binary mixture is based on the CPA-EoS with a uniform thermodynamic table resolution in $(T, log_{10}P, Y_{H_2O})$ axes of (11×101×21) points covering ranges of (290-310 K, 0.01-3.01 bar, 0.9999-1).

6.1.3 Results and discussion

6.1.3.1 Comparison with experimental data

The fields of gas volume fraction (α_g) and pressure (P) are illustrated in Fig. 6.3. It can be observed the development of a low pressure region that starts at the sharp corner of the rectangular nozzle inlet, where flow separation takes place (see Fig. 6.4a). When the pressure in this region drops below the saturation pressure of the liquid, cavitation occurs, as indicated by the gas volume fraction field. For this developing cavitation condition, the obtained results are qualitatively in good agreement with the instantaneous experimental image [220], as depicted in Fig. 6.3c. Under such condition, cavitation pockets are generated inside the injector nozzle, which are constrained inside the nozzle and not reaching the nozzle exit.

In addition to the qualitative comparison, the numerical results are quantitatively compared with the experimental data of mean axial velocity and root mean square (RMS) of velocity fluctuations, which are acquired by means of Laser Doppler Velocimetry (LDV)

technique. Experimental and numerical mean axial velocity and velocity RMS are shown in Fig. 6.4 at different axial stations of 1.5, 3 and 6 mm from the nozzle inlet.

A fairly good agreement is obtained between the predicted mean velocity and the experimental data at the different axial positions. Regarding the RMS of the fluctuation velocity, the comparison shows a reasonable agreement with the experimental data at ($x = 1.5, 3$ mm), although some deviations can still be observed. At ($x = 6$ mm) the experimental profile is under-predicted by the simulation, showing higher error compared to the other axial locations.

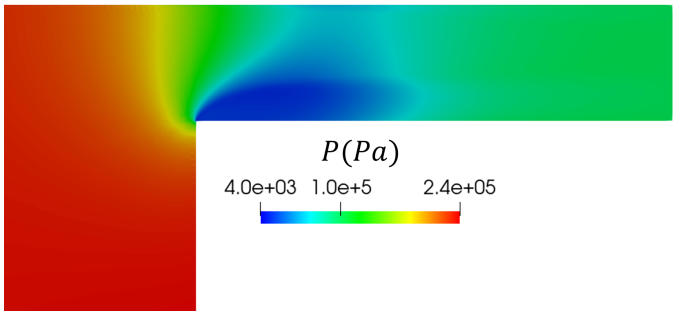

(a)

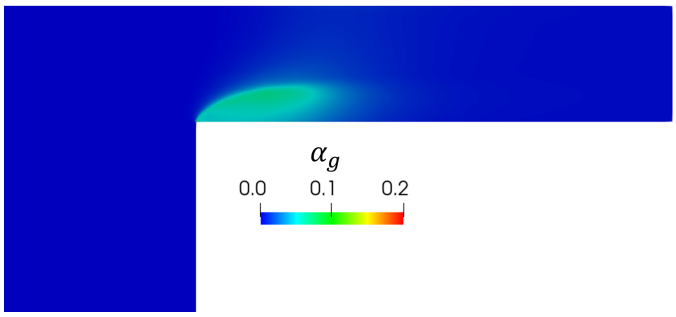

(b)

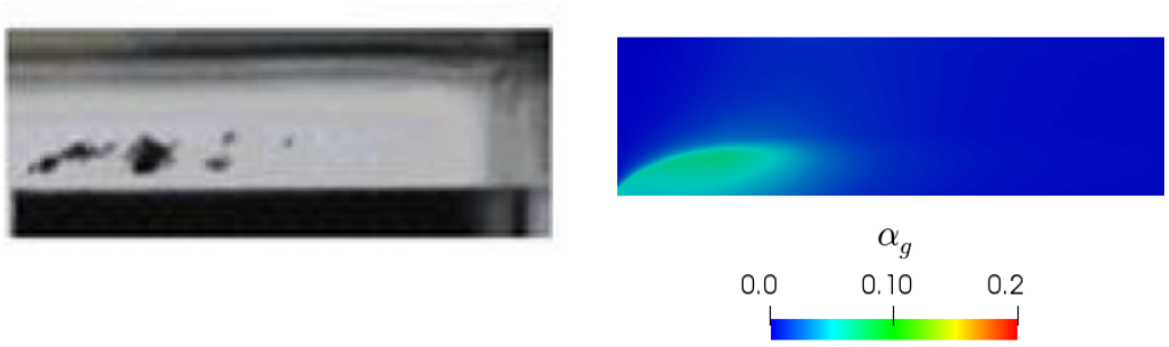

(c)

Figure 6.3: (a) Pressure field, (b) gas volume fraction (α_g) field, and (c) qualitative comparison of the experimental image [220] with the simulation result for the developing cavitation.

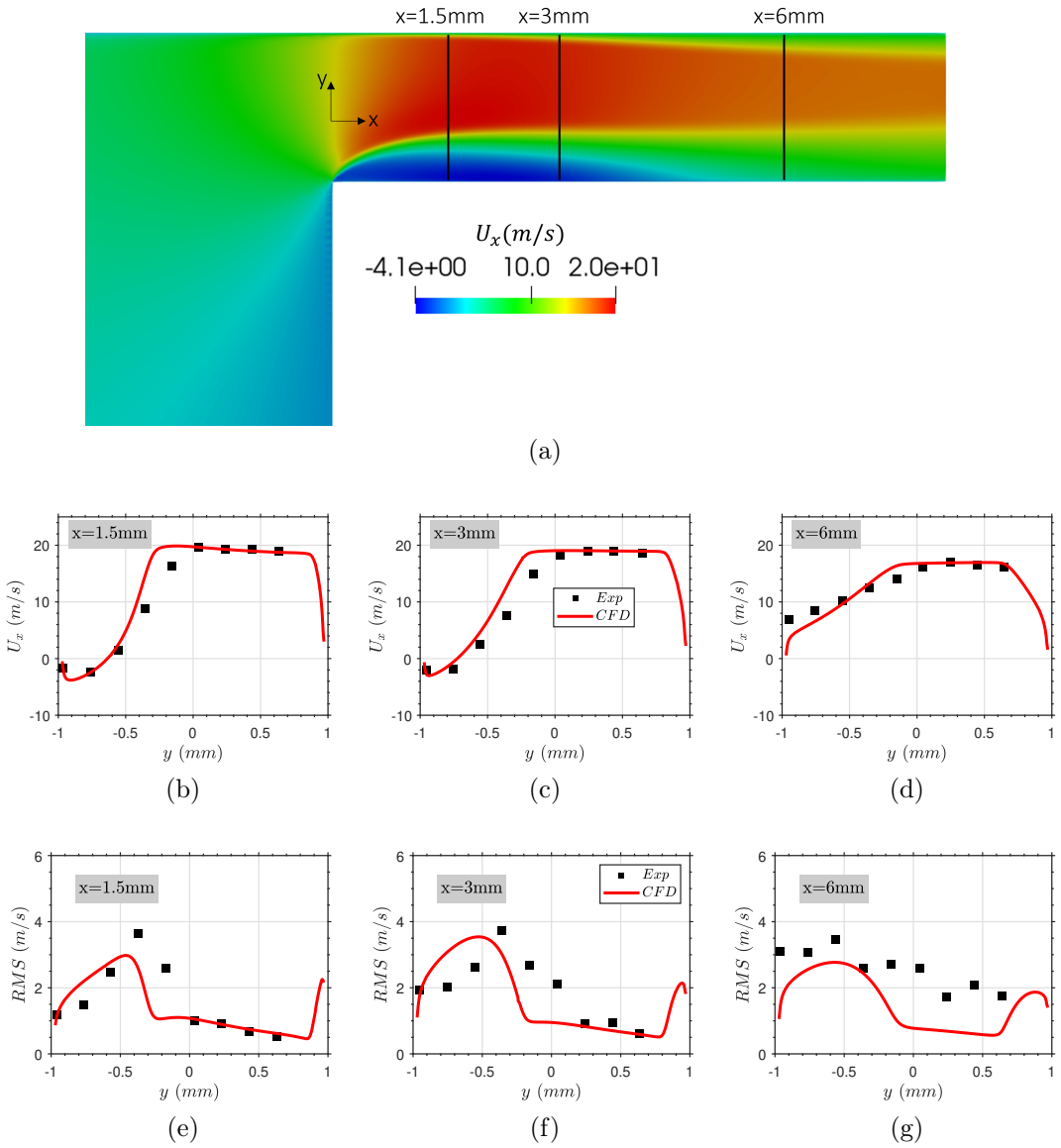

Figure 6.4: (a) Mean axial velocity (U_x) distribution showing the axial locations of the experimental probes, (b-d) Comparison of the numerical and experimental mean axial velocity profiles at different axial locations inside the nozzle, (e-g) Comparison of the numerical and experimental RMS of velocity fluctuations at different axial locations inside the nozzle.

6.1.3.2 Thermodynamic analysis

To further analyze the cavitation development under the considered condition, Fig. 6.5a shows the effect of the initial amount of dissolved nitrogen in the liquid phase on the saturation pressure (P_{sat}). Firstly, for pure water ($Y_{N_2} = 0$), the obtained results from the thermodynamic library using the CPA-EoS shows good agreement with the NIST database [75].

Besides, It can be seen that in the low temperature range, the (H_2O-N_2) mixture saturation pressure increases as the nitrogen concentration increases in the mixture. Such increase of the mixture saturation pressure tends to diminish at higher temperatures.

For the considered initial condition of the current case with ($Y_{N_2} = 1e-05$) and ($T = 300$), the saturation pressure is around 1.38 bar. Figure 6.5b shows the axial profile of the static pressure (P) and the gas volume fraction (α_g) near the bottom wall of the nozzle at ($y/R = -0.99$) (see the coordinate system in Fig. 6.4a). It can be seen the sudden increase of the (α_g) as the pressure drops below the mixture saturation pressure, where the pressure reaches its minimum value near the nozzle inlet corner ($x/L = 0$). As the axial distance further increase towards the nozzle exit, the pressure tends to increase towards the outlet pressure (1 bar) at the nozzle exit, which is also accompanied by a decrease of the (α_g).

This analysis also shows that (α_g) is still greater than zero near the nozzle exit, as shown in Fig. 6.5b, since the specified outlet pressure (1 bar) is lower than the mixture saturation pressure, (1.38 bar). These results again highlight the significant effects of the initial dissolved gas in the injected liquid on cavitation, as previously discussed in [25, 102, 253].

The obtained results here provides a first assessment and validation of the RFM model to capture the cavitation development. The next steps would involve an industrial configuration, to further assess and validate the model capability for cavitation simulation, as will be shown in the next section.

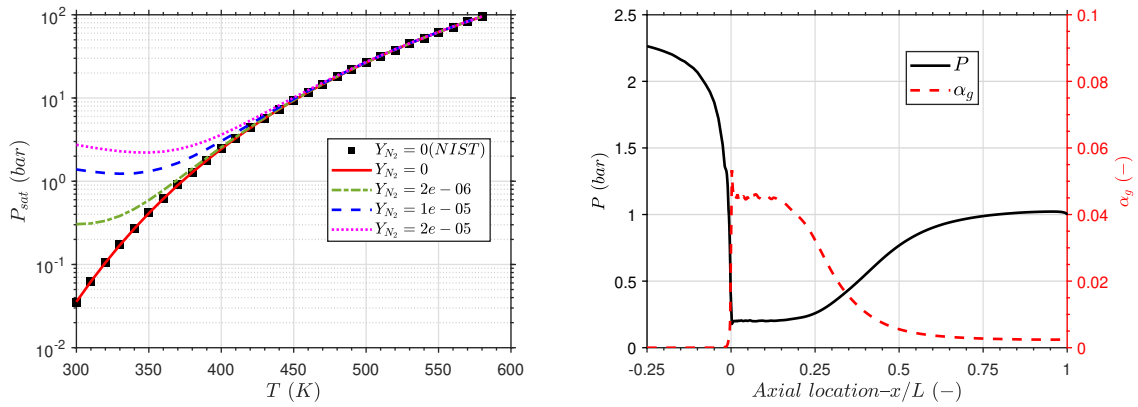

(a) (b)

Figure 6.5: (a) Variation of the saturation pressure (P_{sat}) with different (N_2) concentration in the feed for water. (b) Axial profiles of the pressure (P) and gas volume fraction (α_g) near the bottom wall of the nozzle ($y/R = -0.99$). Y_{N_2} denotes the nitrogen mass fraction.

6.2 Industrial injector using renewable fuel

6.2.1 Case description

The investigated test case in the current section is based on a heavy-duty diesel injector of Woodward L'Orange GmbH. The objective here was to investigate the cavitation formation inside the injector using ammonia as a promising renewable fuel. The examined injector geometry was based on a common rail 7-hole tip injector. The main dimensions of the injector are listed in Table. 6.2. The simulated geometry here considered only one seventh of the full injector geometry, as shown in Fig. 6.6. The needle valve was assumed to be still at its maximum lift of 480 μm. The operating conditions of the injector are summarized in Table. 6.3.

Geometrical characteristics	
Orifice diameter (μm)	319
Orifice length (mm)	1.26
Inlet orifice rounding (mm)	0.075
K-factor $(D_{in} - D_{out})/10$	0
Sac volume (mm^3)	1.15

Table 6.2: Main dimensions of the injector

P_{inj} (bar)	T_{inj} (K)	P_{out} (bar)
750	343	50

Table 6.3: Operating conditions of the simulated test case including the injection pressure (P_{inj}), injection temperature (T_{inj}), and outlet pressure (P_{out}).

6.2.2 Computational set-up and numerical methods

Computational set-up

The simulated geometry (only one seventh of the fully injector geometry) along with the grid structure at the center-plane are depicted in Fig. 6.6. The base mesh size is set to 100 μm, where various mesh embedding levels have been employed, resulting in three grids (see Table. 6.4) used for grid sensitivity analysis.

Grid no.	Minimum cell size (μm)	Number of cells (M)
1	12.5	$\sim$ 0.83
2	6.25	$\sim$ 1.15
3	3.125	$\sim$ 2.84

Table 6.4: Grid resolutions employed in the grid sensitivity study.

The employed boundary conditions are described in Fig. 6.6. A pressure and temperature boundary conditions of (750 bar, 343 K) are imposed at the injector inlet. A hemispherical volume is added to the orifice exit in order to avoid the interference of the outlet boundary on the cavitation development inside the orifice.

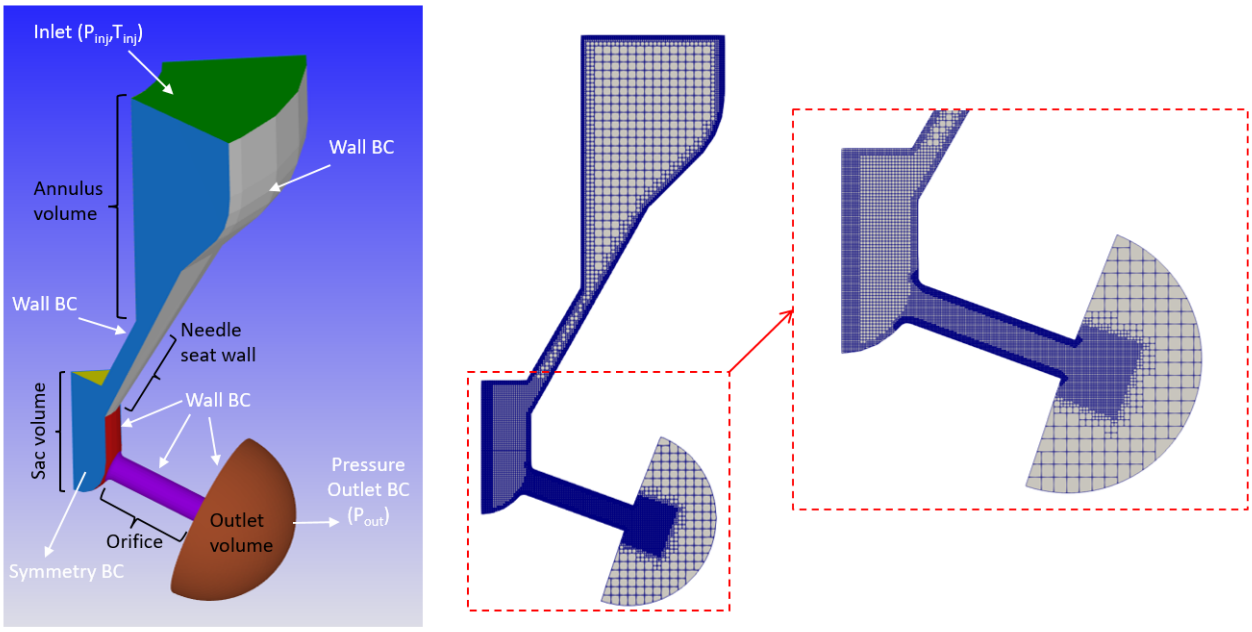

Figure 6.6: Simulated geometry (only one seventh of the fully injector geometry) along with the boundary conditions. The computational mesh is also shown at the domain central cut section. The insert shows the refined mesh within the injector orifice.

A pressure outlet boundary condition is set at outlet volume, which is relaxed from 750 bar to 50 bar in a time interval of 0.1 ms to facilitate the simulation start-up. For the wall boundaries, standard wall treatment has been used. The entire computational domain including the outlet hemispherical volume is initialized with pressure of 750 bar and temperature of 343 K. The initial phase state is single liquid phase ($\alpha_l = 1$), with an initial amount of dissolved nitrogen of ($Y_{N_2} = 2e-05$). The mass fraction of dissolved nitrogen in the feed is chosen to be smaller than the saturation value ($Y_{N_2} \approx 1e-04$) estimated from the VLE solver at ($T = 298$ K, $P = 10.3$ bar), assuming that the liquid ammonia is stored at these conditions, as reported in [66].

Numerical methods

URANS simulations are carried out using the RNG $k-\epsilon$ turbulence model [251] with the default model constants. Simulations are carried out using CONVERGE V3.1.6 employing the updated real fluid PISO algorithm (see Sec. 2.1.5.1). The spatial discretization is second-order accurate using a central difference scheme. The time integration is achieved by a second-order Crank-Nicolson scheme for the momentum equation and a first-order implicit Euler scheme for the rest of the equations. The time step is around 0.6-0.7 ns and adjusted automatically based on a maximum CFL number of 0.5. The computational cost of the simulation using Grid-2 (1.1 M cells) is 48 h of wall clock time for a simulation time of 0.3 ms using 144 cores of the latest generation Intel Skylake G-6140 processors running at 2.3 GHz (ENER440 IFPEN Supercomputer).

The RFM model thermodynamic closure for the (Ammonia/nitrogen) binary mixture is based on the VTPR-EoS with a uniform thermodynamic table resolution in ($T, log_{10}P, Y_{NH_3}$) axes of (201×201×21) points covering ranges of (200-600 K, 0.001-760 bar, 0.9999-1).

6.2.3 Results and discussion

6.2.3.1 Thermodynamic analysis

Cavitation takes place as the pressure drops to or below the saturation pressure. Accordingly, the saturation pressure is an essential index to indicate the cavitation inception. Figure 6.7 illustrates the variation of the saturation pressure with temperature for ammonia (NH_3) at different (N_2) concentrations. First, the comparison of the pure ammonia saturation pressure ($Y_{N_2} = 0$) with the NIST reference data [75] shows a good agreement for the considered temperature range.

Besides, the saturation pressure of the mixture system is very close to that of pure ammonia as the nitrogen mass fraction (Y_{N_2}) is less than 2e-03. Then, more obvious deviation can be observed as (Y_{N_2}) increases to 2e-03. The observed increase of the mixture saturation pressure is more significant at the low temperature range, which tends to diminish at higher temperatures.

It is also interesting to compare the saturation pressure of ammonia to hydrocarbons such as n-dodecane ($C_{12}H_{26}$), which is often used as diesel surrogate in numerical simulations. For instance, at $T = 343\,K$ (fuel temperature), the saturation pressure of pure ammonia is 33 bar, whereas that of n-dodecane is 0.004 bar. This comparison shows that ammonia exhibits a saturation pressure which is several orders of magnitude higher than n-dodecane. Such observations motivates the current study to investigate the cavitation development using ammonia as will be further discussed.

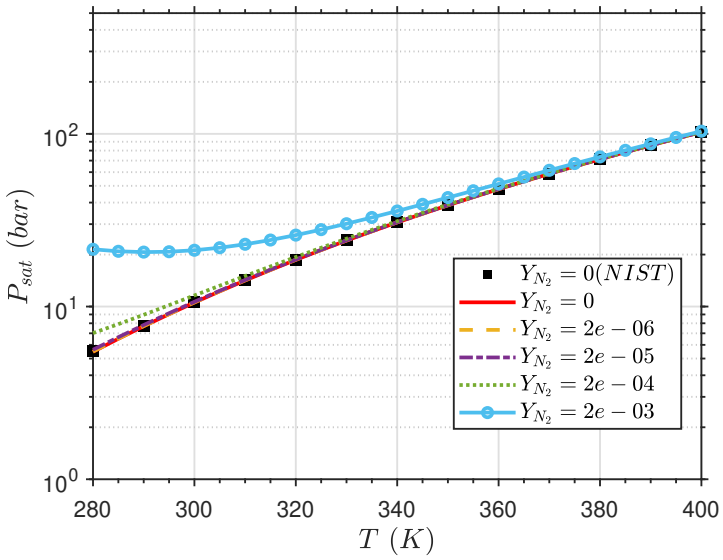

Figure 6.7: Variation of the saturation pressure (P_{sat}) with different (N_2) concentration in the feed for ammonia. Y_{N_2} denotes the nitrogen mass fraction.

6.2.3.2 Numerical results

First, to study the effect of the mesh size on the simulation predictions, Fig. 6.8 shows the variation of the velocity coefficient (C_v) as function of time for the different grid resolutions. The velocity coefficient is defined as ($C_v = u_{eff}/u_{th}$), where (u_{eff}) is the effective velocity at the orifice exit and ($u_{th} = \sqrt{2\Delta P/\rho_l}$) is the theoretical velocity at the orifice exit, computed based on the difference between the injection and outlet pressures (ΔP) and the liquid (fuel) density (ρ_l) at the injection pressure and temperature.

A slight variation of the (C_v) can be observed between Grid 2 and Grid 3, showing that grid convergence is fairly achieved. Accordingly, Grid 2 with a minimum mesh resolution of 6.25 μm inside the injector orifice is used for further calculations and the associated results will be further discussed.

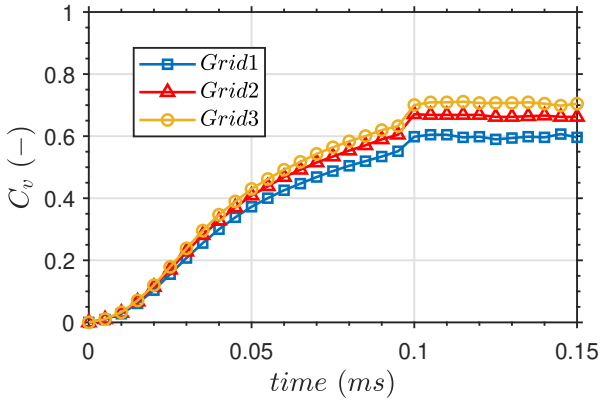

Figure 6.8: Temporal evolution of the of the velocity coefficient (C_v) for the different grid resolutions.

Figure 6.9 illustrates the temporal evolution of the gas volume fraction (α_g) at the injector mid-plane. It can be seen that the cavitation incepts ($t = 0.075$ ms) near the upper side of the orifice inlet. The generated cavitation zone further increases with time and extends to fill a bigger region near the upper wall of the orifice. Besides, at ($t = 0.095$ ms), a cavity can be observed near the central region of the orifice, which is further transported to the orifice exit as time elapsed. At the time greater than ($t = 0.155$ ms), the cavitation pockets show very little variation, indicating that the in-nozzle flow has reached a quasi-steady state conditions.

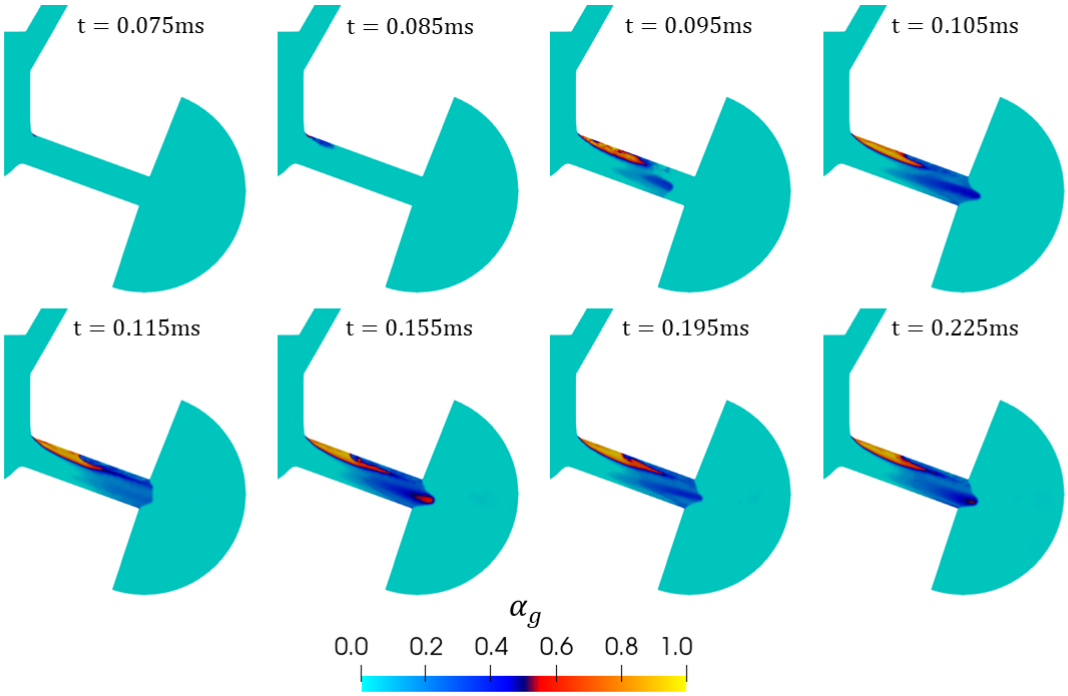

Figure 6.9: Temporal evolution of the of the gas volume fraction (α_g) at the mid-plane of the injector.

To further visualize the cavitation formation within the injector orifice, Fig. 6.10 shows the gas volume fraction and velocity magnitude distributions at different slices along the orifice cross-section at ($t = 0.2\,\text{ms}$), where the flow has reached a quasi-steady state condition. It can be seen the cavitation regions that are formed mainly near the upper wall of the orifice. These regions also correspond to locations, where the velocity is reduced compared to that at the orifice center (see Fig. 6.10 right). Indeed, as the flow arrives to the orifice inlet, it could not accommodate for the abrupt change in direction, leading to flow separation and creating a low pressure region, where cavitation starts to develop. In addition, it can be also observed that cavitation regions are also developed near the center of the orifice (see Fig. 6.10 left). The reason for these cavitation regions will be specified later in the discussion.

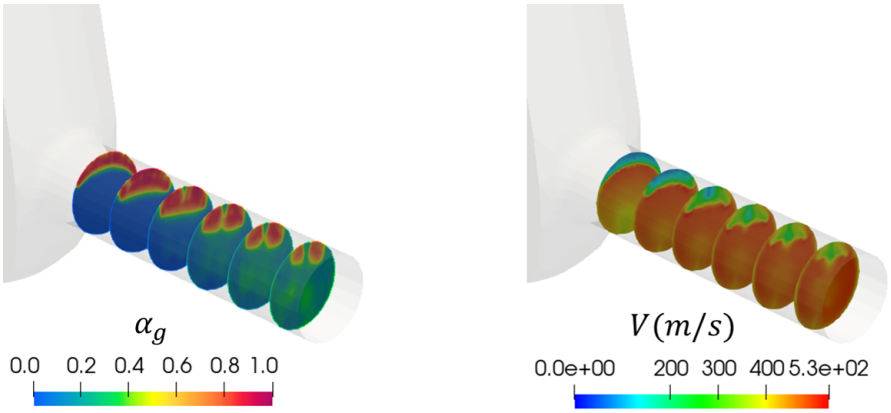

Figure 6.10: Distributions of the gas volume fraction (left) and velocity magnitude (right) at different slices along the orifice cross-section at $t = 0.2\,\text{ms}$.

It is also of interest to quantify the contribution of both the fuel (NH_3) and dissolved non-condensable gas (N_2) to the formed gaseous phase. The employed VLE based model can provide valuable information regarding the phase change process and the composition of each species in each phase. Indeed, Fig. 6.11 illustrates the temporal variation of gas cavities with the iso-surface (α_g=0.9) colored by the volume fraction of nitrogen in the gas phase (α_{g,N_2}) and the pressure. The (α_{g,N_2}) is defined as ($\alpha_{g,N_2} = y_{N2}\,\alpha_g$), where ($y_{N2}$) is the mole fraction of nitrogen in the gas phase.

The results show that contribution of the dissolved N_2 to the cavitation pockets is very small (see the palette of Fig. 6.11a). Based on the constraint ($y_{N2} + y_{NH_3} = 1$), it can be concluded that the cavitation pockets are mainly dominated by the ammonia vapor. In other words, vaporous cavitation is the dominant phase transition process compared to gaseous cavitation. This could be attributed to the relatively high saturation pressure (33 bar) of ammonia, which facilitates the formation of the vaporous cavitation. Indeed, the pressure distribution (Fig. 6.11b) shows that the pressure at the gas cavities is much lower than the saturation pressure, leading to high contribution of ammonia vapor to the gas phase compared to that of nitrogen.

Such behavior of ammonia is different from that reported in previous cavitation studies [25, 97, 253, 95] of hydrocarbon fuels, where gaseous cavitation was found to have a significant contribution to the formed gas cavities.

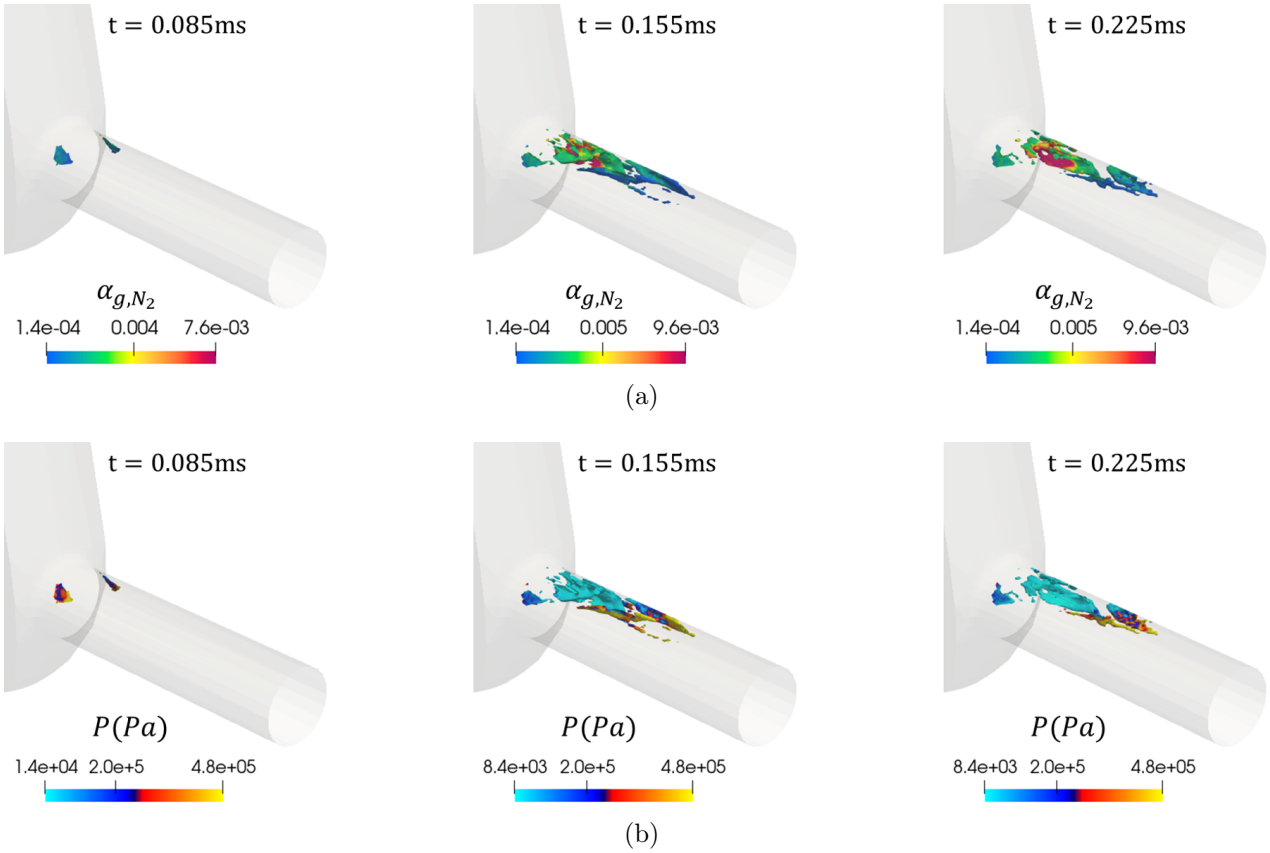

Figure 6.11: Temporal evolution of the iso-surface (α_g=0.9) colored by (a) the volume fraction of nitrogen in the gas-phase (α_{g,N_2}) and (b) the pressure (P).

For further analysis of the cavitation development inside the orifice, the pressure and gas volume fraction variation along the orifice length at both the top wall ($r/R = 0.99$) and center ($r/R = 0$) are depicted in Fig. 6.12. On the one hand, it can be observed that the pressure exhibits a sharp decrease at the top wall slightly after the orifice inlet. As the pressure drops below the saturation pressure (dotted line in Fig. 6.12a), cavitation starts to form as shown by the increase of the (α_g) in Fig. 6.12b.

On the other hand, at the center of the orifice, a smother pressure drop takes place. Indeed, the pressure decreases below the saturation pressure at a longer distance inside the orifice compared to the top wall. Such pressure drop below the saturation value at the orifice center explains the formed gaseous regions that have been observed near the orifice center (see Fig. 6.12c). However, the amount of gas generated at the orifice center is much lower compared to that at the top wall near the orifice inlet, as depicted by the gas volume fraction variation in Fig. 6.12b. Finally, the contribution of ammonia and nitrogen to the total gas volume fraction depicted in Fig. 6.13, shows that the main source of void is the ammonia vapor with a very small contribution of the dissolved N_2 (less than 1%).

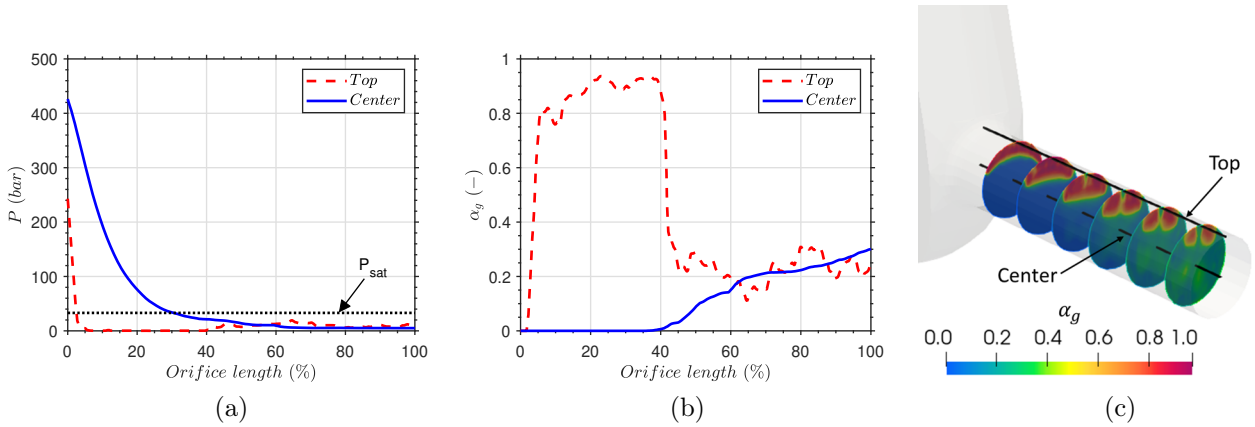

Figure 6.12: Variation of (a) the pressure (P) and (b) the total gas volume fraction (α_g) along the orifice length for the locations shown in (c) at $t = 0.2$ ms. The (P_{sat}) denotes the saturation pressure.

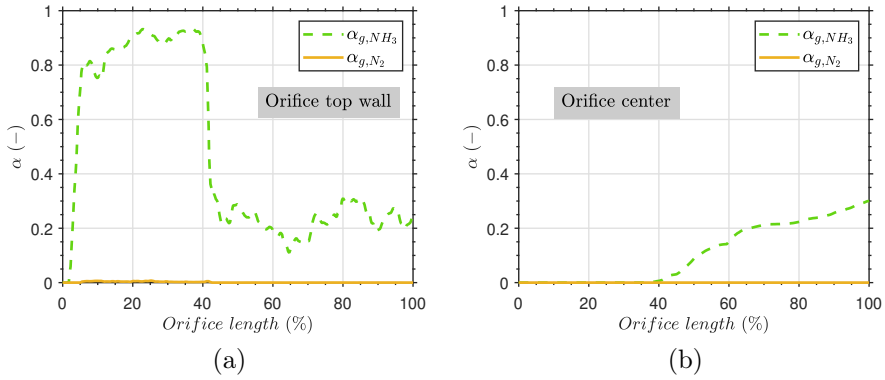

Figure 6.13: Variation of the volume fraction of ammonia (α_{g,NH_3}) and nitrogen (α_{g,N_2}) in the gas phase along the orifice length at the orifice (a) top wall and (b) center.

6.3 Conclusions

In this chapter, the proposed RFM model is employed to investigate the cavitation phenomenon in different configurations. Indeed, the goal here is to assess and validate the RFM model capability for cavitation simulation. In the first test case, the cavitation phenomenon is simulated in a transparent injector configuration, where the model results are compared against available experimental data of Sou et al. [220]. Then, the second test case involved an industrial configuration of a heavy-duty injector, where the cavitation formation is investigated using ammonia as a fuel.

The main conclusions obtained from the two studied configurations can be summarized as follows:

Transparent injector configuration:

- The obtained numerical results have confirmed that the model can tackle the phase transition phenomenon under the considered conditions and fairly reproduce the developing cavitation inside the orifice.
- A quantitative comparison of the obtained results with the experimental data of the mean axial velocity have shown a good agreement. However, the comparison of root mean square (RMS) of velocity fluctuations have shown some deviation from the experimental data especially at the axial location ($x = 6\,\text{mm}$). Future work should consider LES turbulence modeling and an extended configuration to avoid the prescribed outlet pressure boundary condition at the nozzle exit.
- Overall the simulated test case has provided a first validation of the RFM model for cavitation simulation, so that it can be further assessed under more complex configurations.

Industrial injector configuration:

- The obtained numerical results have shown that the model is able to dynamically predict the phase transition process under the considered industrial injector configuration.
- The formed cavitation pockets inside the injector orifice are revealed to be mainly composed of ammonia vapor, with a slight contribution of the dissolved non-condensable nitrogen. In other word, vaporous cavitation was found to be the dominant phase transition process over gaseous cavitation when ammonia is used as fuel with initial amount of dissolved nitrogen ($Y_{N_2} = 2e-05$). Such behavior could be attributed to the relatively high saturation pressure of ammonia. Indeed, P_{sat}=33 bar at T=343 K for instance.
- The formation of gaseous cavities is found to take place not only near the upper wall of the orifice, but also near the orifice center, as the pressure deceases below the saturation pressure. However, the amount of gas generated at the orifice center is much lower compared to that at the top wall near the orifice inlet.

Finally, the employed thermodynamic table based on $log_{10}P$ has also shown its effectiveness to provide adequate table resolution for the pressure axis, which is required for cavitation simulations, as the phase change is mainly driven by the pressure variation.

Chapter 7

Conclusions and Future work

Contents

7.1 Summary and Conclusions

In this thesis, the main objective was to develop a predictive and efficient CFD model for multi-component two-phase flow simulations in the context of diesel and dual-fuel engines under different thermodynamic (sub- and super-critical) regimes, allowing an automatic/ smooth transition between these regimes that can coexist during the fuel injection and mixing events.

To this goal, the current work proposes a fully compressible multi-component two-phase real-fluid model (RFM) with a diffused interface and closed by a thermodynamic equilibrium tabulation method based on various real-fluid equations of state (EoSs). The proposed real-fluid thermodynamic tabulation approach has been extended to handle ternary systems in addition to binary systems. The thermodynamic table is generated using the IFPEN Carnot thermodynamic library, which performs the vapor-liquid equilibrium (VLE) calculation using a robust isothermal–isobaric (TPn) flash coupled to various real-fluid EoSs. Besides, to address high-pressure fuel injection, a real fluid atomization model is proposed, in which the RFM model is coupled to a subgrid-scale (SGS) model, employing a surface density approach to model fuel atomization within the LES framework. Finally, the in-nozzle cavitation modeling is also investigated in different configurations using the proposed RFM model.

The conclusions for each chapter of this thesis are summarized as follows:

In **Chapter 1**, the background and motivation of the current work is first discussed. Then, a bibliographic study and discussions are carried out on the different topics tackled in the current thesis, including fuel injection regimes and modeling approaches, two-phase flow modeling, and cavitation in fuel injectors.

In **Chapter 2**, the governing equations of the proposed RFM model are introduced along with the employed assumptions. The different turbulence modeling approaches were

also discussed, followed by derivation of the filtered transport equations within the LES framework along with the employed subgrid-scale (SGS) models. Then, the tabulated thermodynamic closure is discussed and the coupling between the flow solver the thermodynamic table has been detailed. Finally, the pressure-Poisson equation is derived using the ideal-gas assumption, followed by the derivation of the updated pressure equation for the real-fluid framework.

In **Chapter 3**, the different types of equation of states (EoSs) are first discussed. The theoretical formulations of the PR and CPA EoS employed in the current work are then described. Next, the vapor-liquid equilibrium calculation based on the isothermal-isobaric (TPn) flash is discussed. Then, the methodology of the evaluation of the single and two-phase real-fluid thermodynamic and transport properties is detailed. An overview of the thermodynamic tabulation is subsequently discussed and the adopted tabulation approach for binary and ternary mixtures is detailed. The tabulation procedure using the in-house Carnot thermodynamic library is then described. Finally, this chapter closes with an evaluation of the VLE solver based on the IFPEN Carnot thermodynamic library. The thermodynamic library assessment is carried out by validating the VLE computations with available experimental data for different binary mixtures. In addition, the properties computation for some species of interest in this manuscript are validated against the NIST database. Finally, the variation of the properties of binary and ternary mixtures is illustrated and discussed.

In **Chapter 4**, the proposed model is applied to investigate fuel droplet evaporation in a dual-fuel configuration using highly resolved simulations. Indeed, the goal here is to better understand the phase change and mixing of a single n-dodecane droplet in a bi-component environment composed of nitrogen and methanol at high pressure and temperature, mimicking a DFICE configuration. The study first starts with the model validation against the experimental data of Crua et al. [53], for n-dodecane droplet evaporation in pure nitrogen. Then, the model is further applied to the dual-fuel configuration to investigate the effect of methanol ambient concentration on the phase change and mixing processes. The main conclusions drawn from this chapter include:

- A qualitative comparison of the numerical results with the experiments [53] has shown that the RFM model can capture well the evolution of the n-dodecane droplet evaporation throughout its lifetime under the considered transcritical conditions.

- For the considered ambient temperatures and pressures, the n-dodecane droplet lifetime decreases monotonically with increasing the methanol ambient concentration. However, such decrease in the droplet lifetime is relatively low with methanol ambient mass fraction less than 0.2. The thermodynamic analysis shows that the droplet follows a different thermodynamic path based on the methanol ambient concentration

- The methanol and nitrogen exhibit different behavior in terms of solubility in the liquid phase, which demonstrates that these two compounds should not be lumped in a single surrogate.

- The RFM model closed by a tabulated EoS shows great potential for the computation of two-phase binary and ternary mixtures problems, often encountered in

industry, avoiding the direct evaluation of costly phase equilibrium solver during the simulation run-time [254, 253].

In **Chapter 5**, a real-fluid atomization model is proposed for high-pressure fuel injection and atomization modeling. More specific, the RFM model is coupled to a subgrid-scale (SGS) model using a surface density approach for fuel atomization modeling within the LES framework. The Engine Combustion Network (ECN) Spray A injector non-evaporating and nominal evaporating conditions are used as a reference for the proposed model validation. In addition, a parametric variation of the ECN Spray A is carried out for further assessment and validation of the model under various operating conditions. Finally, this chapter closes with an investigation of the ECN Spray A evaporating baseline condition in a dual-fuel configuration. The main conclusions drawn from this chapter include:

- Under the so-called "non-evaporating ECN Spray A condition", the comparison of the LES-RFM results with the different experimental data in the near-nozzle field, including projected mass density, transverse integrated mass, and liquid volume fraction, has shown a good agreement, which indicates that the RFM model can accurately capture the fuel dispersion under the considered conditions. Besides, the comparison of (RFM-Σ) model results against the experimental projected surface area density along the spray centerline and the SMD radial profiles has shown a satisfactory agreement. Overall, it can be concluded that the proposed RFM-Σ model can accurately predict the fuel dispersion and atomization under the considered conditions.

- Under the evaporating ECN Spray A condition, global spray metrics such as spray liquid and vapor penetrations are well captured by the RFM model compared to the experimental data. Moreover, local analysis shows that the mixture fraction radial distribution favorably agrees with the experimental data within its confidence level.

- The analysis of the of the surface density and SMD results under both the evaporating and non-evaporating conditions has demonstrated the sensitivity of the surface area density model to the vaporization effects. In the dense region of the spray, vaporization tends to enhance the surface area density production, whereas vaporization decreases the surface area density in the dilute spray region. Besides, the mean SMD relatively decreases in the dilute region under the evaporating condition

- The parametric variation of the ECN Spray A, has shown the capability of the RFM model to well predict the variation of the spray penetration compared to the experimental data under various operating conditions, demonstrating a high predictive performance of the model.

- An investigation of the ECN Spray A baseline condition in a dual-fuel (DF) configuration using methanol as a primary fuel has been carried out. Under the considered dual-fuel configuration, the ambient methanol effect on the overall spray evaporation and mixing processes seems to be insignificant (only a small variation of the spray penetrations and n-dodecane mass fraction distribution). However, a remarkable impact on the flame lift-off length, ignition delay time, and pollutant emissions is to be expected as reported in [248].

In **Chapter 6**, the RFM model is employed to assess and validate its capability for cavitation simulation using different configurations. The first configuration involved an academic transparent injector configuration, where the model results are compared against available experimental data of Sou et al. [220]. Then, the second configuration involved an industrial heavy-duty injector, where the cavitation formation is investigated using ammonia as a fuel. The main conclusions drawn from this chapter include:

Transparent injector configuration:

- The obtained numerical results have confirmed that the model can tackle the phase transition phenomenon under the considered conditions and fairly reproduce the developing cavitation inside the orifice. Besides, a quantitative comparison of the obtained results with the experimental data of the mean axial velocity have shown a good agreement. However, the comparison of root mean square (RMS) of velocity fluctuations have shown some deviation from the experimental data. Future work should consider LES turbulence modeling and an extended configuration to avoid the prescribed outlet pressure boundary condition at the nozzle exit.

- Overall the simulated test case has provided a first validation of the RFM model for cavitation simulation, so that it can be further assessed under more complex configurations.

Industrial injector configuration:

- The obtained numerical results have shown that the model is able to dynamically predict the phase transition process under the considered industrial injector configuration while ammonia is used as a fuel.

- The formed cavitation pockets inside the injector orifice are revealed to be mainly composed of ammonia vapor, with a slight contribution of the dissolved non-condensable nitrogen. In other word, vaporous cavitation was found to be the dominant phase transition process over gaseous cavitation when ammonia is used as fuel. Such behavior could be attributed to the relatively high saturation pressure of ammonia. Indeed, P_{sat}=33 bar at T=343 K for instance.

- The formation of gaseous cavities is found to take place not only near the upper wall of the orifice, but also near the orifice center, as the pressure deceases below the saturation pressure. However, the amount of gas generated at the orifice center is much lower compared to that at the top wall near the orifice inlet.

Finally, the employed thermodynamic table based on $log_{10}P$ has also shown its effectiveness to provide adequate table resolution for the pressure axis, which is required for cavitation simulations, as the phase change is mainly driven by the pressure variation.

7.2 Future work

The suggested future work can be summarized as follows:

- The potential of the proposed tabulation approach for ternary systems has been shown for the simulation of different configurations in the current thesis. Indeed, the capability of the model to deal with ternary systems is sufficient to study several industrial configurations. For instance, the proposed model has been recently used in another study to investigate the effect of impurities on the condensation of carbon-dioxide in compressors. Albeit, the table size can sometimes be a cumbersome. Accordingly, alternative approaches should be explored in the future work. A first possible alternative involves using Artificial Neural Network (ANN) as a regression model [136] for the thermodynamic and transport properties to replace the thermodynamic table. Another alternative is to employ an accelerated TPn-flash algorithm [189] with the help of ANN, that could be directly implemented in the CFD code. These approaches could allow the multi-species (more than three) real-fluid simulation feasible and also allow the RFM model extension to deal with the combustion phenomenon, for instance.

- Coupling of the external spray with the internal injector flow, and investigation of in-nozzle cavitation and turbulence development effects on the fuel dispersion and atomization. Also, including the needle motion is indeed essential for more realistic fuel injection simulations.

- To deal with the fuel injection and atomization at conditions with significant slip velocity between the phases, the current formulation of the RFM-Σ model should be improved by adding a transition to the Lagrangian approach [34, 139] once the spray is diluted or accounting for the liquid diffusion due to the slip velocity [169].

- To deal with finite rate phase change processes such as flash boiling, the current formulation of the RFM model based on the local thermodynamic equilibrium assumption should be modified to allow modeling of such phenomena.

- Improving the calculation of the mixture specific heats and sound speed in the VLE region as reported in [236], instead of the linear blending used for the specific heats and the Wood formula used for the sound speed. Besides, an additional alternative would be to compute specific heats by numerical differentiation of the tabulated data of the internal energy and enthalpy. The sound speed can be then computed as $C_s^2 = \gamma \left(\frac{\partial p}{\partial \rho}\right)_{T,X}$, where ($\gamma = C_p/C_v$) and $\left(\frac{\partial p}{\partial \rho}\right)_{T,X}$ can be computed also by numerical differentiation of the tabulated data.

- Investigation of the additional SGS models for the real-fluid EoS within the LES framework, which could have crucial effects as recently reported in [237].

Appendix A

Results of ECN Spray A using CONVERGE V3.1

In this section, the ECN Spray A evaporating condition is recomputed with CONVERGE V3.1.6, employing the modified real-fluid PISO algorithm with the new pressure-Poisson equation (see Sec. 2.1.5.1). The goal here is to assess the accuracy and robustness of the new algorithm in V3.1 compared to its original counterpart in V3.0 using the same numerical setup (see Sec. 5.3.2).

Firstly, the comparison of the computational cost is shown in Table. A.1. The new algorithm in V3.1 is computationally less expensive with a factor of 1.2. This is mainly attributed to the faster convergence (less PISO loops per time step) achieved in V3.1 compared to V3.0.

CONVEGRE Code	Time (Hours)
V3.0.15	$\sim 9 \times 24$
V3.1.6	$\sim 7.5 \times 24$

Table A.1: Comparison of the computational time of the ECN Spray A evaporating condition using CONVERGE V3.0.15 and CONVERGE V3.1.6 with the same CPUs (1024 cores) for Grid 2 (16 M cells) and simulation time of 1 ms.

Furthermore, the accuracy of new algorithm in V3.1 is assessed by comparing the obtained results against the experimental data. Indeed, the comparison of the predicted jet liquid and vapor penetrations with the experimental data is depicted in Fig. A.1. The previously obtained results with V3.0 are also shown. It can be seen that the V3.1 results are in good agreement with the experimental data for both liquid and vapor penetrations.

In addition, the radial distribution of n-dodecane mass fraction is compared between the simulation and the experimental data as depicted in Fig. A.2. The presented numerical result is obtained by time-averaging the LES results in the time interval between 0.4 and 1 ms after the start of injection (during the quasi-steady period). The simulation result with V3.1 again agrees reasonably well with the experimental data within its confidence level.

In summary, the obtained good agreement between the V3.1 results and the experimental data confirms the accuracy of the new real-fluid PISO algorithm. In addition, the robustness of the algorithm is confirmed with less computational cost (see Table. A.1) compared to its original counterpart in V3.0.

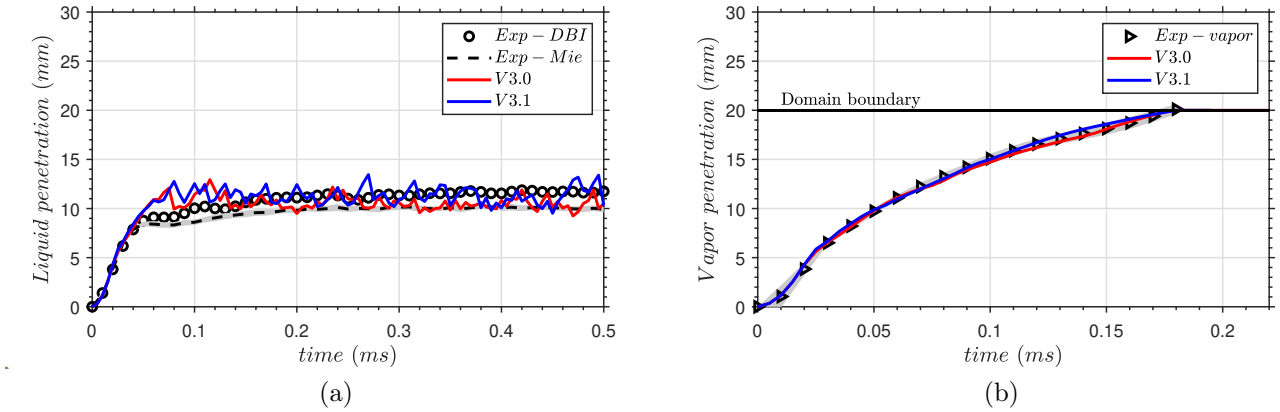

Figure A.1: Evaporating Spray A condition: Comparison of LES results with CONVERGE V3.0 and V3.1 against the experimental data for (a) liquid and (b) vapor penetration lengths. The experimental data corresponds to liquid penetration obtained from diffused back illumination (DBI) [145, 3] and Mie-Scattering [22, 6] techniques and vapor penetration obtained from Schlieren imaging [22, 6]. The shaded grey area represents the uncertainty in the experimental measurements.

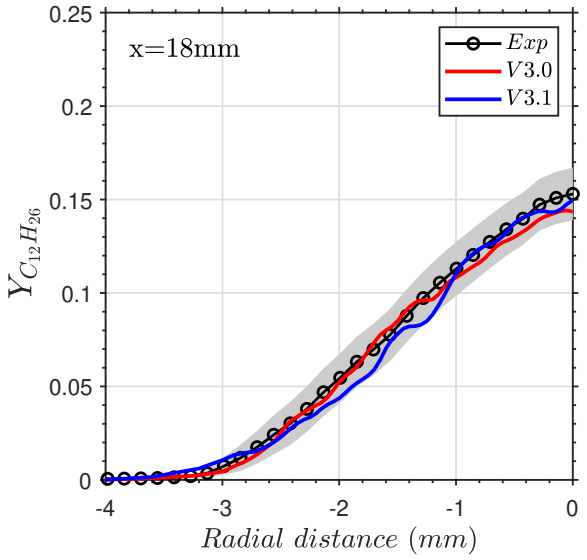

Figure A.2: Evaporating Spray A condition: Comparison of LES results with CONVERGE V3.0 and V3.1 and experimental data [178, 4] of n-dodecane mass fraction radial distribution at an axial distance of 18 mm from the nozzle exit. The shaded grey area represents 95% confidence interval in the experimental measurements.

Appendix B

Resumé étendu en français

Dans cette thèse, l'objectif principal était de développer un modèle CFD prédictif et efficace pour les simulations d'écoulements diphasiques multi-composants dans le contexte de moteurs diesel et bi-carburant sous différents régimes thermodynamiques (sous- et super-critiques), permettant une transition automatique/en douceur entre ces régimes qui peuvent coexister pendant les événements d'injection et de mélange de carburant.

Dans ce but, les travaux en cours proposent un modèle de fluide réel (RFM) biphasique multi-composants entièrement compressible avec une interface diffusée et fermé par une méthode de tabulation d'équilibre thermodynamique basée sur diverses équations d'état de fluide réel (EoSs). L'approche de tabulation thermodynamique des fluides réels proposée a été étendue pour gérer les systèmes ternaires en plus des systèmes binaires. La table thermodynamique est générée à l'aide de la bibliothèque thermodynamique IFPEN Carnot, qui effectue le calcul de l'équilibre vapeur-liquide (VLE) à l'aide d'un flash robuste isotherme-isobare (TPn) couplé à divers EoS fluides réels. En outre, pour traiter l'injection de carburant à haute pression, un modèle d'atomisation de fluide réel est proposé, dans lequel le modèle RFM est couplé à un modèle de sous-maille (SGS), utilisant une approche de densité de surface pour modéliser l'atomisation du carburant dans le cadre LES. Enfin, la modélisation de la cavitation à l'aide du modèle RFM est étudiée dans deux configurations différentes, dont un injecteur transparent utilisant de l'eau et un injecteur industriel utilisant de l'ammoniac.

Les conclusions de chaque chapitre de cette thèse sont résumées comme suit :

Dans le **Chapitre 1**, le contexte et la motivation du travail actuel sont d'abord discutés. Ensuite, une étude bibliographique et des discussions sont menées sur les différents sujets abordés dans la thèse actuelle, notamment les régimes d'injection de carburant et les approches de modélisation, la modélisation des écoulements diphasiques et la cavitation dans les injecteurs de carburant.

Dans le **Chapitre 2**, les équations gouvernantes du modèle RFM proposé sont introduites avec les hypothèses utilisées. Les différentes approches de modélisation de la turbulence ont également été discutées, suivies de la dérivation des équations de transport filtrées dans le cadre LES avec les modèles à l'échelle de sous-maille (SGS) utilisés. Ensuite, la fermeture thermodynamique tabulée est discutée et le couplage entre le solveur de flux et la table thermodynamique a été détaillé. Enfin, l'équation pression-Poisson est dérivée en utilisant l'hypothèse du gaz parfait, suivie de la dérivation de l'équation de

pression mise à jour pour le cadre du fluide réel.

Dans le **Chapitre 3**, les différents types d'équations d'états (EoS) sont d'abord abordés. Les formulations théoriques des PR et CPA EoS employés dans les travaux actuels sont ensuite décrits. Ensuite, le calcul de l'équilibre vapeur-liquide basé sur le flash isotherme-isobare (TPn) est discuté. Ensuite, la méthodologie de l'évaluation des propriétés thermodynamiques et de transport des fluides réels mono et biphasiques est détaillée. Un aperçu de la tabulation thermodynamique est ensuite discuté et l'approche de tabulation adoptée pour les mélanges binaires et ternaires est détaillée. La procédure de tabulation utilisant la bibliothèque thermodynamique interne Carnot est ensuite décrite. Enfin, ce chapitre se termine par une évaluation du solveur VLE basé sur l'IFPEN Bibliothèque thermodynamique Carnot. L'évaluation de la bibliothèque thermodynamique est réalisée en validant les calculs VLE avec les données expérimentales disponibles pour différents mélanges binaires. De plus, le calcul des propriétés de certaines espèces d'intérêt dans ce manuscrit est validé par rapport à la base de données du NIST. Enfin, la variation des propriétés des mélanges binaires et ternaires est illustrée et discutée.

Dans le **Chapitre 4**, le modèle proposé est appliqué pour étudier l'évaporation des gouttelettes de carburant dans une configuration à double carburant à l'aide de simulations hautement résolues. En effet, le but ici est de mieux comprendre le changement de phase et le mélange d'une seule gouttelette de n-dodécane dans un environnement bi-composant composé d'azote et de méthanol à haute pression et température, imitant une configuration DFICE. L'étude commence d'abord par la validation du modèle par rapport aux données expérimentales de Crua et al. [53], pour l'évaporation de gouttelettes de n-dodécane dans l'azote pur. Ensuite, le modèle est ensuite appliqué à la configuration bi-carburant pour étudier l'effet de la concentration ambiante de méthanol sur le changement de phase et le mélange. processus. Les principales conclusions tirées de ce chapitre incluent :

- Une comparaison qualitative des résultats numériques avec les expériences [53] a montré que le modèle RFM peut bien capturer l'évolution de l'évaporation des gouttelettes de n-dodécane tout au long de leur durée de vie dans les conditions transcritiques considérées.
- Pour les températures et pressions ambiantes considérées, la durée de vie des gouttelettes de n-dodécane diminue de manière monotone avec l'augmentation de la concentration ambiante de méthanol. Cependant, une telle diminution de la durée de vie des gouttelettes est relativement faible avec une fraction massique ambiante de méthanol inférieure à 0.2. L'analyse thermodynamique montre que la goutte suit un chemin thermodynamique différent en fonction de la concentration ambiante de méthanol.
- Le méthanol et l'azote présentent des comportements différents en termes de solubilité dans la phase liquide, ce qui démontre que ces deux composés ne doivent pas être regroupés dans un seul substitut.
- Le modèle RFM fermé par un EoS tabulé montre un grand potentiel pour le calcul des problèmes de mélanges binaires et ternaires diphasiques, souvent rencontrés dans l'industrie, évitant l'évaluation directe du coûteux solveur d'équilibre de phase pendant le temps d'exécution de la simulation [254, 253].

Dans le **Chapitre 5**, un modèle d'atomisation de fluide réel est proposé pour l'injection de carburant à haute pression et la modélisation de l'atomisation. Plus précisément, le modèle RFM est couplé à une échelle de sous-maille (SGS) utilisant une approche de densité de surface pour la modélisation de l'atomisation du carburant dans le cadre LES. Les conditions de non-évaporation et d'évaporation nominale de l'injecteur du réseau de combustion du moteur (ECN) Spray A sont utilisées comme référence pour la validation du modèle proposé. De plus, une variation paramétrique de l'ECN Spray A est effectuée pour une évaluation et une validation plus poussées du modèle dans diverses conditions de fonctionnement. Enfin, ce chapitre se termine par une étude de la condition de base d'évaporation de l'ECN Spray A dans une configuration bi-carburant. Les principales conclusions tirées de ce chapitre incluent :

- Dans la condition ECN Spray A sans évaporation, la comparaison des résultats LES-RFM avec les différentes données expérimentales dans le champ proche de la buse, y compris la masse volumique projetée, la masse intégrée transversale et la fraction volumique liquide , a montré un bon accord, ce qui indique que le modèle RFM peut capturer avec précision la dispersion du carburant dans les conditions considérées. En outre, la comparaison des résultats du modèle (RFM-Σ) avec la densité de surface projetée expérimentale le long de la ligne centrale de spray et les profils radiaux SMD a montré un accord satisfaisant. Dans l'ensemble, on peut conclure que le modèle RFM-Σ proposé peut prédire avec précision la dispersion et l'atomisation du carburant dans les conditions considérées.

- Dans la condition d'évaporation ECN Spray A, les mesures globales de spray telles que les pénétrations de liquide de spray et de vapeur sont bien capturées par le modèle RFM par rapport aux données expérimentales. De plus, l'analyse locale montre que la distribution radiale de la fraction de mélange concorde favorablement avec les données expérimentales dans son niveau de confiance.

- L'analyse de la densité de surface et des résultats SMD sous l'effet d'évaporation et des conditions sans évaporation a démontré la sensibilité de la surface modèle de densité de surface aux effets de vaporisation. Dans la région dense du spray, la vaporisation tend à améliorer la production de densité de surface, alors que la vaporisation diminue la densité de surface dans la zone de pulvérisation diluée. D'ailleurs, le la SMD moyenne diminue relativement dans la région diluée dans les conditions d'évaporation.

- La variation paramétrique de l'ECN Spray A, a montré la capacité du Modèle RFM pour bien prédire la variation de la pénétration du spray par rapport à les données expérimentales dans diverses conditions de fonctionnement, démontrant une forte performances prédictives du modèle.

- Une enquête sur l'état de base ECN Spray A dans une configuration bi-carburant (DF) utilisant du méthanol comme combustible primaire a été réalisée. Sous la considération configuration bi-carburant, l'effet du méthanol ambiant sur l'évaporation globale de la pulvérisation et les processus de mélange semblent insignifiants (seulement une petite variation des pénétrations de spray et de la distribution de la fraction massique de *n*-dodécane). Cependant, un impact remarquable sur la flamme la longueur de décollage, le temps de retard à l'allumage et les émissions de polluants sont à prévoir, comme indiqué dans [248].

Dans le **Chapitre 6**, le modèle RFM est utilisé pour évaluer et valider sa capacité de simulation de cavitation à l'aide de différentes configurations. La première configuration impliquait une configuration d'injecteur transparent académique, où le modèle les résultats sont comparés aux données expérimentales disponibles de Sou et al. [220]. Ensuite la deuxième configuration impliquait un injecteur industriel à usage intensif, où la formation de cavitation est étudiée en utilisant de l'ammoniac comme carburant. Les principales conclusions tirées de ce chapitre comprend :

Configuration de l'injecteur transparent :

- Les résultats numériques obtenus ont confirmé que le modèle peut aborder le phénomène de transition de phase dans les conditions considérées et reproduire fidèlement le développement de la cavitation à l'intérieur de l'orifice. Par ailleurs, une comparaison quantitative des résultats obtenus avec les données expérimentales de la vitesse axiale moyenne a montré un bon accord. Cependant, la comparaison de la racine carrée moyenne (RMS) des fluctuations de vitesse a montré un certain écart par rapport aux données expérimentales. Les travaux futurs devraient envisager la modélisation de la turbulence LES et une configuration étendue pour éviter la condition limite de pression de sortie prescrite à la sortie de la buse.

- Dans l'ensemble, le cas de test simulé a fourni une première validation du modèle RFM pour la simulation de la cavitation, de sorte qu'il puisse être évalué plus avant dans des configurations plus complexes.

Configuration injecteur industriel :

- Les résultats numériques obtenus ont montré que le modèle est capable de prédire dynamiquement le processus de transition de phase sous la configuration d'injecteur industriel considérée lorsque l'ammoniac est utilisé comme combustible.

- Les poches de cavitation formées à l'intérieur de l'orifice de l'injecteur se révèlent être principalement composées de vapeur d'ammoniac, avec une légère contribution d'azote non condensable dissous. En d'autres termes, la cavitation vaporeuse s'est avérée être le processus de transition de phase dominant par rapport à la cavitation gazeuse lorsque l'ammoniac est utilisé comme combustible. Un tel comportement pourrait être attribué à la pression de saturation relativement élevée de l'ammoniac. En effet, P_{sat}=33 bar à T=343 K par exemple.

- La formation de cavités gazeuses se produit non seulement près de la paroi supérieure de l'orifice, mais aussi près du centre de l'orifice, lorsque la pression descend en dessous de la pression de saturation. Cependant, la quantité de gaz générée au centre de l'orifice est bien inférieure à celle de la paroi supérieure près de l'entrée de l'orifice.

  Enfin, la table thermodynamique utilisée basée sur $log_{10}P$ a également montré son efficacité pour fournir une résolution de table adéquate pour l'axe de pression, ce qui est nécessaire pour les simulations de cavitation, car le changement de phase est principalement entraîné par la variation de pression.

Bibliography

[1] CMT, Virtual Injection Rate Generator. URL https://www.cmt.upv.es/ECN03.aspx.

[2] Convergent Science, Converge manual, 2021.

[3] Engine Combustion Network (ECN), Measurements of the liquid length for nozzle 210675 using diffused back-illumination (DBI) at Spray A and other conditions, . URL https://ecn.sandia.gov/data/dbi675/.

[4] Engine Combustion Network (ECN), Rayleigh scattering n-dodecane/ambient mixing images for Spray A and several other experimental conditions, . URL https://ecn.sandia.gov/data/bkldaal4mixing/.

[5] Engine Combustion Network (ECN), Near-nozzle mixture derived from x-ray radiography, . URL https://ecn.sandia.gov/rad675/.

[6] Engine Combustion Network (ECN), Diesel Data Search, . URL https://ecn.sandia.gov/ecn-data-search.

[7] Engine Combustion Network (ECN), Modeling Standards and Recommendations, . URL https://ecn.sandia.gov/diesel-spray-combustion/computational-method/modeling-standards/.

[8] Engine Combustion Network (ECN), Spray A geometry. URL https://ecn.sandia.gov/diesel-spray-combustion/target-condition/spray-a-nozzle-geometry.

[9] Engine Combustion Network (ECN), 06/01/2021. URL https://ecn.sandia.gov/.

[10] EDEM ITN PROJECT – Marie Skłodowska-Curie European Industrial Doctorate (EID) network, Grant Agreement no. 861002., 30/12/2020. URL https://edem-itn.eu/.

[11] A. B. Wood. *A Textbook of Sound*. G. Bell and Sons Ltd, London, 1930.

[12] A. Ahmed, G. Tretola, S. Navarro-Martinez, K. Vogiatzaki, B. Duret, J. Reveillon, and F.-X. Demoulin. ATOMIZATION MODELING USING SURFACE DENSITY AND STOCHASTIC FIELDS. *Atomization and Sprays*, 30(4):239–266, 2020. ISSN 1044-5110. doi: 10.1615/AtomizSpr.2020032620.

[13] D. M. Anderson, G. B. McFadden, and A. A. Wheeler. DIFFUSE-INTERFACE METHODS IN FLUID MECHANICS. *Annual Review of Fluid Mechanics*, 30(1): 139–165, 1998. ISSN 0066-4189. doi: 10.1146/annurev.fluid.30.1.139.

[14] A. Andreini, C. Bianchini, S. Puggelli, and F. X. Demoulin. Development of a turbulent liquid flux model for Eulerian–Eulerian multiphase flow simulations. *International Journal of Multiphase Flow*, 81:88–103, 2016. ISSN 03019322. doi: 10.1016/j.ijmultiphaseflow.2016.02.003.

[15] J. Anez, A. Ahmed, N. Hecht, B. Duret, J. Reveillon, and F. X. Demoulin. Eulerian–Lagrangian spray atomization model coupled with interface capturing method for diesel injectors. *International Journal of Multiphase Flow*, 113:325–342, 2019. ISSN 03019322. doi: 10.1016/j.ijmultiphaseflow.2018.10.009.

[16] C. Arcoumanis, H. Flora, M. Gavaises, and M. Badami. Cavitation in Real-Size Multi-Hole Diesel Injector Nozzles. In *SAE Technical Paper Series*, SAE Technical Paper Series. SAE International400 Commonwealth Drive, Warrendale, PA, United States, 2000. doi: 10.4271/2000-01-1249.

[17] O. Asi. Failure of a diesel engine injector nozzle by cavitation damage. *Engineering Failure Analysis*, 13(7):1126–1133, 2006. ISSN 13506307. doi: 10.1016/j.engfailanal.2005.07.021.

[18] M. R. Baer and J. W. Nunziato. A two-phase mixture theory for the deflagration-to-detonation transition (ddt) in reactive granular materials. *International Journal of Multiphase Flow*, 12(6):861–889, 1986. ISSN 03019322. doi: 10.1016/0301-9322(86)90033-9.

[19] B. Balaji, V. Raghavan, K. Ramamurthi, and G. Gogos. A numerical study of evaporation characteristics of spherical n-dodecane droplets in high pressure nitrogen environment. *Physics of Fluids*, 23(6):063601, 2011. ISSN 1070-6631. doi: 10.1063/1.3599700.

[20] H. Baled, R. M. Enick, Y. Wu, M. A. McHugh, W. Burgess, D. Tapriyal, and B. D. Morreale. Prediction of hydrocarbon densities at extreme conditions using volume-translated SRK and PR equations of state fit to high temperature, high pressure PVT data. *Fluid Phase Equilibria*, 317:65–76, 2012. ISSN 03783812. doi: 10.1016/j.fluid.2011.12.027.

[21] D. T. Banuti. Crossing the Widom-line – Supercritical pseudo-boiling. *The Journal of Supercritical Fluids*, 98:12–16, 2015. ISSN 08968446. doi: 10.1016/j.supflu.2014.12.019.

[22] M. Bardi, R. Payri, L. M. Malbec, G. Bruneaux, L. M. Pickett, J. Manin, T. Bazyn, and C. Genzale. ENGINE COMBUSTION NETWORK: COMPARISON OF SPRAY DEVELOPMENT, VAPORIZATION, AND COMBUSTION IN DIFFERENT COMBUSTION VESSELS. *Atomization and Sprays*, 22(10):807–842, 2012. ISSN 1044-5110. doi: 10.1615/AtomizSpr.2013005837.

[23] M. Battistoni and C. N. Grimaldi. Numerical analysis of injector flow and spray characteristics from diesel injectors using fossil and biodiesel fuels. *Applied Energy*, 97:656–666, 2012. ISSN 03062619. doi: 10.1016/j.apenergy.2011.11.080.

[24] M. Battistoni, Q. Xue, S. Som, and E. Pomraning. Effect of Off-Axis Needle Motion on Internal Nozzle and Near Exit Flow in a Multi-Hole Diesel Injector. *SAE*

International Journal of Fuels and Lubricants, 7(1):167–182, 2014. ISSN 1946-3960. doi: 10.4271/2014-01-1426.

[25] M. Battistoni, D. J. Duke, A. B. Swantek, F. Z. Tilocco, C. F. Powell, and S. Som. EFFECTS OF NONCONDENSABLE GAS ON CAVITATING NOZZLES. *Atomization and Sprays*, 25(6):453–483, 2015. ISSN 1044-5110. doi: 10.1615/AtomizSpr.2015011076.

[26] M. Battistoni, Q. Xue, and S. Som. Large-Eddy Simulation (LES) of Spray Transients: Start and End of Injection Phenomena. *Oil & Gas Science and Technology - Revue de l'IFP*, 71(1):4, 2016. ISSN 1294-4475. doi: 10.2516/ogst/2015024.

[27] M. Battistoni, G. M. Magnotti, C. L. Genzale, M. Arienti, K. E. Matusik, D. J. Duke, J. Giraldo, J. Ilavsky, A. L. Kastengren, C. F. Powell, and P. Marti-Aldaravi. Experimental and Computational Investigation of Subcritical Near-Nozzle Spray Structure and Primary Atomization in the Engine Combustion Network Spray D. *SAE International Journal of Fuels and Lubricants*, 11(4):337–352, 2018. ISSN 1946-3960. doi: 10.4271/2018-01-0277.

[28] M. Battistoni, S. Som, and C. F. Powell. Highly resolved Eulerian simulations of fuel spray transients in single and multi-hole injectors: Nozzle flow and near-exit dynamics. *Fuel*, 251:709–729, 2019. ISSN 0016-2361. doi: 10.1016/j.fuel.2019.04.076.

[29] D. Bauer, H. Chaves, and C. ARCOUMANIS. Measurements of void fraction distribution in cavitating pipe flow using x-ray CT. *Measurement Science and Technology*, 23(5):055302, 2012. ISSN 0957-0233. doi: 10.1088/0957-0233/23/5/055302.

[30] P.-A. Beau, M. Funk, R. Lebas, and F.-X. Demoulin. Applying Quasi-Multiphase Model to Simulate Atomization Processes in Diesel Engines: Modeling of the Slip Velocity. In *SAE Technical Paper Series*, SAE Technical Paper Series. SAE International400 Commonwealth Drive, Warrendale, PA, United States, 2005. doi: 10.4271/2005-01-0220.

[31] J. Bellan. Supercritical (and subcritical) fluid behavior and modeling: Drops, streams, shear and mixing layers, jets and sprays. *Progress in Energy and Combustion Science*, 26(4-6):329–366, 2000. ISSN 03601285. doi: 10.1016/S0360-1285(00)00008-3.

[32] B. Biçer and A. Sou. Application of the improved cavitation model to turbulent cavitating flow in fuel injector nozzle. *Applied Mathematical Modelling*, 40(7-8):4712–4726, 2016. ISSN 0307904X. doi: 10.1016/j.apm.2015.11.049.

[33] Z. Bilicki and J. Kestin. Physical aspects of the relaxation model in two-phase flow. *Proceedings of the Royal Society of London. A. Mathematical and Physical Sciences*, 428(1875):379–397, 1990. ISSN 0080-4630. doi: 10.1098/rspa.1990.0040.

[34] G. Blokkeel, B. Barbeau, and R. Borghi. A 3D Eulerian Model to Improve the Primary Breakup of Atomizing Jet. In *SAE Technical Paper Series*, SAE Technical Paper Series. SAE International400 Commonwealth Drive, Warrendale, PA, United States, 2003. doi: 10.4271/2003-01-0005.

[35] V. Boniou, T. Schmitt, and A. Vié. Comparison of interface capturing methods for the simulation of two-phase flow in a unified low-Mach framework. *International Journal of Multiphase Flow*, 149:103957, 2022. ISSN 03019322. doi: 10.1016/j.ijmultiphaseflow.2021.103957.

[36] G. Borghesi and J. Bellan. A priori and a posteriori investigations for developing large eddy simulations of multi-species turbulent mixing under high-pressure conditions. *Physics of Fluids*, 27(3):035117, 2015. ISSN 1070-6631. doi: 10.1063/1.4916284.

[37] S. Brown, L. D. Peristeras, S. Martynov, R. Porter, H. Mahgerefteh, I. K. Nikolaidis, G. C. Boulougouris, D. M. Tsangaris, and I. G. Economou. Thermodynamic interpolation for the simulation of two-phase flow of non-ideal mixtures. *Computers & Chemical Engineering*, 95:49–57, 2016. ISSN 00981354. doi: 10.1016/j.compchemeng.2016.09.005.

[38] E. Brunner, W. Hültenschmidt, and G. Schlichthärle. Fluid mixtures at high pressures IV. Isothermal phase equilibria in binary mixtures consisting of (methanol + hydrogen or nitrogen or methane or carbon monoxide or carbon dioxide). *The Journal of Chemical Thermodynamics*, 19(3):273–291, 1987. ISSN 00219614. doi: 10.1016/0021-9614(87)90135-2.

[39] C. Chauveau, F. Halter, A. Lalonde, and I. Gokalp, editors. *An experimental study on the droplet vaporization: effects of heat conduction through the support fiber*, ILASS-EUROPE, COMO, IT, 2008.

[40] M. C. Cameretti, R. de Robbio, E. Mancaruso, and M. Palomba. CFD Study of Dual Fuel Combustion in a Research Diesel Engine Fueled by Hydrogen. *Energies*, 15(15):5521, 2022. ISSN 1996-1073. doi: 10.3390/en15155521.

[41] Y. Çelebi and H. Aydın. An overview on the light alcohol fuels in diesel engines. *Fuel*, 236:890–911, 2019. ISSN 0016-2361. doi: 10.1016/j.fuel.2018.08.138.

[42] W. G. Chapman, K. E. Gubbins, G. Jackson, and M. Radosz. New reference equation of state for associating liquids. *Industrial & Engineering Chemistry Research*, 29(8):1709–1721, 1990. ISSN 0888-5885. doi: 10.1021/ie00104a021.

[43] C. Chauveau, M. Birouk, F. Halter, and I. Gökalp. An analysis of the droplet support fiber effect on the evaporation process. *International Journal of Heat and Mass Transfer*, 128:885–891, 2019. ISSN 00179310. doi: 10.1016/j.ijheatmasstransfer.2018.09.029.

[44] H. Chaves, M. Knapp, A. Kubitzek, F. Obermeier, and T. Schneider. Experimental Study of Cavitation in the Nozzle Hole of Diesel Injectors Using Transparent Nozzles. In *SAE Technical Paper Series*, SAE Technical Paper Series. SAE International400 Commonwealth Drive, Warrendale, PA, United States, 1995. doi: 10.4271/950290.

[45] B. Chehroudi. Recent Experimental Efforts on High-Pressure Supercritical Injection for Liquid Rockets and Their Implications. *International Journal of Aerospace Engineering*, 2012:1–31, 2012. ISSN 1687-5966. doi: 10.1155/2012/121802.

[46] J. Chesnel, J. Reveillon, T. Menard, and F.-X. Demoulin. LARGE EDDY SIMULATION OF LIQUID JET ATOMIZATION. *Atomization and Sprays*, 21(9):711–736, 2011. ISSN 1044-5110. doi: 10.1615/AtomizSpr.2012003740.

[47] A. Chiapolino, P. Boivin, and R. Saurel. A simple phase transition relaxation solver for liquid-vapor flows. *International Journal for Numerical Methods in Fluids*, 83 (7):583–605, 2017. ISSN 02712091. doi: 10.1002/fld.4282.

[48] A. Chiapolino, P. Boivin, and R. Saurel. A simple and fast phase transition relaxation solver for compressible multicomponent two-phase flows. *Computers & Fluids*, 150:31–45, 2017. ISSN 00457930. doi: 10.1016/j.compfluid.2017.03.022.

[49] A. Chiapolino, R. Saurel, and B. Nkonga. Sharpening diffuse interfaces with compressible fluids on unstructured meshes. *Journal of Computational Physics*, 340: 389–417, 2017. ISSN 00219991. doi: 10.1016/j.jcp.2017.03.042.

[50] V. Chintala and K. A. Subramanian. A comprehensive review on utilization of hydrogen in a compression ignition engine under dual fuel mode. *Renewable and Sustainable Energy Reviews*, 70:472–491, 2017. ISSN 13640321. doi: 10.1016/j.rser.2016.11.247.

[51] T. H. Chung, M. Ajlan, L. L. Lee, and K. E. Starling. Generalized multiparameter correlation for nonpolar and polar fluid transport properties. *Industrial & Engineering Chemistry Research*, 27(4):671–679, 1988. ISSN 0888-5885. doi: 10.1021/ie00076a024.

[52] M. Cristofaro, W. Edelbauer, P. Koukouvinis, and M. Gavaises. A numerical study on the effect of cavitation erosion in a diesel injector. *Applied Mathematical Modelling*, 78:200–216, 2020. ISSN 0307904X. doi: 10.1016/j.apm.2019.09.002.

[53] C. Crua, J. Manin, and L. M. Pickett. On the transcritical mixing of fuels at diesel engine conditions. *Fuel*, 208:535–548, 2017. ISSN 0016-2361. doi: 10.1016/j.fuel.2017.06.091.

[54] R. N. Dahms and J. C. Oefelein. On the transition between two-phase and single-phase interface dynamics in multicomponent fluids at supercritical pressures. *Physics of Fluids*, 25(9):092103, 2013. ISSN 1070-6631. doi: 10.1063/1.4820346.

[55] R. N. Dahms, J. Manin, L. M. Pickett, and J. C. Oefelein. Understanding high-pressure gas-liquid interface phenomena in Diesel engines. *Proceedings of the Combustion Institute*, 34(1):1667–1675, 2013. ISSN 15407489. doi: 10.1016/j.proci.2012.06.169.

[56] L. Davidson and M. Billson. Hybrid LES-RANS using synthesized turbulent fluctuations for forcing in the interface region. *International Journal of Heat and Fluid Flow*, 27(6):1028–1042, 2006. doi: 10.1016/j.ijheatfluidflow.2006.02.025.

[57] J. C. de Hemptine, P. Mougin, A. Barreau, L. Ruffine, S. Tamouza, and R. Inchekel. Application to Petroleum Engineering of Statistical Thermodynamics – Based Equations of State. *Oil & Gas Science and Technology - Revue de l'IFP*, 61(3):363–386, 2006. ISSN 1294-4475. doi: 10.2516/ogst:2006039a.

[58] J.-C. de Hemptinne, J.-M. Ledanois, P. Mougin, and A. Barreau. *Select Thermodynamic Models for Process Simulation - A Practical Guide using a Three Steps Methodology*. Technip, 2012. ISBN 9782901638131. doi: 10.2516/ifpen/2011001.

[59] M. De Lorenzo, P. Lafon, M. Di Matteo, M. Pelanti, J.-M. Seynhaeve, and Y. Bartosiewicz. Homogeneous two-phase flow models and accurate steam-water table look-up method for fast transient simulations. *International Journal of Multiphase Flow*, 95:199–219, 2017. ISSN 03019322. doi: 10.1016/j.ijmultiphaseflow.2017.06.001.

[60] F.-X. Demoulin, J. Reveillon, B. Duret, Z. Bouali, P. Desjonqueres, and T. Menard. TOWARD USING DIRECT NUMERICAL SIMULATION TO IMPROVE PRIMARY BREAK-UP MODELING. *Atomization and Sprays*, 23(11):957–980, 2013. ISSN 1044-5110. doi: 10.1615/AtomizSpr.2013007439.

[61] J. M. Desantes, F. J. Salvador, J. J. López, and J. de La Morena. Study of mass and momentum transfer in diesel sprays based on X-ray mass distribution measurements and on a theoretical derivation. *Experiments in Fluids*, 50(2):233–246, 2011. ISSN 0723-4864. doi: 10.1007/s00348-010-0919-8.

[62] J. M. Desantes, J. M. Garcia-Oliver, J. M. Pastor, and A. Pandal. A COMPARISON OF DIESEL SPRAYS CFD MODELING APPROACHES: DDM VERSUS E-Y EULERIAN ATOMIZATION MODEL. *Atomization and Sprays*, 26(7):713–737, 2016. ISSN 1044-5110. doi: 10.1615/AtomizSpr.2015013285.

[63] J. M. Desantes, J. M. García-Oliver, J. M. Pastor, A. Pandal, E. Baldwin, and D. P. Schmidt. Coupled/decoupled spray simulation comparison of the ECN spray a condition with the -Y Eulerian atomization model. *International Journal of Multiphase Flow*, 80:89–99, 2016. ISSN 03019322. doi: 10.1016/j.ijmultiphaseflow.2015.12.002.

[64] J. M. Desantes, J. M. García-Oliver, J. M. Pastor, I. Olmeda, A. Pandal, and B. Naud. LES Eulerian diffuse-interface modeling of fuel dense sprays near- and far-field. *International Journal of Multiphase Flow*, 127:103272, 2020. ISSN 03019322. doi: 10.1016/j.ijmultiphaseflow.2020.103272.

[65] B. M. Devassy, C. Habchi, and E. Daniel. ATOMIZATION MODELLING OF LIQUID JETS USING A TWO-SURFACE-DENSITY APPROACH. *Atomization and Sprays*, 25(1):47–80, 2015. ISSN 1044-5110. doi: 10.1615/AtomizSpr.2014011350.

[66] P. Dimitriou and R. Javaid. A review of ammonia as a compression ignition engine fuel. *International Journal of Hydrogen Energy*, 45(11):7098–7118, 2020. ISSN 03603199. doi: 10.1016/j.ijhydene.2019.12.209.

[67] Y. Dong, O. Kaario, G. Hassan, O. Ranta, M. Larmi, and B. Johansson. High-pressure direct injection of methanol and pilot diesel: A non-premixed dual-fuel engine concept. *Fuel*, 277:117932, 2020. ISSN 0016-2361. doi: 10.1016/j.fuel.2020.117932.

[68] D. Duke, A. Swantek, Z. Tilocco, A. Kastengren, K. Fezzaa, K. Neroorkar, M. Moulai, C. Powell, and D. Schmidt. X-ray Imaging of Cavitation in Diesel Injectors. *SAE International Journal of Engines*, 7(2):1003–1016, 2014. ISSN 1946-3944. doi: 10.4271/2014-01-1404.

[69] D. J. Duke, A. L. Kastengren, F. Z. Tilocco, A. B. Swantek, and C. F. Powell. X-RAY RADIOGRAPHY MEASUREMENTS OF CAVITATING NOZZLE FLOW. *Atomization and Sprays*, 23(9):841–860, 2013. ISSN 1044-5110. doi: 10.1615/AtomizSpr.2013008340.

[70] D. J. Duke, K. E. Matusik, A. L. Kastengren, A. B. Swantek, N. Sovis, R. Payri, J. P. Viera, and C. F. Powell. X-ray radiography of cavitation in a beryllium alloy nozzle. *International Journal of Engine Research*, 18(1-2):39–50, 2017. ISSN 1468-0874. doi: 10.1177/1468087416685965.

[71] J. K. Dukowicz. A particle-fluid numerical model for liquid sprays. *Journal of Computational Physics*, 35(2):229–253, 1980. ISSN 00219991. doi: 10.1016/0021-9991(80)90087-X.

[72] B. Duret, J. Reveillon, T. Menard, and F. X. Demoulin. Improving primary atomization modeling through DNS of two-phase flows. *International Journal of Multiphase Flow*, 55:130–137, 2013. ISSN 03019322. doi: 10.1016/j.ijmultiphaseflow.2013.05.004.

[73] E. Winklhofer, E. Kull, E. Kelz, and A. Morozov. Comprehensive hydraulic and flow field documentation in model throttle experiments under cavitation conditions. *ILASS-Europe*, 2001. doi: 10.13140/2.1.1716.4161.

[74] V. Ebrahimian and C. Habchi. Towards a predictive evaporation model for multicomponent hydrocarbon droplets at all pressure conditions. *International Journal of Heat and Mass Transfer*, 54(15-16):3552–3565, 2011. ISSN 00179310. doi: 10.1016/j.ijheatmasstransfer.2011.03.031.

[75] E.W. Lemmon, M.L. Huber, M.O. McLinden. NIST reference fluid thermodynamic and transport properties–REFPROP. 2002.

[76] Y. Fang, M. de Lorenzo, P. Lafon, S. Poncet, and Y. Bartosiewicz. An Accurate and Efficient Look-up Table Equation of State for Two-Phase Compressible Flow Simulations of Carbon Dioxide. *Industrial & Engineering Chemistry Research*, 57 (22):7676–7691, 2018. ISSN 0888-5885. doi: 10.1021/acs.iecr.8b00507.

[77] M. Fathi and S. Hickel. Rapid multi–component phase–split calculations using volume functions and reduction methods. *AIChE Journal*, 67(6), 2021. ISSN 0001-1541. doi: 10.1002/aic.17174.

[78] M. Fathi, S. Hickel, and D. Roekaerts. Large eddy simulations of reacting and non-reacting transcritical fuel sprays using multiphase thermodynamics. *Physics of Fluids*, 34(8):085131, 2022. ISSN 1070-6631. doi: 10.1063/5.0099154.

[79] F. Föll, T. Hitz, C. Müller, C.-D. Munz, and M. Dumbser. On the use of tabulated equations of state for multi-phase simulations in the homogeneous equilibrium limit. *Shock Waves*, 29(5):769–793, 2019. ISSN 0938-1287. doi: 10.1007/s00193-019-00896-1.

[80] H. Gaballa, S. Jafari, C. Habchi, and J.-C. de Hemptinne. Numerical investigation of droplet evaporation in high-pressure dual-fuel conditions using a tabulated real-fluid model. *International Journal of Heat and Mass Transfer*, 189:122671, 2022. ISSN 00179310. doi: 10.1016/j.ijheatmasstransfer.2022.122671.

[81] T. García-Córdova, D. N. Justo-García, B. E. García-Flores, and F. García-Sánchez. Vapor−Liquid Equilibrium Data for the Nitrogen + Dodecane System at Temperatures from (344 to 593) K and at Pressures up to 60 MPa. *Journal of Chemical & Engineering Data*, 56(4):1555–1564, 2011. ISSN 0021-9568. doi: 10.1021/je1012372.

[82] J. M. Garcia-Oliver, J. M. Pastor, A. Pandal, N. Trask, E. Baldwin, and D. P. Schmidt. DIESEL SPRAY CFD SIMULATIONS BASED ON THE S- EULERIAN ATOMIZATION MODEL. *Atomization and Sprays*, 23(1):71–95, 2013. ISSN 1044-5110. doi: 10.1615/AtomizSpr.2013007198.

[83] M. Gavaises and A. Andriotis. Cavitation Inside Multi-hole Injectors for Large Diesel Engines and Its Effect on the Near-nozzle Spray Structure. In *SAE Technical Paper Series*, SAE Technical Paper Series. SAE International400 Commonwealth Drive, Warrendale, PA, United States, 2006. doi: 10.4271/2006-01-1114.

[84] M. Gavaises, A. Andriotis, D. Papoulias, N. Mitroglou, and A. Theodorakakos. Characterization of string cavitation in large-scale Diesel nozzles with tapered holes. *Physics of Fluids*, 21(5):052107, 2009. ISSN 1070-6631. doi: 10.1063/1.3140940.

[85] D. Gerard and L. B. Lave. Implementing technology-forcing policies: The 1970 Clean Air Act Amendments and the introduction of advanced automotive emissions controls in the United States. *Technological Forecasting and Social Change*, 72(7): 761–778, 2005. ISSN 00401625. doi: 10.1016/j.techfore.2004.08.003.

[86] H. Ghassemi, S. W. Baek, and Q. S. Khan. Experimental study on binary droplet evaporation at elevated pressures and temperatures. *Combustion Science and Technology*, 178(6):1031–1053, 2006. ISSN 0010-2202. doi: 10.1080/00102200500296697.

[87] E. Giannadakis, D. Papoulias, M. Gavaises, C. ARCOUMANIS, C. Soteriou, and W. Tang. Evaluation of the Predictive Capability of Diesel Nozzle Cavitation Models. In *SAE Technical Paper Series*, SAE Technical Paper Series. SAE International400 Commonwealth Drive, Warrendale, PA, United States, 2007. doi: 10.4271/2007-01-0245.

[88] E. Giannadakis, M. Gavaises, and C. ARCOUMANIS. Modelling of cavitation in diesel injector nozzles. *Journal of Fluid Mechanics*, 616:153–193, 2008. ISSN 0022-1120. doi: 10.1017/S0022112008003777.

[89] S. Gleis, S. Frankl, D. Waligorski, D.-I. M. Prager, and P. D.-I. G. Wachtmeister. Investigation of the High-Pressure-Dual-Fuel (HPDF) combustion process of natural gas on a fully optically accessible research engine. In *SAE Technical Paper Series*, SAE Technical Paper Series. SAE International400 Commonwealth Drive, Warrendale, PA, United States, 2019. doi: 10.4271/2019-01-2172.

[90] A. Gnanaskandan and J. R. Bellan. Large Eddy Simulations of high pressure jets: Effect of subgrid scale modeling. In *55th AIAA Aerospace Sciences Meeting*, Reston, Virginia, 01092017. American Institute of Aeronautics and Astronautics. ISBN 978-1-62410-447-3. doi: 10.2514/6.2017-1105.

[91] G. Godsave. Studies of the combustion of drops in a fuel spray—the burning of single drops of fuel. *Symposium (International) on Combustion*, 4(1):818–830, 1953. ISSN 00820784. doi: 10.1016/S0082-0784(53)80107-4.

[92] Y. Gong, G. Xiao, X. Ma, K. H. Luo, S. Shuai, and H. Xu. Phase transitions of multi-component fuel droplets under sub- and supercritical conditions. *Fuel*, 287: 119516, 2021. ISSN 0016-2361. doi: 10.1016/j.fuel.2020.119516.

[93] D. R. Guildenbecher, C. López-Rivera, and P. E. Sojka. Secondary atomization. *Experiments in Fluids*, 46(3):371–402, 2009. ISSN 0723-4864. doi: 10.1007/s00348-008-0593-2.

[94] N. Gültekin and M. Ciniviz. Examination of the effect of combustion chamber geometry and mixing ratio on engine performance and emissions in a hydrogen-diesel dual-fuel compression-ignition engine. *International Journal of Hydrogen Energy*, 48(7):2801–2820, 2023. ISSN 03603199. doi: 10.1016/j.ijhydene.2022.10.155.

[95] H. Guo, R. Torelli, A. Bautista Rodriguez, A. Tekawade, B. Sforzo, C. Powell, and S. Som. Internal Nozzle Flow Simulations of the ECN Spray C Injector under Realistic Operating Conditions. In *SAE Technical Paper Series*, SAE Technical Paper Series. SAE International400 Commonwealth Drive, Warrendale, PA, United States, 2020. doi: 10.4271/2020-01-1154.

[96] C. Habchi. THE ENERGY SPECTRUM ANALOGY BREAKUP (SAB) MODEL FOR THE NUMERICAL SIMULATION OF SPRAYS. *Atomization and Sprays*, 21(12):1033–1057, 2011. ISSN 1044-5110. doi: 10.1615/AtomizSpr.2012004531.

[97] C. Habchi. A Gibbs Energy Relaxation Model (GERM) for Cavitation Simulation. *Atomization and Sprays*, 25(4):317–334, 2015. ISSN 1044-5110. doi: 10.1615/AtomizSpr.2014010372.

[98] C. Habchi and G. Bruneaux. LES and Experimental investigation of Diesel sprays. *12th ICLASS Triennial Int. Conf. on Liquid Atomization and Spray Systems,Heidelberg, Germany*, 2012. doi: 10.13140/2.1.1044.0648.

[99] C. Habchi and V. Ebrahimian. Gravitational Effects on Multi-component Droplet Evaporation. *Microgravity Science and Technology*, 24(3):229–235, 2012. ISSN 0938-0108. doi: 10.1007/s12217-012-9303-z.

[100] C. Habchi, D. Verhoeven, C. Huynh Huu, L. Lambert, J. L. Vanhemelryck, and T. Baritaud. Modeling Atomization and Break Up in High-Pressure Diesel Sprays. In *SAE Technical Paper Series*, SAE Technical Paper Series. SAE International400 Commonwealth Drive, Warrendale, PA, United States, 1997. doi: 10.4271/970881.

[101] C. Habchi, N. Dumont, and O. Simonin. Multidimentional Simulation of Cavitating Flows in Diesel Injectors by a Homogeneous Mixture Modeling Approach. *Atomization and Sprays*, 18(2):129–162, 2008. ISSN 1044-5110. doi: 10.1615/AtomizSpr.v18.i2.20.

[102] C. Habchi, J. Bohbot, A. Schmid, and K. Herrmann. A comprehensive Two-Fluid Model for Cavitation and Primary Atomization Modelling of liquid jets - Application to a large marine Diesel injector. *Journal of Physics: Conference Series*, 656:012084, 2015. ISSN 1742-6588. doi: 10.1088/1742-6596/656/1/012084.

[103] Hagen Müller, Christoph Niedermeier, Maria Jarczyk, Michael Pfitzner, S. Hickel, and Nikolaus A. Adams. Large-eddy simulation of trans- and supercritical injection. *Progress in Propulsion Physics*, 2016.

[104] L. Hakim, G. Lacaze, and J. Oefelein. Large Eddy Simulation of Autoignition Transients in a Model Diesel Injector Configuration. *SAE International Journal of Fuels and Lubricants*, 9(1):165–176, 2016. ISSN 1946-3960. doi: 10.4271/2016-01-0872.

[105] F. Hempert, S. Boblest, T. Ertl, F. Sadlo, P. Offenhäuser, C. W. Glass, M. Hoffmann, A. Beck, C.-D. Munz, and U. Iben. Simulation of real gas effects in supersonic methane jets using a tabulated equation of state with a discontinuous Galerkin spectral element method. *Computers & Fluids*, 145:167–179, 2017. ISSN 00457930. doi: 10.1016/j.compfluid.2016.12.024.

[106] M. Herrmann. ON SIMULATING PRIMARY ATOMIZATION USING THE REFINED LEVEL SET GRID METHOD. *Atomization and Sprays*, 21(4):283–301, 2011. ISSN 1044-5110. doi: 10.1615/AtomizSpr.2011002760.

[107] J. O. Hirschfelder, C. F. Curtiss, and R. B. Bird. *Molecular Theory Of Gases And Liquids*. 1954.

[108] C. Hirt and B. Nichols. Volume of fluid (VOF) method for the dynamics of free boundaries. *Journal of Computational Physics*, 39(1):201–225, 1981. ISSN 00219991. doi: 10.1016/0021-9991(81)90145-5.

[109] N. Hooftman, M. Messagie, J. van Mierlo, and T. Coosemans. A review of the European passenger car regulations – Real driving emissions vs local air quality. *Renewable and Sustainable Energy Reviews*, 86:1–21, 2018. ISSN 13640321. doi: 10.1016/j.rser.2018.01.012.

[110] L.-P. Hsiang and G. M. Faeth. Drop deformation and breakup due to shock wave and steady disturbances. *International Journal of Multiphase Flow*, 21(4):545–560, 1995. ISSN 03019322. doi: 10.1016/0301-9322(94)00095-2.

[111] R. Issa. Solution of the implicitly discretised fluid flow equations by operator-splitting. *Journal of Computational Physics*, 62(1):40–65, 1986. ISSN 00219991. doi: 10.1016/0021-9991(86)90099-9.

[112] S. Jafari, H. Gaballa, A. Di-Lella, C. Habchi, and J.-C. de Hemptinne. A tabulated real-fluid modeling approach applied to cryogenic LN2-H2 jets evaporation and mixing at transcritical regime. *International Conference on Liquid Atomization and Spray Systems (ICLASS)*, 1(1), 2021. doi: 10.2218/iclass.2021.5988.

[113] S. Jafari, H. Gaballa, C. Habchi, and J.-C. de Hemptinne. Towards Understanding the Structure of Subcritical and Transcritical Liquid–Gas Interfaces Using a Tabulated Real Fluid Modeling Approach. *Energies*, 14(18):5621, 2021. ISSN 1996-1073. doi: 10.3390/en14185621.

[114] S. Jafari, H. Gaballa, C. Habchi, J.-C. de Hemptinne, and P. Mougin. Exploring the interaction between phase separation and turbulent fluid dynamics in multi-species supercritical jets using a tabulated real-fluid model. *The Journal of Supercritical Fluids*, page 105557, 2022. ISSN 08968446. doi: 10.1016/j.supflu.2022.105557.

[115] M.-M. Jarczyk and M. Pfitzner. Large Eddy Simulation of Supercritical Nitrogen Jets. In *50th AIAA Aerospace Sciences Meeting including the New Horizons Forum and Aerospace Exposition*, Nashville, TN, USA, 2012. ISBN 978-1-60086-936-5. doi: 10.2514/6.2012-1270.

[116] H. Jia and G. Gogos. Investigation of liquid droplet evaporation in subcritical and supercritical gaseous environments. *Journal of Thermophysics and Heat Transfer*, 6(4):738–745, 1992. ISSN 0887-8722. doi: 10.2514/3.11560.

[117] H. Jia and G. Gogos. High pressure droplet vaporization; effects of liquid-phase gas solubility. *International Journal of Heat and Mass Transfer*, 36(18):4419–4431, 1993. ISSN 00179310. doi: 10.1016/0017-9310(93)90126-Q.

[118] H. Jia and G. Gogos. Droplet vaporization in subcritical and supercritical environments; high vs low pressure modelling. *Acta Astronautica*, 32(2):121–129, 1994. ISSN 00945765. doi: 10.1016/0094-5765(94)90063-9.

[119] M. Jia, H. Pan, Y. Bian, Z. Zhang, Y. Chang, and H. Liu. CALIBRATION OF THE CONSTANTS IN THE KELVIN-HELMHOLTZ RAYLEIGH-TAYLOR (KH-RT) BREAKUP MODEL FOR DIESEL SPRAY UNDER WIDE CONDITIONS BASED ON ADVANCED DATA ANALYSIS TECHNIQUES. *Atomization and Sprays*, 32(6):1–27, 2022. ISSN 1044-5110. doi: 10.1615/AtomizSpr.2022040203.

[120] X. Jiang, G. A. Siamas, K. Jagus, and T. G. Karayiannis. Physical modelling and advanced simulations of gas–liquid two-phase jet flows in atomization and sprays. *Progress in Energy and Combustion Science*, 36(2):131–167, 2010. ISSN 03601285. doi: 10.1016/j.pecs.2009.09.002.

[121] D. Juric and G. Tryggvason. A Front-Tracking Method for Dendritic Solidification. *Journal of Computational Physics*, 123(1):127–148, 1996. ISSN 00219991. doi: 10.1006/jcph.1996.0011.

[122] M. G. Justino Vaz, E. Geber, F. Koukouvinis, I. K. Karathanassis, C. Rodriguez Fernandez, M. Gavaises, and G. Mouokue. Numerical Simulation of Multicomponent Diesel Fuel Spray Surrogates Using Real-Fluid Thermodynamic Modelling. In *SAE Technical Paper Series*, SAE Technical Paper Series. SAE International400 Commonwealth Drive, Warrendale, PA, United States, 2022. doi: 10.4271/2022-01-0509.

[123] A. K. Kapila, R. Menikoff, J. B. Bdzil, S. F. Son, and D. S. Stewart. Two-phase modeling of deflagration-to-detonation transition in granular materials: Reduced equations. *Physics of Fluids*, 13(10):3002–3024, 2001. ISSN 1070-6631. doi: 10.1063/1.1398042.

[124] I. K. Karathanassis, P. Koukouvinis, E. Kontolatis, Z. Lee, J. Wang, N. Mitroglou, and M. Gavaises. High-speed visualization of vortical cavitation using synchrotron radiation. *Journal of Fluid Mechanics*, 838:148–164, 2018. ISSN 0022-1120. doi: 10.1017/jfm.2017.885.

[125] I. K. Karathanassis, J. Hwang, P. Koukouvinis, L. Pickett, and M. Gavaises. Combined visualisation of cavitation and vortical structures in a real-size optical diesel injector. *Experiments in Fluids*, 62(1), 2021. ISSN 0723-4864. doi: 10.1007/s00348-020-03096-1.

[126] G. A. Karim. *Dual-fuel diesel engines*. CRC Press, 2015.

[127] A. Kastengren, J. Ilavsky, J. P. Viera, R. Payri, D. J. Duke, A. Swantek, F. Z. Tilocco, N. Sovis, and C. F. Powell. Measurements of droplet size in shear-driven atomization using ultra-small angle x-ray scattering. *International Journal of Multiphase Flow*, 92:131–139, 2017. ISSN 03019322. doi: 10.1016/j.ijmultiphaseflow.2017.03.005.

[128] A. L. Kastengren, C. F. Powell, Y. Wang, K.-S. Im, and J. Wang. X-RAY RADIOGRAPHY MEASUREMENTS OF DIESEL SPRAY STRUCTURE AT ENGINE-LIKE AMBIENT DENSITY. *Atomization and Sprays*, 19(11):1031–1044, 2009. ISSN 1044-5110. doi: 10.1615/AtomizSpr.v19.i11.30.

[129] A. L. Kastengren, F. Z. Tilocco, C. F. Powell, J. Manin, L. M. Pickett, R. Payri, and T. Bazyn. ENGINE COMBUSTION NETWORK (ECN): MEASUREMENTS OF NOZZLE GEOMETRY AND HYDRAULIC BEHAVIOR. *Atomization and Sprays*, 22(12):1011–1052, 2012. ISSN 1044-5110. doi: 10.1615/AtomizSpr.2013006309.

[130] R. J. Kee, M. E. Coltrin, and P. Glarborg. *Chemically reacting flow: Theory and practice*. Wiley-Interscience, Hoboken, N.J., 2003. ISBN 9780471261797.

[131] K. Kolovos, P. Koukouvinis, R. M. McDavid, and M. Gavaises. Transient Cavitation and Friction-Induced Heating Effects of Diesel Fuel during the Needle Valve Early Opening Stages for Discharge Pressures up to 450 MPa. *Energies*, 14(10):2923, 2021. ISSN 1996-1073. doi: 10.3390/en14102923.

[132] K. Kolovos, N. Kyriazis, P. Koukouvinis, A. Vidal, M. Gavaises, and R. M. McDavid. Simulation of transient effects in a fuel injector nozzle using real-fluid thermodynamic closure. *Applications in Energy and Combustion Science*, 7:100037, 2021. ISSN 2666352X. doi: 10.1016/j.jaecs.2021.100037.

[133] G. M. Kontogeorgis, E. C. Voutsas, I. V. Yakoumis, and D. P. Tassios. An Equation of State for Associating Fluids. *Industrial & Engineering Chemistry Research*, 35 (11):4310–4318, 1996. ISSN 0888-5885. doi: 10.1021/ie9600203.

[134] P. Koukouvinis, H. Naseri, and M. Gavaises. Performance of turbulence and cavitation models in prediction of incipient and developed cavitation. *International Journal of Engine Research*, 18(4):333–350, 2017. ISSN 1468-0874. doi: 10.1177/1468087416658604.

[135] P. Koukouvinis, A. Vidal-Roncero, C. Rodriguez, M. Gavaises, and L. Pickett. High pressure/high temperature multiphase simulations of dodecane injection to nitrogen: Application on ECN Spray-A. *Fuel*, 275:117871, 2020. ISSN 0016-2361. doi: 10.1016/j.fuel.2020.117871.

[136] P. Koukouvinis, C. Rodriguez, J. Hwang, I. Karathanassis, M. Gavaises, and L. Pickett. Machine Learning and transcritical sprays: A demonstration study of their potential in ECN Spray-A. *International Journal of Engine Research*, page 146808742110202, 2021. ISSN 1468-0874. doi: 10.1177/14680874211020292.

[137] G. Lacaze, A. Misdariis, A. Ruiz, and J. C. Oefelein. Analysis of high-pressure Diesel fuel injection processes using LES with real-fluid thermodynamics and transport. *Proceedings of the Combustion Institute*, 35(2):1603–1611, 2015. ISSN 15407489. doi: 10.1016/j.proci.2014.06.072.

[138] Le Ning, Q. Duan, Z. Chen, H. Kou, B. Liu, B. Yang, and K. Zeng. A comparative study on the combustion and emissions of a non-road common rail diesel engine fueled with primary alcohol fuels (methanol, ethanol, and n-butanol)/diesel dual fuel. *Fuel*, 266:117034, 2020. ISSN 0016-2361. doi: 10.1016/j.fuel.2020.117034.

[139] R. Lebas, G. Blokkeel, P.-A. Beau, and F.-X. Demoulin. Coupling Vaporization Model With the Eulerian-Lagrangian Spray Atomization (ELSA) Model in Diesel Engine Conditions. In *SAE Technical Paper Series*, SAE Technical Paper Series. SAE International400 Commonwealth Drive, Warrendale, PA, United States, 2005. doi: 10.4271/2005-01-0213.

[140] R. Lebas, T. Menard, P. A. Beau, A. Berlemont, and F. X. Demoulin. Numerical simulation of primary break-up and atomization: DNS and modelling study. *International Journal of Multiphase Flow*, 35(3):247–260, 2009. ISSN 03019322. doi: 10.1016/j.ijmultiphaseflow.2008.11.005.

[141] A. H. Lefebvre and V. G. McDonell. *Atomization and Sprays*. CRC Press, Second edition. | Boca Raton : Taylor & Francis, CRC Press, 2017., 2017. ISBN 9781315120911. doi: 10.1201/9781315120911.

[142] P. C. Ma, Y. Lv, and M. Ihme. An entropy-stable hybrid scheme for simulations of transcritical real-fluid flows. *Journal of Computational Physics*, 340:330–357, 2017. ISSN 00219991. doi: 10.1016/j.jcp.2017.03.022.

[143] P. C. Ma, H. Wu, T. Jaravel, L. Bravo, and M. Ihme. Large-eddy simulations of transcritical injection and auto-ignition using diffuse-interface method and finite-rate chemistry. *Proceedings of the Combustion Institute*, 37(3):3303–3310, 2019. ISSN 15407489. doi: 10.1016/j.proci.2018.05.063.

[144] G. M. Magnotti and C. L. Genzale. Detailed assessment of diesel spray atomization models using visible and X-ray extinction measurements. *International Journal of Multiphase Flow*, 97:33–45, 2017. ISSN 03019322. doi: 10.1016/j.ijmultiphaseflow.2017.08.002.

[145] J. Manin, M. Bardi, and L. M. Pickett. Evaluation of the liquid length via diffused back-illumination imaging in vaporizing diesel sprays. *The Eighth International Conference on Modeling and Diagnostics for Advanced Engine Systems (COMODIA)*, pages 665–673, 2012.

[146] J. Manin, M. Bardi, L. M. Pickett, R. N. Dahms, and J. C. Oefelein. Microscopic investigation of the atomization and mixing processes of diesel sprays injected into high pressure and temperature environments. *Fuel*, 134:531–543, 2014. ISSN 0016-2361. doi: 10.1016/j.fuel.2014.05.060.

[147] F. E. Marble and J. E. Broadwell. The Coherent Flame Model for Turbulent Chemical Reactions.

[148] H. MASUOKA, Y. ARAI, and A. S. SAITO. Application of the perturbation theory to vapor-liquid equilibria of systems containing ammonia. *JOURNAL OF CHEMICAL ENGINEERING OF JAPAN*, 10(3):171–175, 1977. ISSN 0021-9592. doi: 10.1252/jcej.10.171.

[149] J. Matheis and S. Hickel. Multi-component vapor-liquid equilibrium model for LES of high-pressure fuel injection and application to ECN Spray A. *International Journal of Multiphase Flow*, 99:294–311, 2018. ISSN 03019322. doi: 10.1016/j.ijmultiphaseflow.2017.11.001.

[150] W. O. H. Mayer, A. H. A. Schik, B. Vielle, C. Chauveau, I. Gokalp, D. G. Talley, and R. D. Woodward. Atomization and Breakup of Cryogenic Propellants Under High-Pressure Subcritical and Supercritical Conditions. *Journal of Propulsion and Power*, 14(5):835–842, 1998. ISSN 0748-4658. doi: 10.2514/2.5348.

[151] T. Ménard, S. Tanguy, and A. Berlemont. Coupling level set/VOF/ghost fluid methods: Validation and application to 3D simulation of the primary break-up of a liquid jet. *International Journal of Multiphase Flow*, 33(5):510–524, 2007. ISSN 03019322. doi: 10.1016/j.ijmultiphaseflow.2006.11.001.

[152] M. L. Michelsen. The isothermal flash problem. Part II. Phase-split calculation. *Fluid Phase Equilibria*, 9(1):21–40, 1982. ISSN 03783812. doi: 10.1016/0378-3812(82)85002-4.

[153] M. L. Michelsen and E. M. Hendriks. Physical properties from association models. *Fluid Phase Equilibria*, 180(1-2):165–174, 2001. ISSN 03783812. doi: 10.1016/S0378-3812(01)00344-2.

[154] R. S. Miller, K. Harstad, and J. Bellan. Evaluation of equilibrium and non-equilibrium evaporation models for many-droplet gas-liquid flow simulations. *International Journal of Multiphase Flow*, 24(6):1025–1055, 1998. ISSN 03019322. doi: 10.1016/S0301-9322(98)00028-7.

[155] R. Mishra, D. Jiwani, and D. Jarrahbashi. Three-component multi-fluid modeling of pseudo-cavitation phenomenon in diesel injector nozzles. *International Journal of Engine Research*, page 146808742199334, 2021. ISSN 1468-0874. doi: 10.1177/1468087421993348.

[156] M.-G. Mithun, P. Koukouvinis, and M. Gavaises. Numerical simulation of cavitation and atomization using a fully compressible three-phase model. *Physical Review Fluids*, 3(6), 2018. doi: 10.1103/PhysRevFluids.3.064304.

[157] N. Mitroglou, M. Lorenzi, M. Santini, and M. Gavaises. Application of X-ray micro-computed tomography on high-speed cavitating diesel fuel flows. *Experiments in Fluids*, 57(11), 2016. ISSN 0723-4864. doi: 10.1007/s00348-016-2256-z.

[158] N. Mitroglou, V. Stamboliyski, I. K. Karathanassis, K. S. Nikas, and M. Gavaises. Cloud cavitation vortex shedding inside an injector nozzle. *Experimental Thermal and Fluid Science*, 84:179–189, 2017. ISSN 08941777. doi: 10.1016/j.expthermflusci.2017.02.011.

[159] H. Müller, C. A. Niedermeier, J. Matheis, M. Pfitzner, and S. Hickel. Large-eddy simulation of nitrogen injection at trans- and supercritical conditions. *Physics of Fluids*, 28(1):015102, 2016. ISSN 1070-6631. doi: 10.1063/1.4937948.

[160] S. Navarro-Martinez. Large eddy simulation of spray atomization with a probability density function method. *International Journal of Multiphase Flow*, 63:11–22, 2014. ISSN 03019322. doi: 10.1016/j.ijmultiphaseflow.2014.02.013.

[161] F. Nicoud, H. B. Toda, O. Cabrit, S. Bose, and J. Lee. Using singular values to build a subgrid-scale model for large eddy simulations. *Physics of Fluids*, 23(8): 085106, 2011. ISSN 1070-6631. doi: 10.1063/1.3623274.

[162] B. M. Ningegowda, F. N. Z. Rahantamialisoa, A. Pandal, H. Jasak, H. G. Im, and M. Battistoni. Numerical Modeling of Transcritical and Supercritical Fuel Injections Using a Multi-Component Two-Phase Flow Model. *Energies*, 13(21):5676, 2020. ISSN 1996-1073. doi: 10.3390/en13215676.

[163] H. Nomura, Y. Ujiie, H. J. Rath, J. Sato, and M. Kono. Experimental study on high-pressure droplet evaporation using microgravity conditions. *Symposium (International) on Combustion*, 26(1):1267–1273, 1996. ISSN 00820784. doi: 10.1016/S0082-0784(96)80344-4.

[164] G. Nykteri, P. Koukouvinis, S. R. G. Avila, C.-D. Ohl, and M. Gavaises. A S-U two-fluid model with dynamic local topology detection: Application to high-speed droplet impact. *Journal of Computational Physics*, page 109225, 2020. ISSN 00219991. doi: 10.1016/j.jcp.2019.109225.

[165] F. Örley, T. Trummler, S. Hickel, M. S. Mihatsch, S. J. Schmidt, and N. A. Adams. Large-eddy simulation of cavitating nozzle flow and primary jet break-up. *Physics of Fluids*, 27(8):086101, 2015. ISSN 1070-6631. doi: 10.1063/1.4928701.

[166] P. Pakseresht and S. V. Apte. Volumetric displacement effects in Euler-Lagrange LES of particle-laden jet flows. *International Journal of Multiphase Flow*, 113:16–32, 2019. ISSN 03019322. doi: 10.1016/j.ijmultiphaseflow.2018.12.013.

[167] A. Panchal and S. Menon. A hybrid Eulerian-Eulerian/Eulerian-Lagrangian method for dense-to-dilute dispersed phase flows. *Journal of Computational Physics*, 439: 110339, 2021. ISSN 00219991. doi: 10.1016/j.jcp.2021.110339.

[168] A. Pandal, J. M. Pastor, R. Payri, A. Kastengren, D. Duke, K. Matusik, J. S. Giraldo, C. Powell, and D. Schmidt. Computational and Experimental Investigation of Interfacial Area in Near-Field Diesel Spray Simulation. *SAE International Journal of Fuels and Lubricants*, 10(2):423–431, 2017. ISSN 1946-3960. doi: 10.4271/2017-01-0859.

[169] A. Pandal, B. M. Ningegowda, F. Rahantamialisoa, J. Zembi, H. G. Im, and M. Battistoni. Development of a drift-flux velocity closure for a coupled S -Y spray atomization model. *International Journal of Multiphase Flow*, 141:103691, 2021. ISSN 03019322. doi: 10.1016/j.ijmultiphaseflow.2021.103691.

[170] C. A. Passut and R. P. Danner. Correlation of Ideal Gas Enthalpy, Heat Capacity and Entropy. *Industrial & Engineering Chemistry Process Design and Development*, 11(4):543–546, 1972. ISSN 0196-4305. doi: 10.1021/i260044a016.

[171] S. V. Patankar. *Numerical heat transfer and fluid flow*. Series in computational methods in mechanics and thermal sciences. Taylor & Francis, New York, 1980. ISBN 9780891165224.

[172] F. Payri, V. Bermúdez, R. Payri, and F. J. Salvador. The influence of cavitation on the internal flow and the spray characteristics in diesel injection nozzles. *Fuel*, 83 (4-5):419–431, 2004. ISSN 0016-2361. doi: 10.1016/j.fuel.2003.09.010.

[173] F. Payri, R. Payri, F. J. Salvador, and J. Martínez-López. A contribution to the understanding of cavitation effects in Diesel injector nozzles through a combined experimental and computational investigation. *Computers & Fluids*, 58:88–101, 2012. ISSN 00457930. doi: 10.1016/j.compfluid.2012.01.005.

[174] V. B. Pedrozo, I. May, W. Guan, and H. Zhao. High efficiency ethanol-diesel dual-fuel combustion: A comparison against conventional diesel combustion from low to full engine load. *Fuel*, 230:440–451, 2018. ISSN 0016-2361. doi: 10.1016/j.fuel.2018.05.034.

[175] A. Péneloux, E. Rauzy, and R. Fréze. A consistent correction for Redlich-Kwong-Soave volumes. *Fluid Phase Equilibria*, 8(1):7–23, 1982. ISSN 03783812. doi: 10.1016/0378-3812(82)80002-2.

[176] D.-Y. Peng and D. B. Robinson. A New Two-Constant Equation of State. *Industrial & Engineering Chemistry Fundamentals*, 15(1):59–64, 1976. ISSN 0196-4313. doi: 10.1021/i160057a011.

[177] X. Petit, G. Ribert, G. Lartigue, and P. Domingo. Large-eddy simulation of supercritical fluid injection. *The Journal of Supercritical Fluids*, 84:61–73, 2013. ISSN 08968446. doi: 10.1016/j.supflu.2013.09.011.

[178] L. M. Pickett, J. Manin, C. L. Genzale, D. L. Siebers, M. P. B. Musculus, and C. A. Idicheria. Relationship Between Diesel Fuel Spray Vapor Penetration/Dispersion and Local Fuel Mixture Fraction. *SAE International Journal of Engines*, 4(1):764–799, 2011. ISSN 1946-3944. doi: 10.4271/2011-01-0686.

[179] L. M. Pickett, J. Manin, A. Kastengren, and C. Powell. Comparison of Near-Field Structure and Growth of a Diesel Spray Using Light-Based Optical Microscopy and X-Ray Radiography. *SAE International Journal of Engines*, 7(2):1044–1053, 2014. ISSN 1946-3944. doi: 10.4271/2014-01-1412.

[180] L. M. Pickett, C. L. Genzale, and J. Manin. UNCERTAINTY QUANTIFICATION FOR LIQUID PENETRATION OF EVAPORATING SPRAYS AT DIESEL-LIKE CONDITIONS. *Atomization and Sprays*, 25(5):425–452, 2015. ISSN 1044-5110. doi: 10.1615/AtomizSpr.2015010618.

[181] M. Pilch and C. A. Erdman. Use of breakup time data and velocity history data to predict the maximum size of stable fragments for acceleration-induced breakup of a liquid drop. *International Journal of Multiphase Flow*, 13(6):741–757, 1987. ISSN 03019322. doi: 10.1016/0301-9322(87)90063-2.

[182] J. Poblador-Ibanez and W. A. Sirignano. Temporal atomization of a transcritical liquid n-decane jet into oxygen. *International Journal of Multiphase Flow*, 153: 104130, 2022. ISSN 03019322. doi: 10.1016/j.ijmultiphaseflow.2022.104130.

[183] B. E. Poling, J. M. Prausnitz, and J. P. O'Connell. *The properties of gases and liquids*. McGraw-Hill, New York and Bogota and Milan etc., 5th ed. edition, 2001. ISBN 9780070116825.

[184] S. B. Pope. Ten questions concerning the large-eddy simulation of turbulent flows. *New Journal of Physics*, 6:35, 2004. doi: 10.1088/1367-2630/6/1/035.

[185] S. Praneeth and J.-P. Hickey. Uncertainty quantification of tabulated supercritical thermodynamics for compressible Navier-Stokes solvers. *arXiv: Computational Physics*, 2018. URL https://www.semanticscholar.org/paper/Uncertainty-quantification-of-tabulated-for-solvers-Praneeth-Hickey/ba217692c78764fd428e70223e81a98921072d75.

[186] Y. Qi, K. K. Srinivasan, S. R. Krishnan, H. Yang, and K. C. Midkiff. Effect of hot exhaust gas recirculation on the performance and emissions of an advanced injection low pilot-ignited natural gas engine. *International Journal of Engine Research*, 8 (3):289–303, 2007. ISSN 1468-0874. doi: 10.1243/14680874JER02306.

[187] L. Qiu and R. D. Reitz. Simulation of supercritical fuel injection with condensation. *International Journal of Heat and Mass Transfer*, 79:1070–1086, 2014. ISSN 00179310. doi: 10.1016/j.ijheatmasstransfer.2014.08.081.

[188] L. Qiu and R. D. Reitz. An investigation of thermodynamic states during high-pressure fuel injection using equilibrium thermodynamics. *International Journal of Multiphase Flow*, 72:24–38, 2015. ISSN 03019322. doi: 10.1016/j.ijmultiphaseflow.2015.01.011.

[189] J. Qu, T. Faney, J.-C. de Hemptinne, S. Yousef, and P. Gallinari. PTFlash : A vectorized and parallel deep learning framework for two-phase flash calculation. *Fuel*, 331:125603, 2023. ISSN 0016-2361. doi: 10.1016/j.fuel.2022.125603.

[190] H. H. Rachford and J. D. Rice. Procedure for Use of Electronic Digital Computers in Calculating Flash Vaporization Hydrocarbon Equilibrium. *Journal of Petroleum Technology*, 4(10):19–3, 1952. ISSN 0149-2136. doi: 10.2118/952327-G.

[191] O. REDLICH and J. N. S. KWONG. On the thermodynamics of solutions; an equation of state; fugacities of gaseous solutions. *Chemical reviews*, 44(1):233–244, 1949. ISSN 0009-2665. doi: 10.1021/cr60137a013.

[192] R. D. Reitz. Modeling atomization processes in high-pressure vaporizing sprays. *Atomisation and Spray technology*, 3:309–337, 1987.

[193] R. D. Reitz and J. C. Beale. MODELING SPRAY ATOMIZATION WITH THE KELVIN-HELMHOLTZ/RAYLEIGH-TAYLOR HYBRID MODEL. *Atomization and Sprays*, 9(6):623–650, 1999. ISSN 1044-5110. doi: 10.1615/AtomizSpr.v9.i6.40.

[194] B. Reveille, A. Kleemann, V. Knop, and C. Habchi. Potential of Narrow Angle Direct Injection Diesel Engines for Clean Combustion: 3D CFD Analysis. In *SAE Technical Paper Series*, SAE Technical Paper Series. SAE International400 Commonwealth Drive, Warrendale, PA, United States, 2006. doi: 10.4271/2006-01-1365.

[195] G. Ribert, X. Petit, and P. Domingo. High-pressure methane-oxygen flames. Analysis of sub-grid scale contributions in filtered equations of state. *The Journal of Supercritical Fluids*, 121:78–88, 2017. ISSN 08968446. doi: 10.1016/j.supflu.2016.08.020.

[196] G. Ribert, P. Domingo, and L. Vervisch. Analysis of sub-grid scale modeling of the ideal-gas equation of state in hydrogen–oxygen premixed flames. *Proceedings of the Combustion Institute*, 37(2):2345–2351, 2019. ISSN 15407489. doi: 10.1016/j.proci.2018.07.054.

[197] Richards, K.J., Senecal, P.K., and Pomraning, E. CONVERGE 3.0, Convergent Science, Madison, WI (2021).

[198] C. Rodriguez, A. Vidal, P. Koukouvinis, M. Gavaises, and M. A. McHugh. Simulation of transcritical fluid jets using the PC-SAFT EoS. *Journal of Computational Physics*, 374:444–468, 2018. ISSN 00219991. doi: 10.1016/j.jcp.2018.07.030.

[199] C. Rodriguez, H. B. Rokni, P. Koukouvinis, A. Gupta, and M. Gavaises. Complex multicomponent real-fluid thermodynamic model for high-pressure Diesel fuel injection. *Fuel*, 257:115888, 2019. ISSN 0016-2361. doi: 10.1016/j.fuel.2019.115888.

[200] S. Yang. *Modeling of Diesel Injection in Subcritical and Supercritical Conditions. PhD dissertation, University of Paris-Saclay.* PhD thesis, 2019.

[201] F. L. Sacomano Filho, A. Carvalho Santos, A. Vié, and G. C. Krieger Filho. A new robust modeling strategy for multi-component droplet heat and mass transfer in general ambient conditions. *International Journal of Heat and Mass Transfer*, 194:123102, 2022. ISSN 00179310. doi: 10.1016/j.ijheatmasstransfer.2022.123102.

[202] K. Saha, S. Som, and M. Battistoni. INVESTIGATION OF HOMOGENEOUS RELAXATION MODEL PARAMETERS AND THEIR IMPLICATIONS FOR GASOLINE INJECTORS. *Atomization and Sprays*, 27(4):345–365, 2017. ISSN 1044-5110. doi: 10.1615/AtomizSpr.2017016338.

[203] R. Saurel and R. Abgrall. A Multiphase Godunov Method for Compressible Multifluid and Multiphase Flows. *Journal of Computational Physics*, 150(2):425–467, 1999. ISSN 00219991. doi: 10.1006/jcph.1999.6187.

[204] R. Saurel and C. Pantano. Diffuse-Interface Capturing Methods for Compressible Two-Phase Flows. *Annual Review of Fluid Mechanics*, 50(1):105–130, 2018. ISSN 0066-4189. doi: 10.1146/annurev-fluid-122316-050109.

[205] R. Saurel, F. PETITPAS, and R. ABGRALL. Modelling phase transition in metastable liquids: Application to cavitating and flashing flows. *Journal of Fluid Mechanics*, 607:313–350, 2008. ISSN 0022-1120. doi: 10.1017/S0022112008002061.

[206] S. S. Sazhin. Advanced models of fuel droplet heating and evaporation. *Progress in Energy and Combustion Science*, 32(2):162–214, 2006. ISSN 03601285. doi: 10.1016/j.pecs.2005.11.001.

[207] J. Schlottke and B. Weigand. Direct numerical simulation of evaporating droplets. *Journal of Computational Physics*, 227(10):5215–5237, 2008. ISSN 00219991. doi: 10.1016/j.jcp.2008.01.042.

[208] J. Schlottke, E. Dulger, and B. Weigand. A VOF-based 3D numerical investigation of evaporating, deformed droplets. *Progress in Computational Fluid Dynamics, An International Journal*, 9(6/7):426, 2009. ISSN 1468-4349. doi: 10.1504/PCFD.2009.027374.

[209] D. P. Schmidt, C. J. Rutland, and M. L. Corradini. A FULLY COMPRESSIBLE, TWO-DIMENSIONAL MODEL OF SMALL, HIGH-SPEED, CAVITATING NOZZLES. *Atomization and Sprays*, 9(3):255–276, 1999. ISSN 1044-5110. doi: 10.1615/AtomizSpr.v9.i3.20.

[210] G. H. Schnerr and J. Sauer. Physical and numerical modelling of unsteady cavitation dynamics. *ICMF, 4th International Conference on Multiphase Flow*, 2001.

[211] J. Seagrave, J. D. McDonald, E. Bedrick, E. S. Edgerton, A. P. Gigliotti, J. J. Jansen, L. Ke, L. P. Naeher, S. K. Seilkop, M. Zheng, and J. L. Mauderly. Lung toxicity of ambient particulate matter from southeastern U.S. sites with different contributing sources: Relationships between composition and effects. *Environmental health perspectives*, 114(9):1387–1393, 2006. ISSN 0091-6765. doi: 10.1289/ehp.9234.

[212] L. C. SELLE, N. A. OKONG'O, J. Bellan, and K. G. HARSTAD. Modelling of subgrid-scale phenomena in supercritical transitional mixing layers: an a priori study. *Journal of Fluid Mechanics*, 593:57–91, 2007. ISSN 0022-1120. doi: 10.1017/S0022112007008075.

[213] B. A. Sforzo, K. E. Matusik, C. F. Powell, A. L. Kastengren, S. Daly, S. Skeen, E. Cenker, L. M. Pickett, C. Crua, and J. Manin. Fuel Nozzle Geometry Effects on Cavitation and Spray Behavior at Diesel Engine Conditions. In *Proceedings of the 10th International Symposium on Cavitation (CAV2018)*. ASME Press, 2018. ISBN 9780791861851. doi: https://doi.org/10.1115/1.861851_ch90.

[214] A. Sharma. Level set method for computational multi-fluid dynamics: A review on developments, applications and analysis. *Sadhana*, 40(3):627–652, 2015. ISSN 0256-2499. doi: 10.1007/s12046-014-0329-3.

[215] J. Shinjo. Recent Advances in Computational Modeling of Primary Atomization of Liquid Fuel Sprays. *Energies*, 11(11):2971, 2018. ISSN 1996-1073. doi: 10.3390/en11112971.

[216] J. Shinjo and A. Umemura. Simulation of liquid jet primary breakup: Dynamics of ligament and droplet formation. *International Journal of Multiphase Flow*, 36(7):513–532, 2010. ISSN 03019322. doi: 10.1016/j.ijmultiphaseflow.2010.03.008.

[217] S.Jafari. *Numerical modeling of transcritical turbulent jets using a tabulated real-fluid approach. PhD dissertation, University of Paris-Saclay.* PhD thesis, 2022.

[218] G. Soave. Equilibrium constants from a modified Redlich-Kwong equation of state. *Chemical Engineering Science*, 27(6):1197–1203, 1972. ISSN 00092509. doi: 10.1016/0009-2509(72)80096-4.

[219] A. Sou, S. Hosokawa, and A. Tomiyama. Effects of cavitation in a nozzle on liquid jet atomization. *International Journal of Heat and Mass Transfer*, 50(17-18):3575–3582, 2007. ISSN 00179310. doi: 10.1016/j.ijheatmasstransfer.2006.12.033.

[220] A. Sou, B. Biçer, and A. Tomiyama. Numerical simulation of incipient cavitation flow in a nozzle of fuel injector. *Computers & Fluids*, 103:42–48, 2014. ISSN 00457930. doi: 10.1016/j.compfluid.2014.07.011.

[221] K. K. Srinivasan, S. R. Krishnan, S. Singh, K. C. Midkiff, S. R. Bell, W. Gong, S. B. Fiveland, and M. Willi. The Advanced Injection Low Pilot Ignited Natural Gas Engine: A Combustion Analysis. *Journal of Engineering for Gas Turbines and Power*, 128(1):213–218, 2006. ISSN 0742-4795. doi: 10.1115/1.1915428.

[222] K. K. Srinivasan, S. R. Krishnan, and Y. Qi. Cyclic Combustion Variations in Dual Fuel Partially Premixed Pilot-Ignited Natural Gas Engines. *Journal of Energy Resources Technology*, 136(1):042203, 2014. ISSN 0195-0738. doi: 10.1115/1.4024855.

[223] G. Strotos, P. Koukouvinis, A. Theodorakakos, M. Gavaises, and G. Bergeles. Transient heating effects in high pressure Diesel injector nozzles. *International Journal of Heat and Fluid Flow*, 51:257–267, 2015. doi: 10.1016/j.ijheatfluidflow.2014.10.010.

[224] G. Strotos, I. Malgarinos, N. Nikolopoulos, and M. Gavaises. Predicting the evaporation rate of stationary droplets with the VOF methodology for a wide range of ambient temperature conditions. *International Journal of Thermal Sciences*, 109: 253–262, 2016. ISSN 12900729. doi: 10.1016/j.ijthermalsci.2016.06.022.

[225] S. Subramaniam. Lagrangian–Eulerian methods for multiphase flows. *Progress in Energy and Combustion Science*, 39(2-3):215–245, 2013. ISSN 03601285. doi: 10.1016/j.pecs.2012.10.003.

[226] Y. Sun and C. Beckermann. Diffuse interface modeling of two-phase flows based on averaging: Mass and momentum equations. *Physica D: Nonlinear Phenomena*, 198 (3-4):281–308, 2004. ISSN 01672789. doi: 10.1016/j.physd.2004.09.003.

[227] M. Sussman, P. Smereka, and S. Osher. A Level Set Approach for Computing Solutions to Incompressible Two-Phase Flow. *Journal of Computational Physics*, 114(1):146–159, 1994. ISSN 00219991. doi: 10.1006/jcph.1994.1155.

[228] A. Tekawade, B. A. Sforzo, K. E. Matusik, K. Fezzaa, A. L. Kastengren, and C. F. Powell. Time-resolved 3D imaging of two-phase fluid flow inside a steel fuel injector using synchrotron X-ray tomography. *Scientific reports*, 10(1):8674, 2020. doi: 10.1038/s41598-020-65701-x.

[229] H. Terashima and M. Koshi. Approach for simulating gas–liquid-like flows under supercritical pressures using a high-order central differencing scheme. *Journal of Computational Physics*, 231(20):6907–6923, 2012. ISSN 00219991. doi: 10.1016/j.jcp.2012.06.021.

[230] R. Torelli, S. Som, Y. Pei, Y. Zhang, and M. Traver. Influence of fuel properties on internal nozzle flow development in a multi-hole diesel injector. *Fuel*, 204:171–184, 2017. ISSN 0016-2361. doi: 10.1016/j.fuel.2017.04.123.

[231] C. Traxinger, M. Pfitzner, S. Baab, G. Lamanna, and B. Weigand. Experimental and numerical investigation of phase separation due to multicomponent mixing at high-pressure conditions. *Physical Review Fluids*, 4(7), 2019. doi: 10.1103/PhysRevFluids.4.074303.

[232] C. Traxinger, J. Zips, M. Banholzer, and M. Pfitzner. A pressure-based solution framework for sub- and supersonic flows considering real-gas effects and phase separation under engine-relevant conditions. *Computers & Fluids*, 202:104452, 2020. ISSN 00457930. doi: 10.1016/j.compfluid.2020.104452.

[233] G. Tretola, K. Vogiatzaki, and S. Navarro-Martinez. Effect of the density ratio variation on the dynamics of a liquid jet injected into a gaseous cross-flow. *Physics of Fluids*, 33(9):092120, 2021. ISSN 1070-6631. doi: 10.1063/5.0064149.

[234] G. Tretola, K. Vogiatzaki, and S. Navarro-Martinez. Implementation of a probabilistic surface density volume of fluid approach for spray atomisation. *Computers & Fluids*, 230:105121, 2021. ISSN 00457930. doi: 10.1016/j.compfluid.2021.105121.

[235] T. Trummler, D. Rahn, S. J. Schmidt, and N. A. Adams. LARGE EDDY SIMULATIONS OF CAVITATING FLOW IN A STEP NOZZLE WITH INJECTION INTO GAS. *Atomization and Sprays*, 28(10):931–955, 2018. ISSN 1044-5110. doi: 10.1615/AtomizSpr.2018027386.

[236] P. Tudisco and S. Menon. Analytical framework for real-gas mixtures with phase-equilibrium thermodynamics. *The Journal of Supercritical Fluids*, 164:104929, 2020. ISSN 08968446. doi: 10.1016/j.supflu.2020.104929.

[237] U. Unnikrishnan, J. C. Oefelein, and V. Yang. Subgrid modeling of the filtered equation of state with application to real-fluid turbulent mixing at supercritical pressures. *Physics of Fluids*, 34(6):065112, 2022. ISSN 1070-6631. doi: 10.1063/5.0088074.

[238] A. Vallet and R. Borghi. Modélisation eulerienne de l'atomisation d'un jet liquide. *Comptes Rendus de l'Académie des Sciences - Series IIB - Mechanics-Physics-Astronomy*, 327(10):1015–1020, 1999. ISSN 12874620. doi: 10.1016/S1287-4620(00)87013-1.

[239] A. Vallet, A. A. Burluka, and R. Borghi. DEVELOPMENT OF A EULERIAN MODEL FOR THE "ATOMIZATION" OF A LIQUID JET. *Atomization and Sprays*, 11(6):24, 2001. ISSN 1044-5110. doi: 10.1615/AtomizSpr.v11.i6.20.

[240] J. van der Waals. The Equation of State for Gases and Liquids, Nobel Lectures in Physics, 1967.

[241] A. Vidal, K. Kolovos, M. R. Gold, R. J. Pearson, P. Koukouvinis, and M. Gavaises. Preferential cavitation and friction-induced heating of multi-component Diesel fuel surrogates up to 450MPa. *International Journal of Heat and Mass Transfer*, 166:120744, 2021. ISSN 00179310. doi: 10.1016/j.ijheatmasstransfer.2020.120744.

[242] J.-H. Wang, S. Yang, C. Habchi, X. Y. Hu, and N. A.Adams. A multi-component real-fluid two-phase flow solver with high-order finite-difference schemes. *ILASS-Europe, 29th Conference on Liquid Atomization and Spray Systems*, 2019.

[243] Y. Wang, L. Qiu, R. D. Reitz, and R. Diwakar. Simulating cavitating liquid jets using a compressible and equilibrium two-phase flow solver. *International Journal of Multiphase Flow*, 63:52–67, 2014. ISSN 03019322. doi: 10.1016/j.ijmultiphaseflow.2014.03.006.

[244] C. Ware, W. Knight, and D. Wells. Memory intensive statistical algorithms for multibeam bathymetric data. *Computers & Geosciences*, 17(7):985–993, 1991. ISSN 00983004. doi: 10.1016/0098-3004(91)90093-S.

[245] L. Wei and P. Geng. A review on natural gas/diesel dual fuel combustion, emissions and performance. *Fuel Processing Technology*, 142:264–278, 2016. ISSN 03783820. doi: 10.1016/j.fuproc.2015.09.018.

[246] M. S. Wertheim. Fluids with highly directional attractive forces. IV. Equilibrium polymerization. *Journal of Statistical Physics*, 42(3-4):477–492, 1986. ISSN 0022-4715. doi: 10.1007/BF01127722.

[247] G. Xiao, K. H. Luo, X. Ma, and S. Shuai. A molecular dynamics study of fuel droplet evaporation in sub- and supercritical conditions. *Proceedings of the Combustion Institute*, 37(3):3219–3227, 2019. ISSN 15407489. doi: 10.1016/j.proci.2018.09.020.

[248] S. Xu, S. Zhong, K. M. Pang, S. Yu, M. Jangi, and X.-S. Bai. Effects of ambient methanol on pollutants formation in dual-fuel spray combustion at varying ambient temperatures: A large-eddy simulation. *Applied Energy*, 279:115774, 2020. ISSN 03062619. doi: 10.1016/j.apenergy.2020.115774.

[249] Q. Xue, S. Som, P. K. Senecal, and E. Pomraning. Large Eddy Simulation of fuel-spray under non-reacting IC engine conditions. *Atomization and Sprays*, 23(10): 925–955, 2013. ISSN 1044-5110. doi: 10.1615/AtomizSpr.2013008320.

[250] Q. Xue, M. Battistoni, C. F. Powell, D. E. Longman, S. P. Quan, E. Pomraning, P. K. Senecal, D. P. Schmidt, and S. Som. An Eulerian CFD model and X-ray radiography for coupled nozzle flow and spray in internal combustion engines. *International Journal of Multiphase Flow*, 70:77–88, 2015. ISSN 03019322. doi: 10.1016/j.ijmultiphaseflow.2014.11.012.

[251] V. Yakhot, S. A. Orszag, S. Thangam, T. B. Gatski, and C. G. Speziale. Development of turbulence models for shear flows by a double expansion technique. *Physics of Fluids A: Fluid Dynamics*, 4(7):1510–1520, 1992. ISSN 0899-8213. doi: 10.1063/1.858424.

[252] B. Yang, Q. Duan, B. Liu, and K. Zeng. Parametric investigation of low pressure dual-fuel direct injection on the combustion performance and emissions characteristics in a RCCI engine fueled with diesel and CH4. *Fuel*, 260:116408, 2020. ISSN 0016-2361. doi: 10.1016/j.fuel.2019.116408.

[253] S. Yang and C. Habchi. Real-fluid phase transition in cavitation modeling considering dissolved non-condensable gas. *Physics of Fluids*, 32(3):032102, 2020. ISSN 1070-6631. doi: 10.1063/1.5140981.

[254] S. Yang, P. Yi, and C. Habchi. Real-fluid injection modeling and LES simulation of the ECN Spray A injector using a fully compressible two-phase flow approach. *International Journal of Multiphase Flow*, 122:103145, 2020. ISSN 03019322. doi: 10.1016/j.ijmultiphaseflow.2019.103145.

[255] P. Yi, S. Jafari, S. Yang, and C. Habchi. Numerical analysis of subcritical evaporation and transcritical mixing of droplet using a tabulated multicomponent vapor-liquid equilibrium model. *ILASS-Europe, 29th Conference on Liquid Atomization and Spray Systems*, 2019.

[256] P. Yi, S. Yang, C. Habchi, and R. Lugo. A multicomponent real-fluid fully compressible four-equation model for two-phase flow with phase change. *Physics of Fluids*, 31(2):026102, 2019. ISSN 1070-6631. doi: 10.1063/1.5065781.

[257] Z. Yue and R. D. Reitz. An equilibrium phase spray model for high-pressure fuel injection and engine combustion simulations. *International Journal of Engine Research*, 20(2):203–215, 2019. ISSN 1468-0874. doi: 10.1177/1468087417744144.

[258] Z. Yue, H. Zhu, C. Wang, Z. Li, H. Wang, M. Yao, and R. D. Reitz. Artificial Neural Network Models for Phase Equilibrium Predictions Under Engine Trans/Supercritical Spray Conditions. *SSRN Electronic Journal*, 2022. doi: 10.2139/ssrn.4181403.

[259] H. Zhang and S. Yang. Multi-component transcritical flow simulation using in situ adaptive tabulation of vapor-liquid equilibrium solutions. *in ILASS-Americas 31st Annual Conference on Liquid Atomization and Spray Systems*, 2021.

[260] L. Zhang, Z. He, W. Guan, Q. Wang, and S. Som. Simulations on the cavitating flow and corresponding risk of erosion in diesel injector nozzles with double array holes. *International Journal of Heat and Mass Transfer*, 124:900–911, 2018. ISSN 00179310. doi: 10.1016/j.ijheatmasstransfer.2018.03.086.

[261] P. J. Zwart, A. G. Gerber, and T. Belamri. A Two-Phase Flow Model for Predicting Cavitation Dynamics. *ICMF, International Conference on Multiphase Flow*, 2004.